

UC San Diego

UC San Diego Electronic Theses and Dissertations

Title

Nonlinear Winkler-based shallow foundation model for performance assessment of seismically loaded structures

Permalink

<https://escholarship.org/uc/item/6b7322bj>

Author

Raychowdhury, Prishati

Publication Date

2008

Peer reviewed|Thesis/dissertation

UNIVERSITY OF CALIFORNIA, SAN DIEGO

**Nonlinear Winkler-based Shallow Foundation Model for Performance Assessment of
Seismically Loaded Structures**

A dissertation submitted in partial satisfaction of the requirements for the degree
Doctor of Philosophy
in
Structural Engineering

by

Prishati Raychowdhury

Committee in charge:

Professor Tara C. Hutchinson, Chair

Professor Ahmed Elgamal

Professor Geoffrey Martin

Professor Jose Restrepo

Professor Peter Shearer

2008

Copyright
Prishati Raychowdhury, 2008
All rights reserved

The dissertation of Prishati Raychowdhury
is approved, and it is acceptable in quality
and form for publication on microfilm:

Chair

University of California, San Diego

2008

DEDICATED TO MY PARENTS

TABLE OF CONTENTS

	Page
SIGNATURE	iii
DEDICATION	iv
TABLE OF CONTENTS	v
LIST OF FIGURES	x
LIST OF TABLES	xxiii
ACKNOWLEDGMENTS	xxv
CURRICULUM VITAE	xxvii
ABSTRACT OF THE DISSERTATION	xxix
Chapter 1: Introduction and Previous Work	1
1.1 Problem Importance	1
1.2 Previous Work	4
1.2.1 Numerical and Analytical Efforts	4
1.2.2 Experimental Efforts	9
1.2.3 Current Design Practice	14
1.3 Summary and Observations from Previous Work	16
1.4 Objective	16
1.5 Scope of the Present Study	17

1.6	Organization of Dissertation	18
Chapter 2: Beam-on-Nonlinear-Winkler- Foundation Model		20
2.1	Introduction	20
2.2	Description of the BNWF Model	20
2.3	Attributes of the BNWF Model	22
2.4	Constitutive Material Models	24
2.4.1	<i>QzSimple1</i> Material	25
2.4.2	<i>PySimple1</i> Material	27
2.4.3	<i>TzSimple1</i> Material	28
2.5	BNWF Model Parameters	28
2.5.1	Ultimate Load Capacity (Vertical and Lateral)	30
2.5.2	Vertical and Lateral stiffness (K_v and K_h)	34
2.5.3	Tension Capacity, TP	47
2.5.4	Soil Type	50
2.5.5	End Length Ratio, R_e	51
2.5.6	Stiffness Intensity Ratio, R_k	55
2.5.7	Spring Spacing, l_e/L	59
2.5.8	Elastic Range, C_r	61
2.5.9	Post-yield Stiffness, k_p	63
2.5.10	Unloading Stiffness, k_{unl}	66
2.6	Limitations of the Proposed BNWF Model	67
2.7	Summary Remarks	69
Chapter 3: Calibration of Mechanistic Springs		70
3.1	Introduction	70
3.1.1	Axial Load Tests	71
3.1.2	Lateral Load Tests	71
3.2	Selection of Basic Input Parameters	78
3.3	Calibration of Shape Parameters	79

3.4	Effect of Backbone Curve Modification on Overall Response	84
3.5	Summary Remarks	92
Chapter 4: BNWF Model Validation		93
4.1	Introduction	93
4.2	Comparison with Tests on Shearwall Footings	94
4.2.1	Effect of Nondimensional Moment to Shear Ratio	97
4.2.2	Effect of Vertical Factor of Safety	98
4.2.3	Effect of Soil Type	98
4.3	Comparison with Tests on Bridge Footings	112
4.3.1	Moment Demand	114
4.3.2	Displacement Demands	114
4.4	Summary Remarks	119
Chapter 5: Parametric Study		121
5.1	Introduction	121
5.2	Experimental Data	122
5.3	Selection of Study Parameters	127
5.4	Results of Parametric Study	128
5.5	Sensitivity Analysis: Tornado Diagram and FOSM Analysis	140
5.5.1	Sensitivity of Each Response Parameter	143
5.5.2	Sensitivity of Overall Footing Response	153
5.6	Summary Remarks	156
Chapter 6: Effect of SFSI on Shearwall Buildings		157
6.1	Introduction	157
6.2	Description of Structures	158
6.3	Footing and Soil Conditions	159
6.4	Numerical Modeling	161
6.4.1	Types of Input Loads	161

6.4.2	Numerical Analysis Parameters	165
6.5	Results and Discussion	165
6.5.1	Eigenvalue Analysis	165
6.5.2	Pushover Analysis	167
6.5.3	Slow Cyclic Analysis	168
6.5.4	Ground Motion Analysis	170
6.6	Energy Dissipation	180
6.7	Comparison with Macro Model	186
6.8	Summary Remarks	188
Chapter 7:	Frame-Shearwall Dual Structure	190
7.1	Introduction	190
7.2	Wall-frame-foundation System Description	191
7.3	Structural Modeling	193
7.4	SFSI Modeling	194
7.5	Selection of Ground Motions	196
7.6	Solution Technique Adopted	196
7.7	Results and Discussion	198
7.7.1	Eigenvalue Analysis	198
7.7.2	Nonlinear Pushover Analysis	198
7.7.3	Time History Response	201
7.7.4	Response Parameters	205
7.8	Summary Remarks	206
Chapter 8:	OpenSees Implementation	209
8.1	Introduction	209
8.2	OpenSees	210
8.3	<i>ShallowFoundationGen</i> Command	211
8.3.1	Argument 1: \$FoundationTag	212
8.3.2	Argument 2: \$ConnectNode	212

8.3.3	Argument 3: \$InputFile	213
8.3.4	Argument 4: \$FootingCondition	215
8.4	Important Implementation Details	218
8.4.1	Node Numbering	218
8.4.2	Material Numbering	218
8.4.3	Element Numbering	220
8.4.4	Geometric Transfer Tag	220
8.4.5	Some Useful Variables	221
8.4.6	Example Problems	221
Chapter 9:	Summary and Conclusions	225
9.1	Summary	225
9.2	Major Conclusions	226
9.3	Scope of Future Work	228
Appendix A:	Normalized Footing Demands	229
Appendix B:	Comparison of Experiment Versus Simulation Results	244
Appendix C:	Ground Motion Details	257
Appendix D:	Input and Output Files for Example Problems	268
D.1	Input and Output Files for Example 1	268
D.2	Input and Output Files for Example 2	274
References	282

LIST OF FIGURES

	Page
Figure 1.1 Different modes of foundation deformation	2
Figure 1.2 Rigid rocking block model (from Housner, 1963)	2
Figure 1.3 Effect of foundation stiffness on structure (from ATC-40, 1996) . . .	3
Figure 1.4 (a) Idealized Winkler foundation model and (b) $M-\theta$ envelopes after Chopra and Yim (1985)	6
Figure 1.5 Winkler foundation modeling and result from Nakaki and Hart (1987)	7
Figure 1.6 Backbone curves after Allotey and Naggar (2007)	8
Figure 1.7 Centrifuge test set-up at University of California, Davis for: (a) shearwall-footing model (Gajan et al., 2003a), (b) bridge-pier-footing model (Ugalde, 2007) and (c) frame-wall-footing model (Chang et al., 2007) (All units in prototype)	11
Figure 2.1 Schematic diagram showing springs and their orientations for typi- cal soil-pile model	22
Figure 2.2 Schematic diagram of the proposed BNWF model for shallow foun- dations	36
Figure 2.3 Model capability in terms of moment-rotation, settlement-rotation and shear-sliding response (based on centrifuge test of strip footing resting on dense dry sand of $D_r = 80\%$ and $FS_v = 2.3$)	37
Figure 2.4 BNWF Mesh discretization with variable stiffness intensity (Harden et al., 2005)	37

Figure 2.5	Various simple material models available for shallow foundation modeling: (a) elastic (b) elastic-perfectly plastic and (c) general hysteretic backbone curves as available in OpenSees (2008)	38
Figure 2.6	Backbone curve of hysteretic materials in parallel after Martin and Yan (1997)	38
Figure 2.7	<i>QzSimple1</i> , <i>PySimple1</i> and <i>TzSimple1</i> material models used in conjunction with zeroLength element	39
Figure 2.8	<i>QzSimple1</i> backbone curve: (a) backbone curves used for soil-pile modeling and (b) general backbone curve	39
Figure 2.9	Cyclic response of <i>QzSimple1</i> (Boulanger, 2000b)	40
Figure 2.10	<i>PySimple1</i> backbone curve	40
Figure 2.11	Cyclic response of <i>PySimple1</i> (Boulanger, 2000a)	41
Figure 2.12	<i>TzSimple1</i> backbone curve	41
Figure 2.13	Cyclic response of <i>TzSimple1</i> (Boulanger, 2000c)	42
Figure 2.14	Rotational input motion applied at the base of a 5m square footing .	42
Figure 2.15	Variation of (a) vertical load capacity and (b) horizontal load capacity with friction angle ϕ' for a 5m square footing with $D_f/B = 0.3$, $c' = 0$ and $\gamma = 16kN/m^3$:	43
Figure 2.16	Effect of change in friction angle ϕ' on the footing response: (a) moment versus rotation and (b) settlement versus rotation	43
Figure 2.17	Effect of change in friction angle ϕ' on the footing response: (a) moment time history, (b) settlement time history	44
Figure 2.18	Sensitivity of friction angle ϕ' on footing response: (a) normalized moment demand and (b) normalized settlement demand	44
Figure 2.19	Vertical and lateral stiffness using expressions of Gazetas (1991a) for the 5m square footing with $D_f/B = 0.3$ and $\nu = 0.4$	46
Figure 2.20	Effect of varying soil modulus of elasticity (E_s) on footing response: (a) moment versus rotation, (b) settlement versus rotation and (c) shear versus sliding	47

Figure 2.21	Variation of normalized: (a) settlement and (b) sliding demands with varying modulus of elasticity of the soil	48
Figure 2.22	Effect of tension capacity TP on a single spring response	49
Figure 2.23	Effect of varying the tension capacity on the overall footing response: (a) moment versus rotation and (b) settlement versus rotation	49
Figure 2.24	Effect of variation in tension capacity on (a) normalized moment and (b) normalized settlement demands of the footing	50
Figure 2.25	Winkler component model of rectangular spread footing (ATC-40, 1996)	52
Figure 2.26	Normalized end length versus footing aspect ratio given by (Harden et al., 2005) along with ATC-40 (1996) recommended value	53
Figure 2.27	Effect of end length ratio R_e on footing response: (a) moment versus rotation and (b) settlement versus rotation	54
Figure 2.28	Sensitivity of end length ratio on settlement demand	54
Figure 2.29	Effect of end length ratio on strip footing with $B/L=0.23$ in terms of (a) moment–rotation and (b) settlement–rotation	55
Figure 2.30	Stiffness intensity ratio (R_k) as a function of footing aspect ratio (Figure from Harden et al. (2005))	57
Figure 2.31	Effect of stiffness ratio on footing response: (a) moment versus rotation and (b) settlement versus rotation	57
Figure 2.32	Stiffness intensity ratio versus normalized settlement demands for the 5m square footing considered here	58
Figure 2.33	Effect of spring spacing on overall footing response: (a)–(b) moment versus rotation and (c)–(d) settlement versus rotation	60
Figure 2.34	Effect of spring spacing on normalized settlement demand	61
Figure 2.35	Effect of varying C_r on a single spring’s load–displacement relationship	62
Figure 2.36	Effect of C_r on footing response	63
Figure 2.37	Effect of C_r on normalized maximum settlement demand	63

Figure 2.38	Effect of parameter α_{80} on a single spring backbone curve	65
Figure 2.39	Effect of varying the parameter α_{80} (by varying c) on the footing: (a) moment versus rotation and (b) settlement versus rotation responses	66
Figure 2.40	Effect of changing the parameter c on the settlement demand: (a) c versus α_{80} and (b) α_{80} versus normalized settlement demand	66
Figure 2.41	Effect of unloading stiffness k_{unl} on a single spring load versus displacement relationship	68
Figure 2.42	Effect of unloading stiffness k_{unl} on footing (a) moment versus rotation and (b) settlement versus rotation responses	68
Figure 3.1	Centrifuge test set-up at UC Davis (Rosebrook and Kutter, 2001a)	72
Figure 3.2	Field test set-up at Texas A & M (Briaud and Gibbens, 1994)	73
Figure 3.3	(a) Dimensions and test set-up (b) Force contribution in lateral resistance (Gadre and Dobry, 1998)	75
Figure 3.4	Footing model set-ups for centrifuge tests (Gadre and Dobry, 1998)	75
Figure 3.5	Test set-up for lateral load tests (Rollins and Cole, 2006)	76
Figure 3.6	Test set-up for passive pressure load tests (Duncan and Mokwa, 2001)	77
Figure 3.7	Variation of (a) z_{50} and (b) k_{factor} for sand with normalized parameter $Q_{ult}/A_f G$ (for q-z material)	79
Figure 3.8	Sample regression analysis to derive the parameter c : (a) Normalized load versus normalized displacement with different c values; (b) Normalized residual load versus normalized displacement; (c) Summation of normalized residual load with varying c	81
Figure 3.9	Variation of (a) C_r and (b) c for sand with normalized parameter $Q_{ult}/A_f G$ (for q-z material)	82
Figure 3.10	Regressed backbone for q-z material overlaid with axial tests (sand)	83
Figure 3.11	Regressed backbone for q-z material for sand (for cleaner view)	84
Figure 3.12	Regressed backbone for p-x material (sand) overlaid with passive tests on clean sand	85

Figure 3.13	Regressed backbone for p-x material (silty sand) overlaid with passive tests on silty sand	86
Figure 3.14	Regressed backbone for t-x material overlaid with sliding tests	87
Figure 3.15	(a) Example structure-foundation system with BNWF model and (b) applied lateral displacement at the top of the structure	88
Figure 3.16	Effect of the modified backbones on the response of a shallow 5m square footing subjected to quasi-static cyclic loading	89
Figure 3.17	Effect of the modified backbones on the response of a shallow 5m x 3m rectangular footing ($B/L = 0.6$) subjected to quasi-static cyclic loading	90
Figure 3.18	Effect of the modified backbones on the response of a shallow 5m x 1.5m rectangular footing ($B/L = 0.3$) subjected to quasi-static cyclic loading	91
Figure 3.19	End q-z spring responses for (a) 5m x 5m footing ($B/L = 1$) (b) 5m x 3m footing ($B/L = 0.6$) (c) 5m x 1.5m footing ($B/L = 0.3$)	92
Figure 4.1	(a) Building-footing test schematic diagram and (b) idealized model	96
Figure 4.2	Footing response comparison for test SSG02-02 (static cyclic test on dense sand with $D_r = 80\%$, $FS_v = 5.2$ and $M/HL = 0.41$): (a) moment-rotation, (b) settlement-rotation, (c) shear-sliding, (d) settlement-sliding and (e) input displacement	99
Figure 4.3	Footing response comparison for test SSG02-03 (static cyclic test on dense sand with $D_r = 80\%$, $FS_v = 5.2$ and $M/HL = 1.75$): (a) moment-rotation, (b) settlement-rotation, (c) shear-sliding, (d) settlement-sliding and (e) input displacement	100
Figure 4.4	Footing response comparison for SSG02-05 (static cyclic test on dense sand with $D_r = 80\%$, $FS_v = 2.6$ and $M/HL = 1.72$): (a) moment-rotation, (b) settlement-rotation, (c) shear-sliding, (d) settlement-sliding and (e) input displacement	101

Figure 4.5	Footing response comparison for test SSG03–02 (static cyclic test on dense sand with $D_r = 80\%$, $FS_v = 2.5$ and $M/HL = 0.45$): (a) moment-rotation, (b) settlement-rotation, (c) shear-sliding, (d) settlement-sliding and (e) input displacement	102
Figure 4.6	Footing response comparison for test SSG03–03 (static cyclic test on dense sand with $D_r = 80\%$, $FS_v = 14.0$ and $M/HL = 1.77$): (a) moment-rotation, (b) settlement-rotation, (c) shear-sliding, (d) settlement-sliding and (e) input displacement	103
Figure 4.7	Footing response comparison for test SSG04–06 (static cyclic test on dense sand with $D_r = 80\%$, $FS_v = 2.3$ and $M/HL = 1.20$): (a) moment-rotation, (b) settlement-rotation, (c) shear-sliding, (d) settlement-sliding and (e) input displacement	104
Figure 4.8	Footing response comparison for test SSG03–07 (dynamic test on dense sand with $D_r = 80\%$, $FS_v = 7.2$ and $M/HL = 1.80$): (a) moment-rotation, (b) settlement-rotation, (c) shear-sliding, (d) settlement-sliding and (e) input acceleration	105
Figure 4.9	Footing response comparison for test SSG04–10 (dynamic test on dense sand with $D_r = 80\%$, $FS_v = 4.0$ and $M/HL = 1.80$): (a) moment-rotation, (b) settlement-rotation, (c) shear-sliding, (d) settlement-sliding and (e) input acceleration	106
Figure 4.10	Footing response comparison for test KRR03–02 (static cyclic test on 100 kPa clay with $FS_v = 2.8$ and $M/HL = 1.80$): (a) moment-rotation, (b) settlement-rotation, (c) shear-sliding, (d) settlement-sliding and (e) input displacement	107
Figure 4.11	Footing response comparison for test KRR03–02 (dynamic test on 100 kPa clay with $FS_v = 2.8$ and $M/HL = 1.70$): (a) moment-rotation, (b) settlement-rotation, (c) input acceleration	108
Figure 4.12	Performance of BNWF model in predicting the shearwall-footing response	111

Figure 4.13	(a) Bridge-footing test schematic after Ugalde (2007) and (b) BNWF idealization	113
Figure 4.14	(a) Moment–rotation and (b) Settlement–rotation for JAU01–E05, (c) Moment–rotation and (d) Settlement–rotation for JAU01–F05, (e) Acceleration time history and (f) Input motion and acceleration response spectra used in the event	115
Figure 4.15	(a) Moment–rotation and (b) Settlement–rotation for JAU01–E06, (c) Moment–rotation and (d) Settlement–rotation for JAU01–F06, (e) Acceleration time history and (f) Input motion and acceleration response spectra used in the event	116
Figure 4.16	(a) Moment–rotation and (b) Settlement–rotation for JAU01–E08, (c) Moment–rotation and (d) Settlement–rotation for JAU01–F08, (e) Acceleration time history and (f) Input motion and acceleration response spectra used in the event	117
Figure 4.17	Summary of bridge results	119
Figure 5.1	Input motions for static tests: (a) SSG02-02 (b) SSG02-03 (c) SSG02-05 (d) SSG03-02 (e) SSG03-03 (f) SSG04-06 (tests by Gajan et al. (2003a,b, 2006))	125
Figure 5.2	Input motions for dynamic tests: (a) SSG03-07 (b) SSG04-10, carried out by Gajan et al. (2003b, 2006)	126
Figure 5.3	Input acceleration time histories: (a) Shake-5 for JAU01-E05 and JAU01-F05 tests, (b) Shake-6 for JAU01-E06 and JAU01-F06 tests, and (c) Shake-8 for JAU01-E08 and JAU01-F08 tests (Ugalde, 2007)	126
Figure 5.4	Mean normalized demands versus friction angle, ϕ' : (a) moment, (b) shear, (c) sliding, (d) settlement and (e) rotation	135
Figure 5.5	Variation of all mean normalized demands with friction angle, ϕ'	135
Figure 5.6	Variation of mean normalized demands with Poisson’s ratio, ν	136
Figure 5.7	Vertical and lateral stiffness variation with Poisson’s ratio (stiffness calculated after Gazetas (1991a))	136

Figure 5.8	Variation of mean normalized demands with Modulus of elasticity, E_s	137
Figure 5.9	Variation of mean normalized demands with tension capacity, TP	137
Figure 5.10	Variation of mean normalized demands with end length ratio, R_e	138
Figure 5.11	Variation of mean normalized demands with stiffness ratio, R_k	138
Figure 5.12	Variation of mean normalized demands with spring spacing, l_e/L	139
Figure 5.13	Tornado diagram for normalized moment demand	145
Figure 5.14	Tornado diagram for normalized shear demand	146
Figure 5.15	Tornado diagram for normalized sliding demand	146
Figure 5.16	Tornado diagram for normalized settlement demand	147
Figure 5.17	Tornado diagram for normalized rotation demand	147
Figure 5.18	Relative variance contribution for normalized moment demand from FOSM analysis	148
Figure 5.19	Relative variance contribution for normalized shear demand from FOSM analysis	148
Figure 5.20	Relative variance contribution for normalized sliding demand from FOSM analysis	149
Figure 5.21	Relative variance contribution for normalized settlement demand from FOSM analysis	149
Figure 5.22	Relative variance contribution for normalized rotation demand from FOSM analysis	150
Figure 5.23	Relative variance contribution for normalized moment demand from FOSM analysis (keeping TP constant)	150
Figure 5.24	Relative variance contribution for normalized shear demand from FOSM analysis (keeping TP constant)	151
Figure 5.25	Relative variance contribution for normalized sliding demand from FOSM analysis (keeping TP constant)	151
Figure 5.26	Relative variance contribution for normalized settlement demand from FOSM analysis (keeping TP constant)	152

Figure 5.27	Relative variance contribution for normalized rotation demand from FOSM analysis (keeping TP constant)	152
Figure 5.28	Sensitivity of overall norm relative error	154
Figure 5.29	Relative variance contribution for overall norm relative error from FOSM analysis	155
Figure 5.30	Relative variance contribution for overall norm relative error ignoring tension capacity	155
Figure 6.1	Plan view of the benchmark structure with shear walls considered in OpenSees simulations. Tributary area for the vertical loads carried by the wall footings is shown in grey (adapted from Gajan et al. (2008))	158
Figure 6.2	Geometry and dimensions of the shearwall-footing models (units in m): (a) 1-story building, (b) 4-story building, (c) 5-story building	159
Figure 6.3	Numerical model of 4-story reference structure	162
Figure 6.4	Slow cyclic input drift	163
Figure 6.5	Acceleration time history of (a) gm-1 (50% in 50 yrs), (b) gm-2 (10% in 50 yrs), and (c) gm-3 (2% in 50 yrs)	163
Figure 6.6	Elastic 5% damped (a) acceleration response spectra and (b) displacement response spectra for motions shown in Figure 6.5 with the fundamental periods of three buildings overlaid	164
Figure 6.7	Nonlinear pushover analysis	168
Figure 6.8	Footing response for cyclic loading of 1-story building	169
Figure 6.9	Footing response for cyclic loading of 4-story building	169
Figure 6.10	Footing response for cyclic loading of 5-story building	170
Figure 6.11	Footing response for 1-story building	171
Figure 6.12	Structural response for 1-story building	171
Figure 6.13	Footing response for 4-story building	172
Figure 6.14	Structural response for 4-story building	172
Figure 6.15	Footing response for 5-story building	173
Figure 6.16	Structural response for 5-story building	173

Figure 6.17	Displacement demands of the models	178
Figure 6.18	Summary of structural and footing demands normalized by fixed base demands: (a)-(c) moment demand, (d)-(f) shear demand, (g)-(i) peak roof acceleration demand, (j)-(l) total drift demand	179
Figure 6.19	Energy dissipation E_D in a cycle of harmonic vibration determined from experiment (Chopra, 1995)	180
Figure 6.20	Estimation of damping in shear-sliding loop	182
Figure 6.21	Energy dissipation at the base of footings in terms of equivalent viscous damping, ζ_{eq} (%): (a) rocking mode, (b) sliding mode	183
Figure 6.22	Energy dissipation per cycle in (a)rocking mode (gm-50/50),(b)sliding mode (gm-50/50), (c)rocking mode (gm-10/50),(d)sliding mode (gm-10/50), (e)rocking mode (gm-2/50),(f)sliding mode (gm-2/50)	185
Figure 6.23	Fraction of energy dissipated in (a) rocking mode and (b) sliding mode	186
Figure 6.24	Consequence of energy dissipation	186
Figure 6.25	Contact Interface Model after Gajan (2006)	187
Figure 6.26	Comparison with macro model after Gajan (2006): (a) moment–rotation and (b) settlement–rotation	188
Figure 7.1	Prototype frame-wall-foundation combined system (units in mm)	192
Figure 7.2	Schematic diagram showing frame-wall-foundation OpenSees model	193
Figure 7.3	Five percent damped acceleration response spectra for: (a) near fault motions and (b) ordinary (other) motions used in this study	197
Figure 7.4	First three periods of the structures with different base conditions and factors of safety	199
Figure 7.5	Nonlinear pushover response for the shearwall-frame-foundation system	200
Figure 7.6	Nonlinear pushover response for the 'frame only' system	200

Figure 7.7	Global lateral force-displacement response of the wall-frame structure: Whittier motion (a) $FS_v = 10$ and (b) $FS_v = 3$ and Landers motion (a) $FS_v = 10$ and (b) $FS_v = 3$	202
Figure 7.8	Shear and moment response of foundations - Landers Motion	203
Figure 7.9	Shear and moment response of foundations - Whittier Motion	204
Figure 7.10	Variation of response parameters as a function of foundation condition: (a)–(b) normalized maximum moment, (c)–(d) normalized maximum shear force, (e)–(f) normalized maximum inter-story drift ratio and (g)–(h) normalized maximum total drift ratio for the building with $FS_v = 10$	207
Figure 7.11	Variation of response parameters as a function of foundation condition: (a)–(b) normalized maximum moment, (c)–(d) normalized maximum shear force, (e)–(f) normalized maximum inter-story drift ratio and (g)–(h) normalized maximum total drift ratio for the building with $FS_v = 3$	208
Figure 8.1	Part of the OpenSees class hierarchy	211
Figure 8.2	Different footing conditions: (a) Fixed base, (b) Elastic base sliding restricted, (c) Elastic base with sliding allowed, (d) Nonlinear base sliding restricted and (e) Nonlinear base with nonlinear sliding allowed	217
Figure 8.3	Tributary area capacity calculation	219
Figure 8.4	Example 1: Shearwall resting on a strip footing	223
Figure 8.5	Results for (a) Wall force-displacement response (b) Extreme end vertical spring response (Example 1)	223
Figure 8.6	Example 2:(a) Elevation and (b) Plan of the single-bay frame	224
Figure 8.7	Example 2: Node and element configuration for foundation-2 and column-2	224
Figure 8.8	Example 2: (a)Force-displacement response (b) Extreme end vertical spring response	224

Figure A.1	Normalized demands for all tests (with varying ϕ)	230
Figure A.2	Normalized demands for all tests (with varying ν)	231
Figure A.3	Normalized demands for all tests (with varying E_s)	232
Figure A.4	Normalized demands for all tests (with varying TP)	233
Figure A.5	Normalized demands for all tests (with varying R_e)	234
Figure A.6	Normalized demands for all tests (with varying R_k)	235
Figure A.7	Normalized demands for all tests (with varying l_e/L)	236
Figure B.1	Footing response comparison for test <i>SSG02 – 02</i> (static cyclic test on dense sand ($D_r = 80\%$) with $FS_v = 5.2$ and $M/H/L = 0.41$) . . .	245
Figure B.2	Footing response comparison for test <i>SSG02 – 03</i> (static cyclic test on dense sand ($D_r = 80\%$) with $FS_v = 5.2$ and $M/H/L = 1.75$) . . .	246
Figure B.3	Footing response comparison for test <i>SSG02 – 05</i> (static cyclic test on dense sand ($D_r = 80\%$) with $FS_v = 2.6$ and $M/H/L = 1.72$) . . .	247
Figure B.4	Footing response comparison for test <i>SSG03 – 03</i> (static cyclic test on dense sand ($D_r = 80\%$) with $FS_v = 14.0$ and $M/H/L = 1.77$) . . .	248
Figure B.5	Footing response comparison for test <i>SSG04 – 06</i> (static cyclic test on dense sand ($D_r = 80\%$) with $FS_v = 2.3$ and $M/H/L = 1.20$) . . .	249
Figure B.6	Footing response comparison for test <i>SSG03 – 07</i> (dynamic test on dense sand ($D_r = 80\%$) with $FS_v = 7.2$ and $M/H/L = 1.80$)	250
Figure B.7	Footing response comparison for test <i>SSG04 – 10</i> (dynamic test on dense sand ($D_r = 80\%$) with $FS_v = 4.0$ and $M/H/L = 1.80$)	251
Figure B.8	Footing response comparison for test <i>KRR03 – 02</i> (static cyclic test on 100 kPa clay with $FS_v = 2.8$ and $M/H/L = 1.80$)	252
Figure B.9	Footing response comparison for test <i>KRR03 – 03</i> (dynamic test on 100 kPa clay with $FS_v = 2.8$ and $M/H/L = 1.70$)	253
Figure B.10	Footing response comparison for (a) Station E and (b) Station F during shake-5 (dynamic test on dense sand with $D_r = 80\%$)	254
Figure B.11	Footing response comparison for (a) Station E and (b) Station F during event shake-6 (dynamic test on dense sand with $D_r = 80\%$)	255

Figure B.12	Footing response comparison for (a) Station E and (b) Station F during event shake-8 (dynamic test on dense sand with $D_r = 80\%$)	256
Figure C.1	Acceleration, velocity, displacement time histories and response spectra for GM1: Imperial Motion	258
Figure C.2	Acceleration, velocity, displacement time histories and response spectra for GM2: Landers Motion	259
Figure C.3	Acceleration, velocity, displacement time histories and response spectra for GM3: Northridge Motion	260
Figure C.4	Acceleration, velocity, displacement time histories and response spectra for GM4: Kobe Motion	261
Figure C.5	Acceleration, velocity, displacement time histories and response spectra for GM5: Chi Chi Motion	262
Figure C.6	Acceleration, velocity, displacement time histories and response spectra for GM6: San Fernando Motion	263
Figure C.7	Acceleration, velocity, displacement time histories and response spectra for GM7: North palmspring Motion	264
Figure C.8	Acceleration, velocity, displacement time histories and response spectra for GM8: Whittier.pdf	265
Figure C.9	Acceleration, velocity, displacement time histories and response spectra for GM9: Loma Prieta Motion	266
Figure C.10	Acceleration, velocity, displacement time histories and response spectra for GM10: Turkey Motion	267

LIST OF TABLES

	Page
Table 1.1 Summary of N-g centrifuge experiments	12
Table 1.2 Summary of 1-g large-scale experiments on shallow foundation	14
Table 2.1 BNWF model parameters	29
Table 2.2 Equations for determining shallow foundation stiffness after Gazetas (1991a) as summarized in ATC-40 (1996).	45
Table 3.1 Axial Tests on strip and square footing (For q-z material)	72
Table 3.2 Lateral tests on square footing (For p-x material)	74
Table 3.3 Lateral tests on square footing (For t-x material)	75
Table 3.4 Shape parameters for defining the spring material backbone curves . .	84
Table 4.1 Details of the shearwall footing tests considered for model evaluation	95
Table 4.2 BNWF model parameters used for idealized building test model . . .	97
Table 4.3 Summary of shearwall-footing response prediction	110
Table 4.4 Test details considered for the comparison study of bridge dynamic tests resting on dry sand with $D_r = 80\%$ conducted by Ugalde (2007) (prototype scale)	113
Table 4.5 Model input parameters for use in the comparison study	113
Table 4.6 Summary of bridge comparison results	118
Table 5.1 Test matrix considered for the parametric study (All tests are on dense dry sand with $D_r = 80\%$ and the units are in prototype scale) .	123

Table 5.2	Parameter matrix considered for the study	128
Table 5.3	Experimental Demands	130
Table 5.4	FOSM analysis for normalized moment demand	143
Table 6.1	Properties of three models considered in this study	159
Table 6.2	Derived capacity and stiffness of the foundation	160
Table 6.3	Eigenvalue analysis results	167
Table 6.4	Capacity assessment (from pushover analysis)	167
Table 6.5	Summary table of maximum footing demands	175
Table 6.6	Summary peak drift and roof acceleration demands	175
Table 6.7	Summary footing demands for fixed, elastic and nonlinear base conditions	176
Table 6.8	Summary of peak drift ratio and roof acceleration demands for fixed, elastic and nonlinear base conditions	177
Table 7.1	Structural members material properties	194
Table 7.2	Basic properties for soil subgrade	195
Table 7.3	Derived properties of the strip and square footings	195
Table 7.4	Details of the selected ground motions	197
Table 7.5	First three periods of the structures with different base conditions and factors of safety	198
Table 8.1	Material Tag assignment for the various footing conditions	220
Table A.1	Normalized force and displacement demands (with varying ϕ)	237
Table A.2	Normalized force and displacement demands (with varying ν)	238
Table A.3	Normalized force and displacement demands (with varying E_s)	239
Table A.4	Normalized force and displacement demands (with varying TP)	240
Table A.5	Normalized force and displacement demands (with varying R_e)	241
Table A.6	Normalized force and displacement demands (with varying R_k)	242
Table A.7	Normalized force and displacement demands (with varying l_e/L)	243

ACKNOWLEDGMENTS

I would like to take the opportunity to express my sincere gratitude towards my thesis adviser and committee chair Professor Tara Hutchinson for her continuous support and guidance during my entire doctoral program. Her insightful thoughts, helpful comments and cheerful encouragement are deeply appreciated. Thanks also to my other committee members for spending their valuable time and effort reading this document and providing thoughtful comments.

This research work has been supported by the Pacific Earthquake Engineering Research Center (PEER). PEER is supported by the National Science Foundation (NSF) under Award Number EEC-9701568. No doubt that I feel proud to be a part of that prestigious research group.

I would like to thank Professors Bruce Kutter (University of California, Davis), Jonathan Stewart (University of California, Los Angeles), Helmut Krawinkler (Stanford University) and Goeff Martin (University of Southern California) for providing their valuable suggestions at several points of my study.

Special thanks to Dr. Sivapalan Gajan, Mr. Jeremy Thomas, Mr. Jose Ugalde, and Ms. Key Rosebrook for letting me use their experimental data; without which, this research would have not been completed. Thanks to Miss Christine Goulet for her technical cooperation in some aspects. Thanks to Professors Ross Boulanger and Scott Brandenburg for sharing their implementation codes of spring material models.

I would like to acknowledge my gratitude towards all the faculty members and staff of the Department of Civil and Environmental Engineering, University of California, Irvine, where I spent the first three years of my PhD program and learned many things.

I have worked very closely with Miss Barbara Chang during my doctoral study. She is a great colleague and nice friend with whom I have enjoyed every bit of our work together.

Time spent with Giri, Ting, Chen, Swagata, Prasenjit, Debasis, Shraboni and Sutapa made my tough life as a graduate student much smoother.

This is a perfect occasion to acknowledge my deepest gratitude towards my parents and my sweet, loving sister for being the constant source of encouragement throughout my life.

The support and affection from my parents-in-law and siblings-in-law have also been very delightful and cherishable.

Finally, my heartiest acknowledgment towards my best friend and my life partner Dr. Samit Ray Chaudhuri, who has always been sharing my joys and sorrows with his unique cheerful assurance. Without his technical, emotional and ethical supports, I would not be in a position to write this dissertation. It is him, who made my dreams come true.

CURRICULUM VITAE

Education

Ph.D.	Structural Engineering University of California, San Diego, CA	2008
M. Tech.	Civil Engineering Indian Institute of Technology, Kanpur, India	2003
B.E.	Civil Engineering Indian Institute of Engineering, Science and Technology (Formerly, Bengal Engineering College) West Bengal, India	1999

Publications

- Raychowdhury, P. and Hutchinson, T. C., (2008). “Performance Evaluation of a Nonlinear Winkler-based Shallow Foundation Model using Centrifuge Test Results”. *Earthquake Engineering and Structural Dynamics*, (Submitted).
- Raychowdhury, P. and Hutchinson, T. C., (2008). “Nonlinear Material Models for Winkler-based Shallow Foundation Response Evaluation”. *In Proceedings of the GeoCongress*, New Orleans, Louisiana.
- Raychowdhury, P. and Hutchinson, T. C., (2008). “Material Model Parameters for Shallow Foundation Numerical Analysis”. *In Proceedings of the 4th Earthquake Engineering and Soil Dynamics Conference (GEESD-IV)*, Sacramento, California.
- Gajan, S., Hutchinson, T. C., Kutter, B. L., Raychowdhury, P., Ugalde, J. A., and Stewart, J. P., (2008). “Numerical Models for the Analysis and Performance-Based Design of Shallow Foundations Subjected to Seismic Loading”. Pacific Earthquake Engineering Research Center (PEER) Report 2008/XX.
- Raychowdhury, P. and Hutchinson, T. C., (2007). “Winkler-based Modeling of Shallow Foundation and Effect of Their Seismic Deformations on Structural Response”. *In Proceedings of the Conference on Civil Engineering in the New Millennium: Opportunities and Challenges (CENeM)*, Howrah, India.

- Chang, B., Raychowdhury, P., Hutchinson, T. C., Thomas, J., Gajan, S., Kutter, B., (2007). “Evaluation of the Seismic Performance of Combined Frame-Wall-Foundation Structural Systems through Centrifuge Testing”. *In Proceedings of the 4th International Conference on Earthquake Geotechnical Engineering (4ICEGE)*, Thessaloniki, Greece.
- Chang, B. J., Thomas, J. M., Raychowdhury, P., Gajan, S., Kutter, B. L., Hutchinson, T. C., (2007). “Soil-Foundation-Structure Interaction: Shallow Foundations. Centrifuge Data Report for the JMT02 Test Series”. Report No. SSRP 07/24.
- Chang, B. J., Raychowdhury, P., Hutchinson, T. C., Gajan, S., Kutter, B. L., and Thomas, J. (2006). “Centrifuge Testing of Combined Frame-Wall-Foundation Structural Systems”. *In Proceedings of the 8th US National Conference on Earthquake Engineering (8NCEE)*, San Francisco, California.
- Hutchinson, T. C., Raychowdhury, P., and Chang, B. J. (2006). “Nonlinear Structure and Foundation Response during Seismic Loading: Dual Lateral Load Resisting Systems”. *In Proceedings of the 8th US National Conference on Earthquake Engineering (8NCEE)*, San Francisco, California.

ABSTRACT OF THE DISSERTATION

Nonlinear Winkler-based Shallow Foundation Model for Performance Assessment of Seismically Loaded Structures

By

Prishati Raychowdhury

Doctor of Philosophy in Structural Engineering

University of California, San Diego, 2008

Professor Tara C. Hutchinson, Chair

When a structure supported on shallow foundations is subjected to inertial loading due to earthquake ground motion, the foundation may undergo sliding, settling and rocking movements. If the capacity of the foundation is mobilized, the soil-foundation interface will dissipate significant amounts of vibrational energy, resulting in a reduction in structural force demand. This energy dissipation and force demand reduction may enhance the overall performance of the structure, if potential consequences such as excessive tilting, settlement or bearing failure are accounted for. Despite this potential benefit, building codes, particularly for new construction, discourage designs that allow foundation capacity mobilization. This lack of acceptance to embrace soil-foundation-structure interaction (SFSI) as a design inelastic mechanism may stem from the well founded concern that significant uncertainties exist in characterization of soils. More importantly, the lack of well-calibrated modeling tools, coupled with parameter selection protocols cast in a simplistic fashion are lacking.

In this work, a numerical model based on the Beam-on-Nonlinear-Winkler-Foundation (BNWF) concept is developed to capture the above mentioned foundation behavior. The BNWF model is selected due to its relative simplicity, ease of calibration, and acceptance in engineering practice. The soil-foundation interface is assumed to be an assembly of discrete, nonlinear elements composed of springs, dashpots and gap elements. Spring

backbone curves typically used for modeling soil-pile response are taken as a baseline and further modified for their usefulness in shallow footing modeling. Evaluation of the model and associated parameter selection protocol is conducted using a suite of centrifuge experiments involving square and strip footings, bridge and building models, static and dynamic loading, sand and clay tests, a range of vertical factors of safety and aspect ratios. It is observed that the model can reasonably predict experimentally measured footing response in terms of moment, shear, settlement and rotational demands. In addition, the general hysteresis shape of the moment–rotation, settlement–rotation and shear–sliding curves is reasonably captured. However, the model consistently under estimates the sliding demand measured in the experiments, perhaps due to the lack of coupling between the vertical and lateral modes of response.

Following the model validation, input parameter sensitivity is investigated using tornado diagram analysis and the First-Order-Second-Moment (FOSM) method. Among the parameters required for the BNWF modeling, the vertical tension capacity and friction angle have the most significant effect on the capability of the model to capture force and displacement demands.

The model is then exercised by studying the response of shearwall–foundation and shearwall–frame–foundation systems. These analyses indicate that if reliably quantified and designed, SFSI has great potential for reducing system level seismic forces and inter-story drift demands.

Finally, the proposed model is implemented within the framework of OpenSees (an open source finite element software package developed by the Pacific Earthquake Engineering Research center) to encourage its use within engineering community.

Chapter 1

Introduction and Previous Work

1.1 Problem Importance

Shallow foundations undergoing inelastic sliding, settling and rocking movements under earthquake loading (Figure 1.1) can provide a very useful mechanism for dissipating energy. This dissipation of energy results in a reduction of the force demand to the structure. Although all modes of the foundation's movement (sliding, settling and rocking) have the potential to dissipate energy, of particular interest is the mode of rocking, as transient rocking tends towards a natural recentering, resulting in a more stable response. This concept was first studied by Housner (1963) who integrated a rigid block model that was allowed to rock (Figure 1.2); and subsequently developed closed-form equations to estimate kinetic energy loss. The expressions were used to evaluate the seismic stability of the rigid structure subjected to lateral loads. It has subsequently been suggested that a certain amount of rocking of a shallow foundation can enhance the overall performance of buildings. The associated reduction in forces due to this rocking based energy dissipation mechanism can assist with minimizing the relative vulnerability of individual structural components as well

as maximizing the potential system-level energy dissipation, which is useful for retrofit of existing buildings.

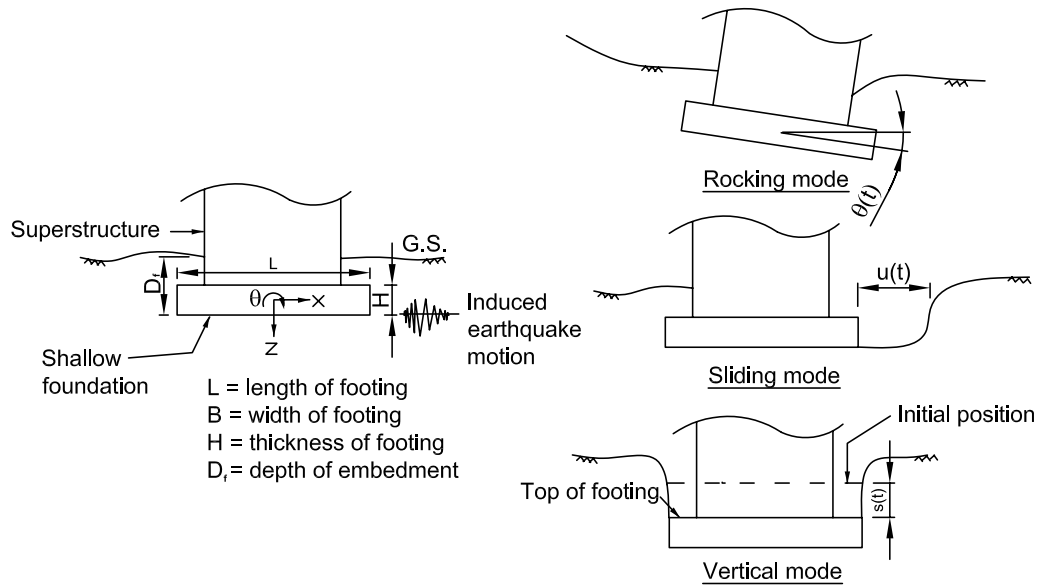


Figure 1.1: Different modes of foundation deformation

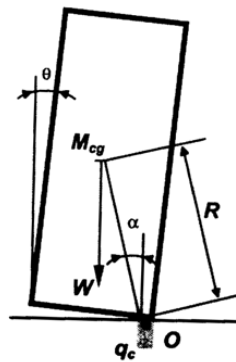


Figure 1.2: Rigid rocking block model (from Housner, 1963)

While there have been some efforts considering the energy dissipative potential of rocking shearwalls, the same concept should also be applicable to shallow foundations of moment frame building and bridge columns. Alternatively, modern designs also embrace the use of combined structural systems, where multiple types of lateral load resisting struc-

tural elements are present. For example, it is not uncommon, due to architectural or other requirements, to intermix shearwalls with moment-frames, within the same line of action, to resist seismic loads. In this case, the shearwall is sensitive to loads, while the moment frame is sensitive to displacements. Therefore, rocking of the foundation supporting the shearwall will most likely protect it by reducing its force demand. However, an increase in the displacement demand to the frame will be observed, especially at the interface between the two lateral resisting elements. This excessive displacement can cause damage to the frame, especially at the beam-column joints, as shown in Figure 1.3. In addition, excessive displacements of frame may cause damage to the displacement sensitive non-structural components such as partition wall and window glasses. Therefore, in order to take the advantage of flexible shallow foundation, it is important to have a balance between the benefits due to reduction in the force demands and detriments due to increase in the displacement demands.

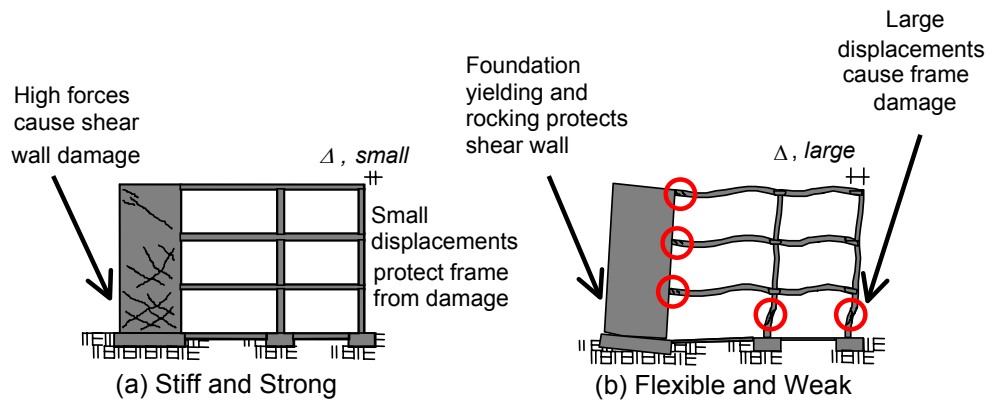


Figure 1.3: Effect of foundation stiffness on structure (from ATC-40, 1996)

If the benefits of an inelastically behaving soil-foundation interface can be harnessed, both new and retrofit design methodologies would be impacted. However, one must note that care be taken to assure that: first, transient and/or permanent settlement, sliding and

rotation due to the nonlinear behavior of the foundation is not excessive, and second, force demands at the foundation level must be limited to assure that bearing failure does not occur.

1.2 Previous Work

Numerous studies have been conducted to understand soil-Foundation-structure-interaction (SFSI) either analytically, numerically or through physical tests. In this section, an overview of previous work related to shallow foundation modeling (numerical and analytical) and its physical behavior (from centrifuge, shake table and field tests) is presented. The current design practice for accounting for soil-structure-interaction (SSI) for buildings supported on shallow foundations is also discussed.

1.2.1 Numerical and Analytical Efforts

As evident by the numerous recent analytical and experimental studies, there has been increased interest within the community on evaluating (and allowing) the inelastic response of shallow foundations during seismic loading (e.g. Harden et al., 2006; Gajan, 2006; Gazetas, 2006; Allotey and Naggar, 2007; Zhang and Tang, 2007; Apostolou et al., 2007). Common approaches for modeling the shallow foundation response, considering SFSI include: (i) continuum finite element and boundary element approaches, (ii) macro-element formulations, and (iii) Winkler-based approaches. The continuum approach assumes the soil medium as a semi-infinite and isotropic medium consisting of discrete, compacted particles with intergranular forces. Soil-layering and anisotropy can be accounted for using this method of analysis. Although this approach is more realistic when modeling the

soil medium, it generally involves extensive computational effort. Macro-element methods model the shallow footing behavior by lumping SSI typically within a single element, and use a plasticity-based formulation (Cremer et al., 2001; Gajan, 2006; Paolucci et al., 2007).

Winkler-based approaches may use only 1D spring elements, or 1D spring elements in combination with 2D or 3D soil elements to represent the overall behavior of the soil-structure interface. The Winkler spring approach is appealing in design due to its simplicity and minimal computational effort. Furthermore, the mechanistic nature of spring-based models can simplify calibration, if response data exists. In this work, the concept of Winkler modeling is adopted. Therefore, related studies in this context will be reviewed.

Early work in New Zealand led efforts to use Winkler-based models for capturing shallow foundation rocking response. Among these efforts, Taylor et al. (1981) and Bartlett (1976) summarized an analytical model for predicting moment-rotation behavior of rigid footings using elastic-perfectly-plastic springs coupled with Coulomb slider elements. Elastic-plastic springs were considered to only have compression capacity, while Coulomb slider elements captured the uplifting of the foundation.

Psycharis (1981) developed a model with two approaches: (i) a two-spring model and (ii) a distributed Winkler spring model. Nonlinearity at the foundation interface was considered by three mechanisms: (i) viscous dampers, (ii) elastic-perfectly plastic springs, and (iii) an impact mechanism allowing dissipation of energy at impact. Comparison of the solutions from theoretical equations developed on the basis of the two spring system and distributed spring system were provided using response results from the Milliken Library building and a ground motion recording from the 1971 San Fernando earthquake.

Chopra and Yim (1985) presented an analytical study evaluating the rocking response

of an SDOF system considering uplifting of the foundation. In this study, individual spring elements were considered linear elastic (Figure 1.4). For SDOF systems, the authors developed simplified expressions to determine the base shear resistance of flexible structures allowed to uplift. It was observed that for a multi-story building structure, although the foundation flexibility and uplift have considerable effect on the fundamental mode of vibration, they have little effect on higher modes.

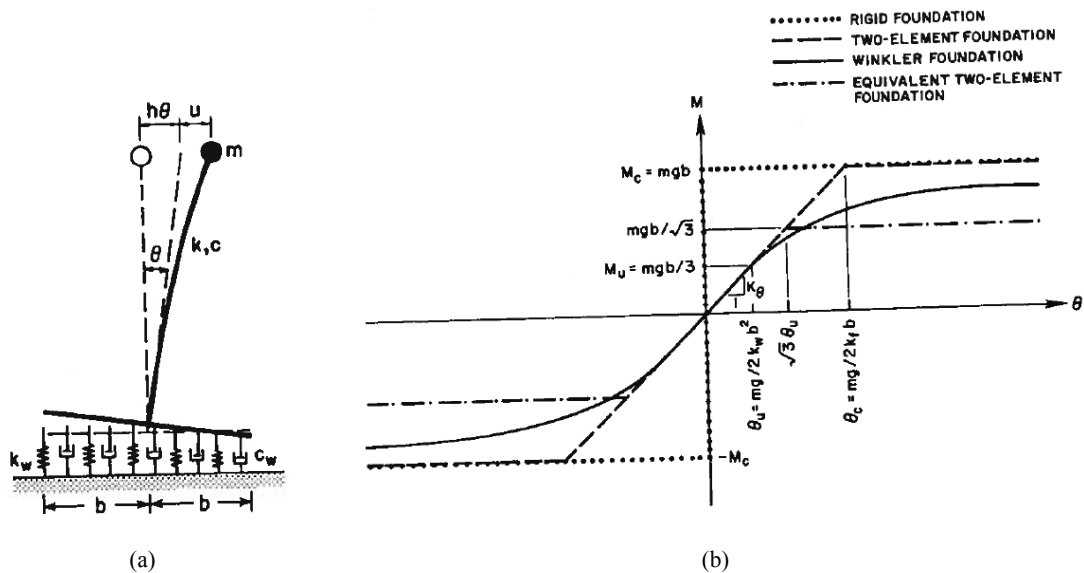


Figure 1.4: (a) Idealized Winkler foundation model and (b) $M-\theta$ envelopes after Chopra and Yim (1985)

Nakaki and Hart (1987) used discretely placed vertical elastic springs with viscous dampers at the base of a shearwall structure (Figure 1.5). Winkler springs with zero tension capacity and elastic compressive resistance were used here. The inelastic shearwall structure was modeled using a nonlinear stiffness degrading hysteretic model. As one may expect, the structure with a flexible Winkler base was found to have a longer period than that of the fixed base structure. Uplift of the foundation caused greater ductility demands on the structure.

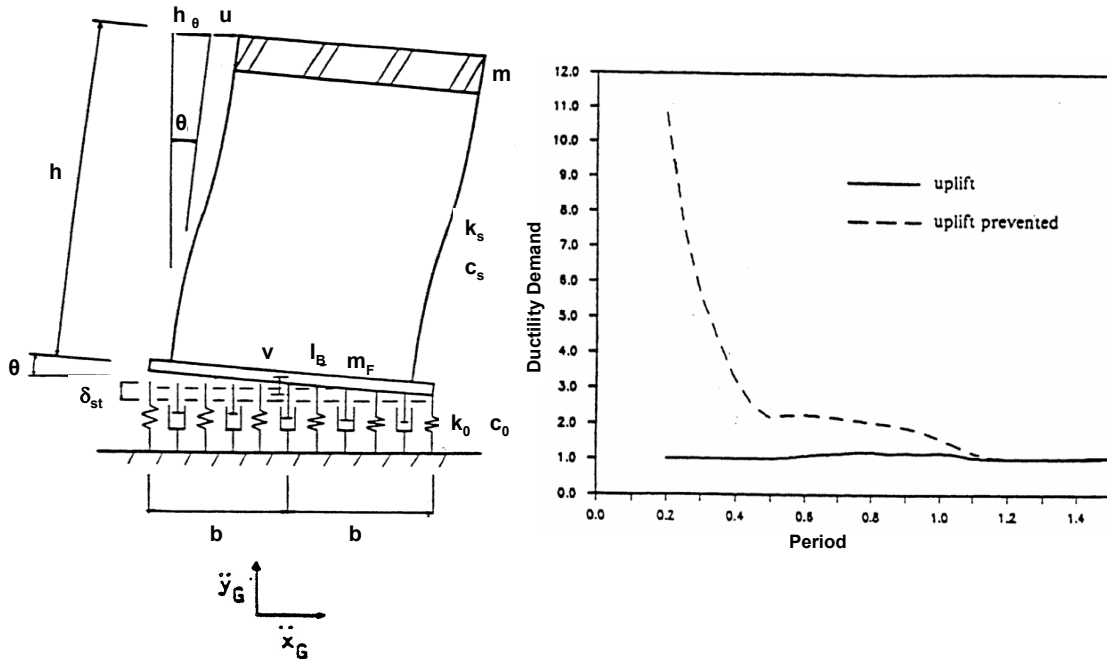


Figure 1.5: Winkler foundation modeling and result from Nakaki and Hart (1987)

Fenves (1998) modeled uplift of pile caps using a composite element of multiple elastic-perfectly-plastic spring elements with gapping capability. The compression and tension sides of the load-displacement curves were unsymmetric to capture the reduced capacity under uplift, and gapping elements were used to capture permanent settlement. It was observed that the vertical factor safety had a significant influence on moment capacity, vertical settlement and energy dissipation.

Harden et al. (2005) developed a Winkler type finite element model to account for the nonlinear behavior of shallow strip footings subjected to lateral cyclic loads. Pile-calibrated nonlinear spring backbone curves were used in this study. It was shown in this study that the response from the numerical simulations compares satisfactorily with centrifuge and one-g model tests on shallow foundations loaded with both slow cyclic and dynamic base excitation. It was also observed that by experimental unloading stiffness, rather than more

traditional elastic stiffness such as that of Gazetas (Gazetas, 1991c) provides better results. Based on this study, suggestions are made to introduce the provision of foundation uplift in performance-based design (Harden et al., 2006). Although the study of Harden et al. (2005) provided a methodology for analyzing the seismic response of nonlinear shallow foundations using Winkler's approach, the calibration of the model was primarily conducted using moment dominated strip footings. Short walls with low aspect ratios and square to rectangular footings were not considered in this study.

Allotey and Naggar (2007) adopted a Winkler-based modeling concept for capturing the cyclic response of shallow foundations. Piece-wise linear backbone curves shown in Figure 1.6 were adopted from the authors' previous work (Allotey and Naggar, 2003). It is observed from their work that the model is able to predict the moment-rotation and settlement response reasonably well. However, the model is not able to capture the sliding response adequately which may be due to lack of coupling between the various modes of deformation.

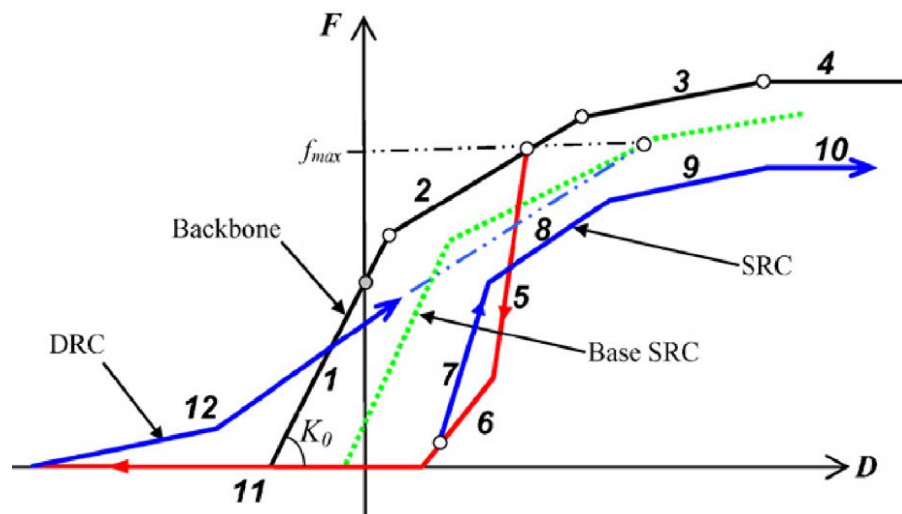


Figure 1.6: Backbone curves after Allotey and Naggar (2007)

1.2.2 Experimental Efforts

1.2.2.1 N-g Centrifuge Experiments

The underlying philosophy of centrifuge experiments is to scale down a prototype structure, in terms of its geometry, while applying an increased gravitational force (of N -g, e.g., between $N = 20$ -100 times that of gravity). Through similitude laws, this results in the retention of prototype soil stresses at the model scale (e.g. Kutter, 1997). The importance of retaining soil stresses (and thus strength) in physical model testing of geotechnical systems is well known, thus centrifuge testing has become a well established and popular technique. In the context of the rocking shallow foundation problem, the centrifuge is a valuable tool for investigating the performance of the soil-foundation system, since the nonlinearity of the system is mainly attributed to the soil behavior.

Gadre and Dobry (1998) conducted cyclic tests on a model embedded square footing and studied the lateral response at various displacement levels. The relative contributions of the base and sides in terms of sliding as well as the active and passive earth pressures at the sides of the foundations were evaluated. Three-dimensional static nonlinear finite element analysis were also conducted to simulate the centrifuge results. It was observed that passive pressure accounts for more than 50% of the total resistance for the embedded footings.

Recently, several series of tests have been conducted using the 9 m radius centrifuge at the University of California, Davis (UCD), considering a scale factor $N = 20$ (Rosebrook and Kutter, 2001a,b,c; Gajan et al., 2003a,b; Thomas et al., 2004; Chang et al., 2007; Ugalde, 2007). These tests were done using shallow strip and square footings with a range of vertical factors of safety and for different types of loading (monotonic, vertical and lat-

eral slow cyclic and dynamic). Experiments by Rosebrook and Kutter (2001a,b,c); Gajan et al. (2003a,b); Thomas et al. (2004) were conducted on strip and square shallow footings supporting single/double shearwall structures, whereas Ugalde (2007) conducted tests on shallow footings supporting model bridge piers. Chang et al. (2007) tested shallow footings supporting combined load resisting system consisting of a shearwall and a moment frame. This test series showed the combined effect of structural nonlinearity and foundation nonlinearity on the overall system response.

Figure 1.7 shows the centrifuge test set-up for the different tests conducted at UCD. Table 1.1 summarizes the details of these and their centrifuge experiments on shallow foundations. Key observations from the centrifuge tests conducted at UCD are as follows (Rosebrook and Kutter, 2001a,b,c; Gajan et al., 2003a,b; Thomas et al., 2004; Chang et al., 2007; Ugalde, 2007):

- Degradation in rotational stiffness, as a result of foundation yielding is observed.
- A significant amount of energy dissipation is observed in moment-rotation and shear-sliding response.
- This energy dissipation results in permanent footing displacements as the foundation yields.
- Both moment capacity and shear capacity increase with an increase in depth of embedment. The rate of increase of shear capacity is slightly higher than that of moment capacity.
- Foundation stiffness degradation and permanent footing displacement are dependent

on the following parameters: soil density, soil type, footing size, aspect ratio, embedment, static vertical factor of safety FS_v and amplitude of cyclic loading.

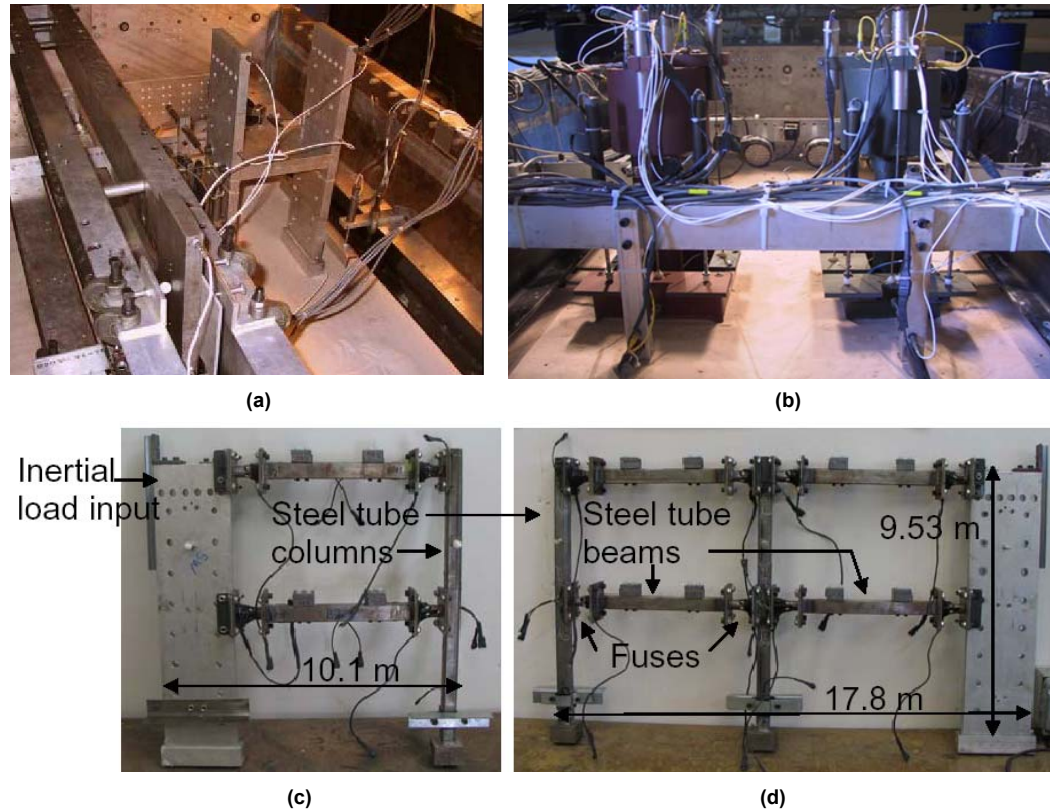


Figure 1.7: Centrifuge test set-up at University of California, Davis for: (a) shearwall-footing model (Gajan et al., 2003a), (b) bridge-pier-footing model (Ugalde, 2007) and (c) frame-wall-footing model (Chang et al., 2007) (All units in prototype)

1.2.2.2 One-g Experiments

One-g experiments, using either base input (e.g. through a shake table) or inertially loaded (e.g. through structure-mounted hydraulic jacks) have been conducted to investigate SSI effects of shallow foundations. These tests are advantageous as they preserve true scaling of soil-to-structure grain size characteristics. However, they are hampered by large scale, which drives individual experiment costs substantially. Furthermore, the limited size

Table 1.1: Summary of N-g centrifuge experiments

Test Series	Reference	Soil Type	Footing Size (m x m)	Depth of Embedment (m)	FSv Range	Wall Type
GD98	Gadre and Dobry (1998)	Dry sand, Dr = 75%	1.14 x 1.14	1.14	..	No wall
KRR01	Rosebrook and Kutter (2001a)	Dry sand, Dr = 60-80%	2.67 x 0.69	0.3	1.6-6.5	Double
KRR02	Rosebrook and Kutter (2001b)	Dry sand, Dr = 60%	2.67 x 0.70	0	1.6-4.1	Double
KRR03	Rosebrook and Kutter (2001c)	Clay, Cu=100 kPa	2.67 x 0.69	0	2.8-4.8	Double
SSG02	Gajan et al. (2003a)	Dry sand, Dr =80%	2.84 x 0.69	0	3.4-9.6	Single
SSG03	Gajan et al. (2003b)	Dry sand, Dr =80%	2.84 x 0.70	0.7	1.3-11.5	Single
SSG04	Gajan et al. (2006)	Dry sand, Dr =80%	2.84 x 0.65	0	1.67-4	Single
SSG04	Gajan et al. (2006)	Dry sand, Dr =80%	1.0 x 1.0	0-0.8	6.0-11	Double
JMT02	Chang et al. (2007)	Dry sand, Dr =80%	2.84 x 0.69 & 1.0 x 1.0	0.5	3.0-12	Single w/ frame
JAU01	Ugalde et al. (2007)	Dry sand, Dr =80%	5.4 x 5.4 & 7.1 x 7.1	1.72	17-31	Bridge pier

of the soil box may cause boundary effects to the free-field soil conditions. Nevertheless, the value of large one-g testing is well recognized to complement knowledge gained through centrifuge testing, therefore, it is useful to review selected one-g experimental studies (Table 1.2).

Perhaps one of the first detailed shallow footing rocking experiments at one-g, where the emphasis was on observing the nonlinear moment-rotation behavior, were those in New Zealand led by Professor Taylor and his students (Barlett, 1976; Wiessing, 1979; Taylor et al., 1981). Tests by Barlett (1976) and Wiessing (1979) used the same load apparatus and test procedure, with different soil mediums. Barlett (1976) conducted tests on a small plate footing of size $0.5\text{m} \times 0.25\text{m}$ resting on clay with a vertical factor of safety ranging from 1.5 to 8. Wiessing (1979) carried out cyclic tests on the same footings supported on sand with a FS_v ranging from 2 to 10. These studies concluded that design of a spread footing capable of yielding the soil at a moment less than the moment capacity of the

column, can avoid column hinging at the base of the column. This approach to earthquake resistant design was later applied in New Zealand Codes (Taylor and Williams, 1979). Note that degradation of soil with increasing loading amplitude and energy dissipation were also observed in all the tests.

One-g experiments were conducted at the European Laboratory for Structural Assessment (ELSA) in Italy (Negro et al., 1998). The system considered consisted of a one meter square foundation, placed on a saturated Ticino sand base, subjected to static vertical, slow cyclic and dynamic cyclic events. Two relative densities, $D_r = 85\%$ and $D_r = 45\%$ were considered in these experiments. The loading protocol consisted of single reversed symmetric cycles of increasing amplitude. These tests also indicated that the vertical factor of safety has a significant effect on the damping and level of distortion of the foundation. A lower factor of safety allowed additional densification and softening, and therefore resulted in more energy dissipation.

Maugeri et al. (2000) performed shake table tests on a shallow strip footing resting on a dry cohesionless soil subjected to eccentrically applied loading. To investigate the real failure mechanism of the foundation, four colored layers of sand were introduced into the deposit at different depths. The experimental failure mechanism was investigated by measuring the displacements of the colored layers excavated after the test. A reduction in seismic bearing capacity is observed with introducing eccentricity. It was also observed that a large residual rotation of 24° was induced due to the eccentricity while only 1° rotation was observed for vertical load with no eccentricity.

Knappett et al. (2004) conducted a series of experiments on a one-g shake table at Cambridge University to measure seismic deformations and observed the failure mechanism of

a shallow foundation using Particle Image Velocimetry (PIV) combined with high-speed videography and photogrammetry. Experimental results were compared with analytical theories available in the literature. It was observed that for structures with a center of mass well above the foundation level, moment effects are significant resulting in large reduction in the bearing capacity due to uplift. Depth of embedment and surcharge were observed to influence the failure mechanism. The study focused on the reduction in bearing capacity due to rocking and uplifting foundations, however, important parameters that govern the rocking behavior, such as; soil stiffness, soil density, friction angle, footing aspect ratio and footing rigidity were not considered.

Table 1.2: Summary of 1-g large-scale experiments on shallow foundation

Test Series	Reference	Soil Type	Relative Density of Soil	Size of Footing (m x m)	Depth of Embedment (m)	FSv range
Bartlett	Bartlett (1976)	Clay		0.50 x 0.25	0	1.5-8
Weissing	Weissing (1979)	Dry sand	93%	0.50 x 0.26	0	2.0-10
TRISEE	Negro et al. (1998)	Dry sand	85% and 45%	1.0 x 1.0	1	12.5-20.7
Maugeri	Maugeri et al. (2000)	Dry sand	53%	0.95 x 0.4	0.1	..
Cambridge	Knappett et al. (2004)	Dry sand	67%	0.5 x 0.3	0.1	high

1.2.3 Current Design Practice

There are a number of design codes that are used in practice to estimate seismic demands to structures. Buildings for example were designed according to ATC-40 (1996); FEMA 356 (2000); Uniform Building Code (1997); NEHRP (2000); IBC (2006) and ASCE-7 (2005). ATC-40 (1996) and FEMA 356 (2000) account for SFSI by using Winkler springs with elastic stiffness suggested by Gazetas (1991a). NEHRP (2000) and ASCE-7 (2005) account for SFSI using an increased period and modified damping ratio of the soil-structure system. The increased period and modified damping ratio approach in current codes (NEHRP, 2000; ASCE-7, 2005) largely came from recent studies using measured

building response data. For example, Stewart et al. (1999) summarized procedures to predict SSI effects and conducted system identification using measured building responses. In this study, both inertial and kinematic interaction mechanisms of SSI were considered. The SSI model consisted of a single-degree-of-freedom (SDOF) structure with a rigid circular footing resting on the surface of a viscoelastic half-space. A simplified method was proposed to lengthen the natural period of the system and modify the damping to account for the SSI. Period and damping factors were dependent on the following parameters: soil condition, shear-wave velocity, hysteretic damping ratio, Poisson's ratio of soil, footing flexibility and shape, depth of embedment, natural period and damping of the fixed-base structure and level of ground shaking. The model was calibrated from a database of 47 sites including 26 sites with mat foundations and 21 sites with pile or drilled shaft foundations. The period lengthening and damping estimation methods were then incorporated in NEHRP (2000). Changes included modification in the calculation of foundation stiffness, introducing dynamic rocking stiffness and decreasing the depth range over which the half-space is evaluated (Stewart et al., 1999). The modified NEHRP (2000) SFSI model is found to remove statistically significant biases in period lengthening predictions from the pre-NEHRP (2000) model.

Although current design codes account for SFSI by introducing elastic and elastic-perfectly-plastic springs or period elongation, they do not account for the smooth elastic-plastic transition of the mechanistic springs, the uplift of the foundation explicitly or the energy dissipation due to uplift and nonlinearity. Accounting for these aspects would provide more realistic estimates of structural performance and therefore lead to safer seismic design.

1.3 Summary and Observations from Previous Work

The development of realistic numerical models of the foundation with its supporting subgrade soil, which can reasonably capture its nonlinear rocking behavior has been recognized as an important and complex problem in earthquake engineering. Although a number of experimental and analytical studies have been undertaken to study shallow footing behavior, its interaction with supporting soil and its effect on isolated structural components (simple rigid structures), it is still unclear how to appropriately model this behavior. In addition, only a few studies have been conducted to consider the effect of foundation rocking and uplift on the nonlinear behavior of moment-frame and shearwall combined structures. To-date spring-based models used for shallow footing modeling have been calibrated against lateral pile load test data [e.g. Matlock (1970); API (1987)]. In addition, code-based documents that provide methods for modeling suggest elastic-plastic backbone curves. It is clear that the backbone curve representing the response at the soil-shallow footing interface will be nonlinear, however, it is not clear how one goes about defining this curve, and particularly those attributes of the curve, which are not directly correlated with soil element tests.

1.4 Objective

The objective of this study is to develop, validate, and exercise a nonlinear Winkler-based model for capturing the inelastic behavior of shallow foundations subjected to seismic loading. The model is intended to be used for seismic performance assessment and design of shallow footing-structure system to harnesses the potential beneficial energy dissipative capabilities of the footing when behaving inelastically.

1.5 Scope of the Present Study

To accomplish the objective noted above, a numerical modeling methodology for capturing the nonlinear response of shallow foundations subjected to seismic loading is presented. The soil-foundation interface is assumed to be an assembly of discrete, nonlinear springs that are capable of capturing gapping and radiation damping. The overall BNWF (Beam-on-Nonlinear-Winkler Foundation) numerical model is intended to capture moment-rotation, shear-sliding and axial force-settlement behavior of shallow footings by using mechanistic Winkler springs with a minimal number of input parameters such that the model can easily be implemented in any finite element (FE) environment and interpreted by a design engineer. The inertial interaction between structure, foundation and soil is considered in this approach, while kinematic interaction is neglected. The backbone curves typically used for modeling soil-pile response are used as a baseline and developed further for their usefulness in shallow footing modeling, by calibrating against a variety of shallow foundation tests. The performance of the model is then assessed using a suite of centrifuge experiments involving square and strip footings, bridge and building models, static and dynamic loading, sand and clay tests, a range of vertical factors of safety and aspect ratios. Input parameter sensitivity is then investigated using tornado diagram analysis and the First-Order-Second-Moment (FOSM) method. The model is then exercised using prototypical shearwall-footing and shearwall-frame-foundation combined building structure. Finally, the proposed model is implemented within the framework of OpenSees for use of engineering community.

1.6 Organization of Dissertation

This dissertation is organized into eight chapters. The outline of the chapters are as follows:

- Chapter 1 provides the background, motivation and scope of the research. Previous work in the field of shallow foundation modeling and testing are discussed.
- Chapter 2 provides a detailed description of the proposed BNWF shallow foundation model, describing its capabilities, special features and limitations.
- Chapter 3 describes the calibration of the spring backbone curves against shallow foundation tests.
- Chapter 4 presents the validation of the model against a series of centrifuge experiments on model bridge and building shallow foundations.
- Chapter 5 presents a sensitivity analysis to evaluate the various model input parameters.
- Chapter 6 and 7 present numerical studies exercising the proposed model. Chapter 6 focuses on shearwall-footing systems, whereas Chapter 7 focuses on a frame-shearwall-footing system.
- Chapter 8 describes the implementation of the model into a general purpose finite element analysis platform.
- Chapter 9 summarizes the research and provides conclusions and needs for future study.

- Appendices include: (A) normalized footing demands, (B) comparison of experimental versus simulation results, (C) ground motion details and (D) example input and output scripts for the implementation.

Chapter 2

Beam-on-Nonlinear-Winkler-Foundation Model

2.1 Introduction

This study has adopted the concept of a Beam-on-Nonlinear-Winkler-Foundation (BNWF) to model the two-dimensional (2D) behavior of a shallow foundation under seismic loading. For this purpose, a mesh of nonlinear one-dimensional mechanistic spring elements that connects a structural foundation with the surrounding soil (free-field) is used to model vertical, moment resistance, and lateral resistances. The constitutive models and the parameters required for the BNWF model along with their influence on model response are discussed in this chapter.

2.2 Description of the BNWF Model

The two-dimensional (2D) shallow foundation model constructed herein is considered as a flexible, elastic beam supported by a number of discrete, nonlinear Winkler springs.

The elastic beam is modeled using one-dimensional beam-column elements with three degrees-of-freedom (DOF) per node to represent loads and deformations in the horizontal, vertical, and rotational directions. Individual nonlinear Winkler springs are independent of each other and considered as one-dimensional *zeroLength* elements in the framework of OpenSees, where nonlinearity is represented using modified versions of the *QzSimple1*, *PySimple1* and *TzSimple1* material models implemented in OpenSees by Boulanger (2000a,b,c). The modifications are made based on the shallow footing test results (details given in Chapter 3). These elements simulate vertical load-displacement behavior, horizontal passive load-displacement behavior against the side of a footing, and horizontal shear-sliding behavior at the base of a footing, respectively. Implicitly, via the distribution of vertical springs placed along the footing length, moment-rotation behavior is captured. The backbone curves of the original material models are calibrated by assimilating the results of well established pile load tests (Matlock, 1970; Vijayvergiya, 1977; Mosher, 1984; API, 1987; Reese and ÓNeill, Reese and ÓNeill). Since, these material models were originally implemented to model the response of axially and laterally loaded piles, the nomenclature used to describe the springs is based on a coordinate axis for that of a pile (Figure 2.1).

In the current study, to better correlate with the orientation of a shallow foundation, the original orientation has been modified and accordingly the nomenclature has been changed where required (see Figure 2.2). For example, the *TzSimple1* material, where the z-axis is typically along the length of the pile, is used to capture the friction horizontally, along the length of the shallow foundation (i.e., x-axis). Similarly, the *PySimple1* material was originally introduced to capture lateral pile-soil interaction. In the context of a shallow

foundation model, p-y springs are used to capture the passive earth pressure in the horizontal direction for an embedded foundation and thus denoted as p-x springs. The following sections discuss the attributes of the BNWF shallow foundation modeling including its capabilities, the details of the mechanistic springs, important parameters to define the model and its inherent limitations. Implementation details are provided as well.

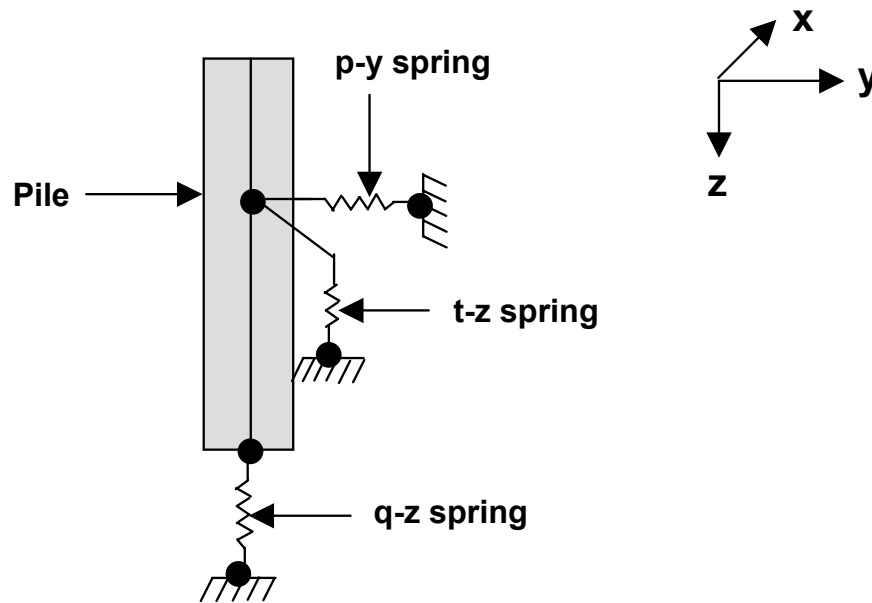


Figure 2.1: Schematic diagram showing springs and their orientations for typical soil-pile model

2.3 Attributes of the BNWF Model

The BNWF shallow foundation model proposed in this work has the following attributes:

- The model can account for behavior of the soil-foundation system due to inelastic soil behavior (material nonlinearity) and uplift (geometric nonlinearity). A distinction is

made herein between material nonlinear and inelastic behavior. While a material can follow a nonlinear load-displacement path, it may not return along the same path (e.g. attain plastic deformation, thus responding inelastically). The materials used in this work are both nonlinear and inelastic. As illustrated in Figure 2.3, nonlinearity can be manifested in moment-rotation, shear-sliding or axial-vertical displacement modes. Inelastic behavior is realized by development of gaps during cyclic loading. As a result, the model can capture rocking, sliding, and permanent settlement of the footing. It also captures hysteretic energy dissipation through these modes.

- A variable stiffness distribution along the length of the foundation can be provided in this model to account for the larger reaction that can develop at the ends of stiff footings subjected to vertical loads. The BNWF model has the capability to provide larger stiffness and finer vertical spring spacing at the end regions of the footing such that the rotational stiffness is accounted for (Figure 2.4).
- In the application of this model, the following numerical parameters worked well to assure numerical stability: (i) the transformation method for solution constraint and (ii) the modified Newton-Raphson algorithm with a maximum of 40 iterations to a convergence tolerance ranging between $1e-8$ and $1e-5$ for solving the nonlinear equilibrium equations. The transformation method transforms the stiffness matrix by condensing out the constrained degrees of freedom. This method reduces the size of the system for multi-point constraints (OpenSees, 2008).

2.4 Constitutive Material Models

OpenSees provides the flexibility of a variety of built in material models to represent the spring constitutive behavior. The simplest approach is to use an elastic model, i.e., assume an initial elastic stiffness and an infinite capacity. However, this assumption of elastic behavior is not realistic at the load demands expected of moderate earthquakes, as it has been seen from previous experiments on shallow foundations. For example, tests by Gajan (2006) demonstrate that the soil under the foundation undergoes significant change when subjected to large loading, and thus yields and behaves nonlinearly.

Another material model that has been used in practice is the elastic-perfectly-plastic (EPP) material. This material model has an initial stiffness, followed by a plastic region. After reaching the yield strain, the material enters into the plastic region, where the material continues to strain without increase in stress. The transition between the elastic and plastic region is very abrupt, which is unlikely in the case of real soil behavior.

A more general hysteretic material model can also be used in OpenSees using parallel and series materials to represent soil springs (Martin and Yan, 1997). The material model can be multi-linear with the backbone curve of the tension and compression regions defined differently as per the modeling need (Figure 2.5). For example, the combination of multiple hysteretic materials in parallel has been used by Martin and Yan (1997) to model bridge abutment soil-structure interaction (Figure 2.6). In the present study, smooth nonlinear backbone curves are used to capture the shallow foundation behavior, as described in the following sections.

2.4.1 *QzSimple1* Material

The *QzSimple1* material has an unsymmetric hysteretic response, with a backbone curve defined by an ultimate load on the compression side and a reduced strength in tension to account for soil's weak strength in tension. The elastic material captures the 'far-field' behavior, while the plastic component captures the 'near-field' permanent displacements (Figure 2.7). Additional gap components (consisting of a drag and a closure spring in parallel) are added in series with the plastic components to capture the behavior associated with foundation uplifting. Radiation damping can be accounted for using a dashpot on the far-field elastic component. The viscous force of this dashpot is proportional to the component of velocity that develops in the far-field elastic component of the material. The backbone curve is thus characterized by an elastic portion, then an increasingly growing inelastic portion (Figure 2.8).

The equations used to describe the *QzSimple1* material model are similar to those used for the *PySimple1* materials described in Boulanger et al. (1999); as mentioned in Boulanger (2000a). In the elastic portion, the equation of the backbone curve is described by

$$q = k_{in}z \quad (2.1)$$

The range of the elastic region is defined by the following relation:

$$q_o = C_r q_{ult} \quad (2.2)$$

where k_{in} = initial elastic stiffness (tangent), q = instantaneous load, z = instantaneous displacement, q_o = load at the yield point, and C_r = parameter controlling the range of the

elastic portion.

In the nonlinear (post-yield) portion, the backbone curve is described by

$$q = q_{ult} - (q_{ult} - q_o) \left[\frac{cz_{50}}{cz_{50} + |z^p - z_o^p|} \right]^n \quad (2.3)$$

where q_{ult} = ultimate load, z_{50} = displacement at which 50% of ultimate load is mobilized, q_o = load at the yield point, z_o = displacement at the yield point, and c and n are the constitutive parameters controlling the shape of the post-yield portion of the backbone curve. The gap component of the spring is a parallel combination of a closure and drag spring. The closure component ($q^c - z^g$) is simply a bilinear elastic spring, which is relatively rigid in compression and very flexible in tension. The nonlinear drag component ($q^d - z^g$) of the curve is controlled by the following equation:

$$q_d = C_d q_{ult} - (C_d q_{ult} - q_o^d) \left[\frac{z_{50}}{z_{50} + 2|z^g - z_o^g|} \right] \quad (2.4)$$

where q^d = drag force on the closure component, $q_o^d = q^d$ at the start of the current loading cycle, $z_o^g = z^g$ at the start of the current loading cycle, and C_d = ratio of the maximum drag (suction) force to the ultimate resistance of the q-z material. The expressions governing both *PySimple1* and *TzSimple1* are quite similar to Equations 2.1-2.4, with variations in the constants n , c and c_r , which control the general shape of the curve (Boulanger, 2000a,c). For the *QzSimple1* material, the backbone behavior is modeled following the Reese and ÓNeill (Reese and ÓNeill) relation for drilled shafts in clay and the Vijayvergiya (1977) relation for piles in sand. The constants c , n and C_r are calibrated with the aforementioned models in Boulanger (2000b), resulting in values of $c = 0.35$, $n = 1.2$ and $C_r = 0.2$ for clay and $c = 12.3$, $n = 5.5$ and $C_r = 0.3$ for sand.

In the current OpenSees implementation, the user specifies the following parameters: type of material, clay (soilType=1) or sand (soilType=2), q_{ult} , z_{50} , suction (tension capacity), and viscous damping ratio. The cyclic response of the *QzSimple1* material as implemented in OpenSees for pile modeling is shown in Figure 2.9.

2.4.2 *PySimple1* Material

The *PzSimple1* material was originally intended to model passive horizontal soil resistance against piles. In this work, this model is envisioned useful for capturing the passive resistance, associated stiffness, and potential gapping of embedded shallow footings subjected to lateral seismic loads. The *PySimple1* material model is characterized by a pinched hysteretic behavior, which more suitably can account for the phenomena of gapping during unloading on the opposite side of the footing. The constants c , n and C_r are fit to backbone curves Matlock (1970) and API (1987) by Boulanger (2000a), and determined to be $c = 10$, $n = 5$ and $C_r = 0.35$ for soft clay and $c = 0.5$, $n = 2$, and $C_r = 0.2$ for drained sand. P-y springs are generally placed at multiple locations along the length of a pile to account for varying soil properties with depth. However, for the shallow foundation modeling discussed here, it is assumed that the soil properties do not significantly vary from the top to the bottom of the footing, thus all properties are lumped at a single spring. They are also not modified as the footing continually settles during the rocking loading. For an OpenSees user, the input parameters for *PySimple1* material model are: p_{ult} , y_{50} , C_d and soil type (clay or sand). The cyclic response of the *PySimple1* material as implemented in OpenSees for pile modeling is shown in Figure 2.11.

2.4.3 *TzSimple1* Material

The *TzSimple1* material was intended to capture the frictional resistance along the length of a pile. The *TzSimple1* material is characterized by a large initial stiffness and a broad hysteresis as anticipated for frictional behavior associated with foundation sliding. Calibrating the models of Reese and ÓNeill (Reese and ÓNeill) and Mosher (1984), Boulanger (2000c) found $c = 0.5, n = 1.5, C_e = 0.708$ and $c = 0.6, n = 0.85, C_e = 2.05$ for clay and sand, respectively (note that here $C_e = C_r$). For an OpenSees user, the input parameters for *TzSimple1* material model are t_{ult} , z_{50} and soil type (clay or sand). The cyclic response of the *TzSimple1* material is shown in Figure 2.13.

2.5 BNWF Model Parameters

As evident from previous sections, the parameters required for the BNWF model are related to soil and footing properties in addition to finite element mesh properties. In the OpenSees implementation, these parameters are divided into two broad categories: (i) user defined parameters and (ii) hard-coded parameters. User defined parameters include capacity (lateral and vertical), soil stiffness (lateral and vertical), footing dimensions (length, width, height and depth of embedment), soil type (sand or clay) and soil tension capacity. The user has two choices to input the capacities and stiffness of the foundation. They can either provide the capacity and stiffness directly (e.g., as obtained from an experiment or theoretically estimated), or they can specify the basic soil and footing properties such as: friction angle, cohesion, shear modulus, Poisson's ratio and unit weight of soil, and the capacity (vertical and lateral) and stiffness (vertical and lateral) will be calculated within the BNWF code. In addition to these parameters, there are other model parameters that

are neither directly related to footing or soil properties nor can they be derived by a well-established theory or experiments. These parameters are related to the finite element mesh specifications and have an effect on the overall foundation response. (see, for example, Harden et al. (2005)). Example of such model parameters are vertical stiffness distribution, end length ratio and number of springs over the length of the foundation.

OpenSees hard-coded parameters include the elastic range, post-yield stiffness, and unloading stiffness. These parameters are hard-coded in the OpenSees implementation and a user can not alter these parameters without modifying the source code. Perhaps, this has been done because it is perceived that these parameters are not significantly dependent of soil and footing parameters and are difficult to determine from an element-level soil test. Table 2.5 shows the list of BNWF user defined and hard-coded parameters. Details of each parameter along with how they influence the overall footing response are described in the following sub-sections.

Table 2.1: BNWF model parameters

User-defined parameters	Hard-coded parameters
<ul style="list-style-type: none"> • Capacity of footing (Q_{ult}, P_{ult} or T_{ult}) • Stiffness of footing (K_v or K_h) • Soil type (sand or clay) • Footing dimensions (L, B, H and D_f) • Tension capacity (TP) • End-length ratio (R_e) • Stiffness intensity ratio (R_k) • Spring spacing (l_e/L) 	<ul style="list-style-type: none"> • Elastic range (C_r) • Post-yield stiffness (K_p) • Unloading stiffness (K_{unl})

2.5.1 Ultimate Load Capacity (Vertical and Lateral)

Capacity of the footing is an important parameter that must be specified by the user. If calculated, the ultimate vertical bearing capacity is determined using the basic soil parameters such as the friction angle, cohesion, length and width of footing, and depth of embedment.

The code calculates the overall footing bearing capacity, and then subdivides it according to tributary area and assigns values to individual springs. The overall ultimate vertical bearing capacity may be calculated based on general bearing capacity equations readily available in any foundation design textbooks (). In this work, the general bearing capacity equation as well as the depth, shape, bearing capacity and inclination factors of Meyerhof (1963) are adopted:

$$q_{ult} = c'N_cF_{cs}F_{cd}F_{ci} + \gamma D_f N_q F_{qs} F_{qd} F_{qi} + 0.5\gamma B N_\gamma F_{\gamma s} F_{\gamma d} F_{\gamma i} \quad (2.5)$$

where q_{ult} = ultimate vertical bearing capacity per unit area of footing, c = cohesion, γ = unit weight of soil, D_f = depth of embedment, B = width of footing; N_c , N_q and N_γ are bearing capacity factors, F_{cs} , F_{qs} and $F_{\gamma s}$ are shape factors, F_{cd} , F_{qd} and $F_{\gamma d}$ are depth factors and F_{ci} , F_{qi} and $F_{\gamma i}$ are inclination factors. The equations for calculating the bearing capacity, shape, depth and inclination factors are as follows:

- Bearing capacity factors

$$\text{(Reissner, 1924):} \quad N_q = \tan^2 \left(45^\circ + \frac{\phi'}{2} \right) e^{\pi \tan \phi'} \quad (2.6)$$

$$\text{(Prandtl, 1921):} \quad N_c = (N_q - 1) \cot \phi^\circ \quad (2.7)$$

$$\text{(Meyerhof, 1963):} \quad N_\gamma = (N_q - 1) \tan(1.4\phi^\circ) \quad (2.8)$$

- Shape factors (Meyerhof, 1963):

For $\phi = 0^\circ$,

$$F_{cs} = 1 + 0.2(B/L) \quad (2.9)$$

$$F_{qs} = F_{\gamma s} = 1 \quad (2.10)$$

For $\phi \geq 10^\circ$,

$$F_{cs} = 1 + 0.2(B/L) \tan^2 \left(45^\circ + \frac{\phi'}{2} \right) \quad (2.11)$$

$$F_{qs} = F_{\gamma s} = 1 + 0.1(B/L) \tan^2 \left(45^\circ + \frac{\phi'}{2} \right) \quad (2.12)$$

- Depth factors (Meyerhof, 1963):

For $\phi = 0^\circ$,

$$F_{cd} = 1 + 0.2(D_f/B) \quad (2.13)$$

$$F_{qd} = F_{\gamma d} = 1 \quad (2.14)$$

For $\phi \geq 10^\circ$,

$$F_{cd} = 1 + 0.2(D_f/B) \tan \left(45^\circ + \frac{\phi'}{2} \right) \quad (2.15)$$

$$F_{qd} = F_{\gamma d} = 1 + 0.1(D_f/B) \tan \left(45^\circ + \frac{\phi'}{2} \right) \quad (2.16)$$

- Inclination factors (Meyerhof, 1963):

$$F_{ci} = F_{qi} = \left(1 - \frac{\beta^\circ}{90^\circ}\right)^2 \quad (2.17)$$

$$F_{\gamma i} = \left(1 - \frac{\beta}{\phi}\right)^2 \quad (2.18)$$

where β = angle of inclination of the load applied to the foundation.

In presence of a shallow water table, the expressions needs to be modified based on Salgado (2006) or Das (2007).

For the *PySimple1* material, the ultimate lateral capacity is determined as the total passive resisting force acting on the front face of the embedded footing. The passive resisting force can be assumed to be a linearly varying pressure distribution (assuming a homogeneous layer) as:

$$p_{ult} = 0.5\gamma K_p D_f^2 \quad (2.19)$$

where p_{ult} = passive earth pressure per unit length of footing, γ = unit weight of soil, and K_p = passive earth pressure coefficient. K_p may be calculated using Coulomb (1776), Rankine (1847), or Logspiral theories (such as Caquot and Kerisel (1948)). In this work, expressions provided in Coulomb (1776) are used. Note that the user may input p_{ult} directly if other theories for passive resistance are of interest.

For the *TzSimple1* material, the ultimate lateral capacity is the total sliding resistance. The frictional resistance can be determined using the general equation for shear strength of a footing soil interface after considering a reasonable base friction angle between soil and the footing base. The equation used to calculate the sliding capacity of a foundation resting on cohesionless soil can be calculated assuming the classical Mohr-Coulomb failure

criteria:

$$t_{ult} = W_g \tan \delta + c' A_f \quad (2.20)$$

where t_{ult} = frictional resistance per unit area of foundation, W_g = weight on the foundation from the structure, δ = angle of friction between foundation and soil, which typically varies from $1/3\phi'$ to $2/3\phi'$, A_f = surface area of the foundation.

The effective friction angle ϕ' is the most important parameter for dictating the ultimate capacity (vertical, frictional and passive) characteristics of the footing. In order to show the effect of friction angle (and thus capacity) on the overall footing response, a square footing of size 5m x 5m embedded 1.72m in cohesionless dry sand of relative density 80%. Note that the footing and soil properties for this simulation are chosen based on bridge pier shallow foundation tests performed at the University of California, Davis (Ugalde, 2007). The footing is subjected to a static sinusoidal rotational input motion while varying the friction angle of soil. The SSI model as described in Figure 2.2 is used. Figure 2.14 shows the rotation time history used as an input motion. Unless otherwise mentioned, the same foundation and input motion is considered in the following sections of this chapter.

Figures 2.15(a)–(b) show the variation in vertical and horizontal load capacities a fraction of friction angle. These capacity calculations are based on 5m square footing with an embedment ratio (D_f/B) of 0.3 and unit weight of 16 kN/m³. V_{ult} is the total horizontal resistance summing passive capacity and sliding capacity (i.e., $T_{ult} + P_{ult}$). It can be seen that varying the friction angle by 10% (from 38° to 42°) changes the ultimate vertical bearing capacity by more than 50% (from 150 MN to 320 MN) The horizontal capacity is not as sensitive to ϕ' when compared to vertical capacity. The horizontal capacity varies from 1.52 MN to 1.79 MN (i.e., a 15% increase of capacity for a 10% increase in ϕ').

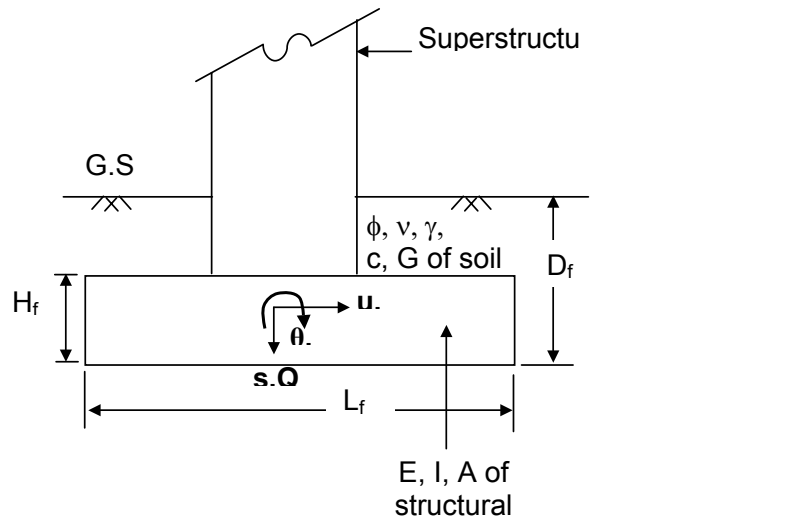
To show the sensitivity of ϕ' on the footing response, Figures 2.16(a)–(b) are provided. Figures 2.16(a), and (b) show the plots of moment versus rotation and settlement versus rotation, respectively, for $\phi' = 40^\circ$ and 42° . It can be observed from Figures 2.16(a)–(b) that by changing ϕ' from 42° to 40° , the moment demand (maximum absolute value) is decreased by 33% while the settlement demand (maximum absolute value) is increased by 65%. It is evident that a small uncertainty in friction angle can make a big difference in the settlement prediction. This can be explained by the fact that an increase in ϕ' results in higher ultimate bearing capacity of individual springs. As a result, the footing with lower capacity undergoes more inelastic deformation producing more settlement. This can also be observed from the time history responses as given in Figure 2.17, where in the beginning (up to time ≈ 650 sec), moment and settlement responses are same for both values of ϕ' .

Figures 2.18(a)–(b) provide a summary of normalized moment and settlement demands, respectively, with varying ϕ' . The maximum moment and settlement demands are normalized by their corresponding values when using the lowest value of ϕ' is selected, i.e., for $\phi' = 38^\circ$. It is observed from Figures 2.18(a)–(b) that if ϕ' is increased from 38° to 42° , the moment demand increases about 36% and the settlement demand decreases about 80%. The responses for moment and settlement demands can be regressed linearly with R^2 value of nearly 98% for both the cases. Note that this range of ϕ' is a reasonable range for dense dry sand (with relative density, D_r of approximately 75-80%), where shallow foundations would commonly be used in practice.

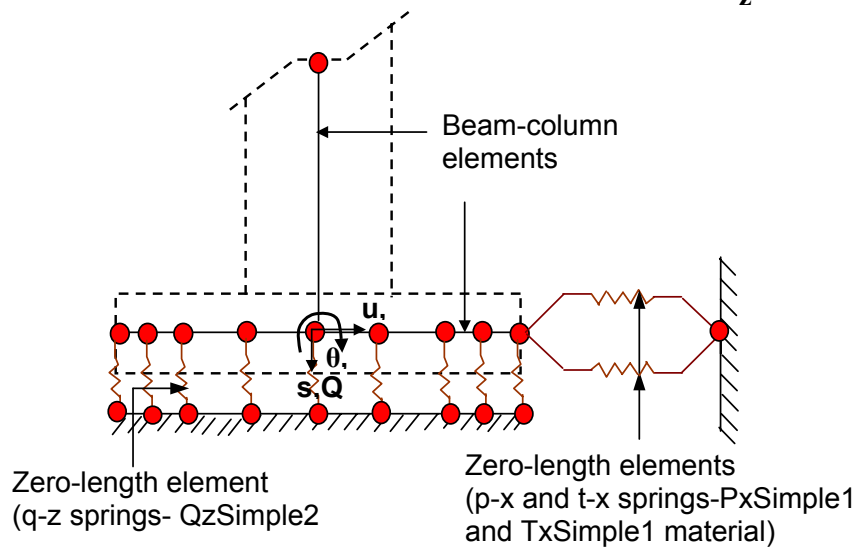
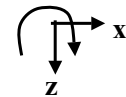
2.5.2 Vertical and Lateral stiffness (K_v and K_h)

The vertical and lateral stiffness are input parameters for both *QzSimple1* and *TzSimple1*, and may be calculated using expressions given by Gazetas (1991a) (also suggested

in ATC-40 (1996)). The rotational stiffness of the foundation is accounted for implicitly via the differential movement of the vertical springs. The rotational stiffness is therefore a function of the distribution of the vertical springs over the length of the footing. The vertical as well as lateral stiffness are highly dependant on the shear modulus of the soil and footing dimensions such as length, width and depth of embedment. The uncertainty in the estimation of shear modulus can greatly affect the stiffness of the springs and response of the entire footing. Therefore, care should be taken when selecting the shear modulus. A range of experimental values of shear modulus for different types of soil can be found in EPRI (1990). Table 2.2 summarizes the equations to calculate stiffness of the footing in different modes such as vertical, lateral and rotational for both surface and embedded footing.



(a)



(b)

Axis	Force	Displacement
x	V	u
z	Q	s
θ	M	θ

Notes:

1. Superstructure elements are not generated by the **ShallowFoundationGen** command. The user must specify the mid node (node in the schematic).
2. p-x and t-x springs are connected to identical end nodes with zero distance between them, however, are they independent.

Figure 2.2: Schematic diagram of the proposed BNWF model for shallow foundations

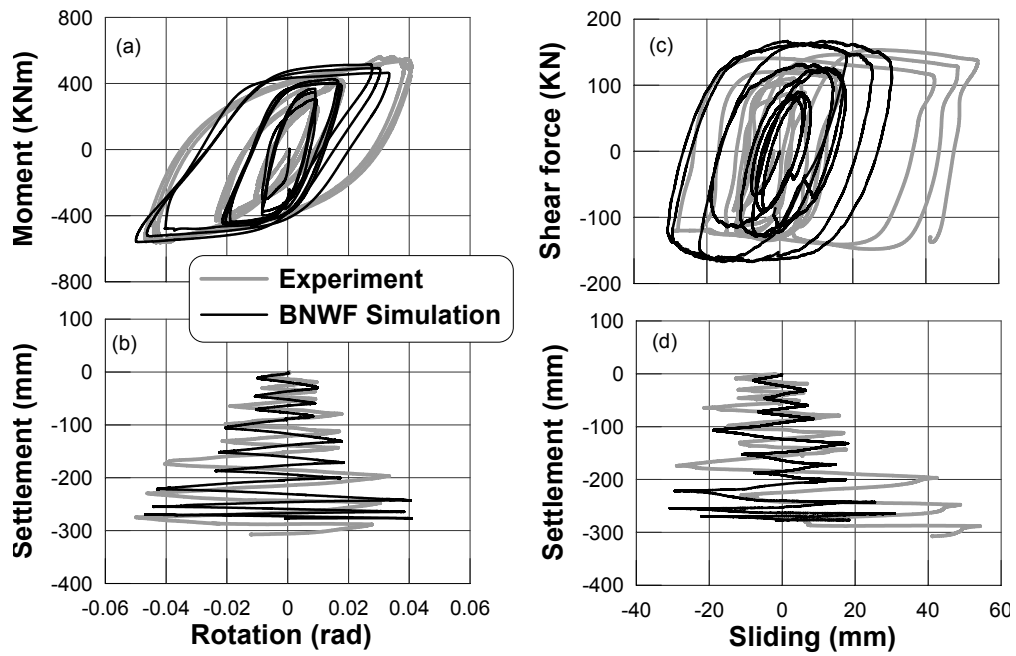


Figure 2.3: Model capability in terms of moment-rotation, settlement-rotation and shear-sliding response (based on centrifuge test of strip footing resting on dense dry sand of $D_r = 80\%$ and $FS_v = 2.3$)

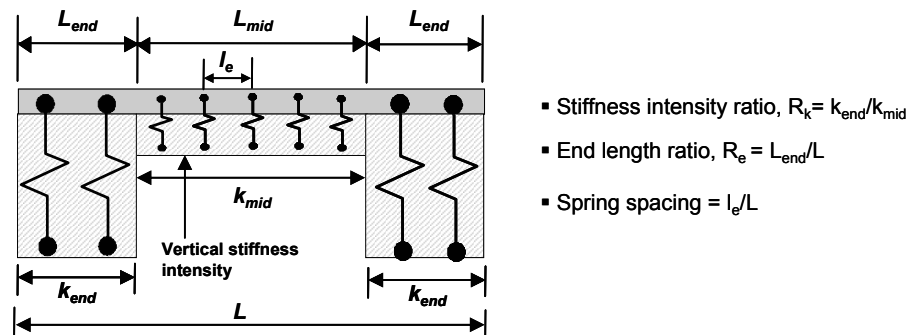


Figure 2.4: BNWF Mesh discretization with variable stiffness intensity (Harden et al., 2005)

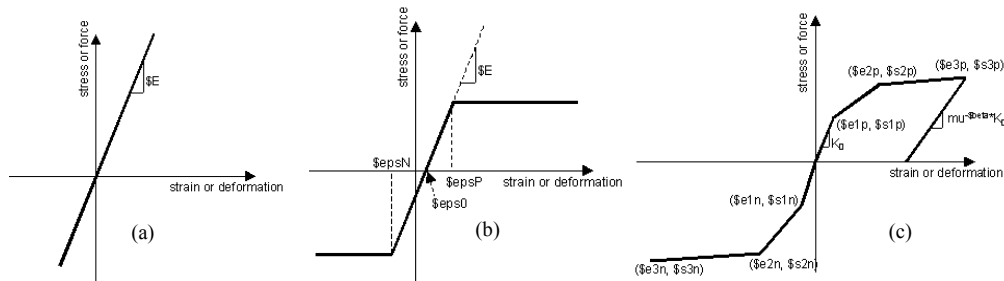


Figure 2.5: Various simple material models available for shallow foundation modeling: (a) elastic (b) elastic-perfectly plastic and (c) general hysteretic backbone curves as available in OpenSees (2008)

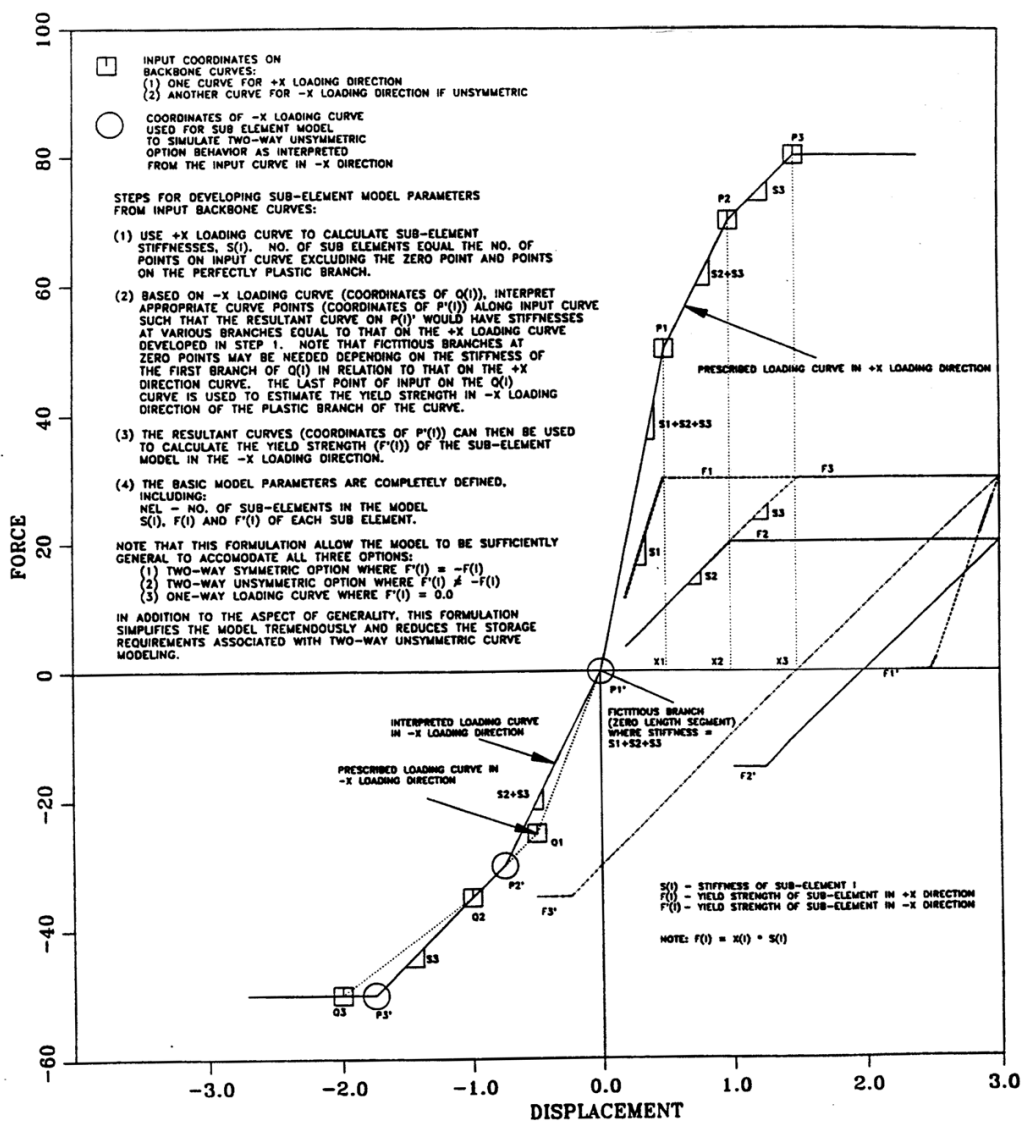


Figure 2.6: Backbone curve of hysteretic materials in parallel after Martin and Yan (1997)

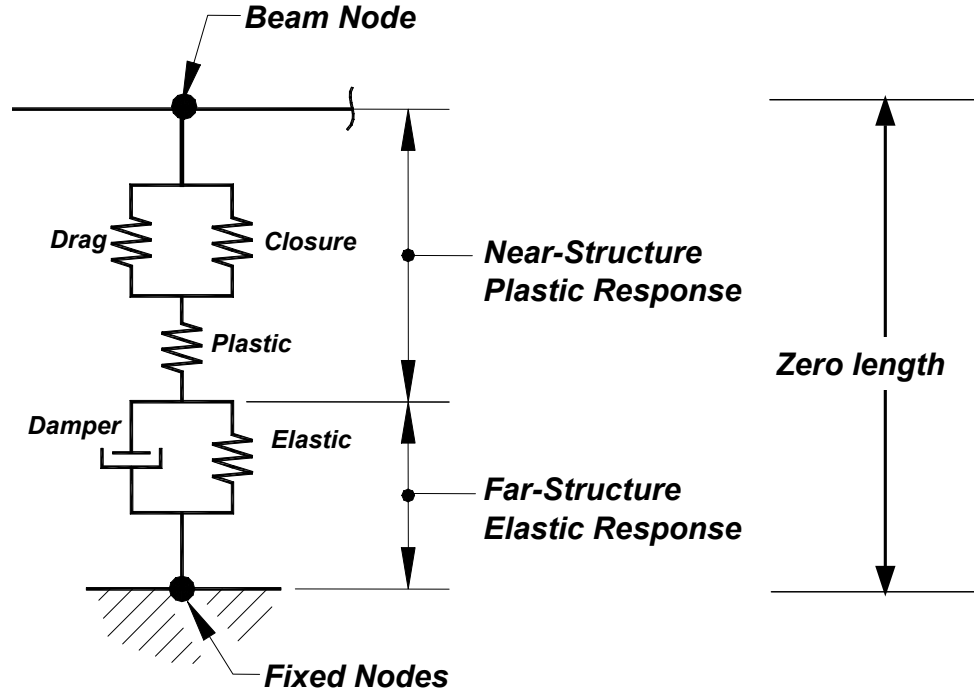


Figure 2.7: $Q_zSimple1$, $P_ySimple1$ and $T_zSimple1$ material models used in conjunction with zeroLength element

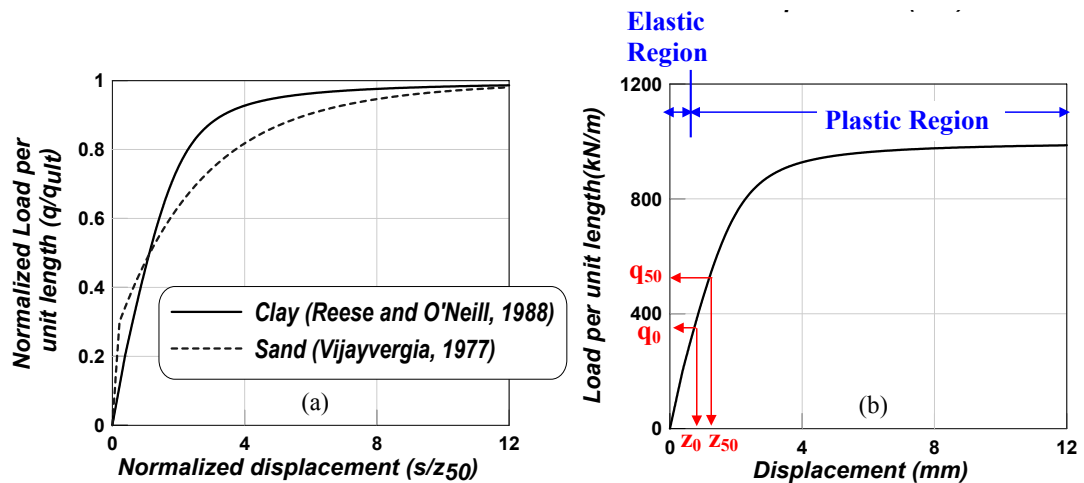


Figure 2.8: $Q_zSimple1$ backbone curve: (a) backbone curves used for soil-pile modeling and (b) general backbone curve

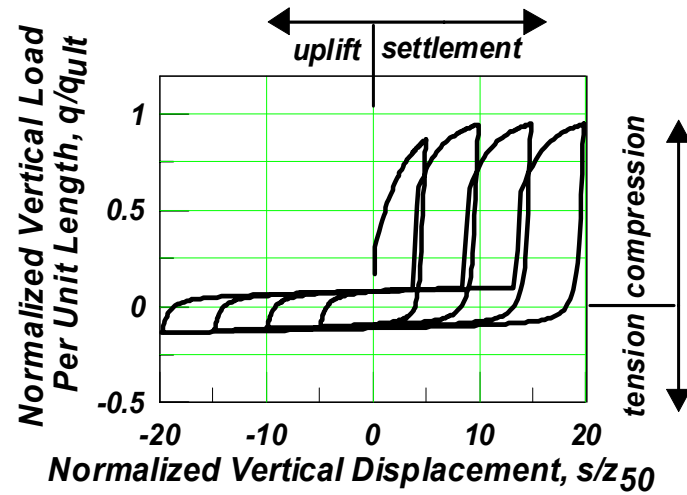


Figure 2.9: Cyclic response of *QzSimple1* (Boulangier, 2000b)

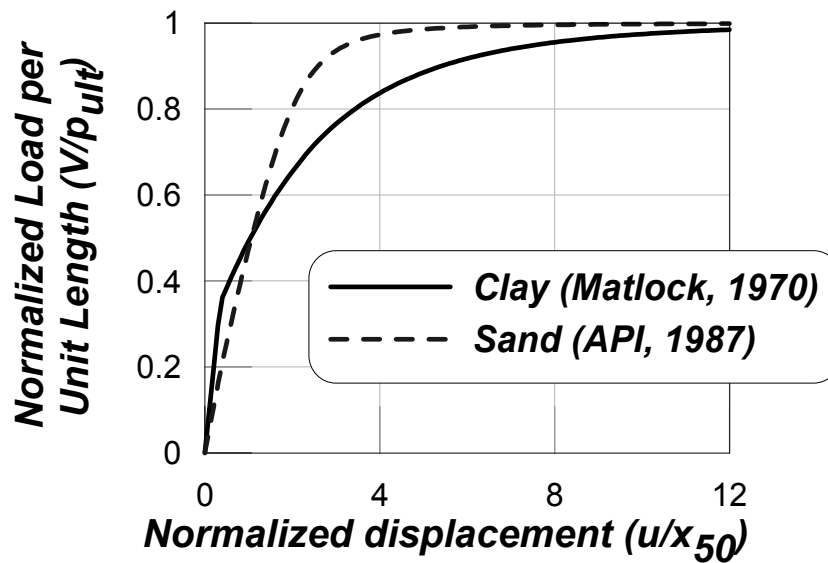


Figure 2.10: *PySimple1* backbone curve

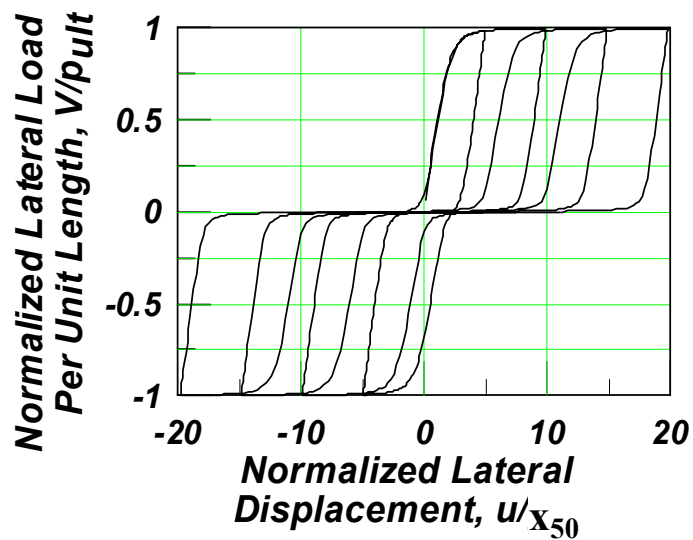


Figure 2.11: Cyclic response of *PySimple1* (Boulanger, 2000a)

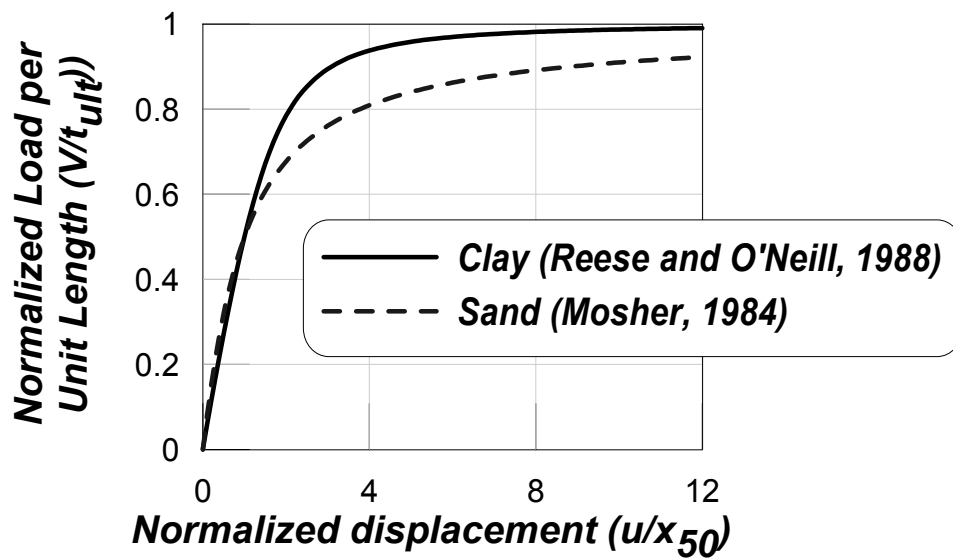


Figure 2.12: *TzSimple1* backbone curve

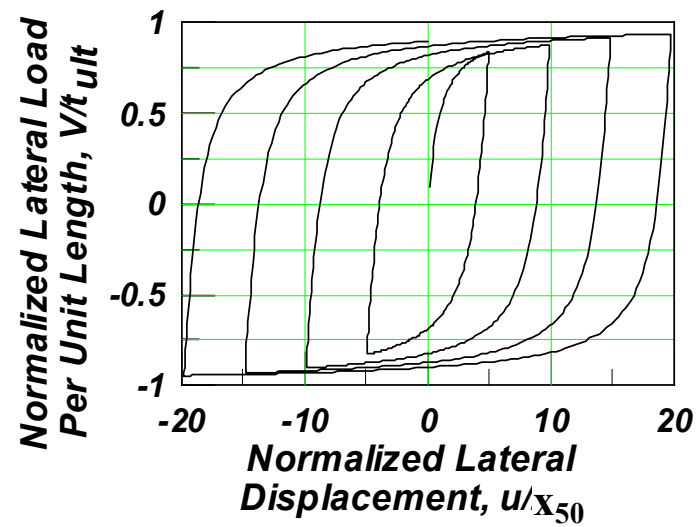


Figure 2.13: Cyclic response of *TzSimple1* (Boulanger, 2000c)

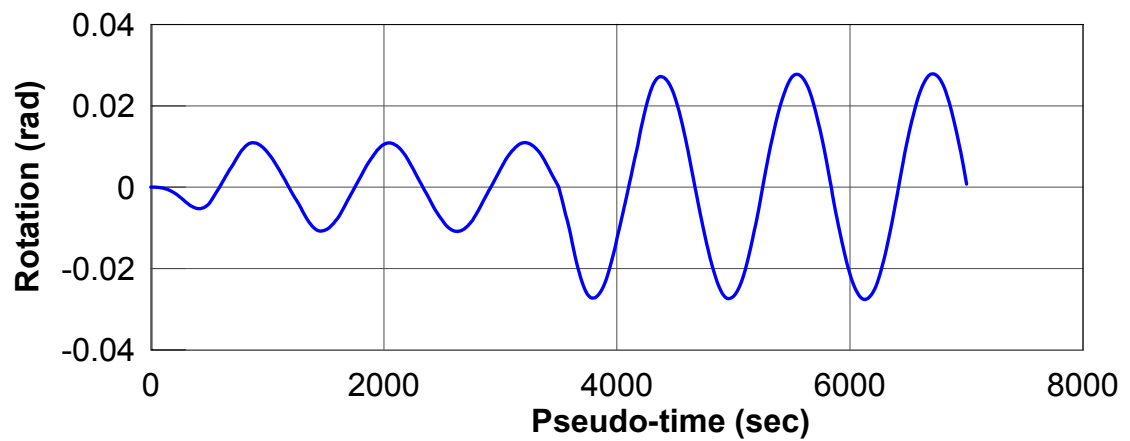


Figure 2.14: Rotational input motion applied at the base of a 5m square footing

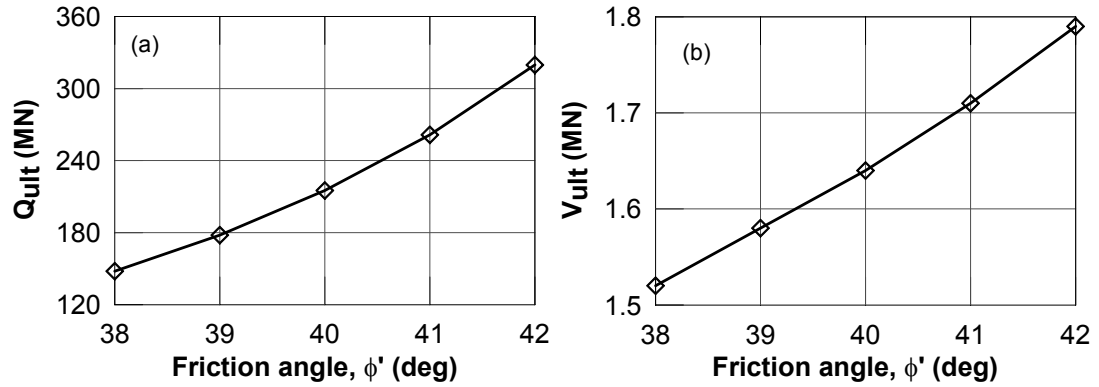


Figure 2.15: Variation of (a) vertical load capacity and (b) horizontal load capacity with friction angle ϕ' for a 5m square footing with $D_f/B = 0.3$, $c' = 0$ and $\gamma = 16kN/m^3$:

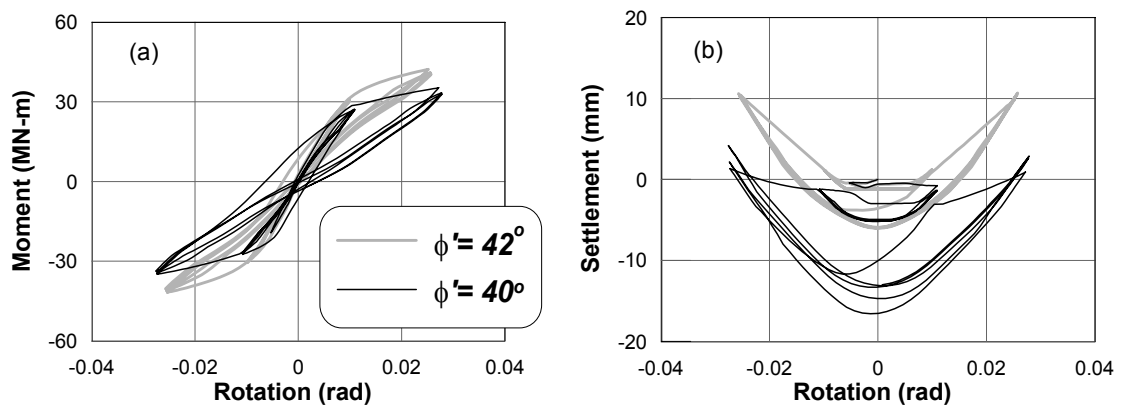


Figure 2.16: Effect of change in friction angle ϕ' on the footing response: (a) moment versus rotation and (b) settlement versus rotation

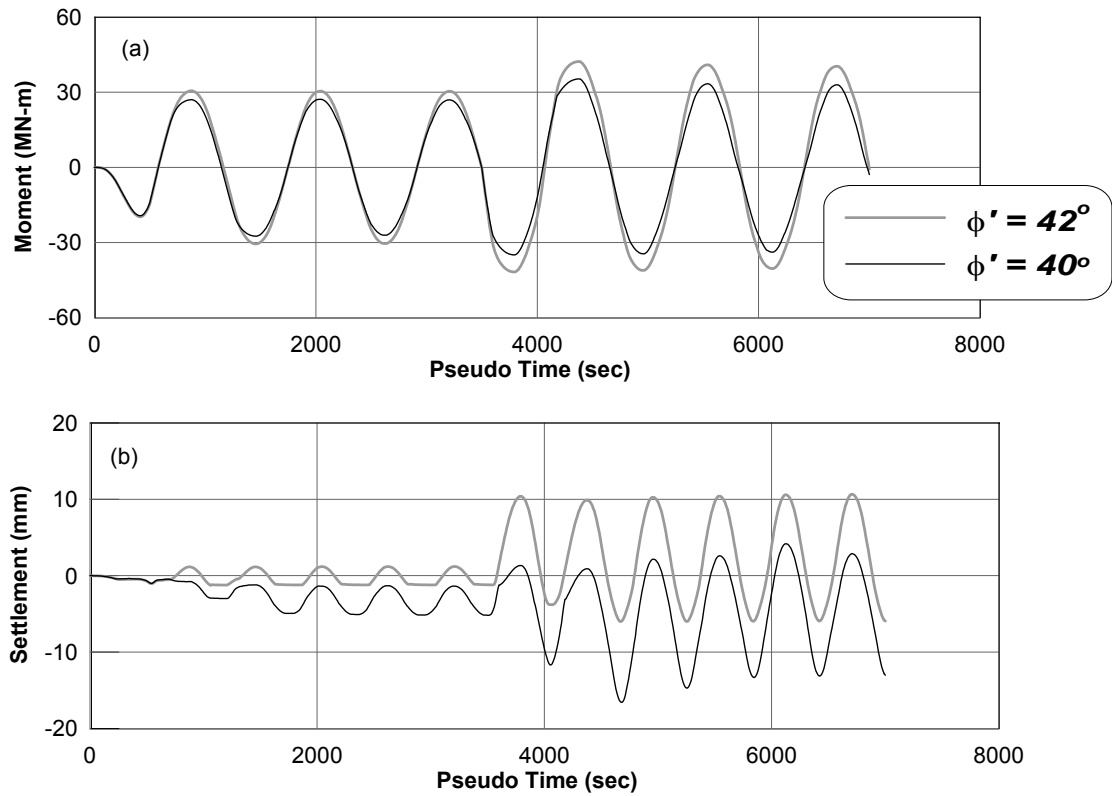


Figure 2.17: Effect of change in friction angle ϕ' on the footing response: (a) moment time history, (b) settlement time history

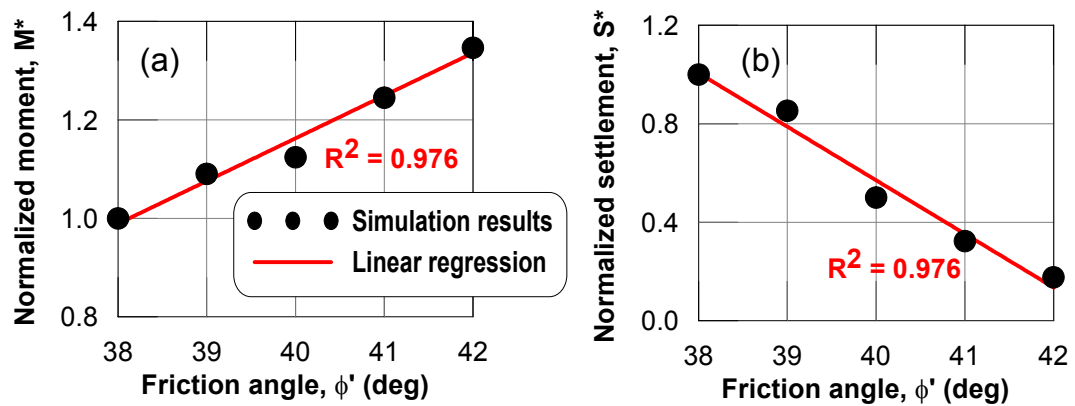
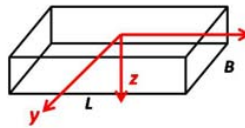


Figure 2.18: Sensitivity of friction angle ϕ' on footing response: (a) normalized moment demand and (b) normalized settlement demand

Table 2.2: Equations for determining shallow foundation stiffness after Gazetas (1991a) as summarized in ATC-40 (1996).

Stiffness	Equation
	Surface Stiffness
Vertical Translation	$K_z' = \frac{GL}{1-\nu} \left[0.73 + 1.54 \left(\frac{B}{L} \right)^{0.75} \right]$ 
Horizontal Translation (toward long side)	$K_y' = \frac{GL}{2-\nu} \left[2 + 2.5 \left(\frac{B}{L} \right)^{0.85} \right]$
Horizontal Translation (toward short side)	$K_x' = \frac{GL}{2-\nu} \left[2 + 2.5 \left(\frac{B}{L} \right)^{0.85} \right] + \frac{GL}{0.75-\nu} \left[0.1 \left(1 - \frac{B}{L} \right) \right]$
Rotation about x-axis	$K_{\theta x}' = \frac{G}{1-\nu} I_x^{0.75} \left(\frac{L}{B} \right)^{0.25} \left(2.4 + 0.5 \frac{B}{L} \right)$
Rotation about y-axis	$K_{\theta y}' = \frac{G}{1-\nu} I_y^{0.75} \left[3 \left(\frac{L}{B} \right)^{0.15} \right]$
	Stiffness Embedment Factors
Embedment Factor, Vertical Translation	$e_z = \left[1 + 0.095 \frac{D_f}{B} \left(1 + 1.3 \frac{B}{L} \right) \right] \left[1 + 0.2 \left(\frac{2L + 2B}{LB} H \right)^{0.67} \right]$
Embedment Factor, Horizontal Translation (toward long side)	$e_y = \left[1 + 0.15 \left(\frac{2D_f}{B} \right)^{0.5} \right] \left\{ 1 + 0.52 \left[\frac{\left(D_f - \frac{H}{2} \right) 16(L+B)H}{BL^2} \right]^{0.4} \right\}$
Embedment Factor, Horizontal Translation (toward short side)	$e_x = \left[1 + 0.15 \left(\frac{2D_f}{L} \right)^{0.5} \right] \left\{ 1 + 0.52 \left[\frac{\left(D_f - \frac{H}{2} \right) 16(L+B)H}{LB^2} \right]^{0.4} \right\}$
Embedment Factor, Rotation about x axis	$e_{\theta x} = 1 + 2.52 \frac{H}{B} \left(1 + \frac{2H}{B} \left(\frac{d}{D_f} \right)^{-0.2} \left(\frac{B}{L} \right)^{0.5} \right)$
Embedment Factor, Rotation about y axis	$e_{\theta y} = 1 + 0.92 \left(\frac{2H}{L} \right)^{0.60} \left(1.5 + \left(\frac{2H}{L} \right)^{1.9} \left(\frac{H}{D_f} \right)^{-0.60} \right)$

Where, K_i = Uncoupled Total Surface Stiffness for a rigid plate on a semi-infinite homogeneous elastic half-space, e_i = Stiffness Embedment Factor for a rigid plate on a semi-infinite homogeneous elastic half-space, L = foundation length, B = foundation width, D_f = depth of embedment, H = foundation thickness, G = Shearing Modulus, ν = Poisson's ratio.

Figure 2.19 shows the variation of vertical and lateral stiffness calculated after Gazetas (1991a) with varying modulus of elasticity of soil E_s for the 5m square footing considered herein. Poisson's ratio ν is assumed as 0.4 for dry dense sand. The shear modulus G_s is calculated from E_s as:

$$G_s = \frac{E_s}{2(1 + \nu)} \quad (2.21)$$

Figures 2.20(a)–(c) show the effect of changing the modulus of elasticity of the soil on the moment versus rotation, settlement versus rotation and shear versus sliding responses respectively of the footing considered here. As expected, the settlement is affected the most when the modulus is varied. A reduction of approximately 36% (from 55 MPa to 35 MPa) in the modulus of elasticity increases the settlement demand by 57%. It is observed that moment and shear demands are not affected considerably by the modulus change. Note also that although the shear-sliding response is in the linear range, the change in stiffness of the foundation causes a comparatively smaller change in the sliding demand.

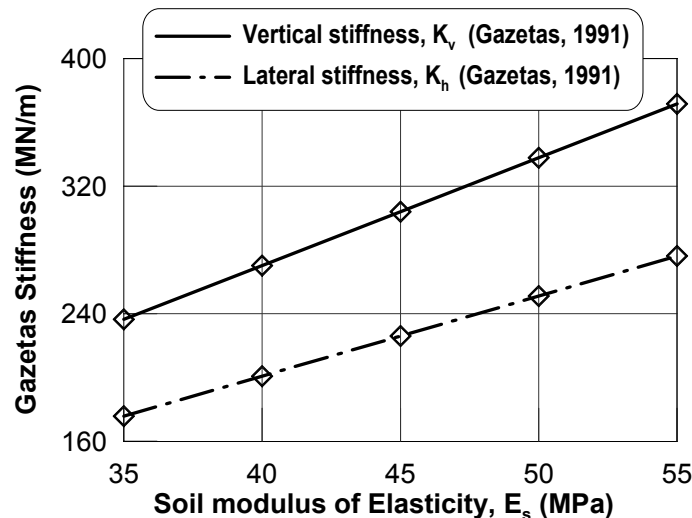


Figure 2.19: Vertical and lateral stiffness using expressions of Gazetas (1991a) for the 5m square footing with $D_f/B = 0.3$ and $\nu = 0.4$

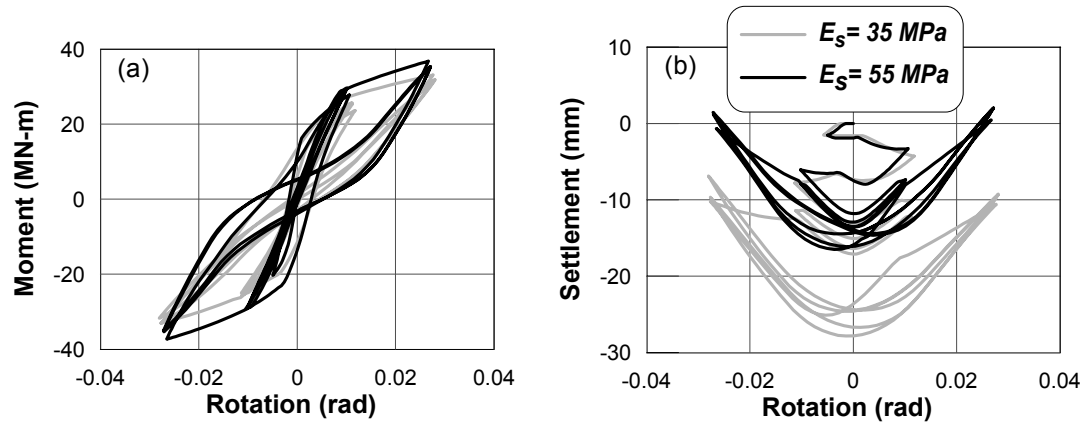


Figure 2.20: Effect of varying soil modulus of elasticity (E_s) on footing response: (a) moment versus rotation, (b) settlement versus rotation and (c) shear versus sliding

Figures 2.21 (a) and (b) show the normalized settlement and sliding demands, respectively, for different values of modulus of elasticity of soil E_s . Since the change in modulus of elasticity (and hence stiffness) does not have a significant effect on the moment and shear demands, only the settlement and sliding demands are shown. Settlement and sliding demands are normalized by their values corresponding to the lowest E_s value (i.e., $E_s = 35$ MPa in this case). One can observe from Figure 2.21(a) that the normalized settlement reaches 0.6 whereas the normalized sliding decreases to 0.71 when E_s is increased from 35 MPa to 55 MPa. It is also observed from Figure 2.21 that the settlement and sliding demands approximately linearly related to E_s with R^2 values of 0.93 and 0.98, respectively.

2.5.3 Tension Capacity, TP

Tension capacity TP of a spring is the maximum amount of suction force that can be taken by a spring. The vertical tension capacity of a footing is manifested via the vertical springs (*QzSimple1* material) and may range from 0–10% of the compression capacity q_{ult} .

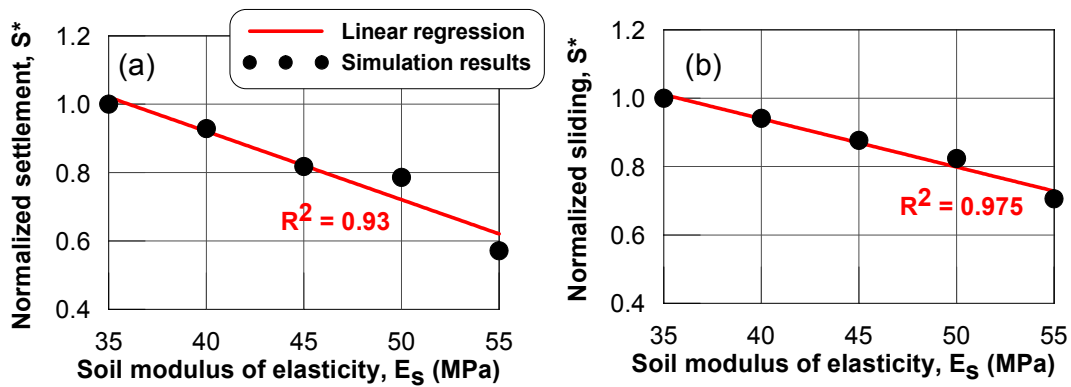


Figure 2.21: Variation of normalized: (a) settlement and (b) sliding demands with varying modulus of elasticity of the soil

For the lateral springs (*PySimple1* and *TzSimple1* materials) modeling passive and sliding resistance, respectively, the tension capacity is same as the compression capacity since the hysteretic behavior of these springs are assumed to be symmetric.

Figure 2.22 demonstrates the effect of varying the tension capacity of a single vertical spring from 0% to 10% on the hysteretic response. One can notice from this figure that changing the tension capacity of a vertical spring will not change the stiffness, capacity or shape of the backbone in the compression side. However, at a displacement of approximately 18mm, the normalized load on the spring becomes zero implying that this is the permanent deformation. Any further unloading from this point results in tension of the spring and as observed from Figure 2.22, for $TP = 0$ and 10%, the ultimate normalized load on the spring is 0 and 0.1.

Figures 2.23(a) and (b) show the moment versus rotation and settlement versus rotation, respectively, for $TP = 0\%$ and 10%. One can observe from these figures that the shape of the moment-rotation and settlement-rotation curves remains the same with different tension capacities. However, the moment capacity increases about 8% with additional tension

capacity provided, while the settlement decreases approximately 20%.

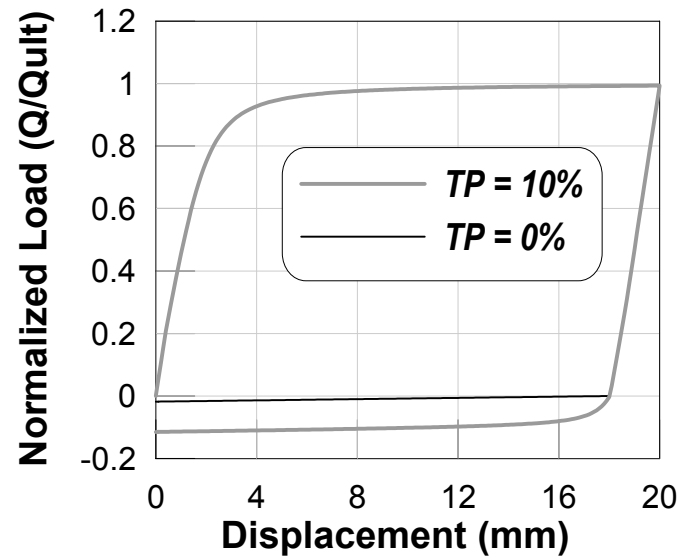


Figure 2.22: Effect of tension capacity TP on a single spring response

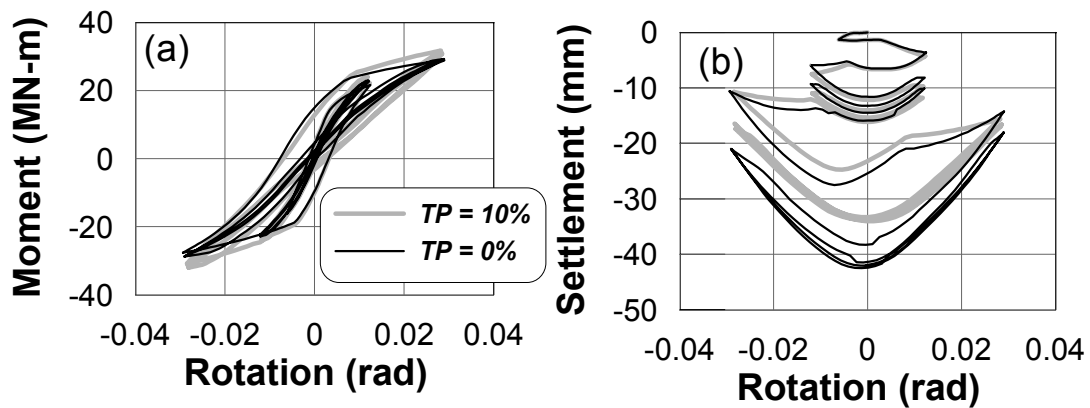


Figure 2.23: Effect of varying the tension capacity on the overall footing response: (a) moment versus rotation and (b) settlement versus rotation

Figures 2.24(a) and (b) show the normalized moment and settlement demands respectively for varying tension capacity TP . The range of tension capacity in these figures is from 0% to 10%. The moment and settlement demands are normalized with respect to their

corresponding no-tension cases (i.e. $TP = 0\%$ case). It can be seen that the moment demand increases linearly with the increase in TP . On the other hand, the settlement demand decreases with increase in TP . The rate of change in settlement demand is higher in the beginning (for TP 0% to 5%) and then it starts to converge (for TP 5% to 10%) for this particular loading case. This can be explained from the fact that a increase in TP of springs results increased stiffness and moment capacity of footing. However, the settlement of the midpoint of the foundation is a function of deformation of individual springs, which exhibit highly nonlinear behavior in both tension and compression sides. Thus, a change in TP produces nonlinear variation of the settlement as observed in Figures 2.24(b).

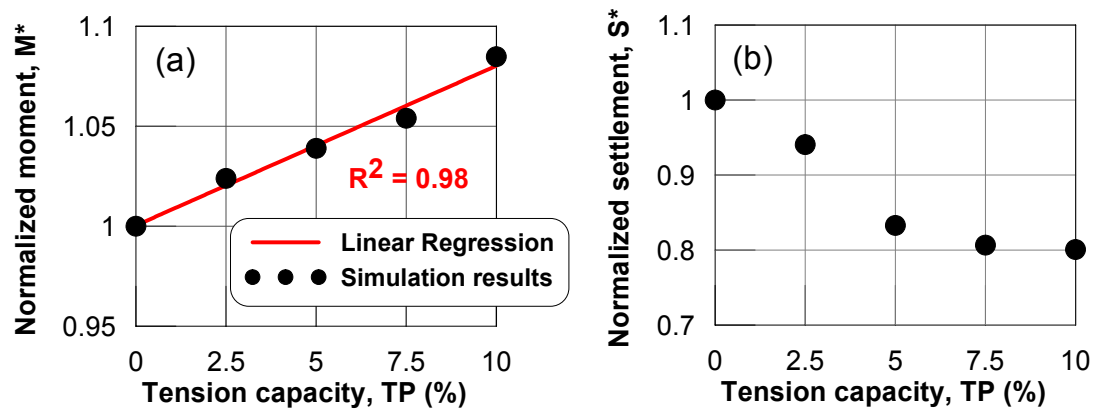


Figure 2.24: Effect of variation in tension capacity on (a) normalized moment and (b) normalized settlement demands of the footing

2.5.4 Soil Type

The user must specify whether the material is sand (Type 1) or clay (Type 2). Sand is assumed to respond under drained conditions and strengths are defined using effective stress strength parameters ($c' = 0, \phi'$). Clay is assumed to respond under undrained conditions and strengths are described using total stress strength parameters ($c', \phi' = 0$). Based on the input

soil type, backbone curves are described using effective or total stress strength parameters, as described above. In addition, corresponding hard-wired (non-user specified) parameters (C_r, c, n) are used to complete the definition of the backbone curve. As described below, when shear strength parameters are specified, they are used with foundation dimensions to calculate ultimate load capacity. Note that currently, $c-\phi$ (or $c'-\phi'$) material backbone curves are not available. However, the OpenSees code can accept as input an externally calculated bearing capacity for a c-f soil, which can be specified along with the Type 1 or 2 designations that corresponds best to the expected material response.

2.5.5 End Length Ratio, R_e

A variable stiffness distribution along the length of the foundation is used in the model to distribute vertical stiffness such that rotational stiffness equates to that of Gazetas (1991c). The parameter R_e is defined as the ratio of length of higher stiffness region to the total length of the footing.

$$R_e = \frac{L_{end}}{L} \quad (2.22)$$

ATC-40 (1996) suggests that a higher intensity of stiffness (stiffer springs) should be placed at the end region. The end region L_{end} is defined as the length of the edge region over which the stiffness is increased. ATC-40 (1996) suggests $L_{end} = B/6$ (B being the width of the footing) from each end of the footing (shown in Figure 2.25) . Note that L_{end} is independent of the footing aspect ratio according to ATC-40 (1996), while Harden et al. (2005) showed that L_{end} varies with footing aspect ratio. For a square footing (aspect ratio=1), the end length ratio after Harden et al. (2005) converges with that of ATC-40 (1996), with a value of about 16% (Figure 2.26). In Figure 2.26, both the curves

corresponding to L_e/B and L_e/L yield same L_e for a specified aspect ratio giving the user flexibility of choosing any of the curves to determine L_e .

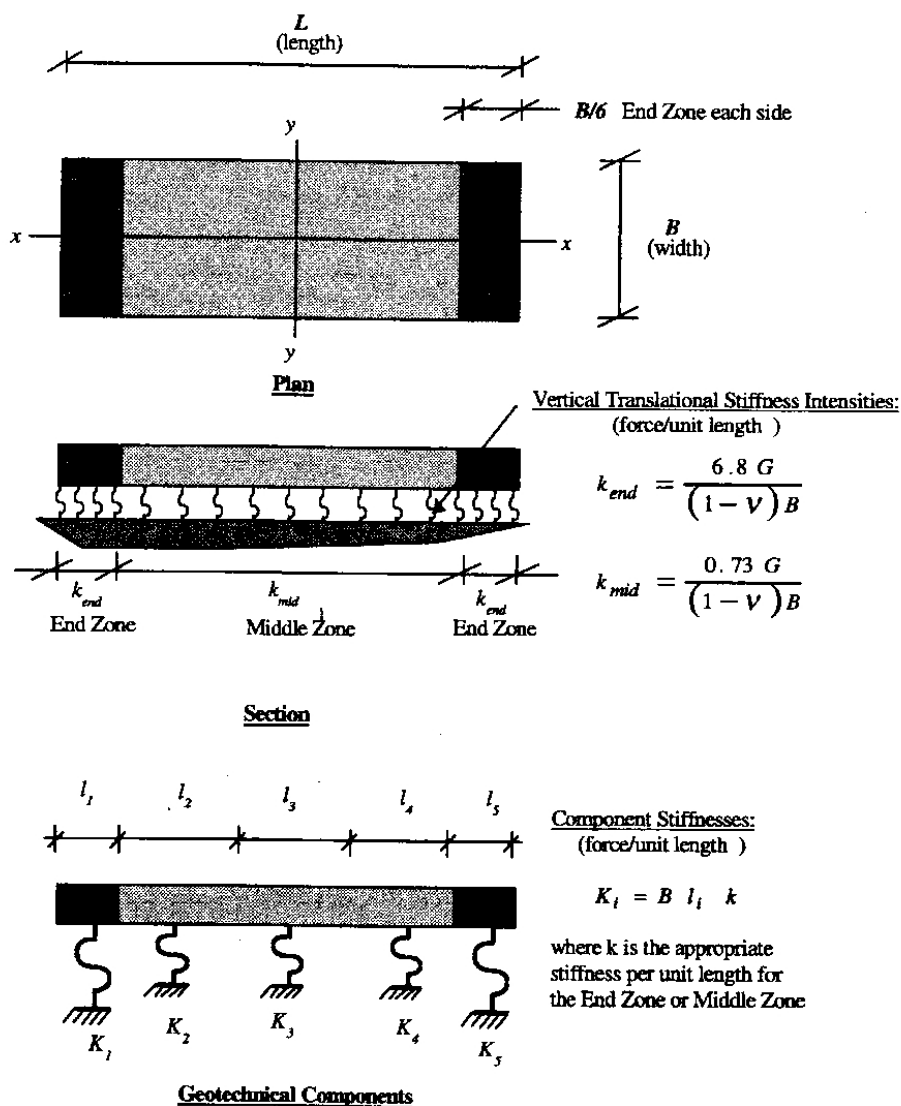


Figure 2.25: Winkler component model of rectangular spread footing (ATC-40, 1996)

In order to show the effect of end length ratio on footing response, moment and settlement of the 5m square footing is simulated and plotted against rotation in Figures 2.27 (a) and (b) respectively for different end length ratios ($R_e = 0\%$ and 16%). From Figures 2.27 (a) and (b), it is seen that a change in end length ratio of about 16% results in change in

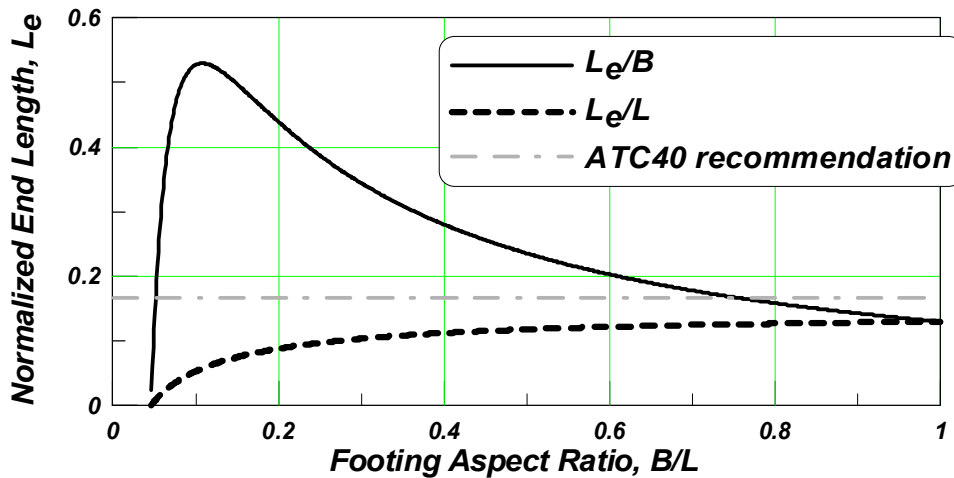


Figure 2.26: Normalized end length versus footing aspect ratio given by (Harden et al., 2005) along with ATC-40 (1996) recommended value

the footing settlement or moment demands. Note that an increase in R_e results in increased stiffer end zones and reduced middle zone (lower stiffness intensity area). As a result, for a given rotation history, a variation in R_e may result in nonlinear variation of footing response considering the fact that (i) the behavior of individual vertical springs (both in tension and compression sides) are highly nonlinear and (ii) tension capacity of vertical springs is very small compared to that of the compression capacity.

Figure 2.28 shows the sensitivity of R_e on normalized settlement demand. Here settlement demand is normalized with respect to the case when uniform spring stiffness distribution is considered (i.e. when $R_e = 0\%$). The range of R_e is varied from 0% (no end region) to 16% (end length region as per ATC-40 (1996)). It is observed from this figure that the normalized settlement demand varies nonlinearly with R_e . As observed from Figure 2.28, a change in R_e from 0 to 16% results in 6% change in the settlement demand for this footing under the given loading history.

Since, it is observed from Figure 2.26 that L_e proposed by Harden et al. (2005) deviates

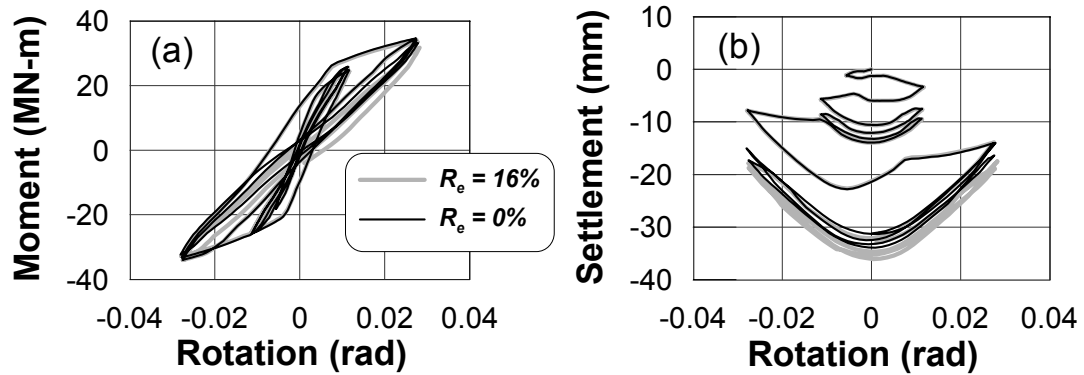


Figure 2.27: Effect of end length ratio R_e on footing response: (a) moment versus rotation and (b) settlement versus rotation

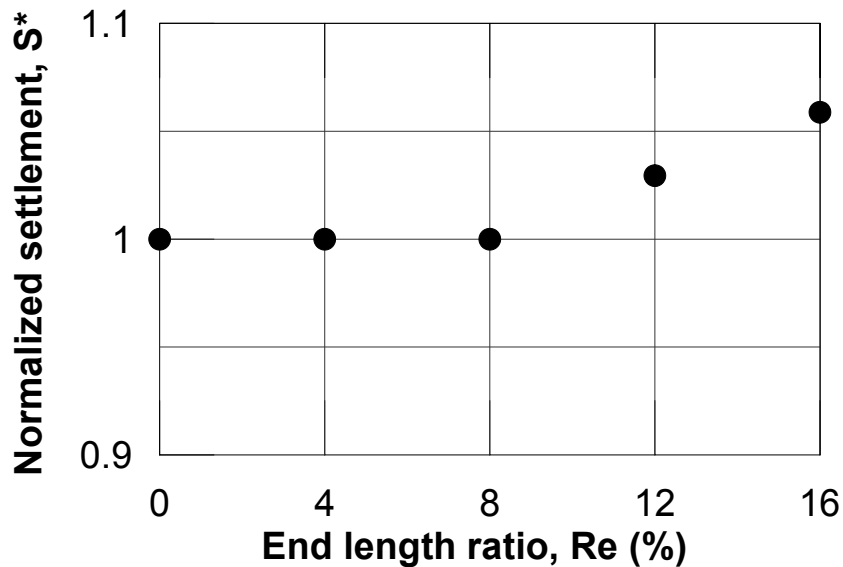


Figure 2.28: Sensitivity of end length ratio on settlement demand

more from ATC-40 (1996) recommendation for lower aspect ratio footings, an additional footing with lower aspect ratio ($B/L = 0.23$) is also considered. The footing size, loading history and soil conditions are taken from test SSG02-05 by Gajan et al. (2003a). The sensitivity of R_e on the strip footing is shown in Figure 2.29. ATC-40 (1996) and Harden et al. (2005) suggested values for a strip footing with $B/L = 0.23$ are considered in this case.

It can be observed from the Figure 2.29, that with an increase in R_e from 10% to 16%, the moment and settlement demands increase by approximately 30% and 20%, respectively. Note that the increase in R_e results in increased rotational stiffness of the footing resulting higher moment demand. However, an increase in R_e (which increases the number of stiffer end springs) produces more permanent deformation of the footing owing to the fact that a stiffer spring with a given capacity yields earlier for a specified input displacement.

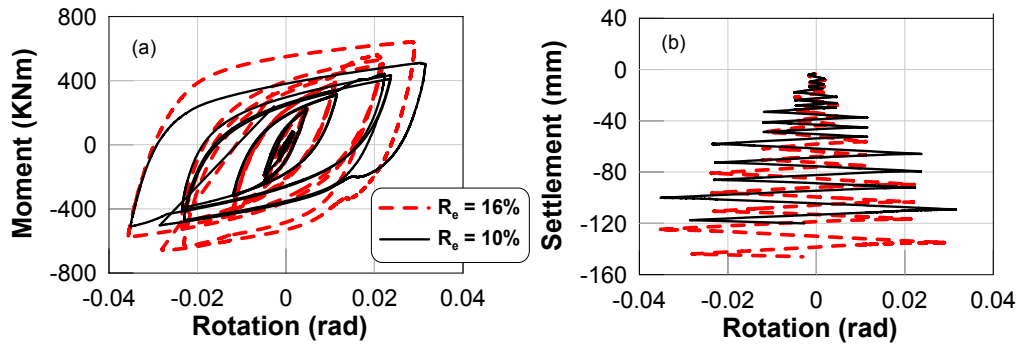


Figure 2.29: Effect of end length ratio on strip footing with $B/L=0.23$ in terms of (a) moment–rotation and (b) settlement–rotation

2.5.6 Stiffness Intensity Ratio, R_k

Stiffness ratio R_k is defined as the ratio of the stiffness intensity at the end regions to that of the mid region.

$$R_k = \frac{k_{end}}{k_{mid}} \quad (2.23)$$

ATC-40 (1996) suggests the end and mid stiffness intensities of the footing as:

$$k_{end} = \frac{6.8G}{(1 - \nu)B} \quad (2.24)$$

$$k_{mid} = \frac{0.73G}{(1 - \nu)B} \quad (2.25)$$

It is seen from Equation 2.24 and 2.25, that the end stiffness intensity should be 9.3 times the mid stiffness intensity, irrespective of the footing dimension and aspect ratio (as also shown in Figure 2.25). Harden et al. (2005) developed an analytical equation for end stiffness ratio. In order to derive this, he equated the theoretical rotation stiffness equation (Gazetas, 1991a) to the rotational component obtained from increasing the stiffness at the end regions. According to his solution, the stiffness ratio varies with footing aspect ratio. Figure 2.30 shows the plot of stiffness intensity ratio with footing aspect ratio as given by Harden et al. (2005) along with the ATC-40 (1996) recommendation. One can observe from this figure that as the footing aspect ratio increases, the stiffness intensity ratio also increases. Over the range of aspect ratios, the stiffness intensity ratio proposed by Harden et al. (2005) always remains below the ATC-40 (1996) recommendation. This implies that ATC-40 (1996) recommendation always gives stiffer end regions when compared to the proposition by Harden et al. (2005) based on Gazetas (1991a) rotation stiffness equation. Note that for a square footing (aspect ratio $B/L=1$), stiffness ratio given in ATC-40 (1996) is nearly twice as much as proposed by Harden et al. (2005).

Figures 2.31(a) and (b) show the effect of varying the end to mid stiffness ratio (R_k) on the moment versus rotation and settlement versus rotation response, respectively, for the 5m square footing. Two different values of R_k are chosen (5 and 9) based on recommendations of ATC-40 (1996) and Harden et al. (2005) for a square footing to demonstrate the effect of R_k on overall footing response. It is observed from Figures 2.31 that although R_k does not have significant effect on the moment demand or rotational stiffness, it changes the

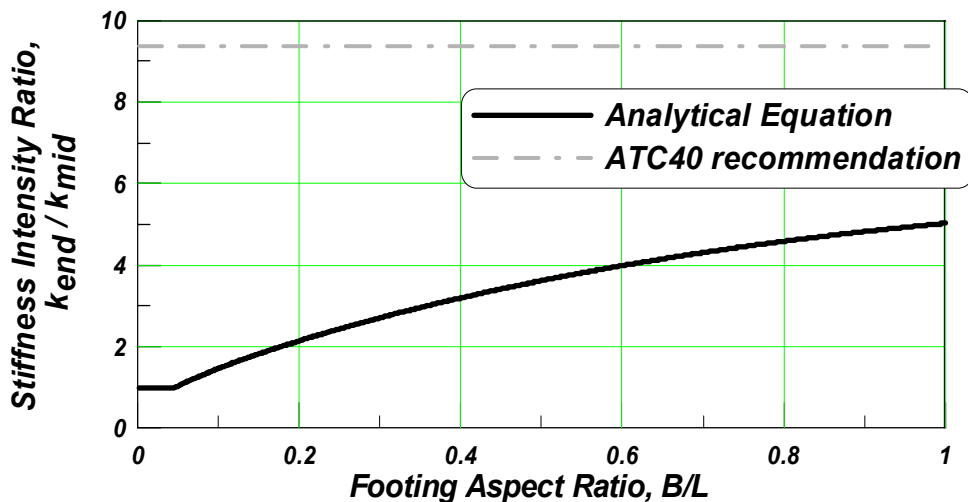


Figure 2.30: Stiffness intensity ratio (R_k) as a function of footing aspect ratio (Figure from Harden et al. (2005))

settlement demand by about 35%. This is due to the fact that an increase in R_k results in lower and higher yield displacement of individual springs at the end and mid regions respectively, as the ultimate load of each spring remains the same. As a result, a variation in R_k changes nonlinear deformation of individual vertical springs (both in tension and compression sides) due to the same applied rotation history resulting in different settlement histories as observed in Figure 2.31(b).

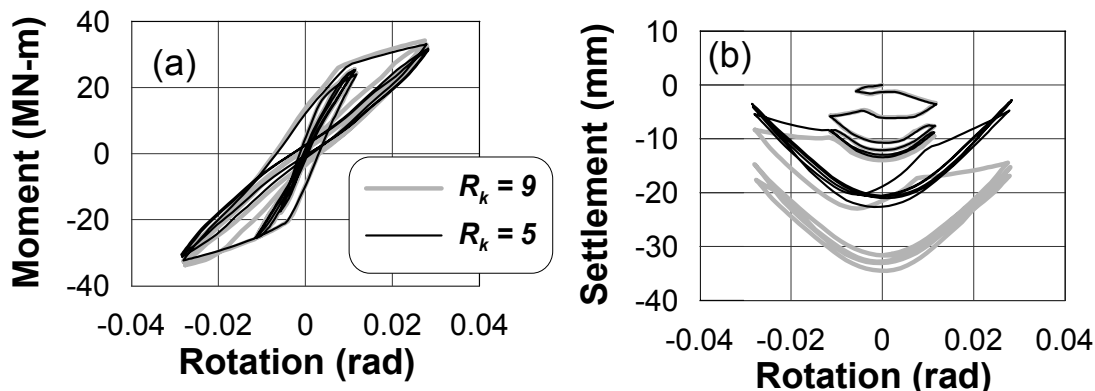


Figure 2.31: Effect of stiffness ratio on footing response: (a) moment versus rotation and (b) settlement versus rotation

Figure 2.32 shows the effect of R_k on settlement demands for the 5m square footing considered before. The settlement presented here is normalized with respect to the settlement when a uniform stiffness distribution is considered (i.e., when $R_k = 1$). It is observed that the settlement demand decreases when the end stiffness intensity increases from uniform distribution to 5 times the mid-stiffness intensity and then starts to increase with increasing stiffness ratio for R_k value greater than 7. Also note that for this case, the settlement demand seems to converge at a stiffness intensity ratio of 5–7, which correlates well with the Harden et al. (2005) suggested R_k value for square footings (he suggested $R_k = 5$ for square footings). However, it goes up again for $R_k = 9$ as observed from Figure 2.32. This nonlinear variation of settlement with R_k is a result of inelastic deformation of individual vertical springs.

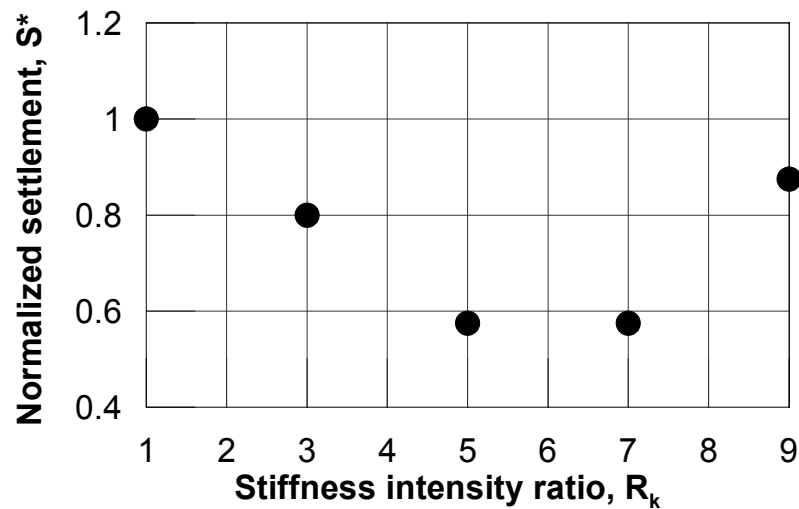


Figure 2.32: Stiffness intensity ratio versus normalized settlement demands for the 5m square footing considered here

2.5.7 Spring Spacing, l_e/L

Another important user defined parameter for the BNWF model is the spacing of springs across the length of the footing or in other words, the length of the individual beam elements of the footing. Note that in the current OpenSees implementation, length of each elements are approximately the same, irrespective of the position of the elements (i.e., whether at mid region or end region). To achieve the higher stiffness intensity at the end regions, the stiffness of the springs at the end regions is increased by the stiffness intensity ratio. The minimum number of springs that must be given for modeling is seven, implying a total number of six beam elements. Two of these elements will be at the mid region while remaining four elements should be at the end regions (two elements within each end region). In general, more than six elements are generally used and to preserve symmetry, the number of elements is selected as even.

It is reasonable to envision that the footing response will tend to converge after a certain number of springs are considered for a BNWF model. Figures 2.33(a)–(d) show the effect of spring spacing on the footing response, considering a model with 60 elements (element length of approximately 2% of total length) and 6 elements (element length of approximately 17% of total length). By comparing Figures 2.33(a) and 2.33(b), one can observe that for the model with a coarser distribution of springs results in a rougher moment–rotation response, as individual springs are spanned across a large footing (beam) distance. Figures 2.33(c) and 2.33(d) show the settlement rotation curves for model with 60 elements and 6 elements, respectively. It is observed from Figures 2.33(c) and 2.33(d) that the spring spacing has a great effect on settlement response. Note also that Figures 2.33(c) and 2.33(d) show the same trend during the first loading zone but after that due to signifi-

cant nonlinear deformation, the curves show significant different patterns.

Figure 2.34 shows the normalized settlement demand of the footing for a range of spring spacings. The settlement demand is normalized with respect to the settlement demand corresponding to a spring spacing of 17% of total length of footing. Note that the maximum spring spacing that can be provided in this model is approximately 17% of total length of footing due to a minimum number of 6 elements, or 7 springs required along the length of the footing. It is observed from Figure 2.34 that the normalized settlement demand tends to converge when the element length is less than or equal to 6% of the total footing length. Note also that the settlement demand obtained using 17% spacing results in a maximum settlement, which is more than twice the value obtained for a spacing of approximately 6%.

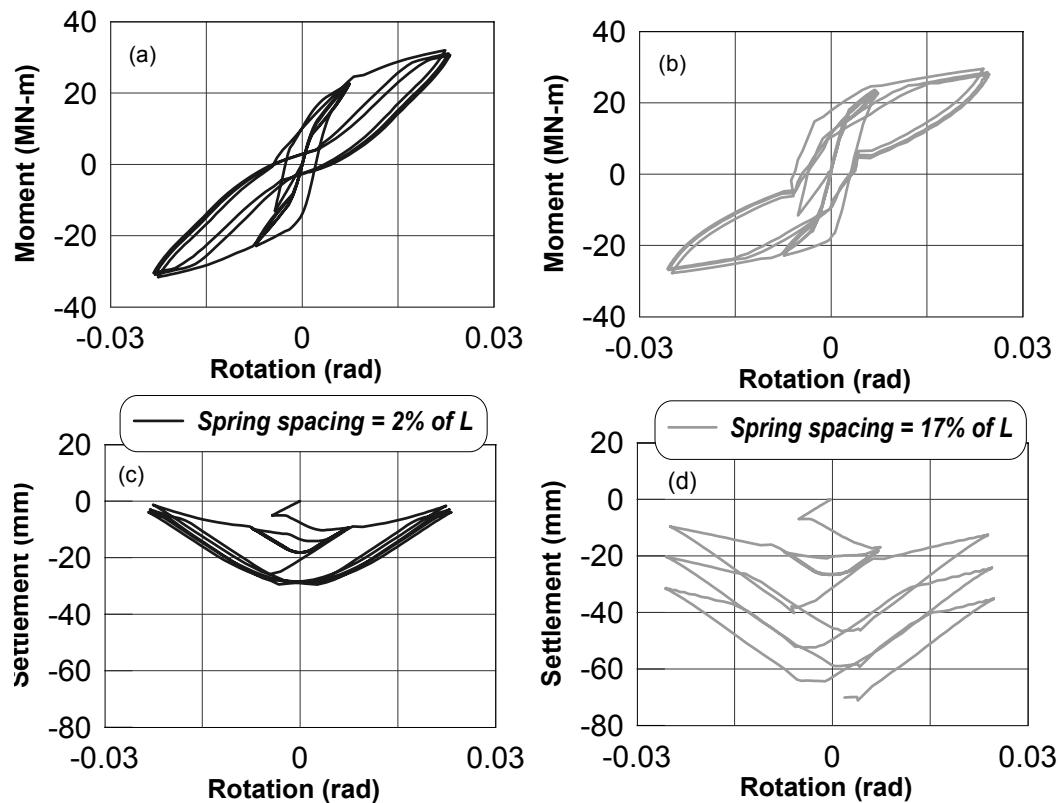


Figure 2.33: Effect of spring spacing on overall footing response: (a)–(b) moment versus rotation and (c)–(d) settlement versus rotation

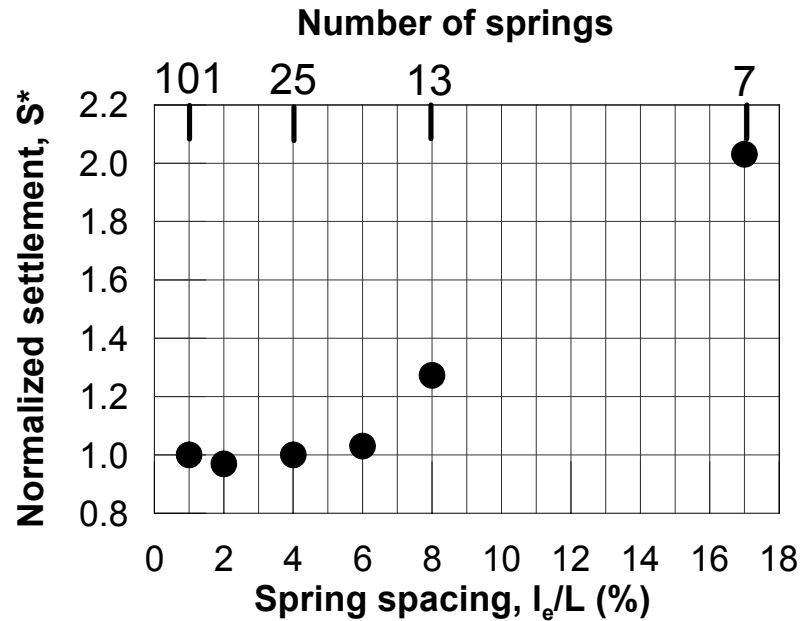


Figure 2.34: Effect of spring spacing on normalized settlement demand

2.5.8 Elastic Range, C_r

C_r is the parameter that controls the range of the elastic region for the backbone curves used for modeling of BNWF. It is the ratio of the load at which a spring starts to behave nonlinear to the ultimate load that the spring can carry (see Equation 2.2). For example, for a spring with $C_r = 0.3$, the spring will start to behave nonlinearly at a load 30% of its ultimate capacity. It is thus clear that for the case of a footing with a given moment capacity, an increase in C_r extends the elastic zone resulting in less permanent settlement and conversely, decreasing C_r resulting more permanent settlement. The range of C_r for springs defined by *QzSimple1*, *PySimple1* and *TzSimple1* materials can be determined by calibrating the springs against shallow footing load tests with loading being applied in one degree of freedom.

The effect of varying C_r on the force–displacement relationship of single q-z spring,

when subjected to a monotonic displacement, is shown in Figure 2.35 by plotting normalized pressure ($= q/q_{ult}$) with spring displacement. One can notice from this figure that an increase in C_r from 0.2 to 0.5 increases the elastic zone considerably. Note that both curves converge to unity asymptotically, indicating that the increase in C_r does not affect the ultimate load capacity.

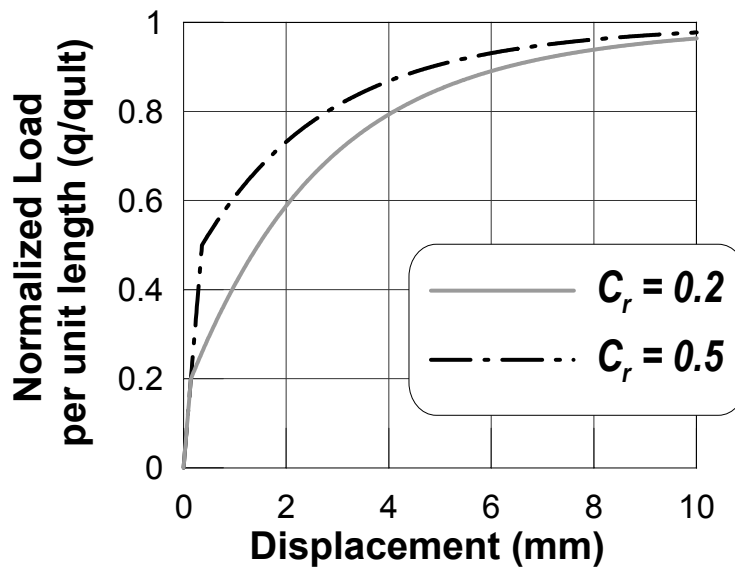


Figure 2.35: Effect of varying C_r on a single spring's load–displacement relationship

In order to show the effect of varying the elastic range on the footing response, the same 5m square footing is subjected to the same cyclic loading (rotation time history) considered before. It is observed from Figures 2.36(a) and (b) that by decreasing the elastic load range from 50% of ultimate load to 20% of ultimate load (from $C_r = 0.2$ to 0.5), the moment demand is not affected, while the settlement demand is increased by about 60%.

Figure 2.37 provides a summary of all analysis cases between the two extremes. The settlement demand is normalized by the settlement demand corresponding to $C_r = 0.2$. It is observed from Figure 2.37 that the settlement demand is decreasing almost linearly (R^2

= 90%) with increasing range of elastic region.

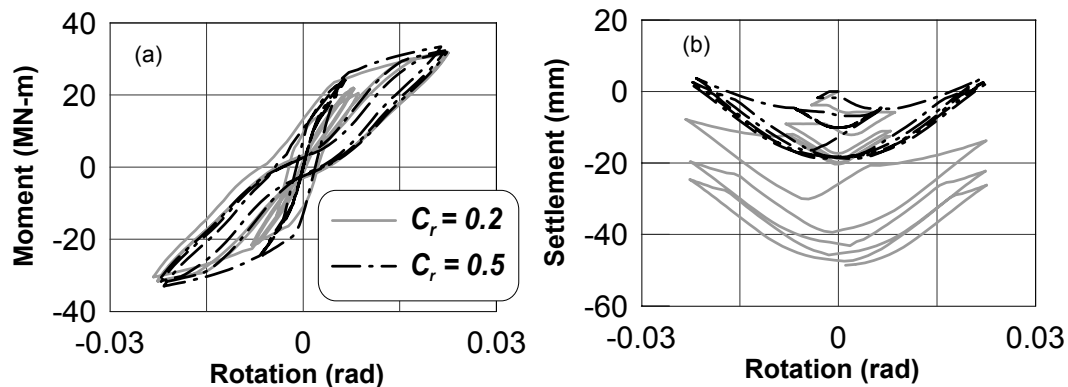


Figure 2.36: Effect of C_r on footing response

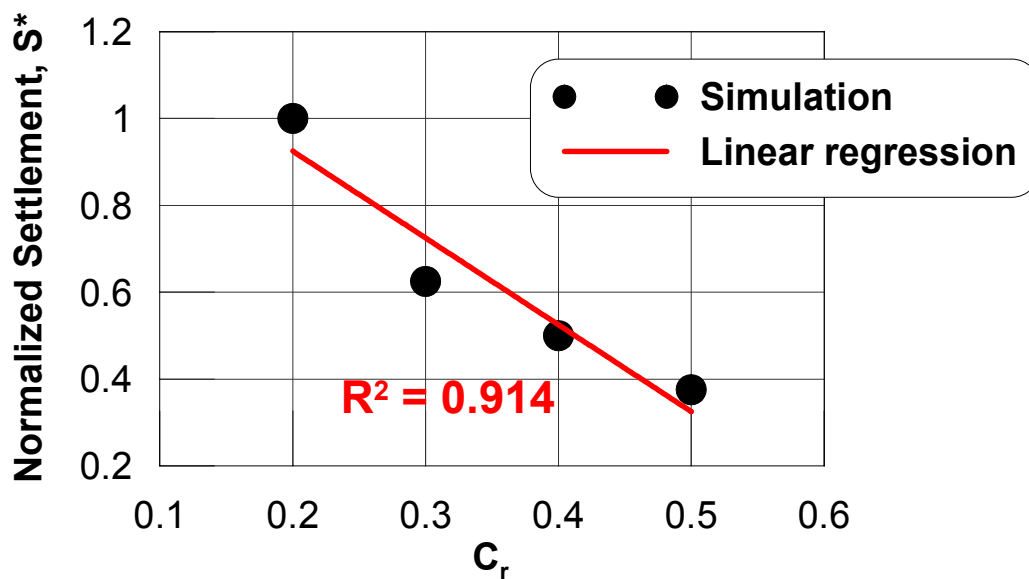


Figure 2.37: Effect of C_r on normalized maximum settlement demand

2.5.9 Post-yield Stiffness, k_p

The shape and instantaneous stiffness of the nonlinear region of any horizontal or lateral backbone curves important to characterize the overall footing response. For example,

the nonlinear stiffness k_p for a vertical spring (*QzSimple1* material) is expressed by the following equation:

$$k_p = n(q_{ult} - q_o) - \left[\frac{(cz_{50})^n}{(cz_{50} - z_o + z)^{(n+1)}} \right] \quad (2.26)$$

Recall that c and n are the aforementioned parameters describing the shape of the backbone curves. For the *QzSimple1* material, these were found by Boulanger (2000b). Similar expressions are used for the lateral springs.

To express the nonlinear tangent stiffness k_p quantitatively as a fraction of the initial stiffness at a particular displacement, a variable α_{80} is introduced. The parameter α_{80} is the ratio of nonlinear tangent stiffness at 80% of the ultimate capacity of a spring, q_{ult} , to the initial elastic stiffness. This definition implies higher values of k_p for respective higher values of α_{80} . Note that α_{80} is a case-specific parameter, which depends on the parameter c along with q_{ult} , z_{50} and soil type (sand or clay). Figure 2.38 presents the normalized pressure q/q_{ult} versus displacement of a single q-z spring to demonstrate how a change in the parameter α_{80} affects the nonlinear stiffness of the backbone curve. To change α_{80} from 0.048 to 0.1, the parameter c is changed, while all others remain constant.

From Figure 2.38, one can observe that the curves corresponding to $\alpha_{80} = 0.048$ and $\alpha_{80} = 0.1$ start to deviate near a normalized load value of 0.3, which is the also the value of elastic range C_r , indicating that the change in c does not have any effect on the initial stiffness, it only changes the post-yield stiffness of the spring. The two backbone curves merge asymptotically to unity at a displacement close to 10 mm. Figures 2.39(a) and (b) show the effect of varying the parameter α_{80} on the moment versus rotation and settlement versus rotation responses, respectively, of the 5m square footing. Varying the α_{80} has the

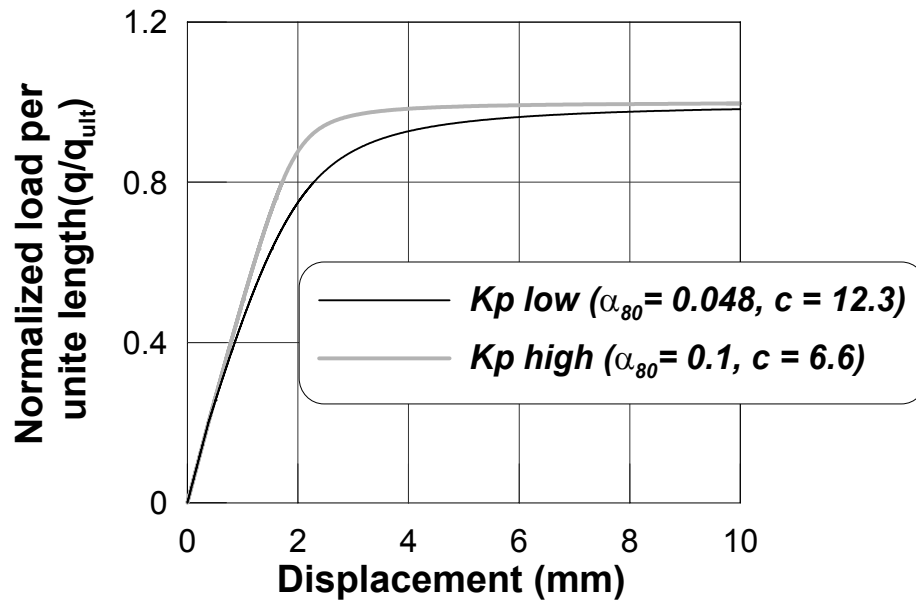


Figure 2.38: Effect of parameter α_{80} on a single spring backbone curve

most pronounced effect on the settlement demand, which decreases approximately 50% when α_{80} is increases by approximately 50%. Note that visibly, the change in the backbone curve presented in Figure 2.38 is not dramatic, in fact it is visibly subtle. Figure 2.39 (b) also indicates that the settlement initially does not deviate much (when in the elastic region), however it deviates more and more in the later portion of the loading cycles. This makes sense as the initial elastic elastic stiffness is same for both cases and only the post-yield tangent stiffness has been varied.

Figure 2.40(a) shows a relation between the parameter c and the parameter α_{80} . One can observe from this figure that the relation between c and α_{80} is not linear. As the c value increases, α_{80} reduces and the rate of this reduction decreases with increasing c . Figure 2.40(b) shows the effect of a change in α_{80} on the normalized settlement demand. Settlement demand is normalized with respect to its value corresponding to $\alpha_{80} = 0.1$. As expected, the settlement demand has a decreasing trend with increase in α_{80} . However,

the relation between settlement demand and α_{80} is nonlinear due to change in nonlinear behavior of individual springs under the rotational history applied to the foundation. Note, for an increase in α_{80} from 5% to 10%, the settlement demand decreases about 53%.

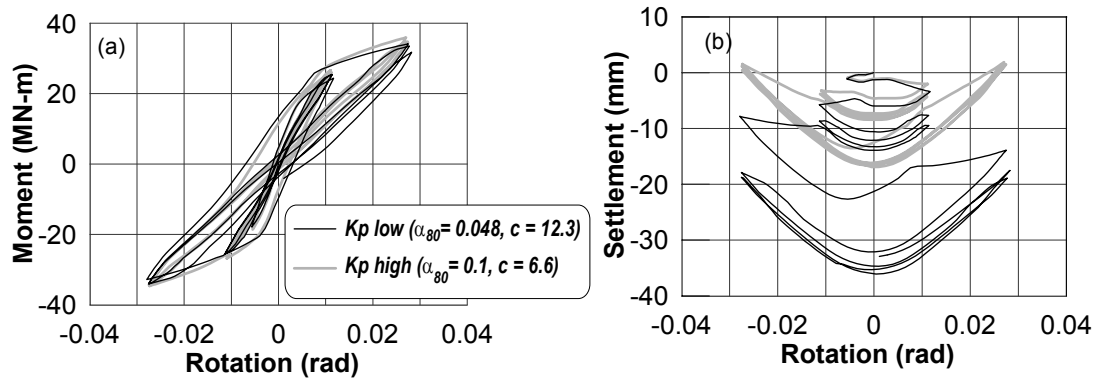


Figure 2.39: Effect of varying the parameter α_{80} (by varying c) on the footing: (a) moment versus rotation and (b) settlement versus rotation responses

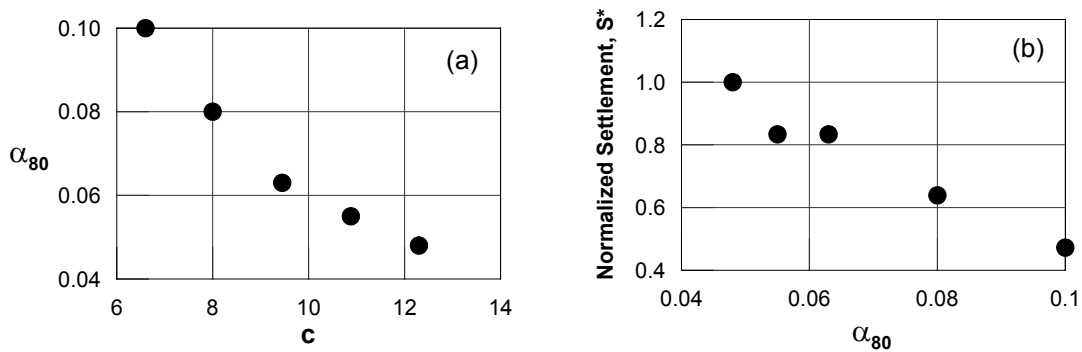


Figure 2.40: Effect of changing the parameter c on the settlement demand: (a) c versus α_{80} and (b) α_{80} versus normalized settlement demand

2.5.10 Unloading Stiffness, k_{unl}

The unloading stiffness k_{unl} is also a parameter used to define the behavior of the vertical and lateral springs. During cyclic loading, the unloading stiffness controls the behavior. Figure 2.41 shows a plot of normalized load versus displacement of a single q-z spring for

two different values of unloading stiffness when subjected to displacement causing loading, unloading and then re-loading on the tension side. One can observe from this figure that the capacity of the spring remains the same for both unloading stiffnesses. However, one can also see that while unloading, a small change in load causes a significant change in displacement for the curve with $k_{unl} = 20\%$ of k_{in} . Note that this selection of k_{unl} is based on the results observed in Gajan et al. (2003a,b); Rosebrook and Kutter (2001a,b,c).

Figures 2.42 (a) and (b) show the effect of changing the unloading stiffness on the moment versus rotation and settlement versus rotation plots, respectively, for the same 5m square footing mentioned earlier. It can be observed from Figure 2.42(a) that the shape of moment rotation curves and the moment demand for the two cases of k_{unl} remain almost the same. However, from Figure 2.42(b), one can observe that the settlement starts to deviate with increasing amplitude of applied rotation. Reducing the unloading stiffness to 20% of the loading stiffness increases the settlement demand by only 9%. Thus the effect of unloading stiffness on the footing responses can be considered to be insignificant.

2.6 Limitations of the Proposed BNWF Model

Inherent limitations of the model are the following:

- Vertical and lateral responses of the foundation are not coupled in this model. Therefore, if the vertical capacity is increased or decreased, it will not affect the shear-sliding response. This might occur, for example, as a result of footing uplift, which decreases shear capacity due to reduced foundation-soil contact area. Similarly, any change in the lateral capacity and stiffness will not affect the axial and moment-rotation response.

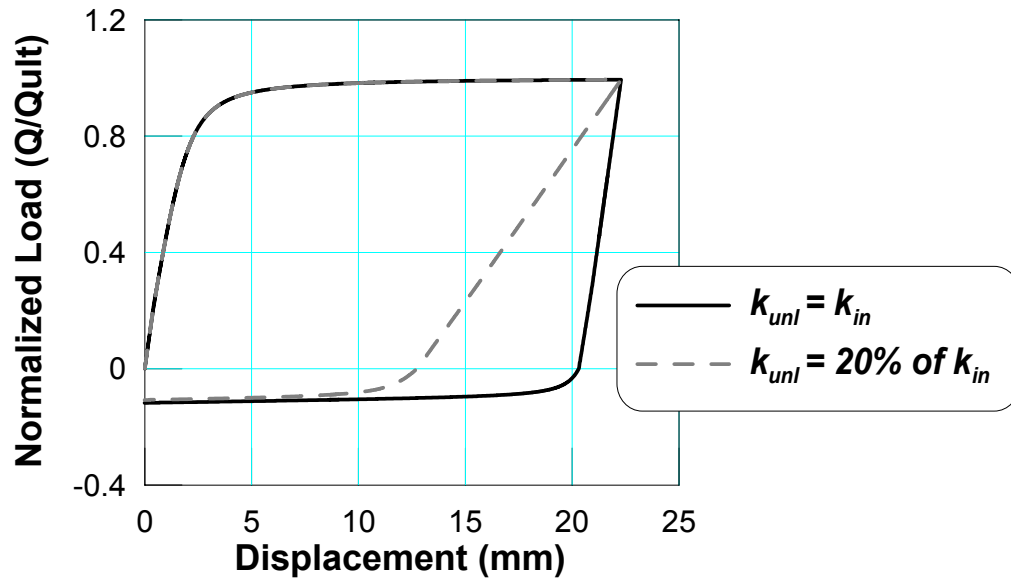


Figure 2.41: Effect of unloading stiffness k_{unl} on a single spring load versus displacement relationship

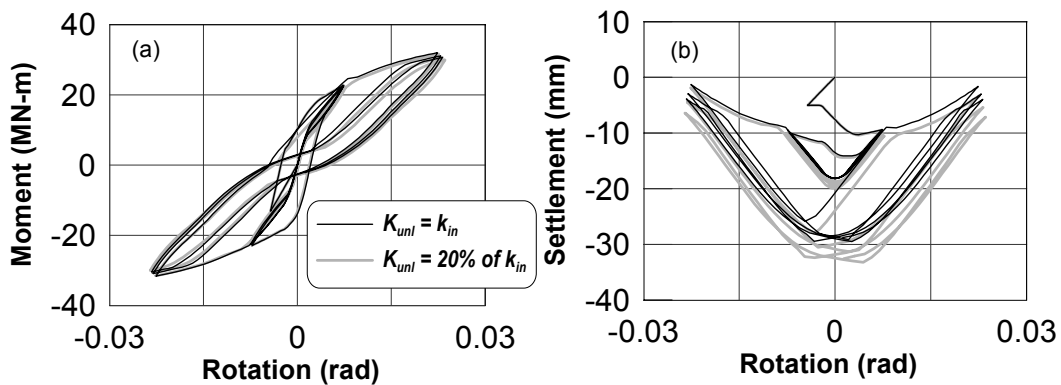


Figure 2.42: Effect of unloading stiffness k_{unl} on footing (a) moment versus rotation and (b) settlement versus rotation responses

- The backbones are defined for either pure sand or pure clay; a mixed, $c - \phi$ soil backbone curves are not explicitly defined. At present, no data exists to calibrate such a model. Nonetheless, the user can define soil parameters (friction angle, cohesion, and shear modulus) to incorporate the strength and stiffness expected for a $c - \phi$ material, while selecting the backbone curve associated with the dominant soil type

(clay or sand). It is noted that the backbone curves are derived in calibration with pile load tests. In the subsequent chapter, these are re-evaluated for tests on shallow footings.

- Individual vertical springs along the base of the footing are independent as common for any Winkler-based modeling procedure. This means that the property (force-deformation behavior) of one spring will not be influenced by the change in property of its neighboring spring. This may not be as important as it may be for piles, where vertically layered soils would be influenced by each other.

2.7 Summary Remarks

In this chapter, a Beam-on-Nonlinear-Winkler-Foundation (BNWF) model for capturing the two-dimensional (2D) behavior of a shallow foundation under seismic loading is described. The model has been implemented within the framework of OpenSees. The details of the model, constitutive behavior of the various spring models and the parameters required for its description along with their influence on model response, are discussed in this chapter. Model parameters such as capacity, stiffness, tension capacity, and spring spacing are shown to have significant effect on the footing response, while parameters such as the stiffness intensity ratio and the end length ratio have a moderate effect. Settlement is seen to be most affected from any changes in the above mentioned input parameters.

Chapter 3

Calibration of Mechanistic Springs

3.1 Introduction

In this chapter, the parameters describing the constitutive relationship of individual unidirectional mechanistic springs used within the proposed BNWF model are calibrated using uniaxial shallow footing load test data. For this purpose, axial footing, sliding footing, and embedded laterally loaded footing test results are used. Two types of parameters describe the backbone curves: (i) basic input parameters and (ii) shape parameters. Basic input parameters are those that are readily derived from soil properties (determined from laboratory or field tests on the soil). For example, initial elastic stiffness (k_{in}) and displacement at 50% of peak stress (z_{50}) are such basic input parameters. Whereas model parameters that define the shape of the curve may not be derived from typical element level soil tests, but rather must be evaluated via a soil-footing system test. These include, for example, the parameters c , n and C_r (Equation 2.2 and Equation 2.3). This chapter discusses both types of input parameters, however with particular focus on the shape parameters.

3.1.1 Axial Load Tests

For calibration of the q-z material model, six axial load tests were conducted on strip footings performed at 20-g centrifugal acceleration at the University of California, Davis (Rosebrock, 2001) and four axial load tests on square footings conducted in field at Texas A & M University (Briaud and Gibbens, 1994) are used. Table 3.1 summarizes the details of these tests. Of the six centrifuge tests that were conducted at Davis, four tests were conducted using medium to dense sand (relative density 60%-80%) and the remaining two involved medium clay (undrained shear strength ≈ 100 kPa). Footings were either surface resting, or moderately embedded (about $0.5 \times$ width of footing). Note that all data for the centrifuge tests presented in Table 3.1 and in subsequent discussions are in prototype units.

For the Texas A&M field tests, square footings were rested at a fairly consistent medium silty sand site with relative density of 55%, friction angle of 34° and water content of 5%. All the footings were embedded into the soil up to a depth between 0.7m-0.9m below ground surface. To determine the soil properties, a series of in-situ tests such as CPT, PMT, SPT, bore-hole-shear, cross-hole-shear and DMT were conducted. Note that these test results were also used to evaluate the adequacy of several numerical and theoretical solutions to derive settlement and ultimate load.

3.1.2 Lateral Load Tests

For calibration of the p-x spring mechanistic model, seven tests are considered (Table 3.2). These include four experiments conducted at 20-g centrifugal acceleration at Rensselaer Polytechnic Institute (RPI) by Gadre and Dobry (1998); two tests on pile caps conducted by Rollins and Cole (2006) and one test on pile caps by Duncan and Mokwa

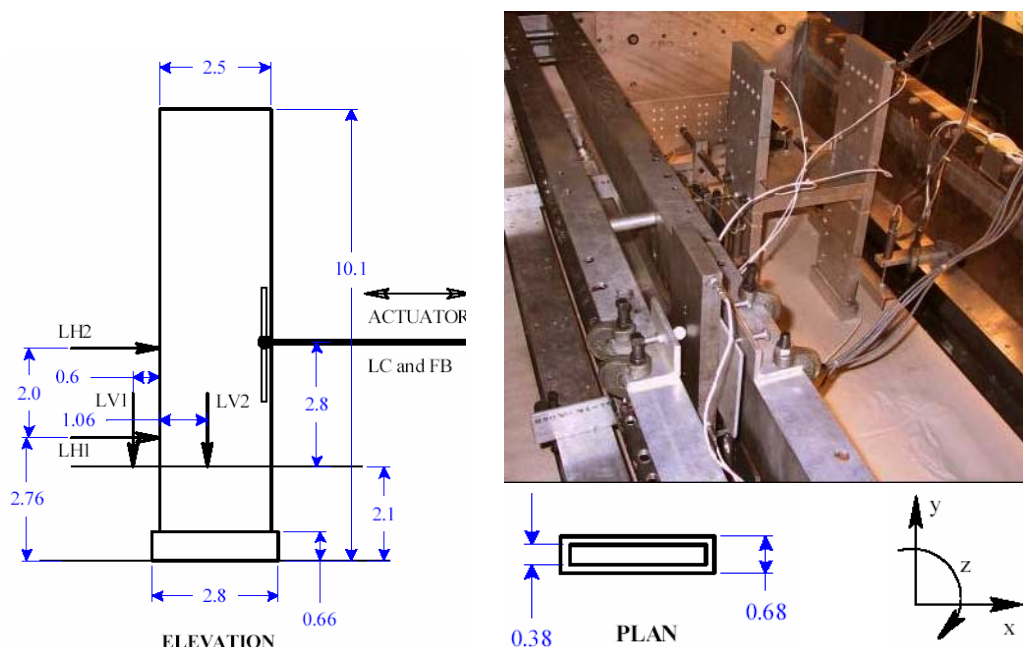


Figure 3.1: Centrifuge test set-up at UC Davis (Rosebrook and Kutter, 2001a)

Table 3.1: Axial Tests on strip and square footing (For q-z material)

	Tests	Reference ¹	Soil Type	L (m)	B (m)	H (m)	D _r (m)	D _r (%)	φ (deg)	C _u (kPa)	γ (kN/m ³)	Q _{ult} (kN)	Z ₅₀ (mm)
Centrifuge Tests at UC Davis (20-g tests)													
Strip Footing	KRR01-s2	RK01	dry sand	2.67	0.69	0.64	0.3	80%	38.3	0	16.0	1115	26.95
	KRR01-s25	RK01	dry sand	2.67	0.69	0.64	0.3	60%	37.0	0	16.0	735	13.71
	KRR01-s28	RK01	dry sand	2.67	0.69	0.64	0.3	60%	37.0	0	16.0	728	13.20
	KRR01-s31	RK01	dry sand	2.54	0.38	0.68	0.3	80%	40.2	0	16.0	368	8.83
	KRR03-AW	RK01	clay	2.67	0.69	0.64	0	0%	0.0	103	17.0	666	7.80
	KRR03-CW	RK01	clay	2.67	0.69	0.64	0	0%	0.0	103	17.0	701	16.46
Field Tests at Texas A & M University (1-g tests)													
Square Footing	TX-Footing1	BG94	silty sand	3.0	3.0	1.22	0.76	55%	34.2	0	15.3	10550	25.56
	TX-Footing2	BG94	silty sand	1.5	1.5	1.22	0.76	55%	34.2	0	15.3	3420	31.00
	TX-Footing3	BG94	silty sand	3.0	3.0	1.35	0.89	55%	34.2	0	15.3	9020	24.52
	TX-Footing4	BG94	silty sand	2.5	2.5	1.22	0.76	55%	34.2	0	15.3	7300	26.32
	TX-Footing5	BG94	silty sand	1.0	1.0	1.17	0.71	55%	34.2	0	15.3	1910	28.36

¹ RK01= Rosebrook & Kutter (2001); BG94 = Briaud & Gibbens (1994)

(2001). The RPI centrifuge tests consisted of a square footing of 1.14m resting on a dry sand of 75% relative density used consistently for each of the tests. Figures 3.3–Figures 3.4 show dimensions and experimental set-ups of the centrifuge tests. In these tests, the contribution of footing lateral resistance is only due to passive resistance at the front of the footing. Sidewall friction and base shear friction are isolated by providing a confining box

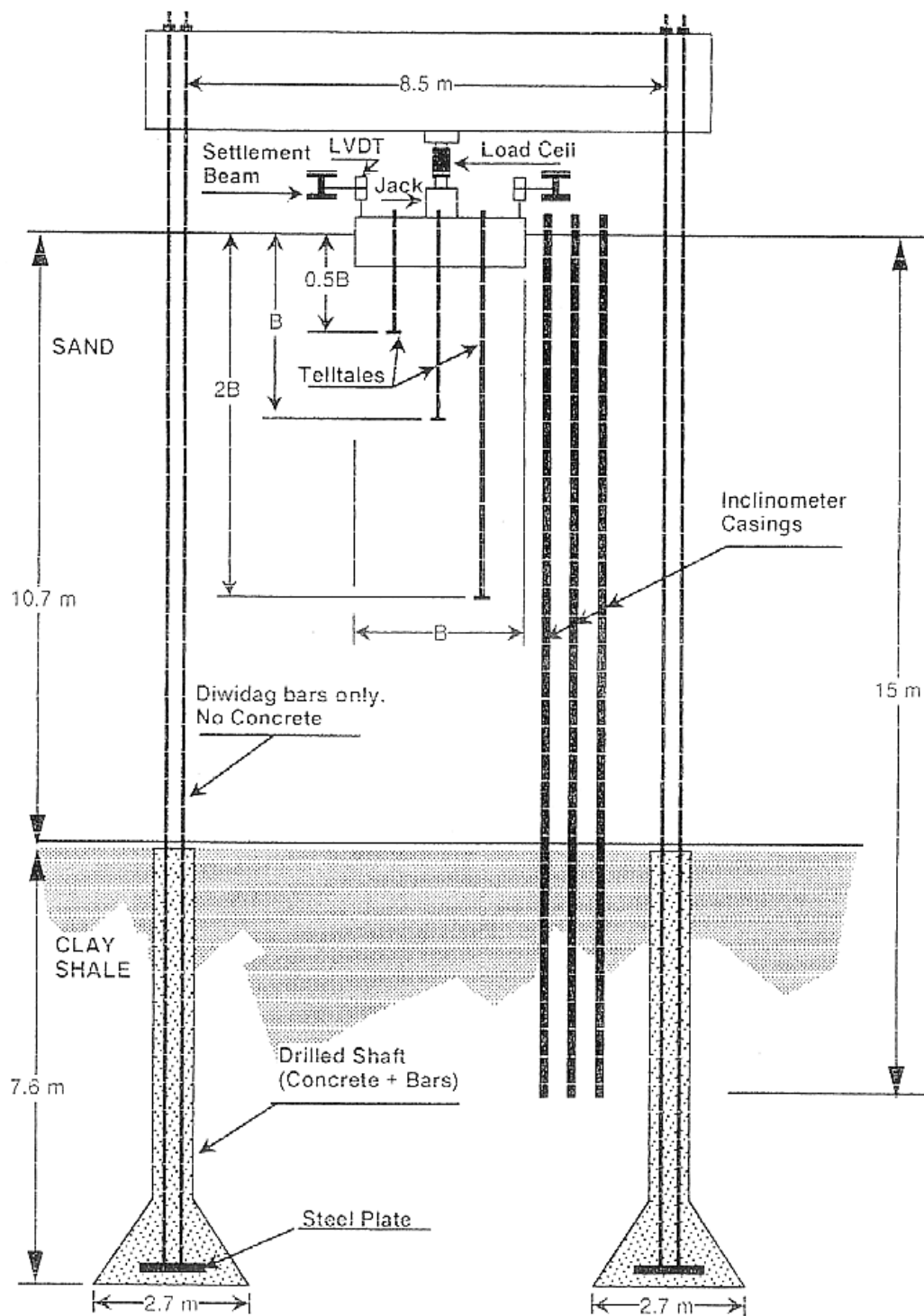


Figure 3.2: Field test set-up at Texas A & M (Briaud and Gibbens, 1994)

over the footing and roller bearings at the bottom of the footing.

Tests by Rollins and Cole (2006) were full-scale rectangular pile cap tests performed in Salt Lake City, Utah on medium clean sand ($D_r = 63\%$) and silty sand ($D_r = 67\%$). Figure 3.5 shows the experimental set up for these tests. Passive forces were derived by subtracting the resistance provided by the pile cap when there was no backfill (i.e. only base friction and pile resistance) from the total lateral resistance. Tests by Duncan and Mokwa (2001) also involved lateral loadings on pile caps, where the sliding resistance of the pile cap and the lateral contribution of piles could be removed, thus providing only passive resistance. These tests were conducted on silty sand with relative density 60%. Figure 3.6 shows the experimental set-up for the tests carried out by Duncan and Mokwa (2001).

For calibration of the t-x spring mechanistic models, the tests conducted by Gadre and Dobry (1998) as mentioned earlier are used (see Table 3.3). For these tests, lateral base friction was isolated to capture footing friction (Figure 3.4).

Table 3.2: Lateral tests on square footing (For p-x material)

	Tests	Reference ¹	Soil Type	L (m)	B (m)	H (m)	D_r (%)	ϕ (deg)	C_u (kPa)	γ (kN/m ³)	P_{ult} (kN)	x_{50} (mm)
Centrifuge Tests on Shallow Footing at RPI, NY												
Square Footing	↑ P	GD98	dry sand	1.14	1.14	0.84	75	39	0.0	16.2	123.0	18
	BSPL-BL-S	GD98	dry sand	1.14	1.14	0.84	75	39	0.0	16.2	142.0	24
	SP-S	GD98	dry sand	1.14	1.14	0.84	75	39	0.0	16.2	128.8	30
	↓ P pull	GD98	dry sand	1.14	1.14	0.84	75	39	0.0	16.2	124.3	11
Field tests on Pile Caps in Utah												
Pile cap	↑ clean sand	RC06	clean sand	5.18	3.05	1.12	63	39	0.0	16.2	1090	4
	silty sand	RC06	silty sand	5.18	3.05	1.12	67	27	27.3	16.6	1428	5
	↓ passive	DM01	silty sand	1.90	1.10	0.90	60	35	48.0	16.2	622	2.6

¹ GD98 = Gadre & Dobry (1998); RC06 = Rollins and Cole (2006); DM01 = Duncan and Mokwa (2001)

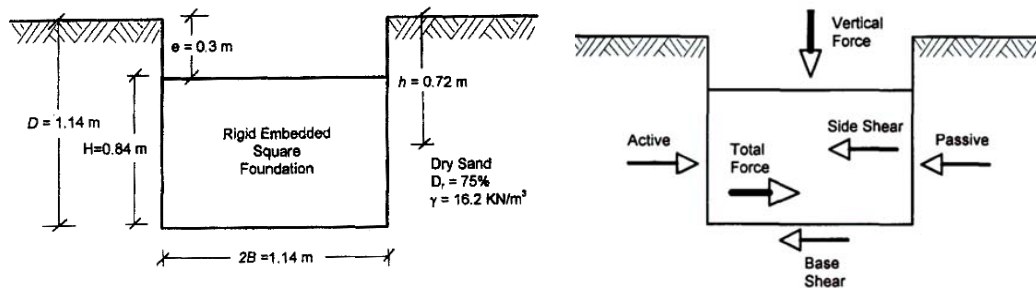


Figure 3.3: (a) Dimensions and test set-up (b) Force contribution in lateral resistance (Gadre and Dobry, 1998)

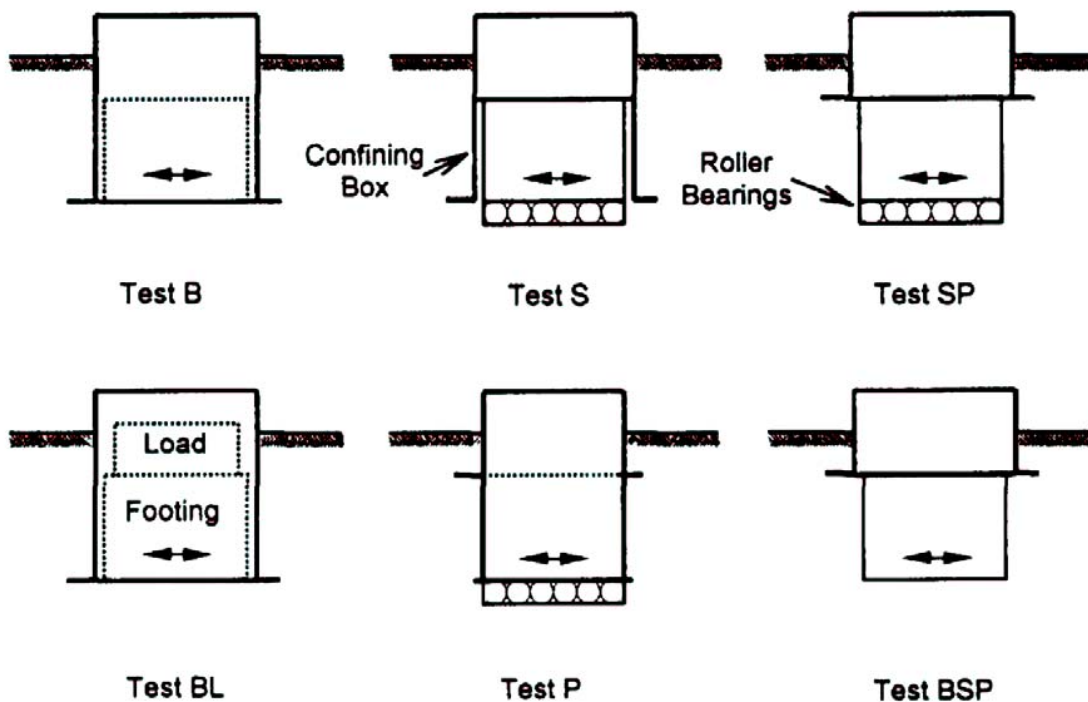


Figure 3.4: Footing model set-ups for centrifuge tests (Gadre and Dobry, 1998)

Table 3.3: Lateral tests on square footing (For t-x material)

	Tests	Reference ¹	Soil Type	L (m)	B (m)	H (m)	D _r (%)	φ (deg)	C _u (kPa)	γ (kN/m ³)	T _{ult} (kN)	x ₅₀ (mm)
Square Footing	B	GD98	dry sand	1.14	1.14	0.84	75	39	0	16.2	45.40	11.6
	BL	GD98	dry sand	1.14	1.14	0.84	75	39	0	16.2	91.75	9.55
	B_pull	GD98	dry sand	1.14	1.14	0.84	75	39	0	16.2	45.40	11.6
	BL_pull	GD98	dry sand	1.14	1.14	0.84	75	39	0	16.2	91.75	9.55

¹GD98 =Gadre & Dobry (1998)

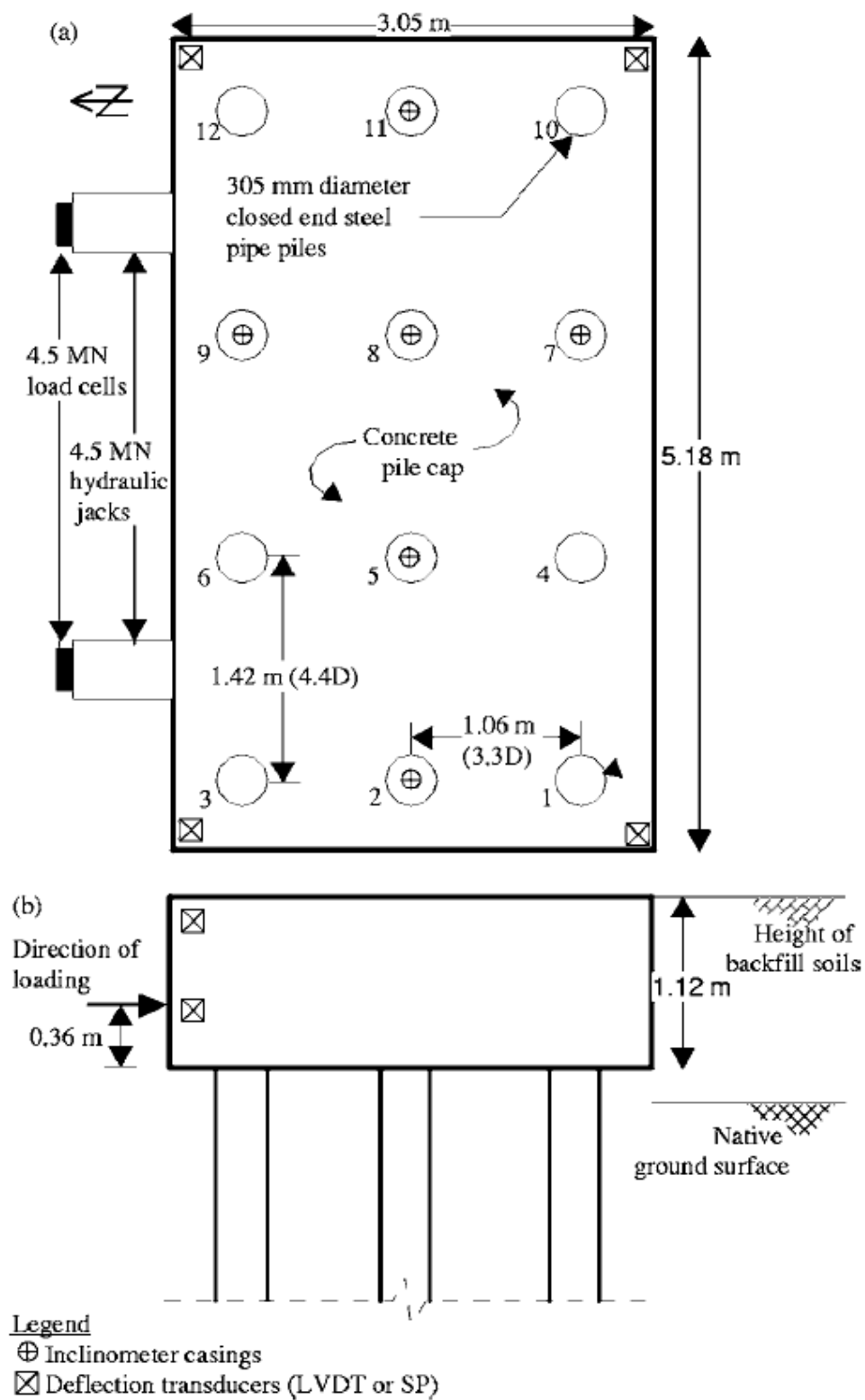


Figure 3.5: Test set-up for lateral load tests (Rollins and Cole, 2006)

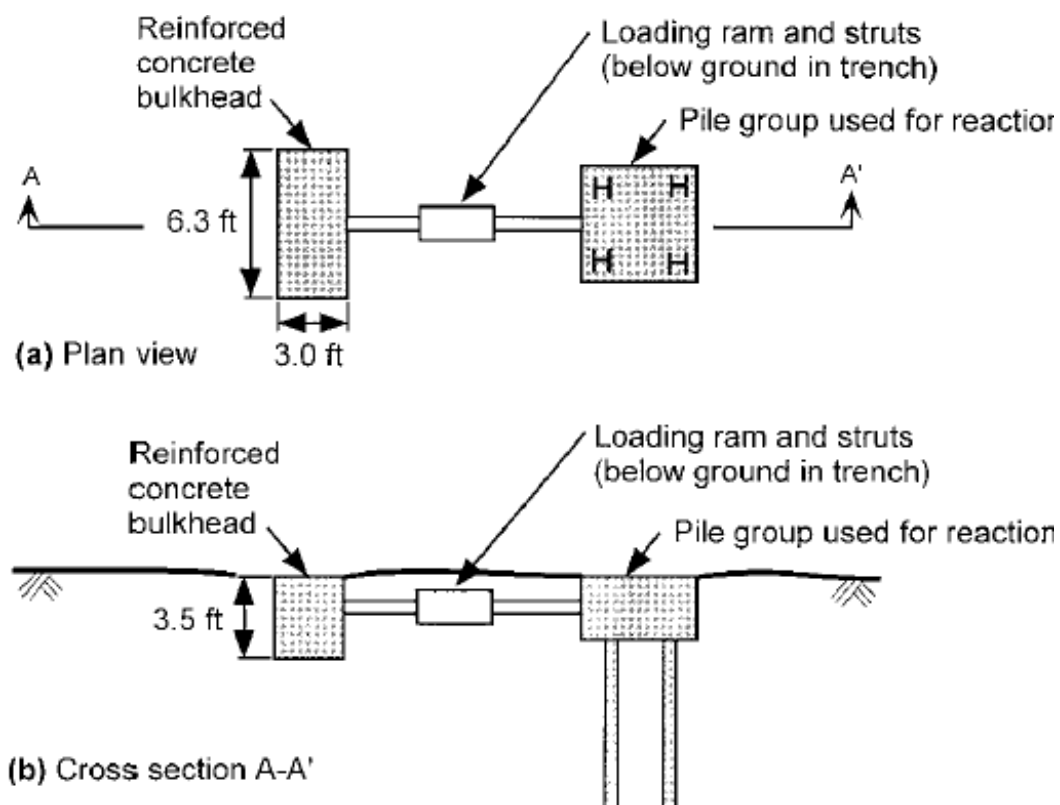


Figure 3.6: Test set-up for passive pressure load tests (Duncan and Mokwa, 2001)

3.2 Selection of Basic Input Parameters

The basic input parameters are evaluated using results from each experiment and compared with theoretical solutions. The mean value of each parameter is selected to define a mean backbone curve. A dimensionless parameter $Q_{ult}/A_f G$ is introduced. This parameter is the ratio of ultimate capacity to shear capacity (i.e. shear modulus multiplied by the area of the footing). Both ultimate capacity and shear capacity are based on the tests on the footing.

Figures 3.7 (a) and (b) show the variation of z_{50} and k_{factor} with the dimensionless parameter $Q_{ult}/A_f G$ for different axial load tests. The parameter z_{50} is the displacement corresponding to 50% of the ultimate load, whereas the parameter k_{factor} is a factor that is used to calculate the initial elastic stiffness given a value of z_{50} using the following relation:

$$k_{in} = k_{factor} \frac{Q_{ult}}{z_{50}} \quad (3.1)$$

Via calibration against pile load tests, the *QzSimple1* material results in a k_{factor} value of 1.39 for sand and 0.525 for clay. If one can calculate initial elastic stiffness from a theoretical solution or using experimental results, then this factor can be used to back-calculate z_{50} which is used in the q-z material model equations. In this study, via calibration against shallow foundation tests, a new set of k_{factor} and z_{50} are obtained. The mean and standard deviation of z_{50} is obtained as: 22.05mm and 7.93mm, respectively. For k_{factor} , the mean and standard deviation are: 1.21 and 0.6, respectively. Note that the analyst need not to input parameters k_{factor} and z_{50} if he is using the proposed BNWF model through the current implementation tool. These parameters will be calculated within the command.

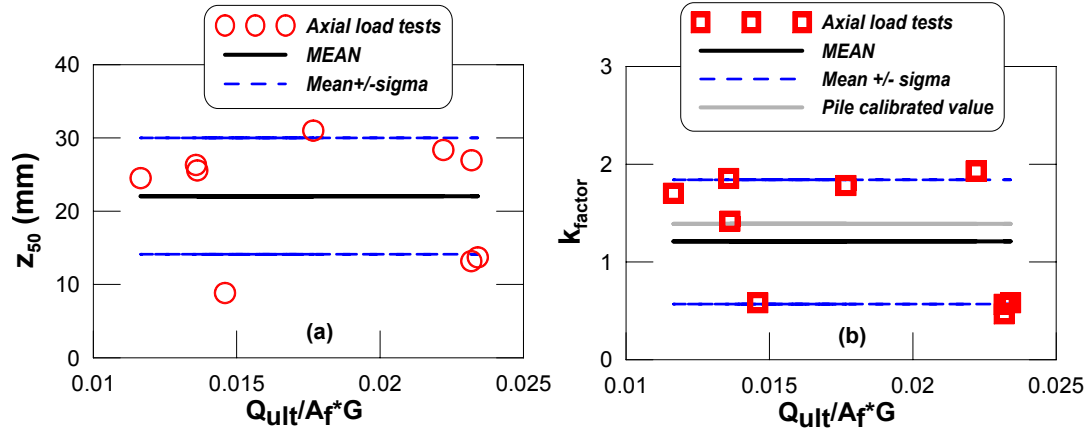


Figure 3.7: Variation of (a) z_{50} and (b) k_{factor} for sand with normalized parameter $Q_{ult}/A_f G$ (for q-z material)

3.3 Calibration of Shape Parameters

By analyzing individual experimental model, and iterating to obtain a best-fit to the experimental response, the parameters describing the shape of the backbone curves are determined. To determine the best-fit value, residual forces for all displacement points are calculated with one parameter varying, while fixing the others. The parameter, which minimizes the residual normalized load (normalized with respect to the ultimate load), is selected as the best-fit value for that particular experiment. Once a set of best-fit values for each parameter and each test is determined, statistics of that parameter are calculated (mean μ and standard deviation σ). Using the calculated μ and $\mu \pm \sigma$ values of each parameter (c , n and C_r), a set of three nonlinear backbone curves is defined. Note that these backbone curves (μ , $\mu + \sigma$ and $\mu - \sigma$) can be treated as the expected, upper limit and lower limit curves.

Figures 3.8(a)-(c) show a sample of the regression method developed to determine the best-fit value for the parameter c . Figure 3.8(a) shows the normalized load-displacement

curve with three different values of c , indicating that backbone with $c = 9$ results in the closest to the experimental response in this particular case. A normalized residual load (ΔQ_{norm}) is calculated next to determine the exact value of c , which results in a minimum ΔQ_{norm} and thus generates a backbone closest to the experimental data (Figure 3.8(b)). The normalized residual load is calculated as:

$$\Delta Q_{norm} = \frac{\sqrt{[\sum(Q_i - Q_{iexp})^2]}}{Q_{ult}} \quad (3.2)$$

where, Q_i = axial load at a particular displacement point i , Q_{iexp} = experimental axial load at that particular displacement point i , and Q_{ult} = ultimate load capacity.

Figure 3.8(b) shows that ΔQ_{norm} is minimized with a $c \approx 9.0$. Figure 3.8(c) then shows the entire range of c plotted against the sum of ΔQ_{norm} , indicating that the parameter c converges at a value of 8.7 to produce minimum value of $\sum \Delta Q_{norm}$. For this particular case, the best-fit or regressed value of the parameter c is determined as 8.7. The same procedure is carried out to obtain best-fit values for all parameters corresponding to all tests.

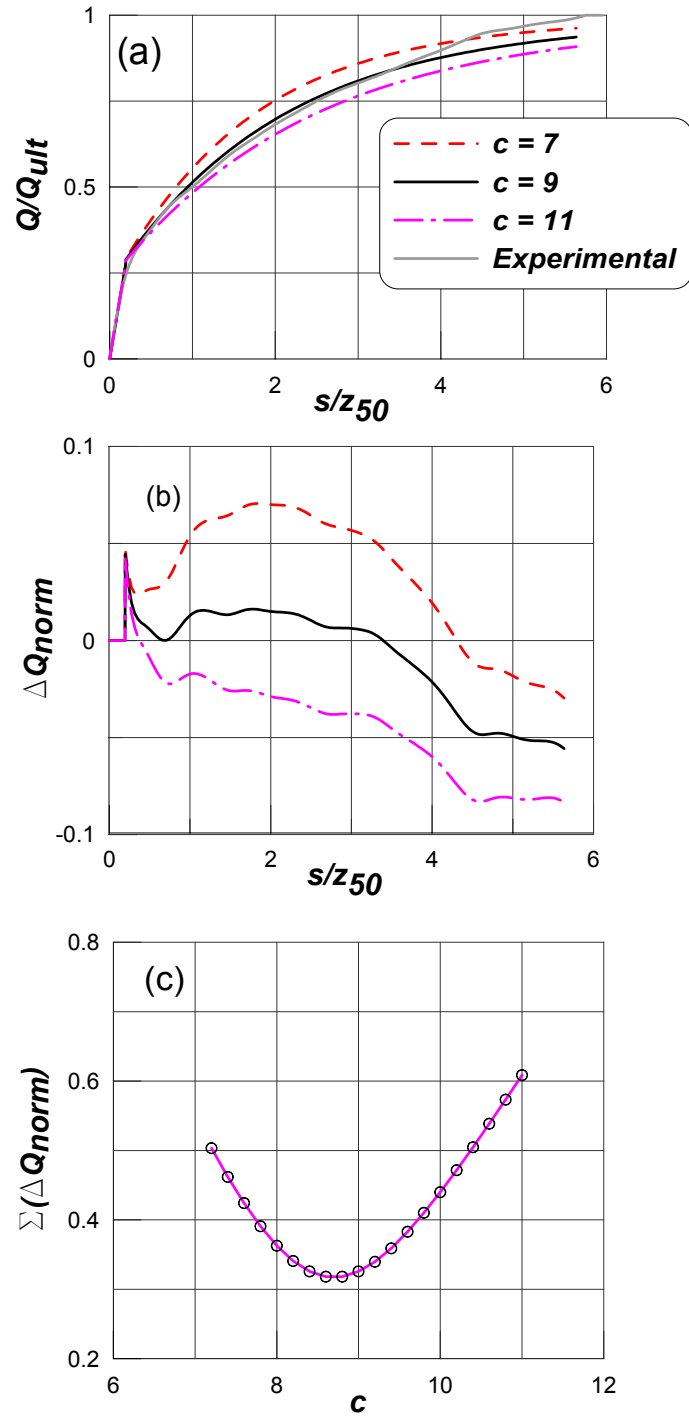


Figure 3.8: Sample regression analysis to derive the parameter c : (a) Normalized load versus normalized displacement with different c values; (b) Normalized residual load versus normalized displacement; (c) Summation of normalized residual load with varying c

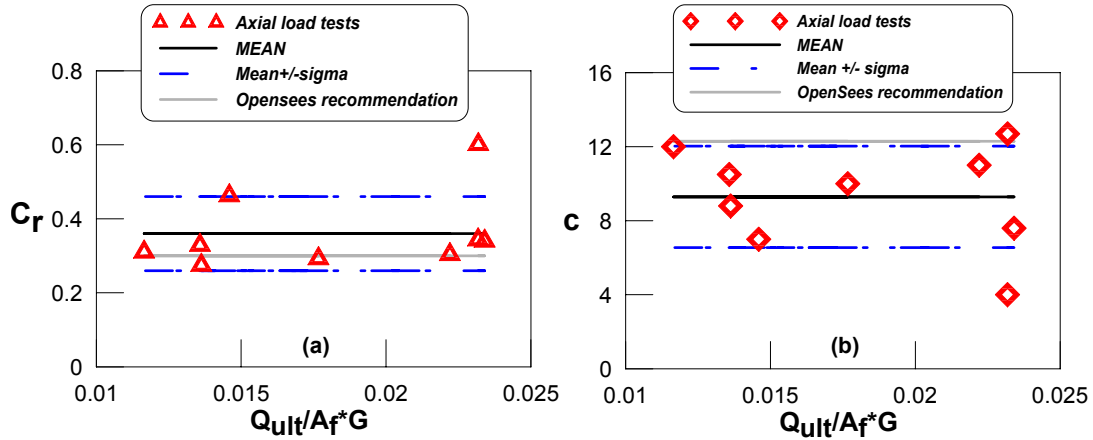


Figure 3.9: Variation of (a) C_r and (b) c for sand with normalized parameter $Q_{ult}/A_f G$ (for q-z material)

Figure 3.9 (a) and (b) show the deviation of the parameter C_r and the parameter c , respectively, for different axial load tests. These parameters are plotted against the unitless parameter, $Q_{ult}/A_f G$. This parameter has both strength and stiffness properties and foundation size in it. It is observed that 90% of the data points are within the range of $(\mu \pm \sigma)$ for both C_r and c . For C_r , the mean and standard deviation are 0.36 and 0.1, respectively. The coefficient of variation is 28%. The value of C_r as per pile load test calibration is 0.3 for sand. The mean and standard deviation of the parameter c is 9.29 and 2.74, respectively, whereas the COV is 30%. The pile-calibrated value of parameter c for sand is 12.3, which is fairly close to the regressed $\mu + \sigma$ value ($c = 12.03$ for $\mu + \sigma$ case).

Figure 3.10 shows the regressed backbone curves overlaid on the test results for q-z materials. Figure 3.11 shows pile-calibrated and shallow footing calibrated backbones for clarity. It is observed that shallow footing calibrated backbones are stiffer in the post-yield region than that of pile-calibrated backbones.

Limited data is available for shallow footings resting on clay, whereby the contributions of load distribution are isolated, therefore q-z material curves are not generated for footings

on clay.

The same procedure is followed to determine the backbones for the p-x and the t-x materials. Figure 3.12 shows the regressed p-x backbone overlaid with the lateral passive load tests considered in the study. Figure 3.12 (a) shows the backbone for sandy soil, while Figure 3.13 (b) shows the same for silty sand. Figure 3.14 shows the backbone of the t-x material overlaid with lateral sliding tests. Table 3.4 summarizes the shape parameter values determined through these regression, compared with those determined via calibration against pile load tests.

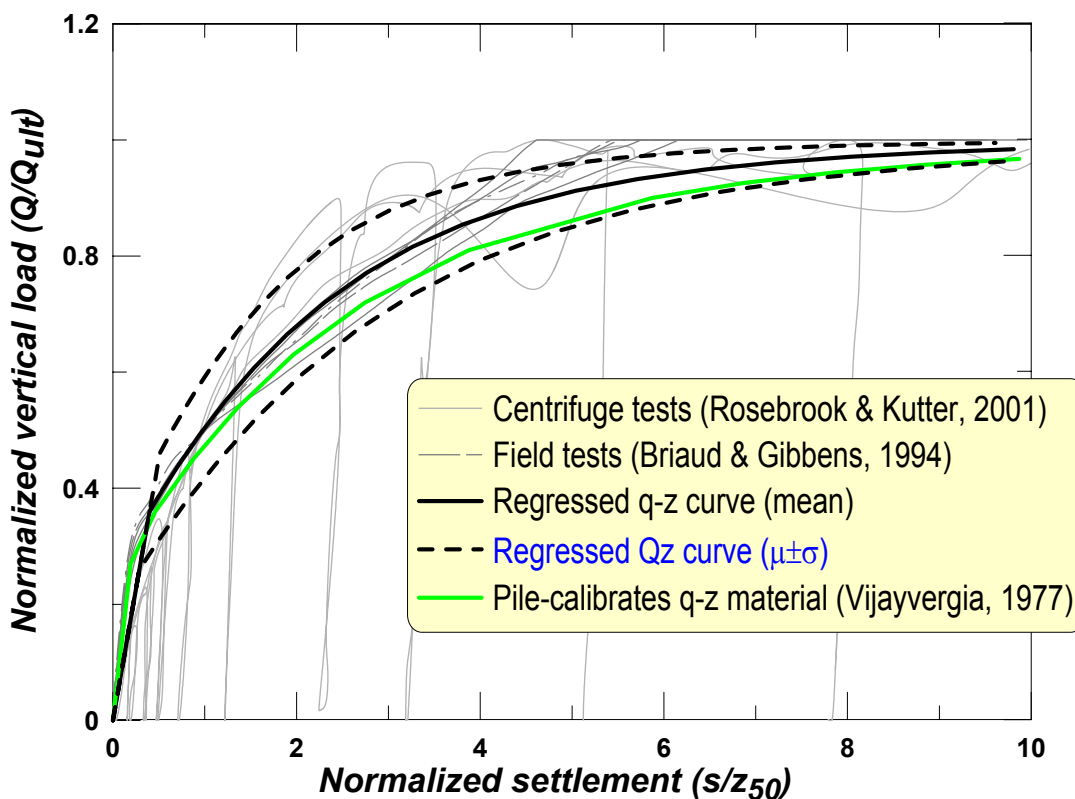


Figure 3.10: Regressed backbone for q-z material overlaid with axial tests (sand)

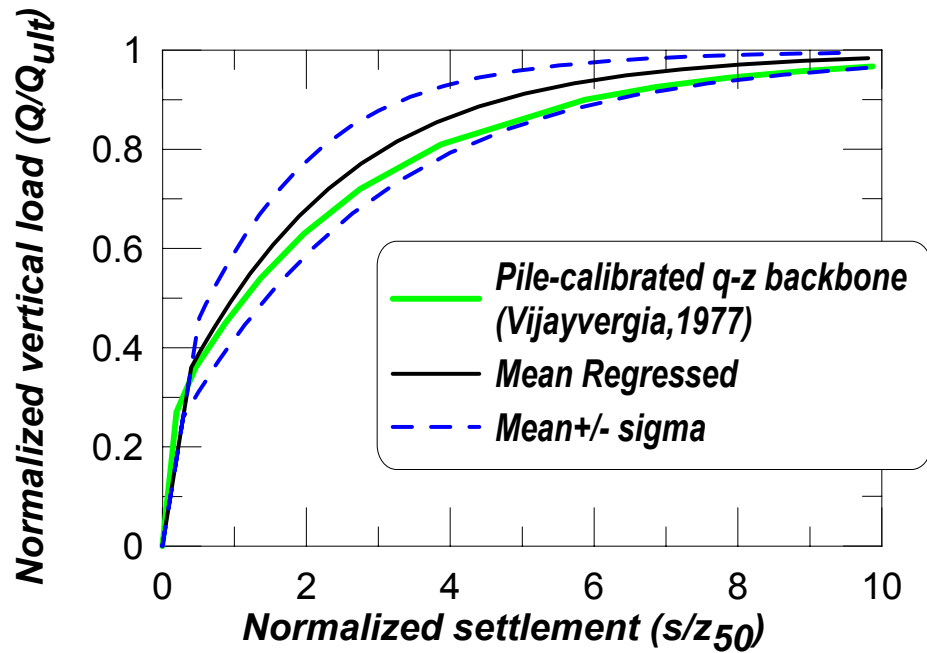


Figure 3.11: Regressed backbone for q-z material for sand (for cleaner view)

Table 3.4: Shape parameters for defining the spring material backbone curves

Material Type	Soil Type	Pile-calibrated values			Proposed shallow foundation-calibrated mean values		
		C_r	n	c	C_r	n	c
QzSimple2	clay ¹	0.20	1.2	0.35	0.22	1.20	0.50
	sand	0.30	5.5	12.30	0.36	5.50	9.29
PySimple2	clay ¹	0.35	5.0	10.00	-	-	-
	sand	0.20	2.0	0.50	0.33	2.00	1.10
TzSimple2	clay ¹	0.50	1.5	0.50	-	-	-
	sand	0.50	0.85	0.60	0.48	0.85	0.26

¹Insufficient data for calibration

3.4 Effect of Backbone Curve Modification on Overall Response

The newly calibrated backbone curves are investigated by considering an example structure-foundation system subjected to a sinusoidal input displacement quasi-statically applied at the top of the structure. Figure 3.15(a) shows a schematic diagram of the ex-

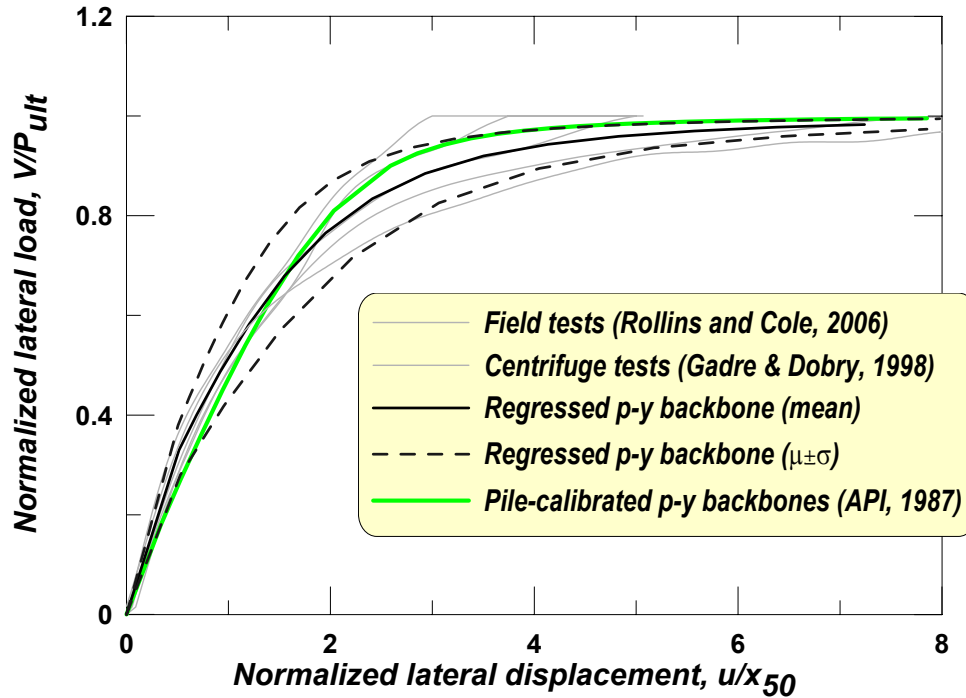


Figure 3.12: Regressed backbone for p-x material (sand) overlaid with passive tests on clean sand

ample structure with the BNWF model and Figure 3.15(b) shows the lateral displacement that has been applied at the top of the structure. The structure is supported on dry dense sand with a relative density 80%. The structure and the soil properties are based on the bridge pier shallow footing tests at the University of California, Davis, by Ugalde (2007). The structure, soil profile and the input rotation is same that is used in Section 2.5 of Chapter 2. The spring array shown in Figure 3.15(a) have been used to capture axial, rotational and lateral responses. Analyses have been conducted using the default (i.e. pile-calibrated) backbone curves and also using the newly derived mean (μ) and mean \pm standard deviation ($\mu \pm \sigma$) backbone curves.

Along with the square footing analysis, two other simulation sets are conducted using the same structure and soil properties, but varying the footing aspect ratios. The vertical

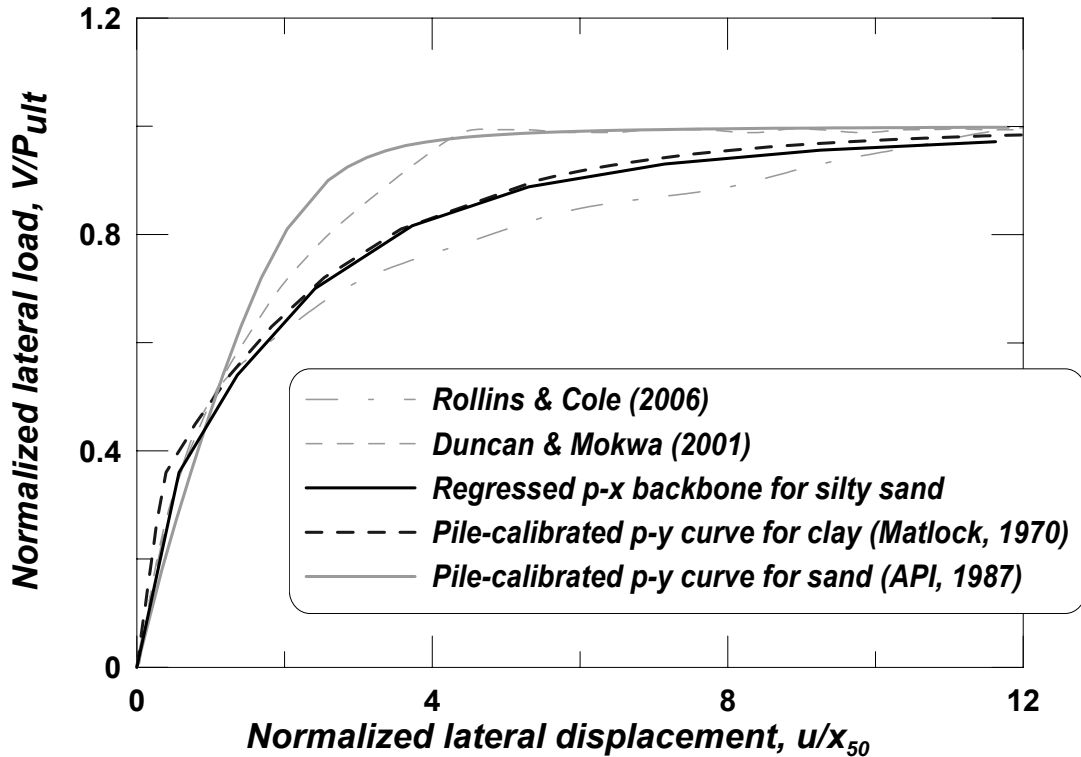


Figure 3.13: Regressed backbone for p-x material (silty sand) overlaid with passive tests on silty sand

factor of safety is held constant for all three cases. The effect of backbone on these three footing-structure systems are shown in Figures 3.16 through 3.18.

Figures 3.16 through 3.18 show the effect of the modified backbone curves on the overall footing response considering the footing to be a square, a rectangular ($B/L = 0.6$) and an almost strip footing ($B/L = 0.3$). The backbone curves used are default (pile-calibrated), mean and mean \pm standard deviation regressed curves for q-z, t-z and p-y springs for sand case. The moment-rotation, settlement-rotation and settlement time histories are shown in Figure 3.16 through 3.18. It is observed that the moment, rotation and rotational stiffness are not significantly affected by the modified backbone curves. The most pronounced effect is observed in the settlement response. It is observed that using a mean modified backbone

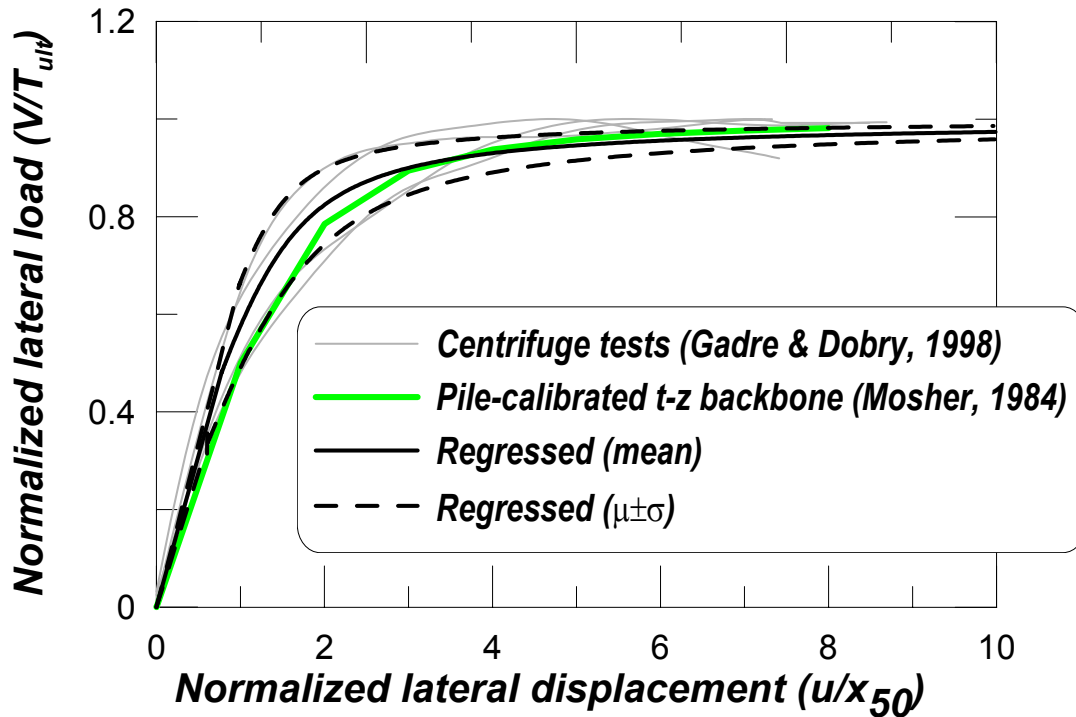


Figure 3.14: Regressed backbone for t-x material overlaid with sliding tests

curve, the settlement of a square footing decreases about 30%, while using the $\mu + \sigma$, this reduction is 50%. When used $\mu - \sigma$ backbones, settlement increased 25%. This makes sense, as the q-z material curves for shallow footings are stiffer and stronger than those obtained from axially loaded piles. For rectangular footings with an aspect ratio of 0.6 ($B/L = 0.6$), it is observed that settlement decreases approximately 40% using the mean regressed curves. This reduction is about the same for the $\mu \pm \sigma$ curves. For the rectangular footing with $B/L = 0.3$, the settlement reduction is 48% for mean and 29% for $\mu + \sigma$, while it increases $\approx 10\%$ using $\mu - \sigma$ backbone.

One can notice that the peak settlement is decreasing with reducing the aspect ratio for the three footing cases. Since the footings with lower aspect ratios have lower ultimate capacity, the vertical load on them has also been reduced to keep the FS_v same. Thus

the footing behavior is approaching elastic, resulting less inelastic deformation (thus less settlement) as the width is being reduced. This can be explained from looking at Figure 3.19 which shows the end q-z spring response of the three footings.

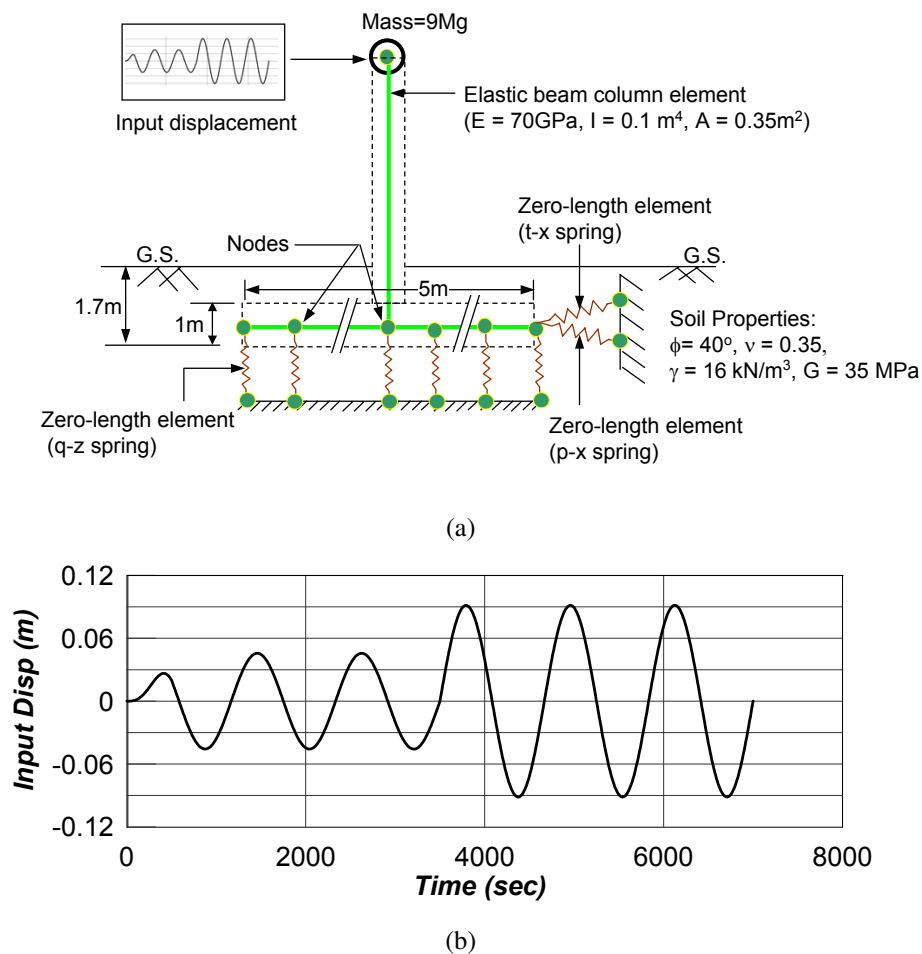


Figure 3.15: (a) Example structure-foundation system with BNWF model and (b) applied lateral displacement at the top of the structure

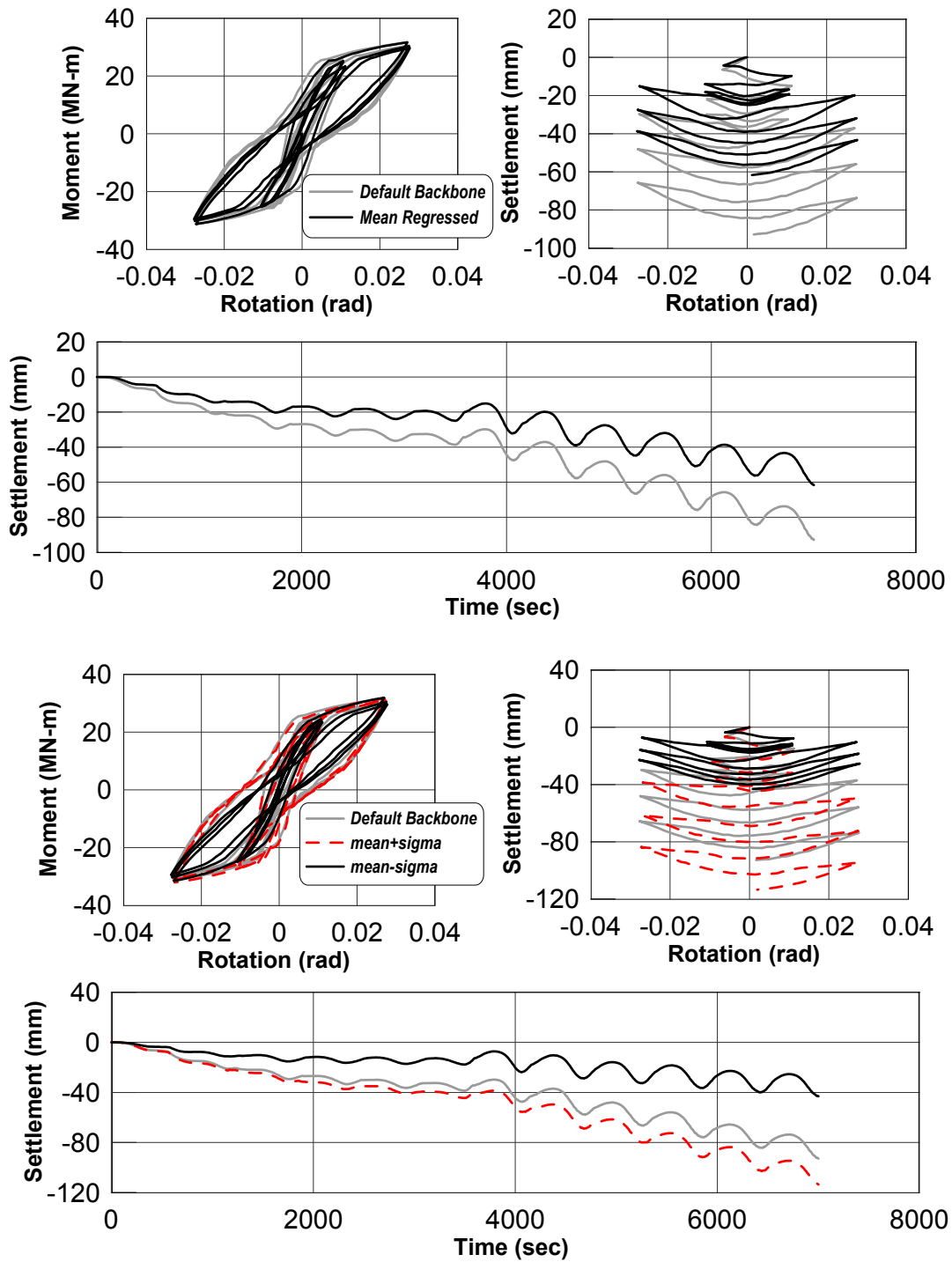


Figure 3.16: Effect of the modified backbones on the response of a shallow 5m square footing subjected to quasi-static cyclic loading

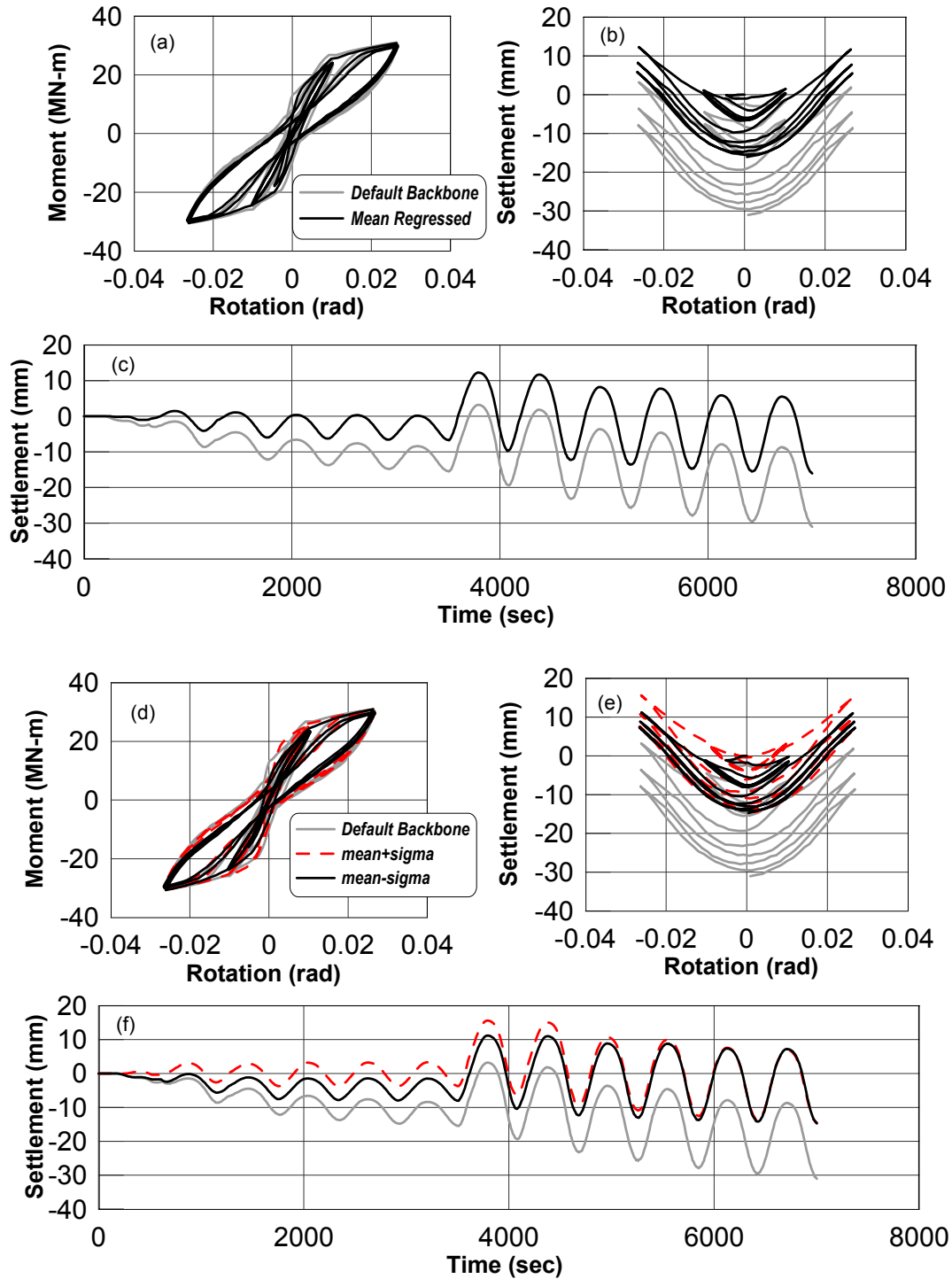


Figure 3.17: Effect of the modified backbones on the response of a shallow 5m x 3m rectangular footing (B/L = 0.6) subjected to quasi-static cyclic loading

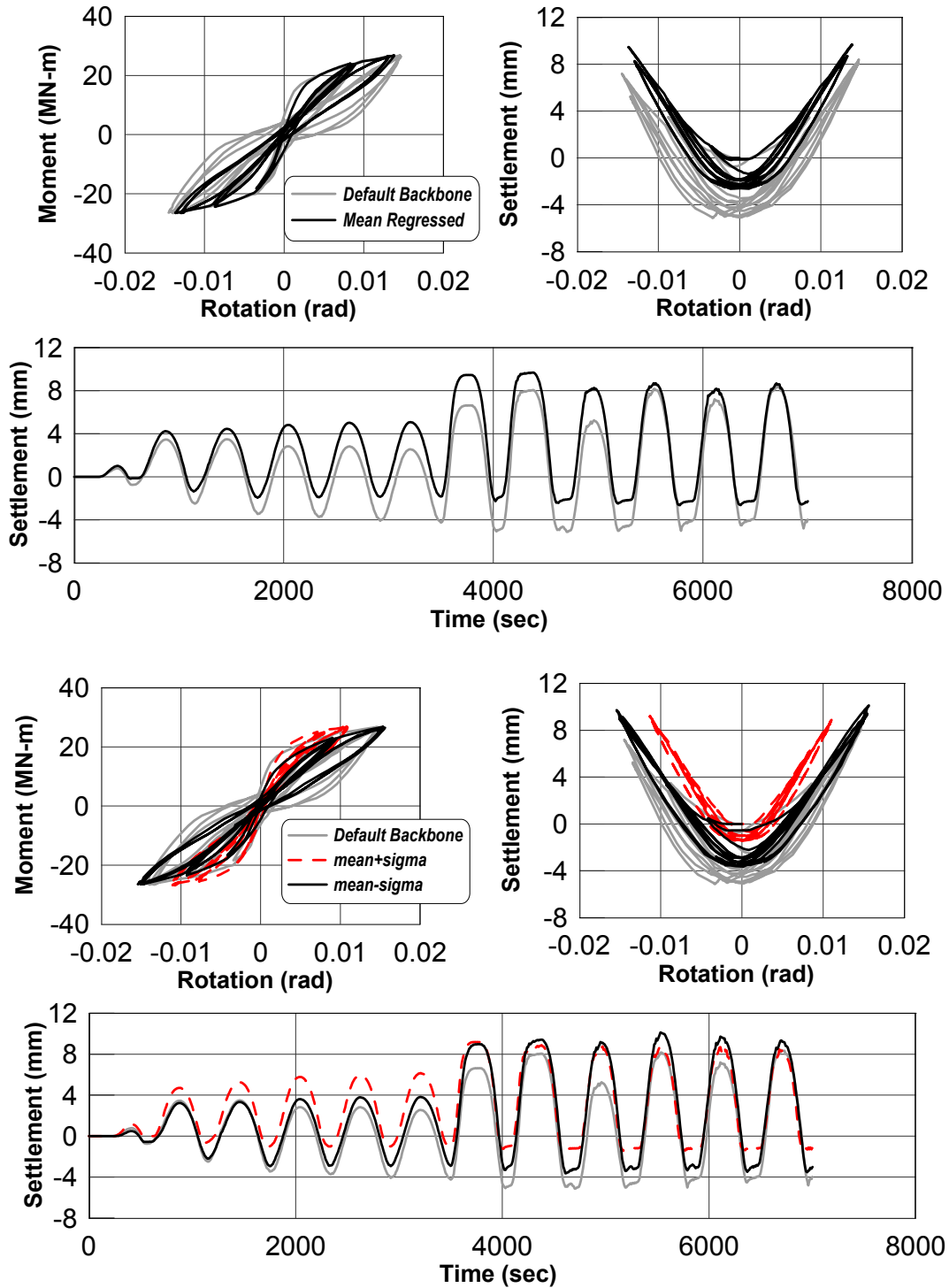


Figure 3.18: Effect of the modified backbones on the response of a shallow 5m x 1.5m rectangular footing (B/L = 0.3) subjected to quasi-static cyclic loading

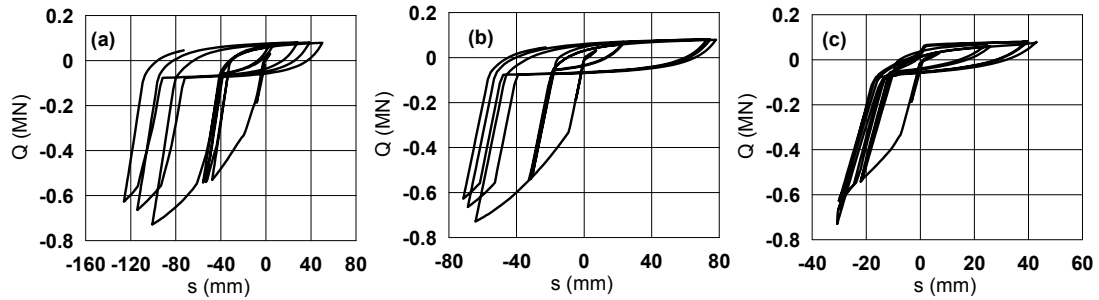


Figure 3.19: End q-z spring responses for (a) 5m x 5m footing ($B/L = 1$) (b) 5m x 3m footing ($B/L = 0.6$) (c) 5m x 1.5m footing ($B/L = 0.3$)

3.5 Summary Remarks

In this chapter the backbone curves for the p-x, q-z and t-x mechanistic springs are calibrated using experimental data from shallow footing tests. Pile test calibrated nonlinear spring models *PySimple1*, *QzSimple1* and *TzSimple1* are used as baselines and are updated considering their comparison against shallow footing tests. Particular focus is placed on determining the parameters that control the shape of the material backbones. The regressed backbone curves turned to be stiffer and stronger from those generated from pile load tests, for the q-z material model, while they are softer and weaker for the p-x and t-x material models. An iterative scheme is used to determine the best fit values and their mean and standard deviation based on available test data. The effect of backbone curve modification is found to have significant effect on the settlement response of the footing.

Chapter 4

BNWF Model Validation

4.1 Introduction

In this chapter, the BNWF model is evaluated in terms of capturing experimental foundation response history. The focus of this chapter is not on parameter selection but on studying whether a BNWF model can actually replicate the experimentally observed behavior of shallow foundations.

To perform the BNWF model validation, two sets of centrifuge test data have been chosen. The first set of data is from a series of building footings (mostly strip footings) supporting shearwalls designed as typical building models. The second set is square footings supporting bridge columns (pictures of the test set-up are shown in Figure 1.7 (a) and (b)). Some of the tests chosen for validation are static cyclic tests, while others are dynamically loaded models using motions wither from past earthquakes or cosine tapered motion. All the tests are carried out at the University of California, Davis. The bridge model and the building model considered for the validation study are different from each other in the following respects:

- All of the shearwall building models rest on strip footings with a B/L ratio ≈ 0.2 , while the bridge model rests on two square footings, one with a width of 5.4 m and another with width 7.1m.
- The range for vertical factor of safety FS_v for the building footings is 2–14, while the range of bridge footing FS_v is 17–31.
- The input motion used for the building models are lateral slow cyclic pushes and cosine tapered dynamic shakes, while the bridge footings were subjected to real earthquake motions, i.e. broad-band signals.
- The structural configuration for the building and bridge models are also different. The structure of the shearwall models is a wall with uniform cross-sectional properties supported by a footing, while the bridge column is a “lollipop” structure with a deck mass and column connected to a shallow square footing.

The model parameters for tests with sand are chosen to be that set of parameters, which gives the best overall response of footing demands as discussed in Chapter 5. For footing resting on clay, model parameters, which are different than those required for footing supported on sand, are assumed based on combination of experimental data and engineering judgements. The following sections discuss the details of the experiments chosen and presents evaluation results against those tests.

4.2 Comparison with Tests on Shearwall Footings

Details of the experiments on shearwall footings are presented in data reports by Rosebrook and Kutter (2001a), Rosebrook and Kutter (2001b), Rosebrook and Kutter (2001c),

Gajan et al. (2003a), Gajan et al. (2003b), and Thomas et al. (2004). Some of the tests were conducted on uniform fine-grained dense dry Nevada sand with a relative density, $D_r = 80\%$ and mean grain size $D_{50} = 0.17\text{mm}$. Some of the tests conducted on remolded San Francisco Bay Mud (Plastic limit, $PL = 35 \sim 40$ and liquid limit, $LL 88 \sim 93$) with an undrained shear strength c_u of clay 100 ± 10 kPa. The general information about the sand tests considered is given in Table 4.2. The two clay tests that are considered here are KRR03–02 (a static test) and KRR03–03 (a dynamic test). These two tests are done on the strip footing of size $2.8\text{m} \times 0.65\text{m}$. Both tests were on surface footing with no embedment provided. The factor of safety FS_v is 2.8 for both tests and nondimensional moment to shear values M/HL are 1.7 and 1.8, respectively for the static and dynamic tests.

Table 4.1: Details of the shearwall footing tests considered for model evaluation

Test Name	Loading Type	Reference	Mass (Mg)	Soil Type	L(m)	B(m)	D/B	FS_v	M/HL
SSG04-06	Static	<i>Gajan et al, 2006</i>	68	Sand, $Dr = 80\%$	2.8	0.65	0	2.3	1.20
SSG03-02	Static	<i>Gajan et al, 2003b</i>	58	Sand, $Dr = 80\%$	2.8	0.65	0	2.5	0.45
SSG02-05	Static	<i>Gajan et al, 2003a</i>	58	Sand, $Dr = 80\%$	2.8	0.65	0	2.6	1.72
SSG02-02	Static	<i>Gajan et al, 2003a</i>	28	Sand, $Dr = 80\%$	2.8	0.65	0	5.2	0.41
SSG02-03	Static	<i>Gajan et al, 2003a</i>	28	Sand, $Dr = 80\%$	2.8	0.65	0	5.2	1.75
SSG03-03	Static	<i>Gajan et al, 2003b</i>	28	Sand, $Dr = 80\%$	2.8	0.65	1	14.0	1.77
KRR03-03	static	<i>Rosebrook and Kutter, 2001c</i>	36	Clay, $Cu = 100$ kPa	2.7	0.65	0	2.8	1.80
SSG04-10	dynamic	<i>Gajan et al, 2006</i>	36	Sand, $Dr = 80\%$	2.8	0.65	0	4.0	1.80
SSG03-07	dynamic	<i>Gajan et al, 2003b</i>	58	Sand, $Dr = 80\%$	2.8	0.65	1	7.2	1.80
KRR03-03	dynamic	<i>Rosebrook and Kutter, 2001c</i>	36	Clay, $Cu = 100$ kPa	2.7	0.65	0	2.8	1.70

Figures 4.1(a) and (b) show the building model test schematic diagram and the idealization of the model used for the simulation work, respectively. Figure 4.1(a) shows the positions and direction of the vertical and lateral displacement transducers and accelerometers along with the shearwall and strip footing schematic diagram. Figure 4.1(b) is the idealized model of the system shown in Figure 4.1(a). Table 4.2 summarizes the user input properties for developing the BNWF models for each experiment case. The input parameters are based on the selection protocol discussed in Chapter 2.

Figures 4.2(a)–(e) through Figures 4.11(a)–(e) show comparison of the model simulation results with the experimental results. Figures 4.2(a)–(d) show moment versus rotation, settlement versus rotation, shear force versus sliding, and settlement versus sliding histories with the simulation shown in black and the experiment shown in gray. Figure 4.2(e) shows the input motion versus time. Same format of figures is also adopted for Figures 4.3(a)–(e) through 4.11(a)–(e). Note that for the static tests the input is slow cyclic displacement at the top of the structure and thus, the time axis represents pseudo time. Additional results showing the time histories of footing responses are provided in Appendix B. The following subsections provide discussions on how the simulation results compare with the experimental observations when different aspects such as nondimensional moment to shear ratio, vertical factor of safety, soil type and loading rate are considered as influencing factors.

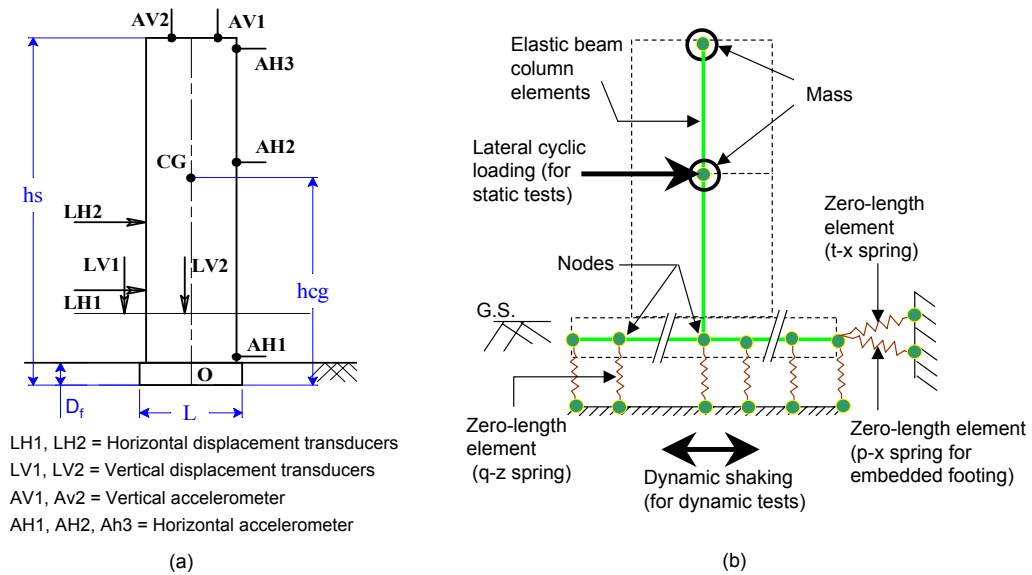


Figure 4.1: (a) Building-footing test schematic diagram and (b) idealized model

Table 4.2: BNWF model parameters used for idealized building test model

Input	SSG04_06	SSG03_02	SSG02_05	SSG02_03	SSG03_03	KRR03_02	SSG04_10	SSG03_07	KRR03_03
Loading	Actuator disp	Actuator disp	Actuator disp	Actuator disp	Actuator disp	Actuator disp	Surface acc	Surface acc	Surface acc
L (m)	2.8	2.8	2.8	2.8	2.8	2.8	2.8	2.8	2.8
B (m)	0.65	0.65	0.65	0.65	0.65	0.65	0.65	0.65	0.65
D_r (m)	0	0	0	0	0.65	0	0	0.65	0
FS_v	2.3	2.5	2.6	5.2	14	2.8	4	7.2	2.8
E (MPa)	45	45	45	45	45	40	45	45	40
ν	0.4	0.4	0.4	0.4	0.4	0.5	0.4	0.4	0.5
TP (%)	10	10	10	10	10	10	10	10	10
R_e (%)	10	10	10	10	10	10	10	10	10
R_k	2.5	2.5	2.5	2.5	2.5	2.5	2.5	2.5	2.5
l_g/L (%)	2	2	2	2	2	2	2	2	2

4.2.1 Effect of Nondimensional Moment to Shear Ratio

The parameters of the tests SSG04–06, SSG03–02 and SSG02–05 are similar with the exception of nondimensional moment to shear ratio M/HL , which ranges from 0.41 (low) to 1.8 (high) for these cases (Figures 4.7, 4.5 and 4.4). These models represent close to the typical design vertical factor of safety (FS_v 3.0), and each are resting on the surface of dense ($D_r = 80\%$) dry sand. It is observed from the figures presented that in a consistent fashion, the model is able to capture reasonably the moment and shear demand observed experimentally, with the exception of the lower M/HL models (Figures 4.2 and 4.5), where the experimental moment and shear demands are approximately 30% higher than that calculated in the simulation. Moreover, results in these figures demonstrate the model is able to reasonably capture the general shapes of the hysteresis loops (unloading and reloading stiffness and fullness of the loops) as well as the characteristics of the settlement-rotation and settlement-sliding behavior, again with the exception of the lowest M/HL model (Figures 4.5). Settlement-rotation and settlement-sliding histories show that the BNWF model predicts a large initial settlement, with subsequent smaller cycles, whereas the experiment observed initially small cycles of settlement per rotation cycle.

In addition, the maximum and residual sliding is not fully captured for the low M/HL model. The asymmetric shear-sliding response observed in the experiment may be due to slight asymmetry of the connection of the wall to the actuator.

4.2.2 Effect of Vertical Factor of Safety

Figures 4.2 to 4.6 present comparable models with varying vertical factors of safety ($FS_v = 2.6, 5.2, \text{ and } 14$). The vertical factor of safety is modified by either increasing the mass or embedding the footing. These plots show that the shapes of the experimental moment-rotation histories become increasingly pinched with increased FS_v indicating less energy dissipation, while the settlement-rotation histories become increasingly parabolic-shaped with increasing FS_v . Notably, these traits are fairly well captured by the BNWF model. However, the model is not able to capture the asymmetric transient and permanent sliding response observed in the high FS_v experiment (SSG03–03, Figure 4.6). Permanent settlement is calculated as approximately 5 mm for the experiment and observed as approximately 18 mm in the experiment. This may be due to the higher shear capacity in the model, and lack of mobilization of this capacity during the simulation.

4.2.3 Effect of Soil Type

Tests SSG02–05 and KRR03–02 are similar with the exception that the former is resting on dense sand and the later on clay (Figure 4.4 and Figure 4.10). To maintain similar factors of safety, the mass of SSG02–05 is larger than that of KRR03–02. The clay model experiment shows an asymmetric moment demand (larger in the pull/negative direction), which is not captured by the model. This may be due to local modifications to the soil that could not be captured with symmetric array of springs. Moreover, the model predicts a large initial

settlement upon the early cycles, whereas in the experiment, small cumulative settlements are observed for the initial displacement cycles. The maximum permanent settlement is under-estimated by approximately 18%, while the peak sliding is under-estimated by approximately 21%. The model does reasonably well in capturing the rotational stiffness during the early cycles and the shear stiffness throughout the loading history.

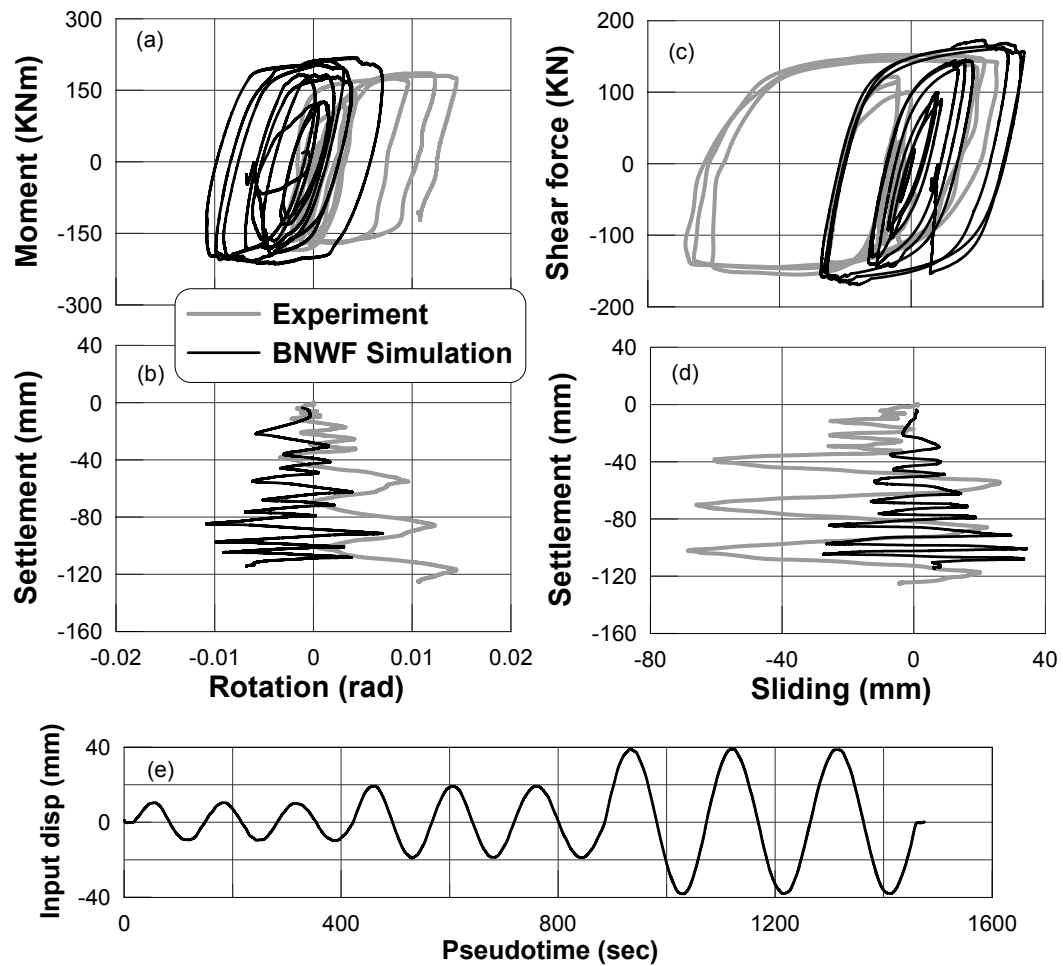


Figure 4.2: Footing response comparison for test SSG02-02 (static cyclic test on dense sand with $D_r = 80\%$, $FS_v = 5.2$ and $M/HL = 0.41$): (a) moment-rotation, (b) settlement-rotation, (c) shear-sliding, (d) settlement-sliding and (e) input displacement

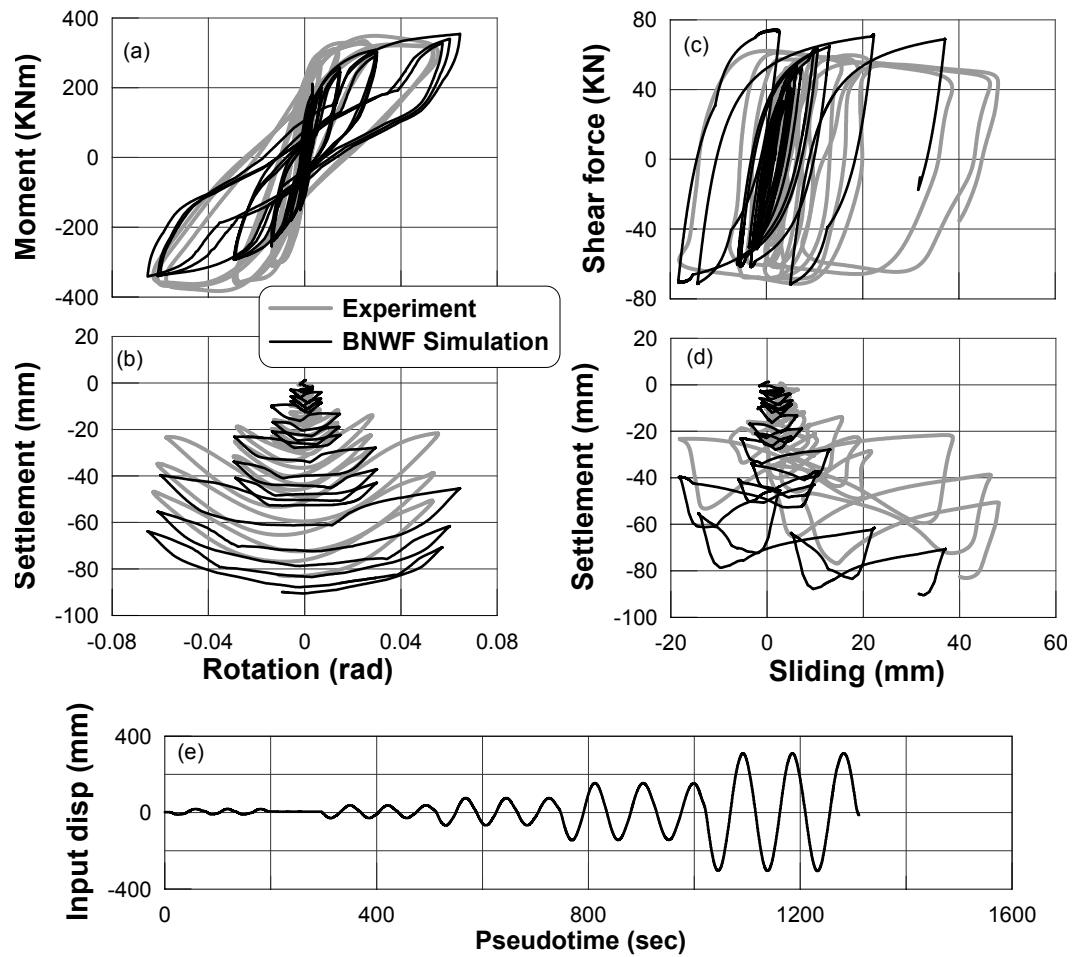


Figure 4.3: Footing response comparison for test SSG02-03 (static cyclic test on dense sand with $D_r = 80\%$, $FS_v = 5.2$ and $M/HL = 1.75$): (a) moment-rotation, (b) settlement-rotation, (c) shear-sliding, (d) settlement-sliding and (e) input displacement

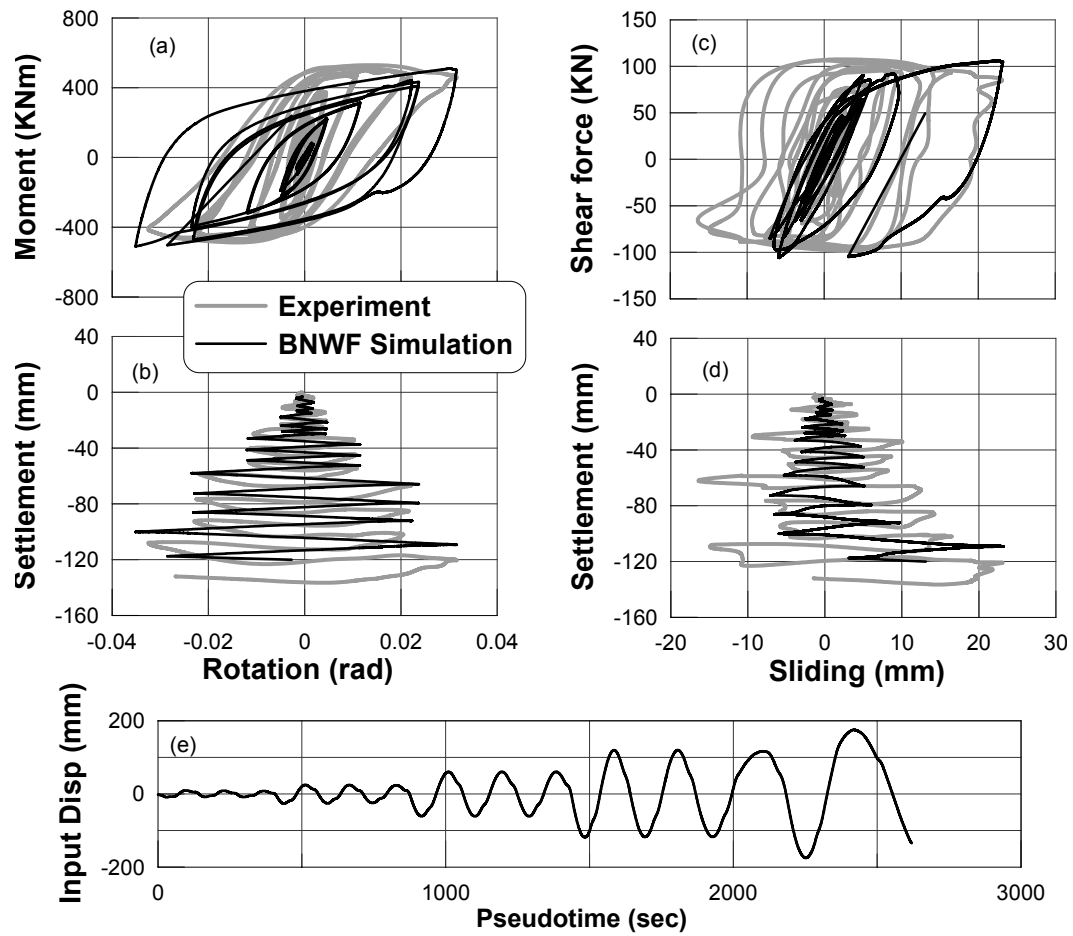


Figure 4.4: Footing response comparison for SSG02-05 (static cyclic test on dense sand with $D_r = 80\%$, $FS_v = 2.6$ and $M/HL = 1.72$): (a) moment-rotation, (b) settlement-rotation, (c) shear-sliding, (d) settlement-sliding and (e) input displacement

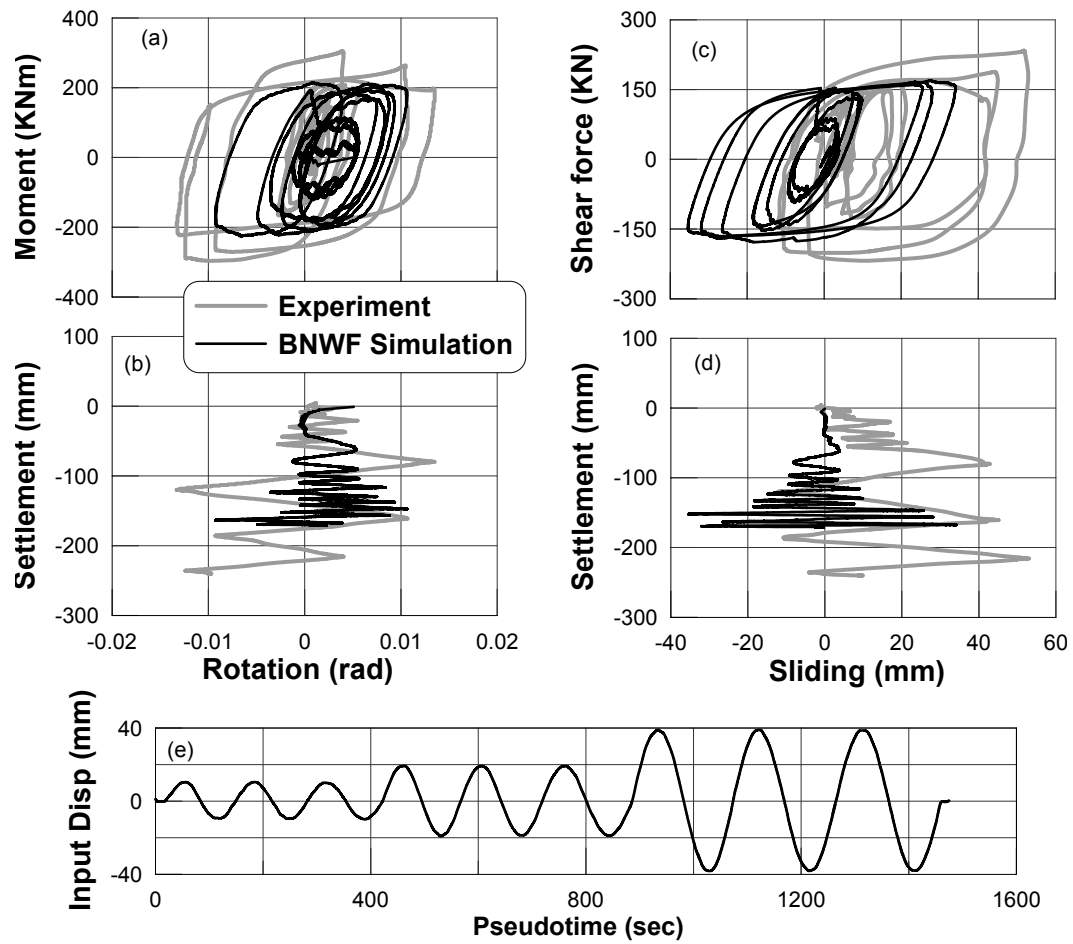


Figure 4.5: Footing response comparison for test SSG03-02 (static cyclic test on dense sand with $D_r = 80\%$, $FS_v = 2.5$ and $M/HL = 0.45$): (a) moment-rotation, (b) settlement-rotation, (c) shear-sliding, (d) settlement-sliding and (e) input displacement

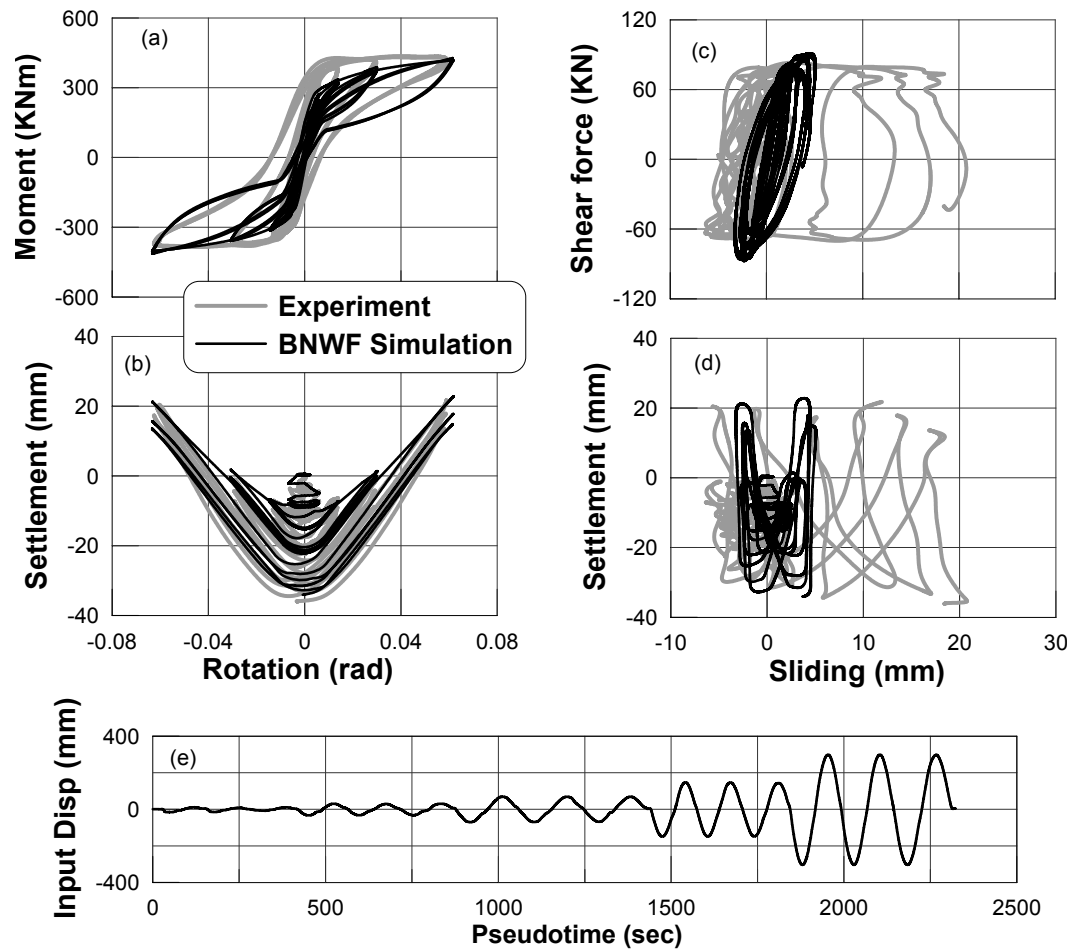


Figure 4.6: Footing response comparison for test SSG03-03 (static cyclic test on dense sand with $D_r = 80\%$, $FS_v = 14.0$ and $M/HL = 1.77$): (a) moment-rotation, (b) settlement-rotation, (c) shear-sliding, (d) settlement-sliding and (e) input displacement

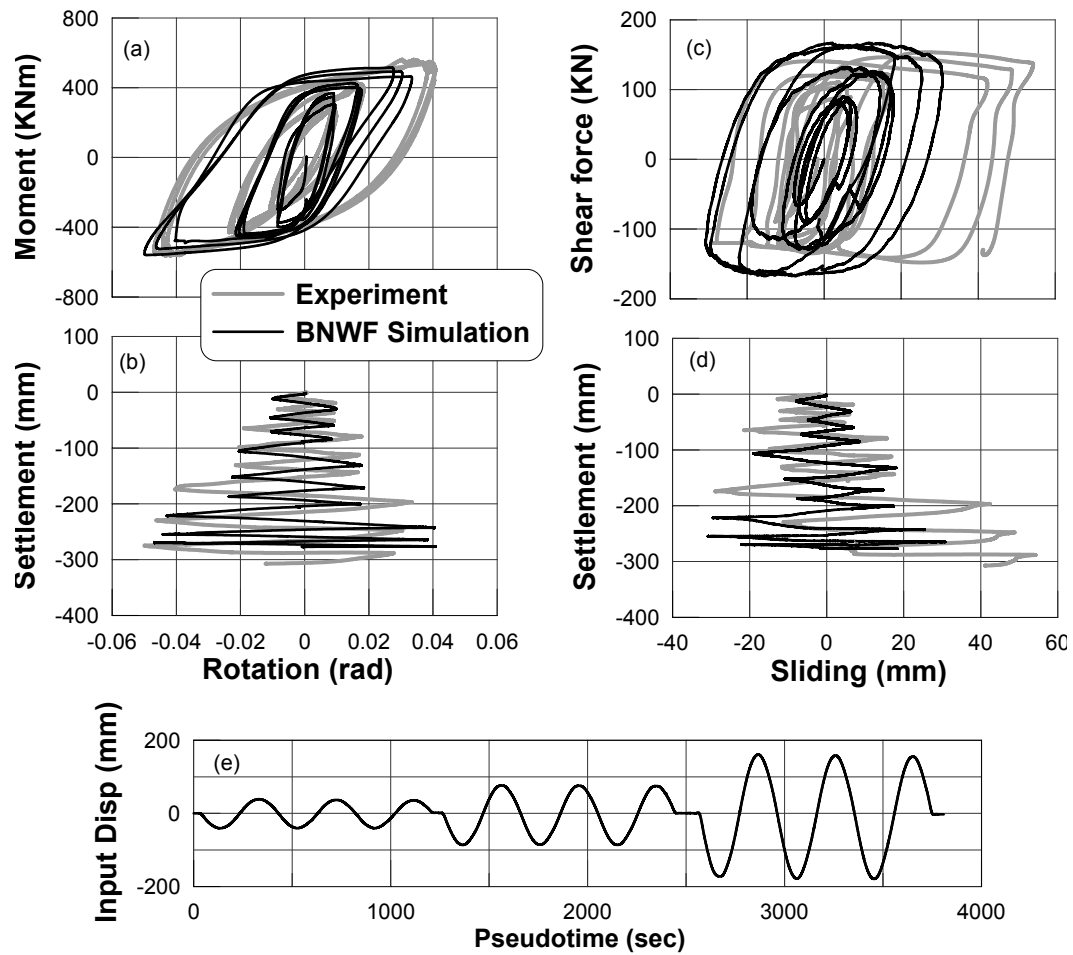


Figure 4.7: Footing response comparison for test SSG04-06 (static cyclic test on dense sand with $D_r = 80\%$, $FS_v = 2.3$ and $M/HL = 1.20$): (a) moment-rotation, (b) settlement-rotation, (c) shear-sliding, (d) settlement-sliding and (e) input displacement

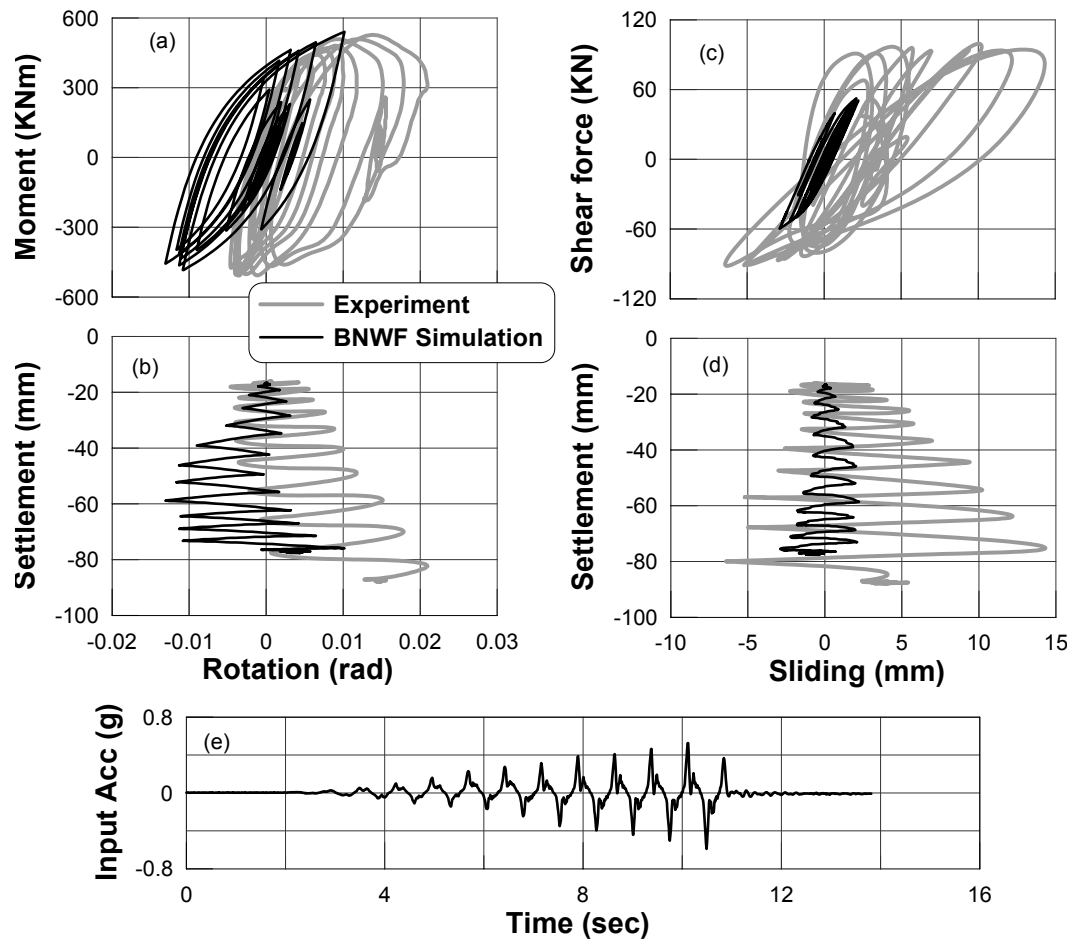


Figure 4.8: Footing response comparison for test SSG03-07 (dynamic test on dense sand with $D_r = 80\%$, $FS_v = 7.2$ and $M/HL = 1.80$): (a) moment-rotation, (b) settlement-rotation, (c) shear-sliding, (d) settlement-sliding and (e) input acceleration

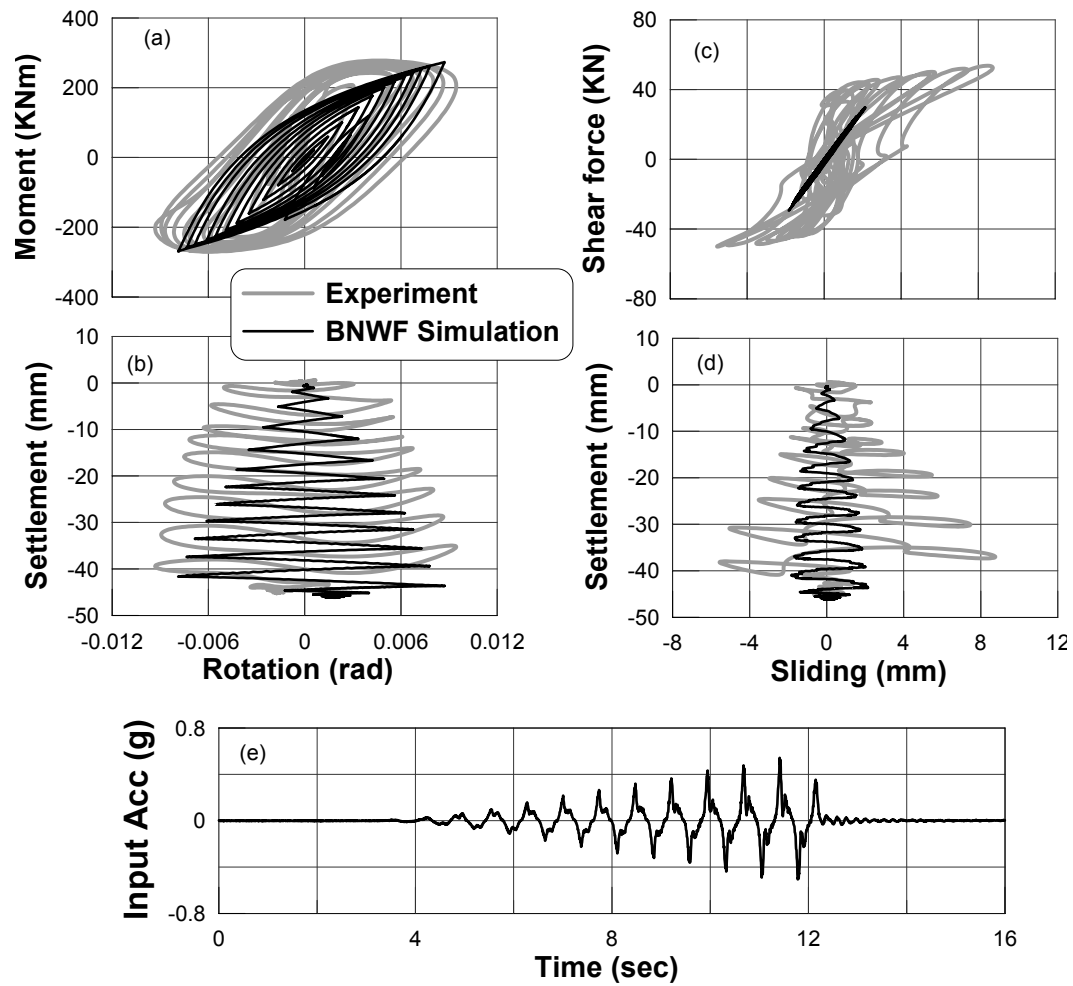


Figure 4.9: Footing response comparison for test SSG04-10 (dynamic test on dense sand with $D_r = 80\%$, $FS_v = 4.0$ and $M/HL = 1.80$): (a) moment-rotation, (b) settlement-rotation, (c) shear-sliding, (d) settlement-sliding and (e) input acceleration

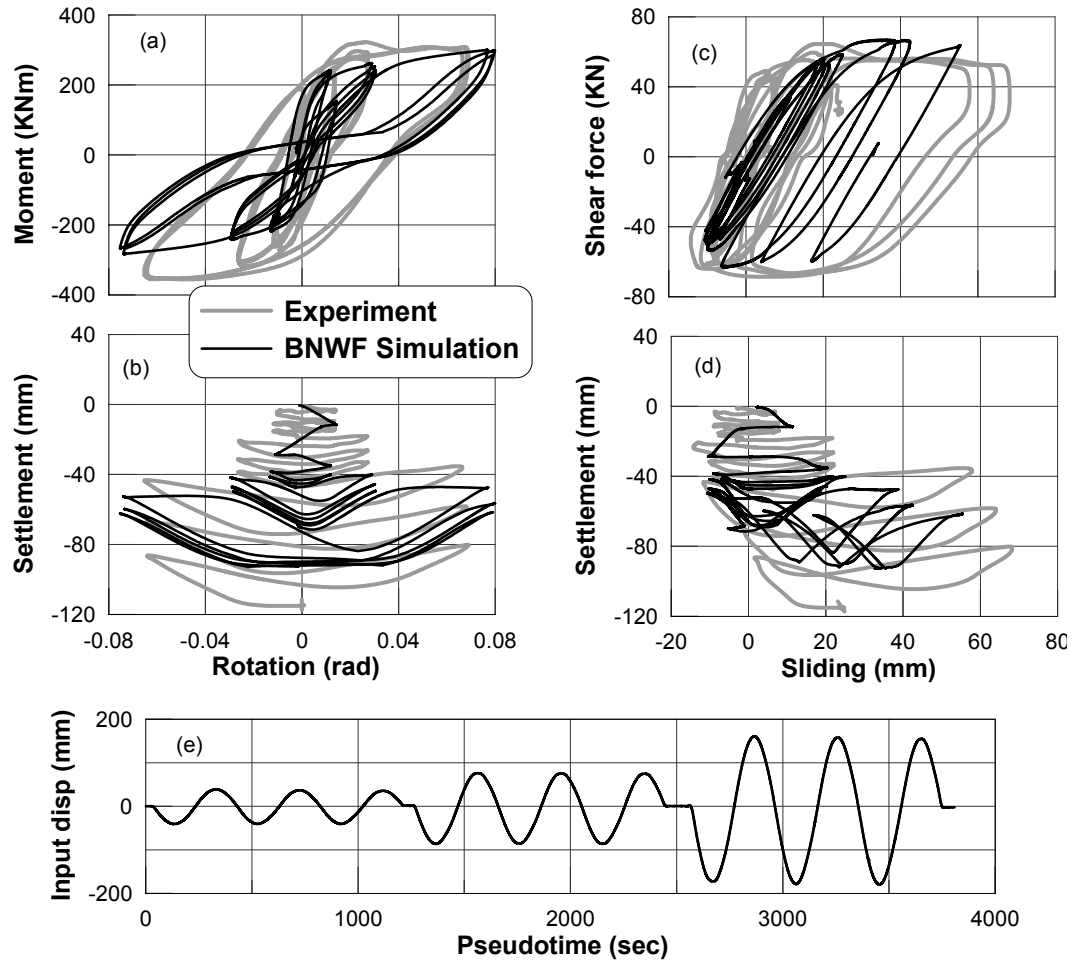


Figure 4.10: Footing response comparison for test KRR03-02 (static cyclic test on 100 kPa clay with $FS_v = 2.8$ and $M/HL = 1.80$): (a) moment-rotation, (b) settlement-rotation, (c) shear-sliding, (d) settlement-sliding and (e) input displacement

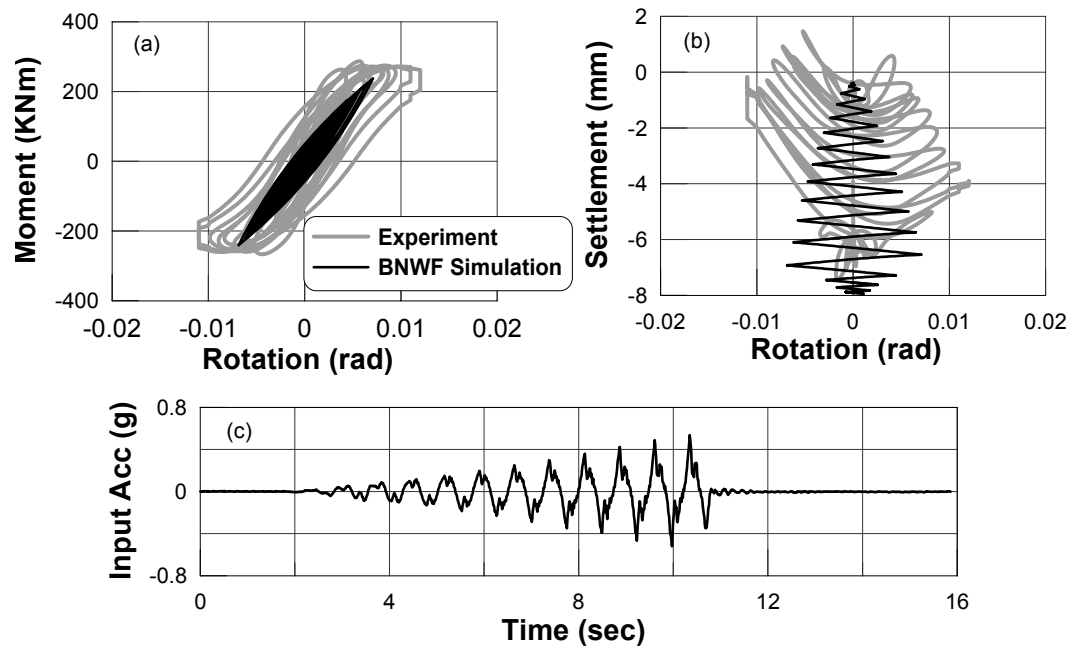


Figure 4.11: Footing response comparison for test KRR03-02 (dynamic test on 100 kPa clay with $FS_v = 2.8$ and $M/HL = 1.70$): (a) moment-rotation, (b) settlement-rotation, (c) input acceleration

Table 4.2.3 summarizes the force and displacement demands obtained from the experiments with that from the simulations for each test. The force demands are the absolute maximum moment $|M_{max}|$ and shear $|V_{max}|$. Displacement demands are the absolute maximum rotation $|\theta_{max}|$, sliding $|u_{max}|$ and settlement $|S_{max}|$. It can be seen from Table 4.2.3 that the mean deviations in estimating the peak demands for moment, rotation, shear, and settlement from experimental results are: 9%, 14%, 16% and 11%, respectively, whereas the mean error in estimating sliding demand is 44%. Although Table 4.2.3 presents the absolute deviations from experiment to simulation, it is hard to know whether the BNWF model is under-predicting or over-predicting the corresponding responses. Figure 4.12 presents a summary of the footing force and displacement demands predicted by the BNWF model. The peak demands predicted by simulation are plotted against the demands obtained in the experiments. The 1:1 line represents the experimental=simulation line. It is observed that the moment, shear and rotation does not follow any trend; in some of the cases they are under-predicted, while in other cases, they are slightly over-predicted, ranging a mean absolute deviation less than 20%. Settlement demand is predicted very well for all the cases except two high settlement cases where peak settlement exceeds 200 mm. Sliding is under-predicted in most of the cases,

Table 4.3: Summary of shearwall-footing response prediction

			Experimental values					BNWF Simulation					Absolute error in BNWF simulation				
Test Name	FSv	MH/L	$ M_{max} $ (MN-m)	$ \theta_{max} $ (rad)	$ V_{max} $ (MN)	$ u_{max} $ (mm)	$ S_{max} $ (mm)	$ M_{max} $ (MN-m)	$ \theta_{max} $ (rad)	$ V_{max} $ (MN)	$ u_{max} $ (mm)	$ S_{max} $ (mm)	$ \varepsilon_M $ (%)	$ \varepsilon_\theta $ (%)	$ \varepsilon_V $ (%)	$ \varepsilon_u $ (%)	$ \varepsilon_S $ (%)
SSG04-06	2.3	1.20	560	0.050	154	54	307	564	0.047	168	30.8	277	1%	6%	9%	43%	10%
SSG03-02	2.5	0.45	306	0.014	226	52	237	224	0.01	182	35	173	27%	29%	19%	33%	27%
SSG02-05	2.6	1.72	530	0.033	108	23	137	511	0.035	106	23	120	4%	6%	2%	0%	12%
KRR03-02	2.8	1.8	356	0.069	69	68	117	300	0.08	67	55	93	16%	16%	3%	19%	21%
KRR03-03	2.8	1.7	287	0.012	no data	no data	7.5	241	0.008	no data	no data	7.8	16%	33%	4%
SSG04-10	4	1.8	278	0.009	54	8	45	273	0.009	30	2.2	47	2%	0%	44%	73%	4%
SSG02-02	5.2	0.41	189	0.014	158	67	126	218	0.015	170	34	115	15%	7%	8%	49%	9%
SSG02-03	5.2	1.75	383	0.063	71	48	83	355	0.065	75	37	91	7%	3%	6%	23%	10%
SSG03-07	7.2	1.8	527	0.02	100	14	88	540	0.013	60	2.2	78	2%	35%	40%	84%	11%
SSG03-03	14	1.77	436	0.063	83	21	36	428	0.063	91	5	34	2%	0%	10%	76%	6%
												MEAN	9%	14%	16%	44%	11%

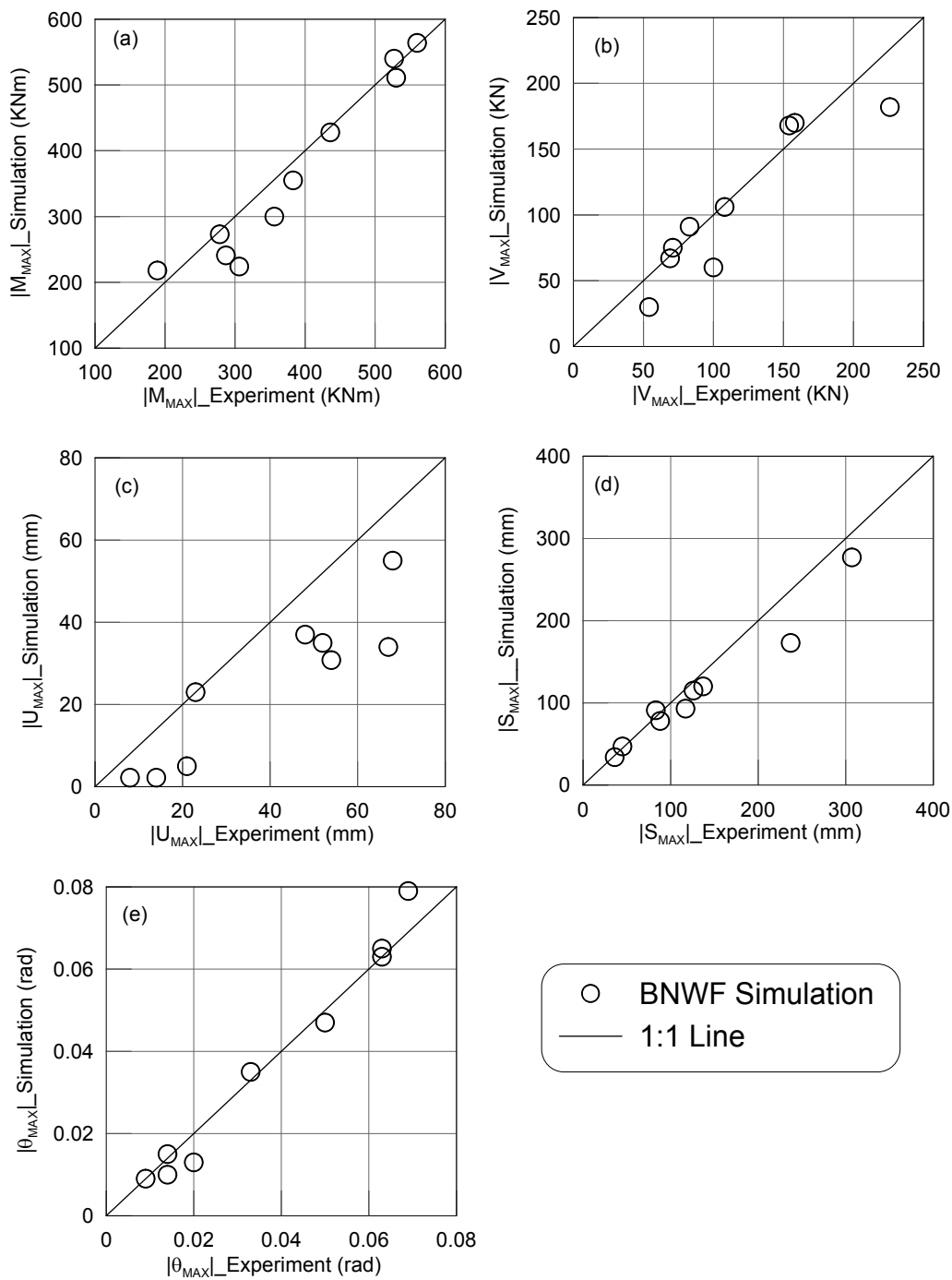


Figure 4.12: Performance of BNWF model in predicting the shearwall-footing response

4.3 Comparison with Tests on Bridge Footings

The bridge-footing tests are conducted by Ugalde (2007) on embedded square footings resting on dense dry Nevada sand of relative density 80%. The model tests were scaled from typical bridge configurations used by Caltrans. The prototype footings were square with widths of 3, 4, or 5 times the diameter of the column (diameter of column = 1.8 m) (Table 4.3). The prototype structure was a typical reinforced concrete single column bridge bent modeled as a "lollipop" structure with a deck mass and column connected to a shallow spread footing. Structures at Stations E and F were subject to dynamic loading using the shaking table mounted on the centrifuge to shake the entire model container. The ground motions imposed on the model container were scaled and filtered motions from recordings in the Tabas 1978 earthquake and a Los Gatos recording of the 1989 Loma Prieta earthquake. These motions come from the near field records posted at the SAC Steel Project (2006) website. Shaking events five, six, and eight were chosen because they are low intensity Events 1–4, and 7 resulted in very little settlement or nonlinear load-deformation of the footing. The motion recorded at the footing level in the free field during the experiment was used as input at the base for the validation of BNWF model. The kinematic effects on the footing are neglected. Figure 4.13 depicts the test schematic of the centrifuge tests on the bridge-footing system carried out at UC Davis along with the BNWF idealization used to model the same system. Table 4.3 tabulates the parameter values used in the comparison study.

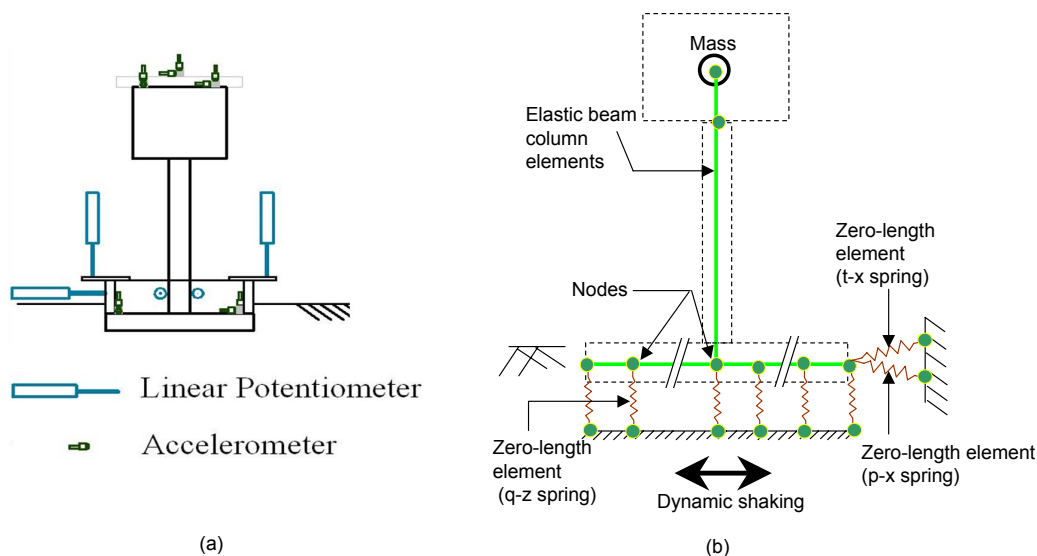


Figure 4.13: (a) Bridge-footing test schematic after Ugalde (2007) and (b) BNWF idealization

Table 4.4: Test details considered for the comparison study of bridge dynamic tests resting on dry sand with $D_r = 80\%$ conducted by Ugalde (2007) (prototype scale)

Test Name	Mass (Mg)	L(m)	B(m)	D_r/B	FS_v	M/HL
JAU01-E05 to E08	1100	5.4	5.4	0.3	17.0	2.50
JAU01-F05 to F08	1172	7.1	7.1	0.24	31.0	1.90

Table 4.5: Model input parameters for use in the comparison study

Input	JAU01-F05	JAU01-E05	JAU01-E06	JAU01-F06	JAU01-E08	JAU01-F08
Loading	Surface acc	Surface acc	Surface acc	Surface acc	Surface acc	Surface acc
L = B (m)	5.4	7.1	5.4	7.1	5.4	7.1
D_r (m)	1.73	1.73	1.73	1.73	1.73	1.73
FS_v	17	31	17	31	17	31
E (MPa)	45	45	45	45	45	45
ν	0.4	0.4	0.4	0.4	0.4	0.4
TP (%)	10	10	10	10	10	10
R_e (%)	16	16	16	16	16	16
R_k	5	5	5	5	5	5
l_e/L (%)	2	2	2	2	2	2

Figures 4.14– 4.16 show the comparison results for the analysis of the bridge-footing tests. It is observed from the BNWF results that the overall prediction of footing demands are reasonably well for all three motions and both the footings in terms of capturing the

shapes of moment-rotation and settlement-rotation curves and predicting peak moment and settlement demands (mean deviation is $\approx 20\%$ as shown in Table 4.3.2). The mean deviation in predicting rotational demand is comparatively higher (36%) because of the smaller value of the peak experimental rotation (a range of 0.003 rad to 0.022 rad). What follows is an discussion of the overall estimation of the demand parameters for the bridge results. Note that there is some initial settlement, which is accrued from the previous loadings.

4.3.1 Moment Demand

The moment capacity of the footing is under predicted by the BNWF model for both Stations F and Station E for all events. The range of under-prediction for the BNWF model is 13% to 25% with a mean of 21%. This may be due to the uncertainty in estimating the bearing capacity of soil. No axial tests were done for these cases, so experimental bearing capacities of the footings are not known. During testing, the soil underneath the footing is compacted and densified from previous loading events and therefore has a greater capacity than estimated theoretically. Another reason for the under-estimation of moment capacity may be due to ignoring the side friction of the embedded footing which may also result in lower moment demands. Note that the footing is becoming embedded deeper and deeper as it settles with subsequent events. Increasing the ultimate capacity would increase the moment capacity of the footing (as shown in sensitivity study in Chapter 5).

4.3.2 Displacement Demands

During small shaking the magnitude of permanent settlement is predicted reasonably well. However, the simulated response of the larger footing (Station F) to the more intense earthquakes (JAU01–F05 and JAU01–F08) over-predicts the permanent settlements

by about 20%. The rotation is under-estimated with a range of 21% to 50%, with a mean value of 36%. The greater deviation in predicting rotation may be due to the fact that the amount of rotation is very small, therefore the percentage error is high, however, the absolute difference between the demands from the experiments and the simulation is not very significant.

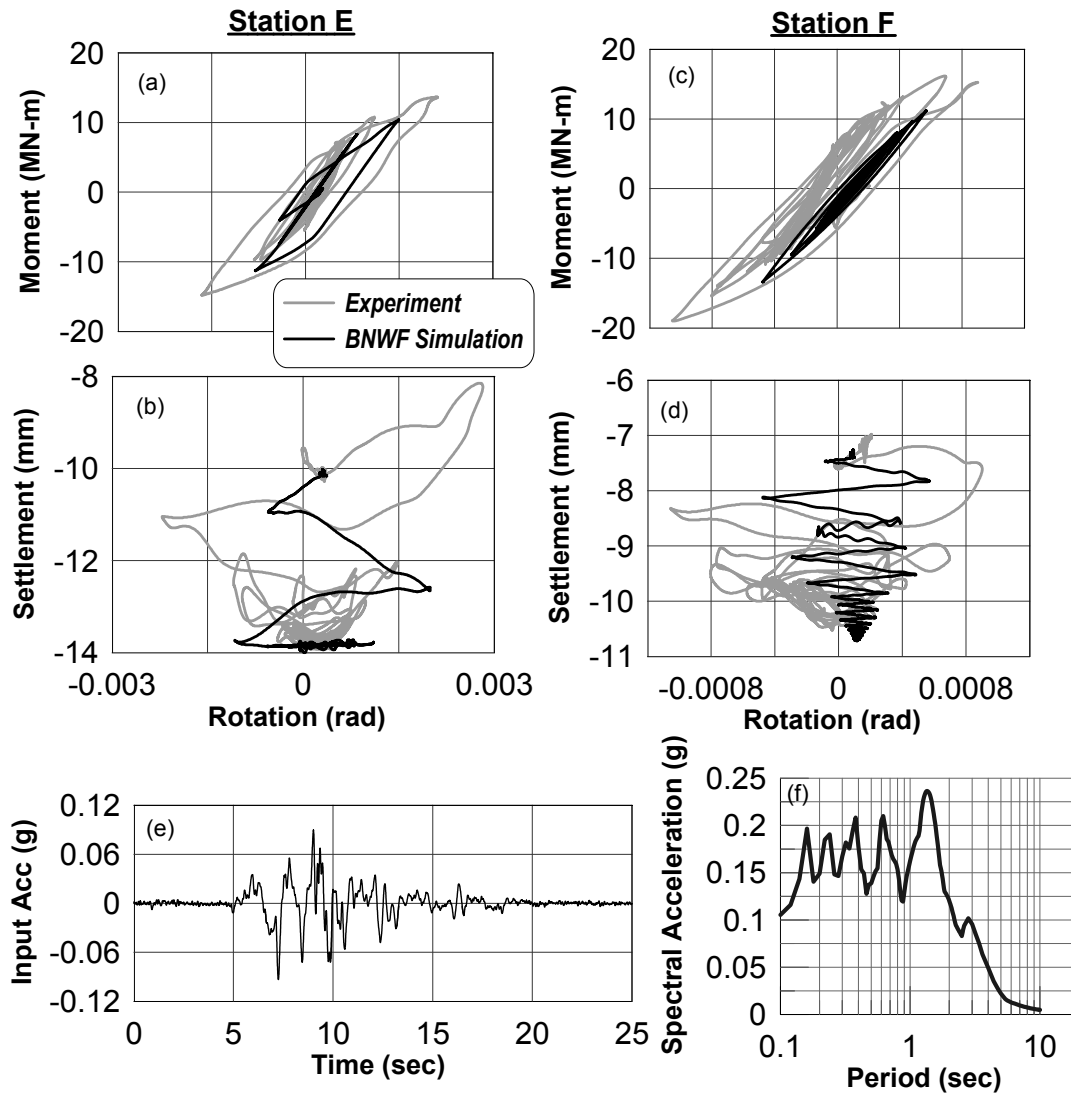


Figure 4.14: (a) Moment–rotation and (b) Settlement–rotation for JAU01–E05, (c) Moment–rotation and (d) Settlement–rotation for JAU01–F05, (e) Acceleration time history and (f) Input motion and acceleration response spectra used in the event

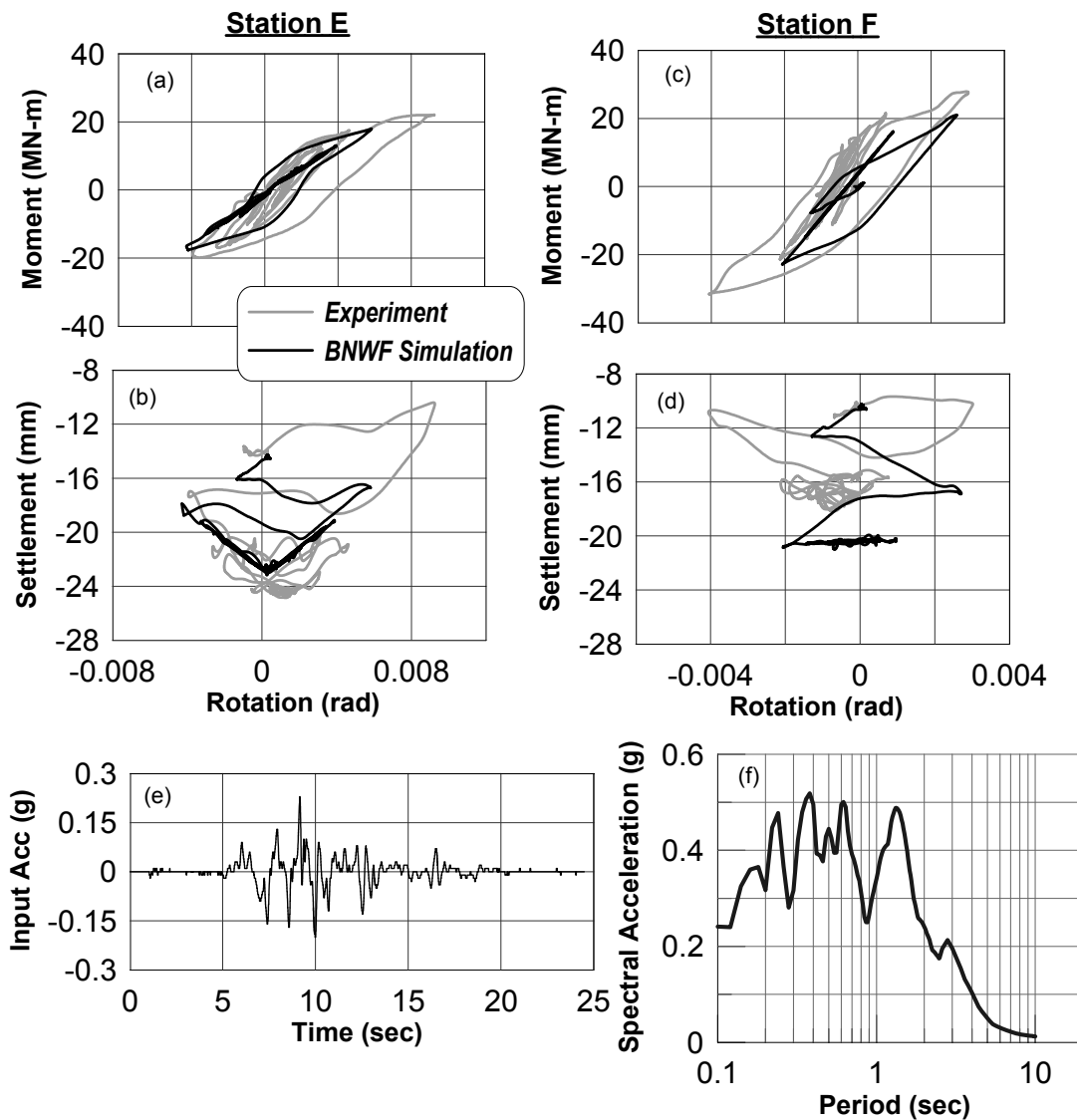


Figure 4.15: (a) Moment–rotation and (b) Settlement–rotation for JAU01–E06, (c) Moment–rotation and (d) Settlement–rotation for JAU01–F06, (e) Acceleration time history and (f) Input motion and acceleration response spectra used in the event

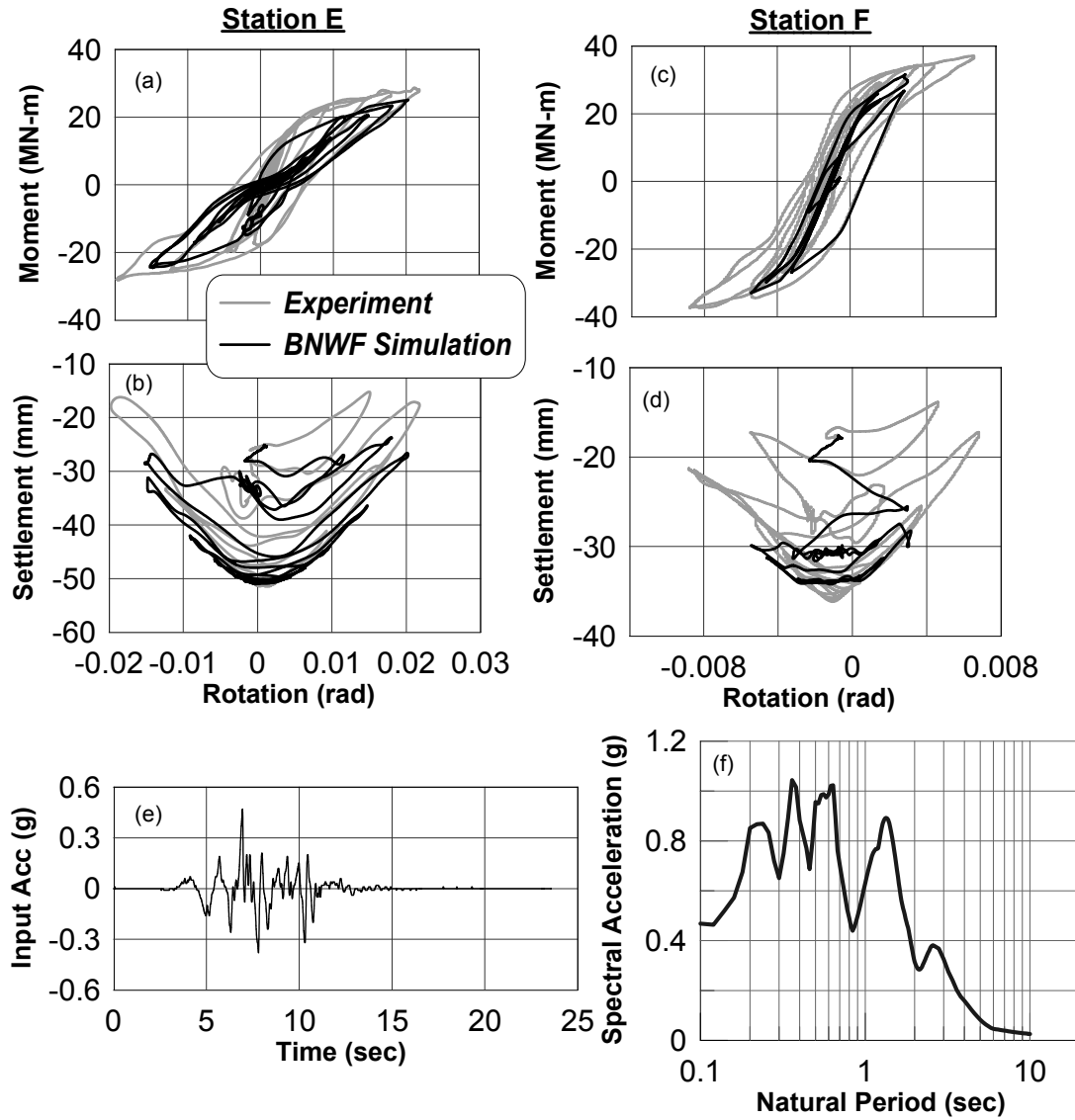


Figure 4.16: (a) Moment–rotation and (b) Settlement–rotation for JAU01–E08, (c) Moment–rotation and (d) Settlement–rotation for JAU01–F08, (e) Acceleration time history and (f) Input motion and acceleration response spectra used in the event

Table 4.6: Summary of bridge comparison results

		Experimental values			BNWF Simulation			Absolute error in BNWF simulation		
Event	Footing width (m)	$ M_{\max} $ (MN-m)	$ \theta_{\max} $ (rad)	$ S_{\max} $ (mm)	$ M_{\max} $ (MN-m)	$ \theta_{\max} $ (rad)	$ S_{\max} $ (mm)	$ \varepsilon_M $ (%)	$ \varepsilon_\theta $ (%)	$ \varepsilon_S $ (%)
JAU01-E05	5.4	14.8	0.0030	4.2	11.1	0.0022	4.0	25	27	5
JAU01-E06	5.4	22.1	0.0093	11.0	16.6	0.0062	8.6	25	33	22
JAU01-E08	5.4	28.7	0.0220	27.0	24.7	0.0174	23.6	14	21	13
JAU01-F05	7.1	19.0	0.0010	3.0	14.1	0.0005	3.4	26	50	13
JAU01-F06	7.1	31.6	0.0040	7.0	23.7	0.0020	11.0	25	50	57
JAU01-F08	7.1	37.4	0.0088	19.0	32.5	0.0057	17.5	13	35	8
MEAN								21	36	20

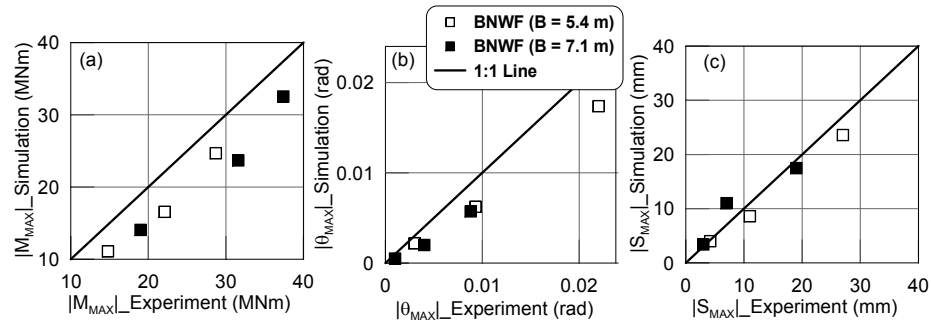


Figure 4.17: Summary of bridge results

4.4 Summary Remarks

- The BNWF model is validated against a set of centrifuge tests on shallow footings. The experiments considered include square and strip footings, bridge and building models, static and dynamic loading, sand and clay tests, a range of vertical factors of safety and a range of aspect ratios.
- Overall, the model compares reasonably well with the experimental results in terms of capturing the shapes of the hysteresis loops and salient features such as maximum moment, shear, rotation and settlement demands.
- However, the moment is under-predicted by the simulation for some of the square footing cases, which may be due to not considering the increase of soil capacity from previous loading cycles and ignoring the side friction at the front of the footing. This under-prediction is less in strip footing cases (building footings) because many of the footings were surface-mounted, therefore side friction provided little contribution to the moment capacity.
- Sliding is under-predicted for all of the cases using the proposed BNWF model.

This under-prediction may be due to inadequate coupling between lateral and vertical springs.

Chapter 5

Parametric Study

5.1 Introduction

To predict the seismic behavior of a shallow foundation using the proposed BNWF model, it is very important to choose the parameters required for the model appropriately. Parameters of particular interest have been studied in Chapter 2. Modeling of any physical process to predict experimentally observed behavior, involves two types of uncertainties; They are (i) model uncertainty and (ii) data uncertainty. The model uncertainty arises mainly due to two reasons. Firstly, a process may be chaotic in nature leading to different outputs in different trials even when the same input is used for all the trials. Secondly, a numerical model may be too simplistic of an approximation to represent the actual physical process involved. Data uncertainty however, involves errors associated with experimental measurements. In this chapter, uncertainty in experimental measurements are ignored due to lack of repeated experiments for the same configuration. However, model uncertainty has been considered by using data from several experiments and taking into account the uncertainty of model parameters.

At first, a parametric study has been performed utilizing a series of experimental data to understand the variability in normalized foundation responses with variation in the values of each of the model parameters. The foundation responses considered in this study include both force and displacement demands (i.e., maximum absolute values). Considered force demands are footing moment and shear, and displacement demands are settlement, sliding and rotation. Each of these responses are normalized by their corresponding experimentally measured values. Experimental data sets are similar (with same additions) to those used in model validation discussed in Chapter 4, i.e. the 20g shallow footing experiments conducted at the University of California, Davis, during the period 2001 to 2006.

Following the parametric study, a sensitivity study has been carried out for each of the normalized responses discussed above. For this purpose, the BNWF model parameters are assumed as Gaussian random variables with truncated negative side distributions (no negative value possible). Sensitivity analyses include the First Order Second Moment (FOSM) method and the Tornado diagram analysis. Finally, a sensitivity analysis is carried out to demonstrate how sensitive each of the model parameters in predicting footing responses when all the above mentioned responses are considered together. To consider all the responses together, L_1 norm error is used. Following sections give the details of experimental data, basis for selection of parametric space, results of parametric study and sensitivity analysis.

5.2 Experimental Data

To understand the effect of model uncertainty on the footing response, a series of centrifuge experiments on shallow footings at UC Davis is considered. The tests considered

have a wide range of static vertical factors of safety (FS_v), footing aspect ratio (B/L), non-dimensional moment-to-shear ratio (M/HL) and depth of embedment (D_f). In addition, some of the tests involved static cyclic loading with varied amplitude, while others used dynamic loading applied by means of base shaking. A total of 14 tests are considered in this study. Details of the tests considered are presented in Table 5.2. The first 8 tests provided in Table 5.2 (i.e., SSG02-02 to SSG04-10) are conducted using strip footings supporting shearwalls. Out of these 8 tests, the first 6 tests are static lateral cyclic and the last 2 are dynamic shakes (using large input motions). The last 6 tests presented in Table 5.2 (i.e., JAU01-E05 to JAU01-F08) are carried out by Ugalde (2007) and they are dynamic shaking tests on shallow square footing supporting bridge pier. In all 14 tests considered in this study, the shallow footings were placed on dense dry Nevada sand with a relative density of 80%. The details of these 14 tests along with schematic diagrams of the experimental setups are given in Chapter 1.

Table 5.1: Test matrix considered for the parametric study (All tests are on dense dry sand with $D_r = 80\%$ and the units are in prototype scale)

Number	Test Name	Loading Type	Reference	Mass (Mg)	L(m)	B(m)	Df/B	FSv	M/(HL)
1	SSG02-02	Static	<i>Gajan et al, 2003a</i>	28	2.8	0.65	0	5.2	0.41
2	SSG02-03	Static	<i>Gajan et al, 2003a</i>	28	2.8	0.65	0	5.2	1.75
3	SSG02-05	Static	<i>Gajan et al, 2003a</i>	58	2.8	0.65	0	2.6	1.72
4	SSG03-02	Static	<i>Gajan et al, 2003b</i>	58	2.8	0.65	0	2.5	0.45
5	SSG03-03	Static	<i>Gajan et al, 2003b</i>	28	2.8	0.65	1	14.0	1.77
6	SSG04-06	Static	<i>Gajan et al, 2006</i>	68	2.8	0.65	0	2.3	1.20
7	SSG03-07	dynamic	<i>Gajan et al, 2003b</i>	58	2.8	0.65	1	7.2	1.80
8	SSG04-10	dynamic	<i>Gajan et al, 2006</i>	36	2.8	0.65	0	4.0	1.80
9	JAU01-E05	dynamic	<i>Ugalde & Kutter, 2007</i>	1100	5.4	5.4	0.3	17.0	2.50
10	JAU01-E06	dynamic	<i>Ugalde & Kutter, 2007</i>	1100	5.4	5.4	0.3	17.0	2.50
11	JAU01-E08	dynamic	<i>Ugalde & Kutter, 2007</i>	1100	5.4	5.4	0.3	17.0	2.50
12	JAU01-F05	dynamic	<i>Ugalde & Kutter, 2007</i>	1172	7.1	7.1	0.24	31.0	1.90
13	JAU01-F06	dynamic	<i>Ugalde & Kutter, 2007</i>	1172	7.1	7.1	0.24	31.0	1.90
14	JAU01-F08	dynamic	<i>Ugalde & Kutter, 2007</i>	1172	7.1	7.1	0.24	31.0	1.90

Figures 5.1(a) to (f) show the input displacements applied at the top of the structures for the first six tests in Table 5.2, respectively. One can observe from Figures 5.1(a)–(f) that, in general, three cycles of a certain amplitude displacement is applied followed by another three cycles of an increased amplitude. In total, an event typically involved three to four amplitude increments. Note that the brief pauses in these will not effect experimental results, as the tests are carried out using dry sand (no pore pressure development) and do not involve inertial load. One can also observe from Figures 5.1(a)–(f) that the displacement history varied from one experiment to another experiment with a maximum amplitude of 40 mm for test SSG02-02 to about 500 mm for test SSG04-06.

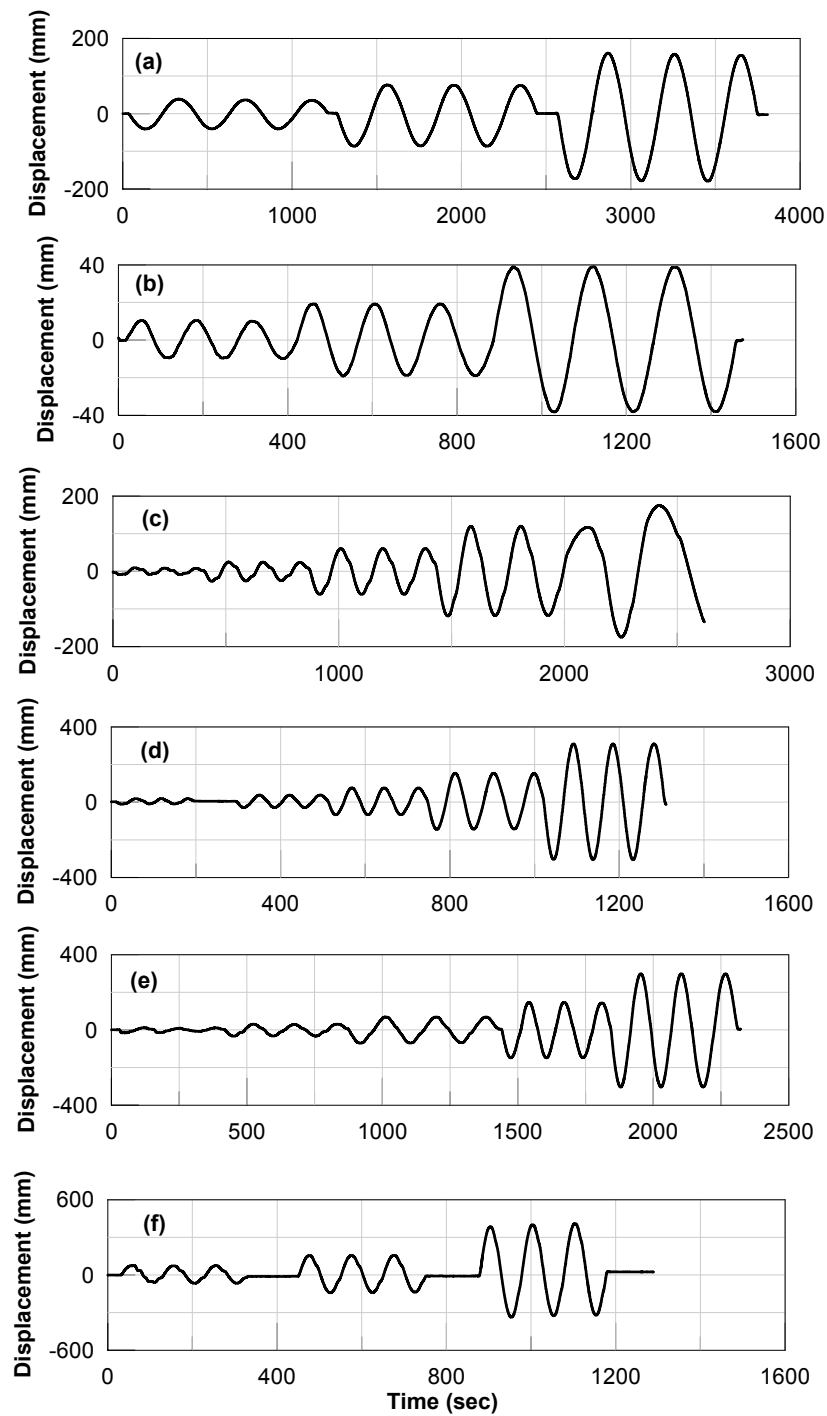


Figure 5.1: Input motions for static tests: (a) SSG02-02 (b) SSG02-03 (c) SSG02-05 (d) SSG03-02 (e) SSG03-03 (f) SSG04-06 (tests by Gajan et al. (2003a,b, 2006))

The input base accelerations for experiments SSG03-07 and SSG04-10 are presented in Figures 5.2(a) and (b), respectively. One can observe from Figures 5.2(a) and (b) that in both cases, ramp-up acceleration time histories are used (i.e., increasing acceleration amplitude). The acceleration time histories for the tests are quite similar with similar frequency content and nearly symmetric amplitudes about the vertical horizontal axis. The maximum recorded input acceleration for these tests is about 0.5 g.

Figures 5.3(a)–(c) show the three input base acceleration time histories used for the last six tests listed in Table 5.2. The acceleration time histories in Figures 5.3(a)–(c) are denoted as Shake-5, Shake-6 and Shake-8, respectively. The peak accelerations for Shake-5 is about 0.07g, for Shake-6 is about 0.25g and for Shake-8 is about 0.45g.

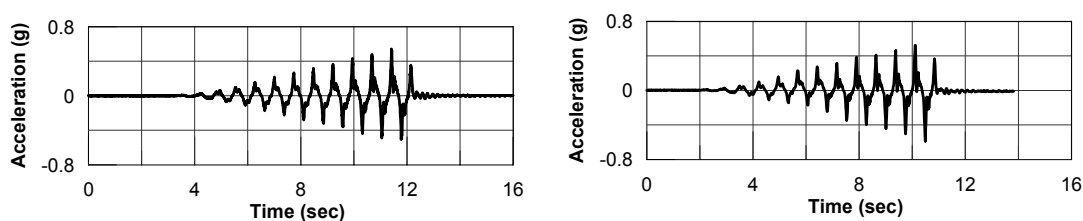


Figure 5.2: Input motions for dynamic tests: (a) SSG03-07 (b) SSG04-10, carried out by Gajan et al. (2003b, 2006)

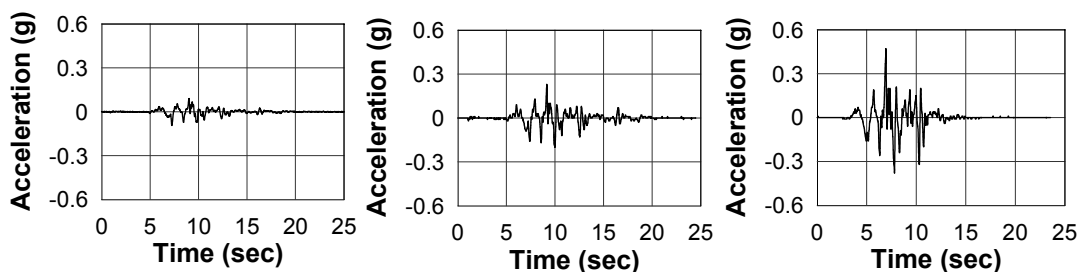


Figure 5.3: Input acceleration time histories: (a) Shake-5 for JAU01-E05 and JAU01-F05 tests, (b) Shake-6 for JAU01-E06 and JAU01-F06 tests, and (c) Shake-8 for JAU01-E08 and JAU01-F08 tests (Ugalde, 2007)

5.3 Selection of Study Parameters

To investigate BNWF model uncertainty, user-selected BNWF model parameters are studied using sensitivity analysis in this chapter. These includes parameters related to basic soil properties along with the parameters involved with BNWF shallow footing mesh properties. Non-user defined (hard-coded) parameters are not considered, as a calibration study on these parameters has been presented in Chapter 3. Also, as the tests considered in this chapter were carried out using dry sand, the model parameters associated with dry sand are the focus in this chapter.

The parameters considered in this analysis are: friction angle, ϕ' , Poisson's ratio ν , Modulus of elasticity of soil E_s , tension capacity TP , end length ratio R_e , stiffness intensity ratio R_k and spring spacing l_e/L . The range of friction angle $\phi' = 38^\circ$ to 42° would commonly be found (for example, Phalen (2003)). The Poisson's ratio ν is selected to range from 0.35 to 0.55 and Modulus of elasticity E_s ranges from 35 MPa to 55 MPa. (EPRI (1990) manual associated with medium to dense sand). The range of tension capacity is taken as a no-tension condition, i.e., $TP = 0\%$ to a maximum uplift capacity of $TP = 10\%$. The end length ratio and stiffness ratio ranges are selected based on Harden et al. (2005) and ATC-40 (1996) recommendations. The end length ratio ranges from no end length (stiffness is equal throughout the length of footing) to an end length ratio of approximately 16% (suggested value by ATC-40 (1996)). The range of stiffness intensity ratio is considered from a uniform distribution i.e., $R_k = 1$, to a stiffness ratio, $R_k = 9$ suggested by ATC-40 (1996) whereas including the R_k values suggested by Harden et al. (2005) between these two extreme values. The spring spacing is considered from 1% to 5%. As it was shown in Chapter 2 (Figure 2.34), that the footing response converges when

a spring spacing of less than or equal to 6% of the footing length is used. Thus, in this study, the range of spring spacings chosen are: 1%, 2%, 3%, 4% and 5%. Table 5.3 shows the parameters and their ranges selected for the sensitivity study.

Table 5.2: Parameter matrix considered for the study

ϕ' (deg)	ν	E_s (MPa)	TP (%)	R_e (%)	R_k	l_e/L (%)
38	0.30	35	0.0	0	1	1
39	0.35	40	2.5	4	3	2
40¹	0.40	45	5.0	8	5	3
41	0.45	50	7.5	12	7	4
42	0.50	55	10.0	16	9	5

¹ default values are shown in grey box, bold text

5.4 Results of Parametric Study

In order to assess the effect of the uncertainty of the input parameters (soil and model) on key response variables, a total of 560 simulations are conducted. For each of the 14 tests and 8 parameters, 5 simulations are performed varying each parameter (5 values for each of them, see Table 5.3), while keeping all other parameters fixed at their default values. The default value of these parameters are the mean values (bold fonts, grey boxed, in Table 5.3). Key response variables are: moment, shear, sliding, settlement and rotation demands (maximum absolute values of each variable). To understand how close these simulated variables are with respect to the corresponding test results, these response variables are normalized by their corresponding experimental value. For example, for test-1, the input motion, which was used for this experiment is applied to the representative BNWF model of a simple shearwall-footing system as used in the experiment, and for a particular set of parameter values, simulated demands are calculated. After all 40 simulations (5

simulations each for 8 parameters) are done for this particular experiment, say i th experiment, the simulated demands for moment $M_{(i,j,k)}^{sim}$, shear $V_{(i,j,k)}^{sim}$, sliding $u_{(i,j,k)}^{sim}$, settlement $S_{(i,j,k)}^{sim}$ and rotation $\theta_{(i,j,k)}^{sim}$ are noted down, where $j = 1, 2, \dots, 8$ and $k = 1, 2, \dots, 5$, respectively, corresponds to each of the eight parameters and five values of each parameters as listed in Table 5.3. Each of these simulated demands are then normalized with respect to the measured demands $M_{(i)}^{exp}$, shear $V_{(i)}^{exp}$, sliding $u_{(i)}^{exp}$, settlement $S_{(i)}^{exp}$ and rotation $\theta_{(i)}^{exp}$ of the i th experiment. Thus, for each experiment, there are 40 simulation results and only one experimental value for each of the five responses. Therefore, normalized maximum absolute moment demand for the k th value of the j th parameter corresponding to the i th test is given by:

$$M_{(i,j,k)}^* = \frac{M_{(i,j,k)}^{sim}}{M_{(i)}^{exp}}, \quad i = 1, 2, \dots, 14; \quad j = 1, 2, \dots, 8; \quad k = 1, 2, \dots, 5 \quad (5.1)$$

Similar expressions are used for shear force, sliding, settlement and rotation. The mean of each normalized demand is then obtained, assuming equal weight to all experiments. For example, the mean normalized maximum absolute moment demand corresponding to k th value of j th parameter is given by:

$$\bar{M}_{(j,k)}^* = \frac{1}{14} \sum_{i=1}^{14} M_{(i,j,k)}^* \quad (5.2)$$

The same procedure is also followed to calculate the mean normalized shear (\bar{V}^*), sliding (\bar{u}^*), settlement (\bar{S}^*) and rotation ($\bar{\theta}^*$) demands.

Table 5.4 shows the experimental demand parameters for each experiment as well as their mean values. The mean values (shown in bold text) are used to normalize the demands obtained from simulations.

The effect of uncertainty of the eight input parameters on the five demand variables

Table 5.3: Experimental Demands

Tests	Moment (MNm)	Shear (MN)	Sliding (mm)	Settlement (mm)	Rotation (rad)
1	186.0	155.0	68.6	125.0	0.01450
2	383.0	71.4	48.1	83.1	0.06290
3	529.8	107.5	23.1	136.6	0.03250
4	305.0	234.0	53.0	240.2	0.01350
5	436.0	83.2	20.8	36.1	0.06263
6	559.5	153.5	54.3	307.5	0.04993
7	527.4	99.5	14.3	88.0	0.02095
8	278.0	53.7	8.8	45.2	0.00945
9	14.8	53.7	8.8	13.9	0.00282
10	22.1	53.7	8.8	13.9	0.00926
11	28.7	53.7	8.8	13.9	0.02179
12	19.0	53.7	8.8	10.5	0.00106
13	31.6	53.7	8.8	10.5	0.00406
14	37.4	53.7	8.8	10.5	0.00880
MEAN	240	91.4	24.5	81.1	0.02244

\bar{M}^* , \bar{V}^* , \bar{u}^* , \bar{S}^* and $\bar{\theta}^*$ has been demonstrated by plotting the variation of the demand variables with the uncertain parameters in Figures 5.4 through 5.12. Figures 5.4(a)–(e) shows the effect of the uncertainty of the friction angle, ϕ' on all five demand parameters. It is observed from Figure 5.4 (a), that the moment demand increases almost linearly with increasing friction angle. The effect of friction angle is pretty significant, as 10% increase in ϕ' increases the moment demand by 27%. This is because with increasing ϕ' , capacity of vertical springs increases as shown in Figure 2.15(a), which increases the overall moment capacity of the system. The same effect can be seen with shear demands. Lateral load bearing capacity of horizontal springs also increases with increasing ϕ' (Figure 2.15b). Figures 5.4(c)–(e) show the effect of ϕ' on the displacement demands of the footing.

To better compare the five new demand parameters with respect to the input parameter ϕ' , the normalized demands are shown in a single plot as shown in Figures 5.5. It is seen from this figure that similar to the moment demand, shear demand is also highly sensitive to ϕ' (increases about 30% for an increase of $\phi' = 38^\circ$ to 42°). As the force demand increases with increasing ϕ' , it may be anticipated that the displacement demand will reduce. Exactly

the same phenomenon is observed here for settlement and rotational demands that decrease as the friction angle increases. An approximately 10% increase in ϕ , results in a reduction of 33% settlement and a 23% rotation. On the contrary, the sliding response seems to increase, which may be due to the fact, that the model remains in the elastic zone in shear-sliding mode (shear capacity is not reached), which makes the sliding increasing with an increase in the shear capacity.

Figure 5.6 shows the effect of uncertainty of Poisson's ratio, ν on the demand variables. It is observed from Figure 5.6, that force demands increase with increasing Poisson's ratio. The amount of increment is not so significant though. With an increase in Poisson's ratio $\nu = 0.3$ to 0.5 (40% increase), the moment demand increases only 7.5%. A similar trend is observed for shear demands, where the shear increases about 5.4% for a 40% increase in ν . For the displacement demands, it is seen that sliding has an increasing trend with increasing Poisson's ratio, while the rotation decreases. Settlement is almost unaffected by the change in Poisson's ratio (changes less than 2% for a change of 40% in Poisson's ratio). This can be explained by observing the effect of Poisson's ratio on vertical and lateral stiffness, respectively. Provided the footing dimensions and Modulus of elasticity of soil are held constant, the vertical and lateral stiffness vary with Poisson's ratio as follows:

$$K_v \propto \frac{1}{(1 - \nu^2)} \quad (5.3)$$

$$K_h \propto \frac{1}{(1 + \nu)(2 - \nu)} \quad (5.4)$$

Figures 5.7(a) and (b) show the dependence of the vertical and lateral stiffness (Gazetas, 1991a), respectively with Poisson's ratio for a strip footing with $B/L \approx 0.3$ and a square

footing. The Modulus of elasticity is fixed at 40 MPa. It is seen from Figures 5.7(a) and (b) that the vertical stiffness K_v has an increasing trend with Poisson's ratio, however, the lateral stiffness K_h has a slightly decreasing trend. This explains the increase in sliding and reduction in settlement and rotation demand with increasing Poisson's ratio. The total increase in sliding is 13%, while the reduction in settlement and rotation are: 4% and 3.3%, respectively.

Figure 5.8 show the effect of uncertainty of Modulus of elasticity E_s on moment, shear, settlement, sliding and rotation demands. It is observed that moment and shear demands have an increasing trend with increasing Modulus of elasticity, while displacement demands have reducing trend with increasing Modulus of elasticity. Increasing E_s increases the vertical and lateral stiffness as shown in Figure 2.19 (in Chapter 2), and thus makes the soil-footing system stiffer and capable of taking more load. For the range of $E_s = 35$ MPa to 55 MPa, both moment and shear demands increase about 13%. Settlement and rotation demands reduce by 8% and 16%, respectively. The relationship between the parameter E_s and the demand variables approximately follow a linear trend.

Figure 5.9 shows the effect of uncertainty in tension capacity TP on the footing demands. It is observed that tension capacity has a highly significant effect on the force and displacement demands. Moment and shear demands increase by about 64% and 77%, respectively, from a no-tension condition to a 10% tension capacity condition. For both cases, it is observed that these demands were under-estimated when no or lower uplift capacities used, approximates to unity were obtained when an uplift capacity of $\approx 5-7\%$ is provided. The force demands tend to be over-estimated when the tension capacity is increased beyond this value.

Of the displacement demands, sliding increases with increasing tension capacity, whereas, settlement and rotation reduces. For sliding demand, initially it remains constant when TP is increased from 0-2.5%, and then it starts increasing drastically. The total increase in sliding demand is about 90% for a change of tension capacity from 0% to 10%. This may be due to the fact that the shear capacity increased, while the shear stiffness is held constant, resulting in an elastic increase in sliding. The settlement demand reduces with increasing uplift capacity. The maximum deviation is very high (about 100%). The best predicted value ($\bar{S}^* \approx 1.0$) occurs at $TP = 3\%$. The rotation demand also has a reducing trend with increasing TP . The maximum deviation with respect to experiments in rotation demand is about 50%. The best predicted value ($\bar{\theta}^* \approx 1.0$) is obtained when the mean value of tension capacity ($TP = 5\%$) is used. For all the demands, the trend of increase or reduction in the demands are linear to moderately non-linear with respect to the input variable TP .

Figure 5.10 shows the effect of uncertainty in end length ratio, R_e on footing demands. The end length ratio is the length at each end as a fraction of total length, where the increased stiffness intensity will apply. It is observed from Figure 5.10 that for this input parameter R_e , all demand variables change in a nonlinear (or may be considered as piecewise linear) fashion. Moment, shear and sliding demands at first decrease with increasing R_e and then start to increase after the mean value ($R_e = 8\%$) is reached. The opposite trend is observed for rotational demand, which increases for the lower R_e value and then reduces beyond the mean value. The settlement demand seems not to change much with R_e (a maximum deviation of only 2% is observed).

Figure 5.11 shows the effect of uncertainty in stiffness intensity ratio (R_K) on footing demands. It is observed that except rotation, all other footing demands decrease slightly

with increase in the stiffness ratio value. The trends are approximately linear. The maximum deviation from experimental mean in moment, shear, sliding, settlement and rotation demands are 12%, 16%, 18%, 12% and 3%, respectively.

It is observed from Figure 5.12 that the spring spacing ratio le/L has a significant effect on the footing demands. With reduction in spring spacing (finer mesh), the moment and shear demands tend to increase, while the settlement and rotational demands tend to decrease. This may be due to the reason that although the total footing capacity and stiffness are kept the same, increasing number of spring along the length actually stiffens the system under this range of loading, thus increasing the force demands, but decreasing the settlement and rotational responses.

The dispersion of the above mentioned parameters considering the 14 test cases are shown in the Appendix A. The tables listing the normalized demand parameters are also given in the same appendix. The normalization for each case is done by the corresponding peak demand value obtained from the experiment.

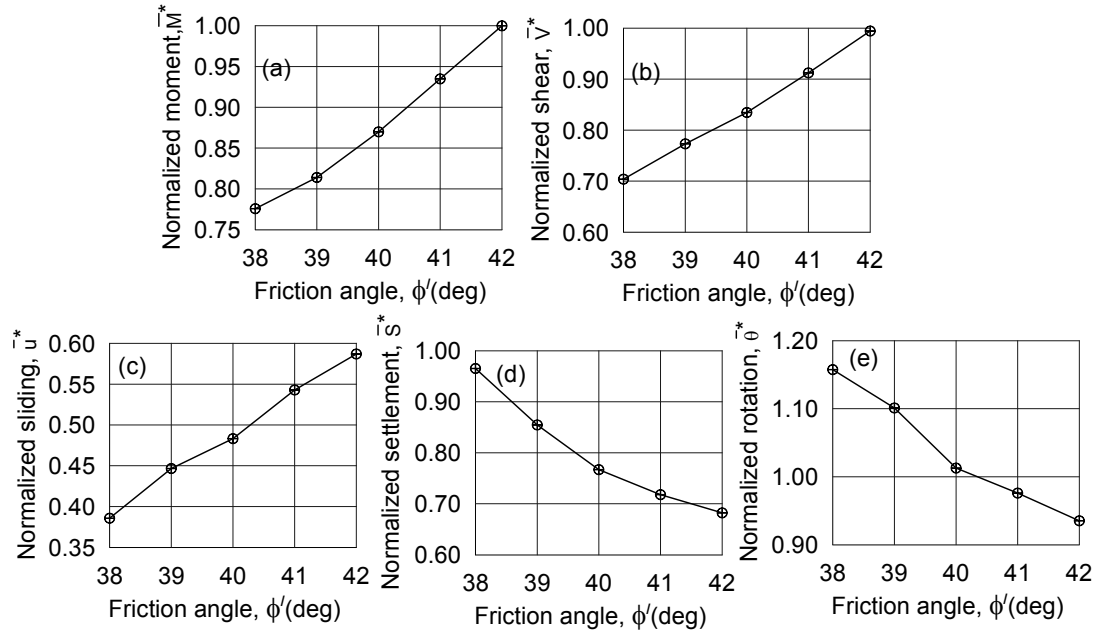


Figure 5.4: Mean normalized demands versus friction angle, ϕ' : (a) moment, (b) shear, (c) sliding, (d) settlement and (e) rotation

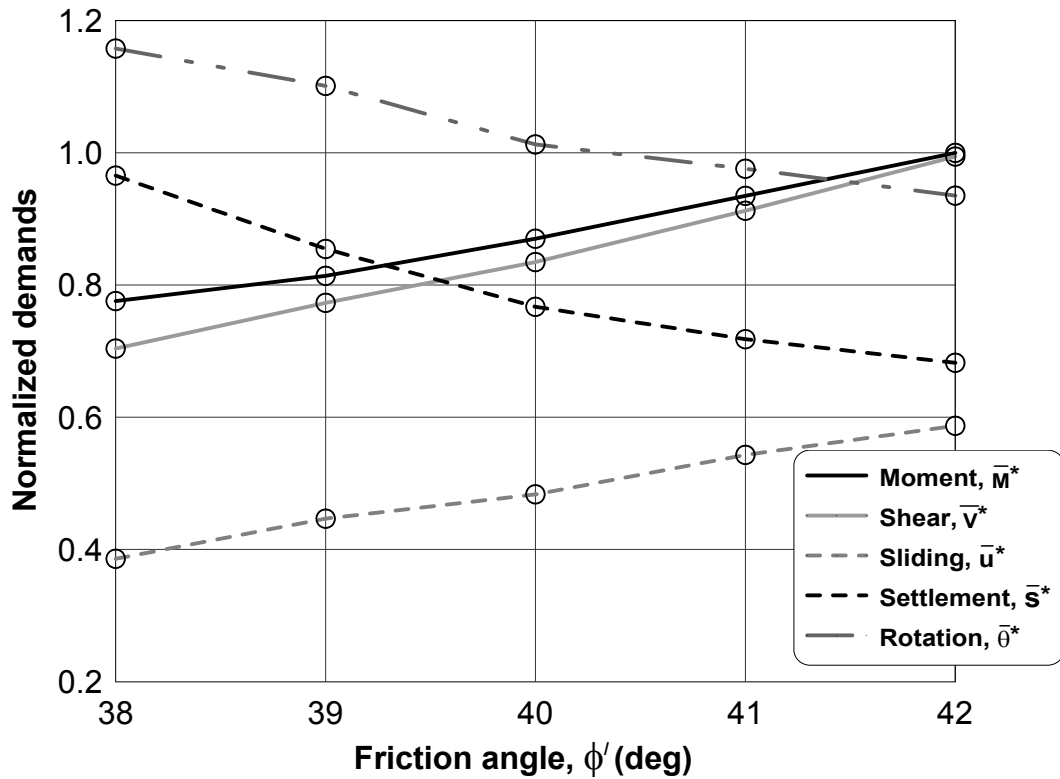


Figure 5.5: Variation of all mean normalized demands with friction angle, ϕ'

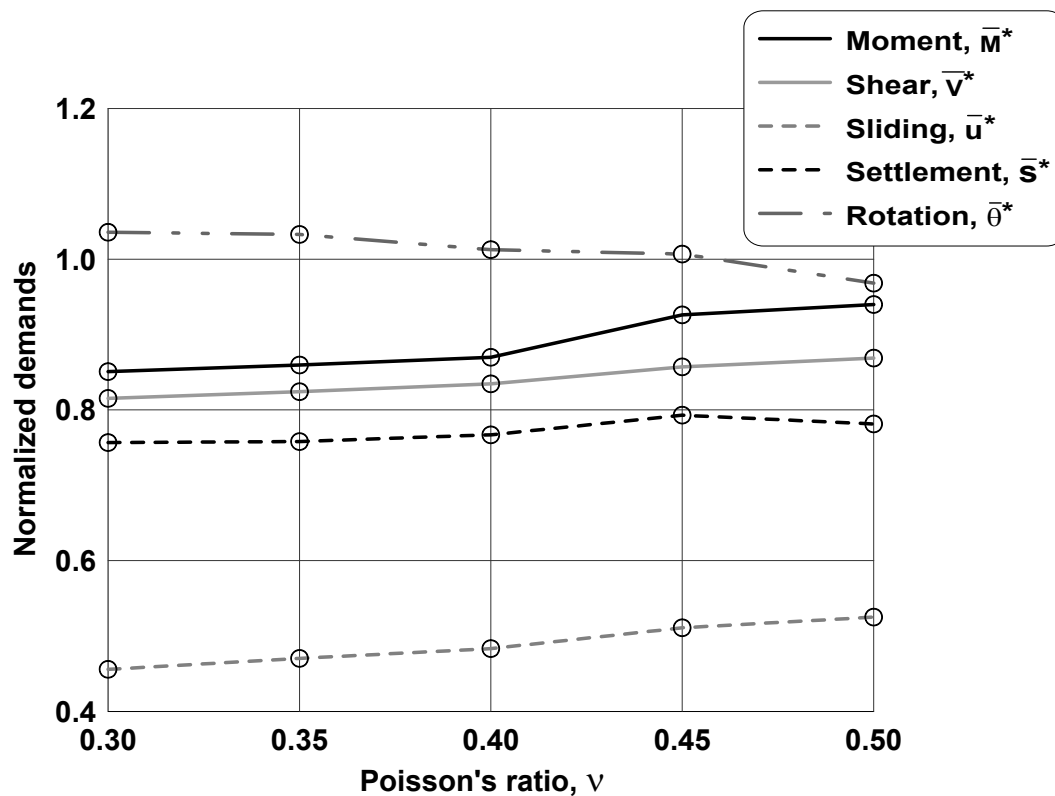


Figure 5.6: Variation of mean normalized demands with Poisson's ratio, ν

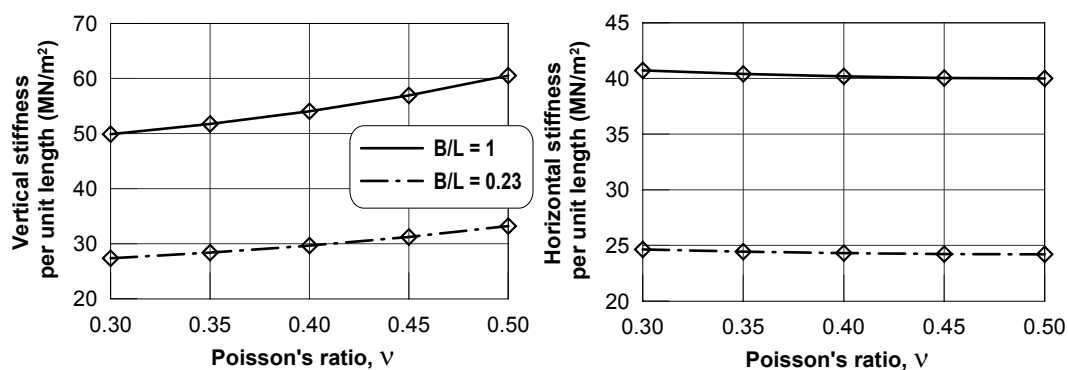


Figure 5.7: Vertical and lateral stiffness variation with Poisson's ratio (stiffness calculated after Gazetas (1991a))

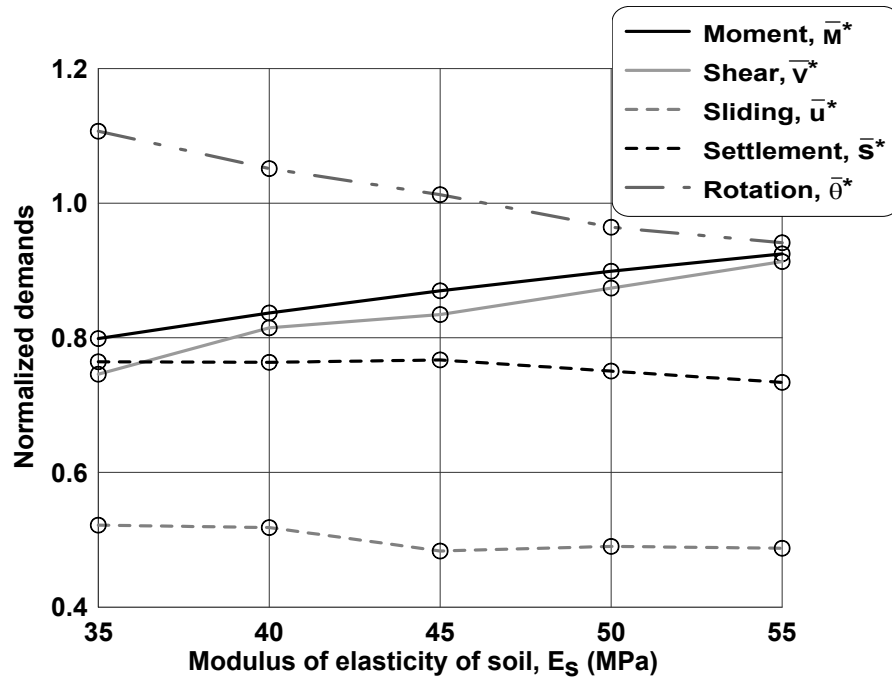


Figure 5.8: Variation of mean normalized demands with Modulus of elasticity, E_s

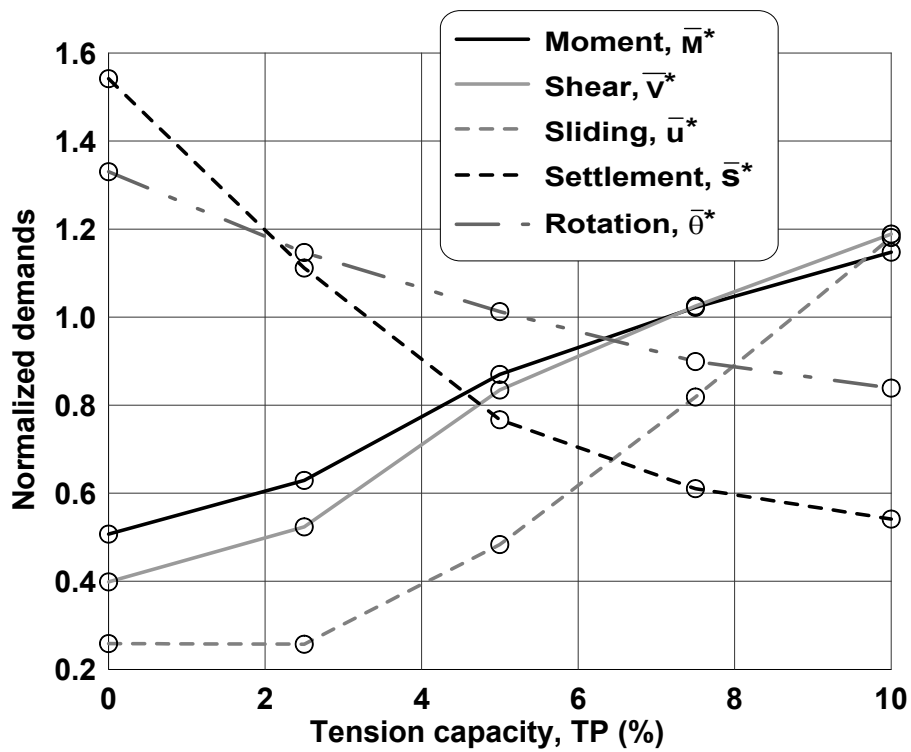


Figure 5.9: Variation of mean normalized demands with tension capacity, TP

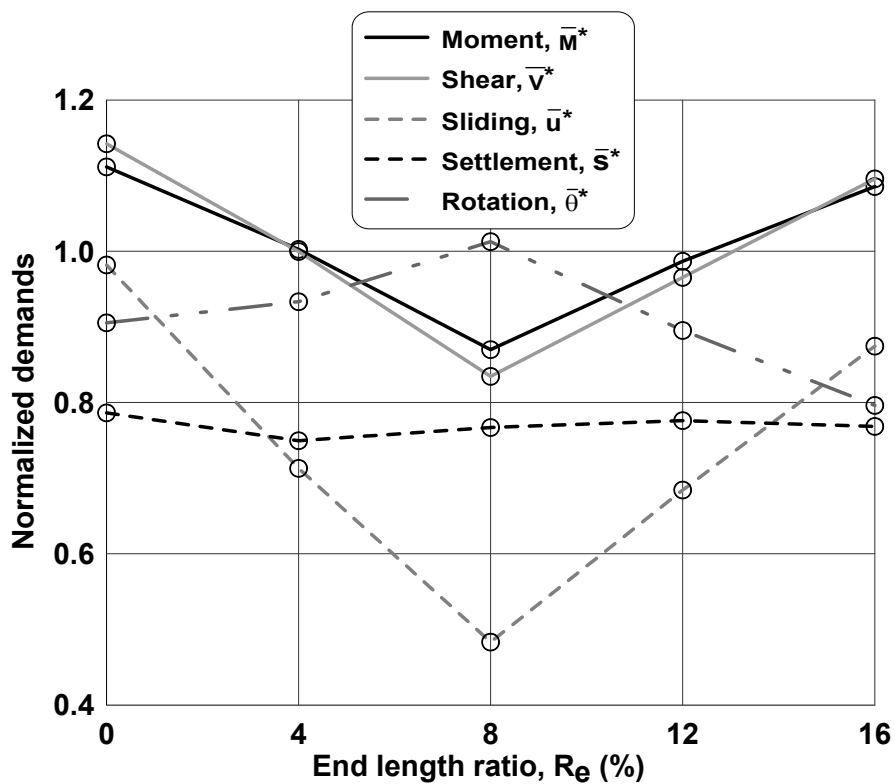


Figure 5.10: Variation of mean normalized demands with end length ratio, R_e

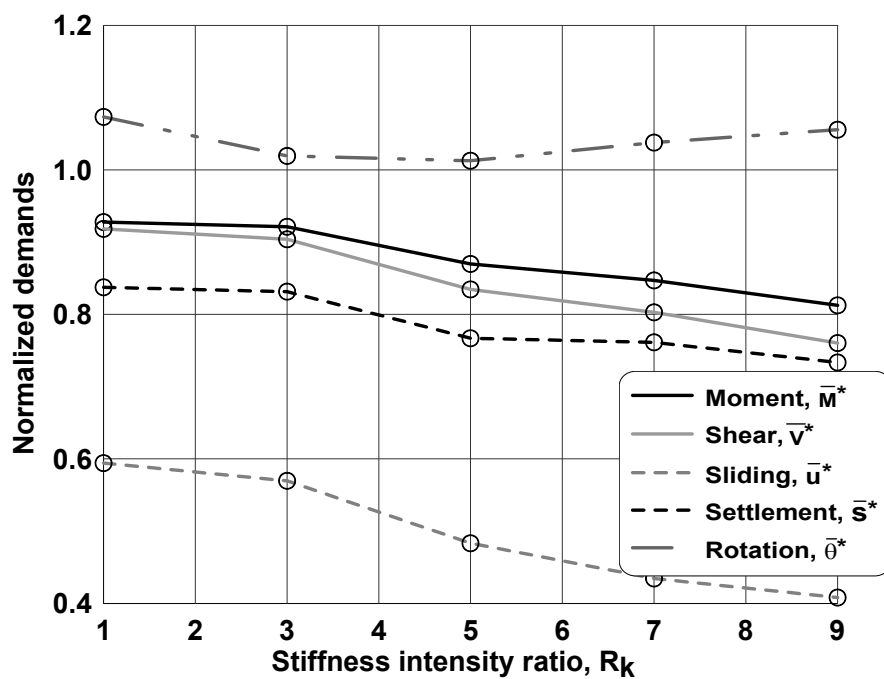


Figure 5.11: Variation of mean normalized demands with stiffness ratio, R_k

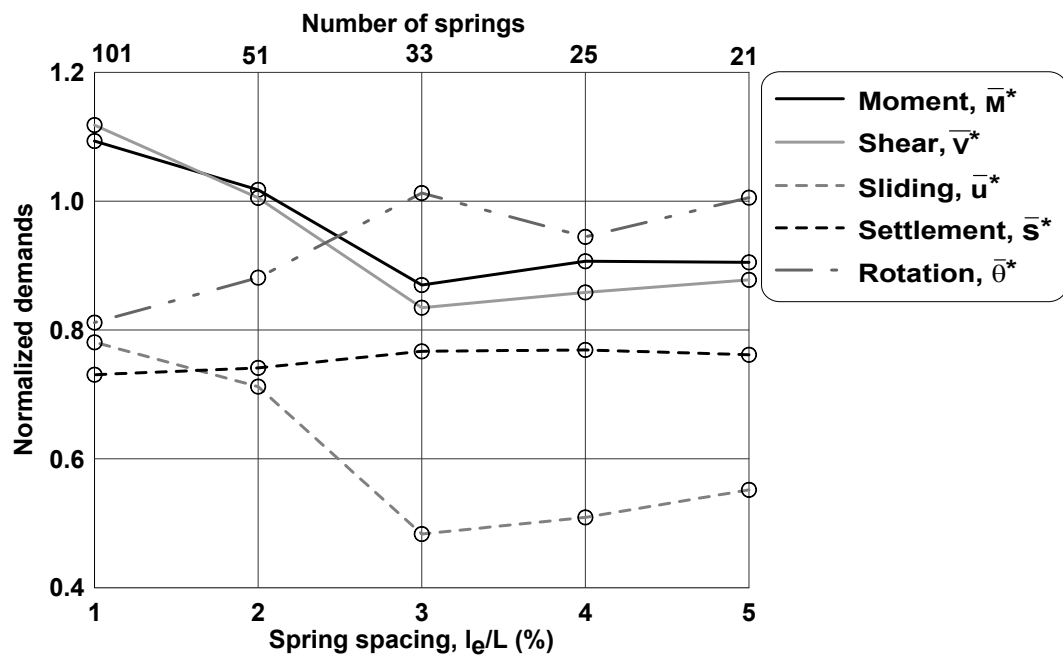


Figure 5.12: Variation of mean normalized demands with spring spacing, l_e/L

5.5 Sensitivity Analysis: Tornado Diagram and FOSM Analysis

Two simple methods, tornado diagrams and First-Order-Second-Moment (FOSM) analyses are used in this study to evaluate the sensitivity of the uncertain input parameters. These two methods provide an approximate sense of the sensitivity of the parameters. For these analyses, the following assumption has been made:

- All uncertain parameters (user defined BNWF model parameters) are assumed to be random variables with a Gaussian distribution, having a truncated negative side distribution.
- All uncertain parameters are assumed to be independent of each other, i.e. the correlation between any two parameters is assumed negligible.
- The upper and lower bounds of the random variables representing these uncertain parameters are assumed to be in 95th and 5th percentile of its probability distribution. This implies that these random variables are known with a 90% confidence interval.
- The relationship between the response variables and the uncertain parameters in question are assumed to be linear or low-to-moderately nonlinear. Although it has been observed in Section 5.4 that some of the footing demands may not be strictly linearly varying with each of the assumed uncertain parameters, in most of the cases approximate linearity holds.

For the tornado diagram analysis, three cases are considered for each parameter, namely, a lower bound case, upper bound and mean value. Assuming a 90% confidence interval

leads to the $\mu + \sigma$ and $\mu - \sigma$, respectively, being the upper and lower bounds of any random variable. If the upper and lower bound values are assumed as L_U and L_L , respectively, then the corresponding mean, μ and standard deviation, σ can be expressed as follows:

$$\mu = \frac{L_L + L_U}{2} \quad (5.5)$$

$$\sigma = \frac{L_L - L_U}{2k} \quad (5.6)$$

where k depends on the level of probability (e.g. $k=1.645$ for a probability of exceedence = 5%).

The absolute difference between the responses corresponding to upper and lower bound parameter values is considered as a swing. The same procedure is followed for all random variables in question. Finally, these swings are plotted in a figure from the top to the bottom in a descending order according to their sizes. This figure, which is called a tornado diagram, demonstrates the relative contribution of each variable to the response under question. The longer swing implies that this corresponding variable has a larger effect on the response than those with a shorter swing. The method described above to create a tornado diagram is followed for all five response variables described in the previous section.

For the FOSM analysis, the response is considered a random variable Z , which has been expressed as a function of the random variables, X_i (for $i = 1 \dots N$) denoting uncertain parameters and Z given by,

$$Z = h(X_1, X_2, \dots, X_N) \quad (5.7)$$

X_i has been characterized by its mean, μ_X and variance σ_X^2 . Now, Z can be expanded using a Taylor series as follows:

$$\begin{aligned} Z &= h(\mu_{X_1}, \mu_{X_2}, \dots, \mu_{X_N}) + \frac{1}{1!} \sum_{i=1}^N (X_i - \mu_{X_i}) \frac{\delta h}{\delta X_i} \\ &+ \frac{1}{2!} \sum_{j=1}^N \sum_{i=1}^N (X_i - \mu_{X_i})(X_j - \mu_{X_j}) \frac{\delta^2 h}{\delta X_i \delta X_j} + \dots \end{aligned} \quad (5.8)$$

Considering only the first order terms of Equation 5.8, and ignoring higher order terms, Z can be approximated as

$$Z \approx h(\mu_{X_1}, \mu_{X_2}, \dots, \mu_{X_N}) + \sum_{i=1}^N (X_i - \mu_{X_i}) \frac{\delta h}{\delta X_i} \quad (5.9)$$

Taking expectation of both sides of Equation 5.7, the mean of Z can be expressed as:

$$\mu_Z = h(\mu_{X_1}, \mu_{X_2}, \dots, \mu_{X_N}) \quad (5.10)$$

Utilizing the second order moment of Z as expressed in Equation 5.9, the variance of Z can be derived as:

$$\begin{aligned} \sigma_Z^2 &\approx \sum_{i=1}^N \sum_{j=1}^N \text{covariance}(X_i, X_j) \frac{\delta h(X_1, X_2, \dots, X_N)}{\delta X_i} \frac{\delta h(X_1, X_2, \dots, X_N)}{\delta X_j} \\ &\approx \sum_{i=1}^N \sigma_{X_i}^2 \left(\frac{\delta h(X_1, X_2, \dots, X_N)}{\delta X_i} \right)^2 \\ &+ \sum_{i=1}^N \sum_{j \neq i}^N \rho_{X_i, X_j} \frac{\delta h(X_1, X_2, \dots, X_N)}{\delta X_i} \frac{\delta h(X_1, X_2, \dots, X_N)}{\delta X_j} \end{aligned} \quad (5.11)$$

where ρ_{X_i, X_j} denotes correlation coefficient for random variables X_i and X_j . The partial derivative of $h(X_1, X_2, \dots, X_N)$ with respect to X_i has been calculated numerically using the finite difference method (central) as follows:

$$\frac{\delta h(X_1, X_2, \dots, X_N)}{\delta X_i} = \frac{h(x_1, x_2, \dots, \mu_i + \Delta x_i, x_N) - h(x_1, x_2, \dots, \mu_i - \Delta x_i, x_N)}{2\Delta x_i} \quad (5.12)$$

In this case, a large number of simulations were performed varying each input parameter individually to approximate the partial derivatives as given in Equation 5.12. The relative variance is calculated for each of the variables for all five response parameters. Table 5.5 shows the results of the approach to determine the relative variance for each parameter for moment demand using the First-Order-Second-Moment method described above. The exact same method is followed to derive the relative variances of parameters for other response variables.

Table 5.4: FOSM analysis for normalized moment demand

Parameters	L_{LX}	L_{UX}	μ_x	σ_x^2	Δ_x	$Z_{\mu+1}$	$Z_{\mu-1}$	$\delta Z/\delta X$	σ_z^2	Relative Variance
ϕ (deg)	38	42	40	1.48	1	0.935	0.814	0.06	0.005	0.075
v	0.3	0.5	0.4	0.004	0.05	0.926	0.86	0.66	0.002	0.022
E (MPa)	35	55	45	36.95	5	0.899	0.837	0.01	0.001	0.020
TP (%)	0	10	5	9.24	2.5	1.022	0.629	0.08	0.057	0.793
Re (%)	0	16	8	23.65	4	0.987	1.002	0.00	0.000	0.001
Rk	1	9	5	5.91	2	0.847	0.921	-0.02	0.002	0.028
le/L (%)	5	1	3	1.48	-1	1.018	0.907	-0.06	0.005	0.063
$\Sigma =$									0.072	1.0

5.5.1 Sensitivity of Each Response Parameter

Figure 5.13 through 5.17 show the tornado diagram analysis for all of the response variables. It is observed from Figure 5.13 that normalized moment is mostly dependant

on tension capacity. Spring spacing, friction angle and stiffness ratio control moment demand moderately. The Modulus of elasticity, end length ratio and Poisson's ratio have little effect on the moment demand. Effect of uncertainty of the parameters on shear demand is very similar to that observed from the moment demand. Shear demand is highly sensitive to tension capacity, spring spacing and stiffness ratio; moderately sensitive to friction angle and Modulus of elasticity and least sensitive to Poisson's ratio. Sliding, Settlement and rotation are also mostly dependent on tension capacity and least dependent on Poisson's ratio. Note that although the tension capacity of sand is generally considered as an unimportant parameter, it is found to be the most sensitive to all the demands considered herein. This may be due to the fact that in comparison with the change (between lower and upper limits) in all other parameters considered in Table 5.3, a 10% change in the tension capacity results in the maximum change in the overall rotational stiffness and moment capacity of this foundation. While a change in the moment capacity and rotational stiffness of the foundation can result in a change in the moment, settlement and rotation demands, a change in the rotational stiffness results in a change in the shear and sliding demands. This is because, the point of application of the resultant lateral force for this case is at a higher location from the center of the foundation and a change in the moment demand attributes to a change in the resultant lateral force. From this set of figures (Figure 5.13– 5.17), it is also observed by looking at the skewness of swings with respect to the mean normalized demands (represented by vertical line) that the relation between the five demand variables and some of the parameters considered here (e.g., R_e) is highly nonlinear. This observation confirms the results presented in terms of normalized demands versus uncertain variables.

Figure 5.18 through 5.22 show the results from First-Order-Second-Moment analysis.

The relative variances are shown for all the parameters for each decision variable. The greater the relative variance for a parameter, the higher the sensitivity of that parameter on the response variable. Trends from the FOSM analysis confirms the results of the tornado diagram analysis. The relative contribution of tension capacity is highest compared to that of other parameters. Poisson's ratio seems to have effectively no effect compared to other parameters on all the responses. Other parameters such as end length ratio, spring spacing, stiffness ratio and Modulus of elasticity of soil have moderate effect on the responses.

Since this analyses are done on a set of tests performed on sand bed, and sand generally does not have significant amount of tension capacity, a revised set of analysis is also done, where the tension is held constant. This set of analyses shows the relative effect of all other parameters when the effect of tension capacity is ignored. Figure 5.23 through 5.27 show the sensitivity of parameters on footing force and displacement demands while keeping the tension capacity constant (at a value of 5%). It is observed that friction angle is mostly controlling the moment, shear, settlement, sliding and rotational responses when tension capacity is not varied.

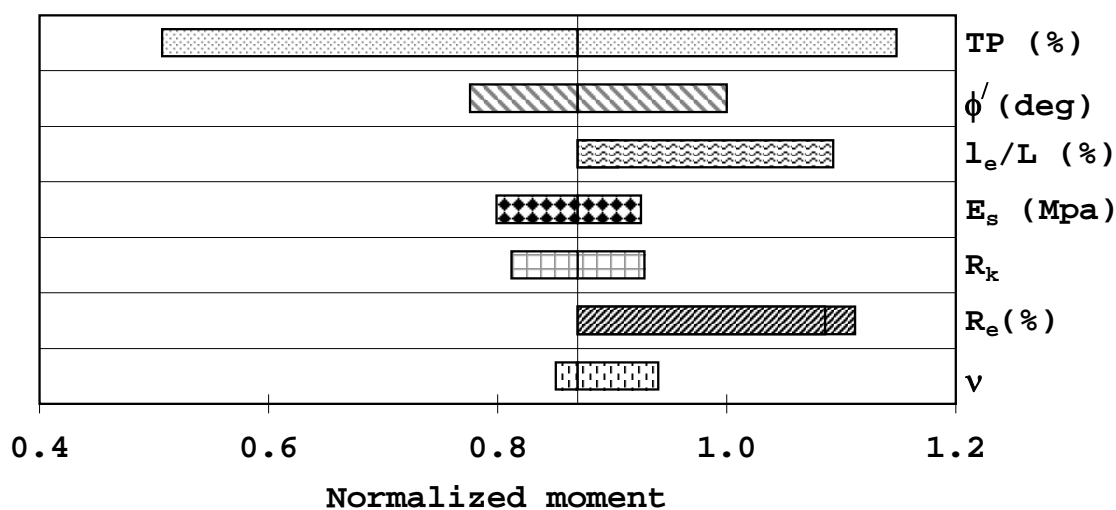


Figure 5.13: Tornado diagram for normalized moment demand

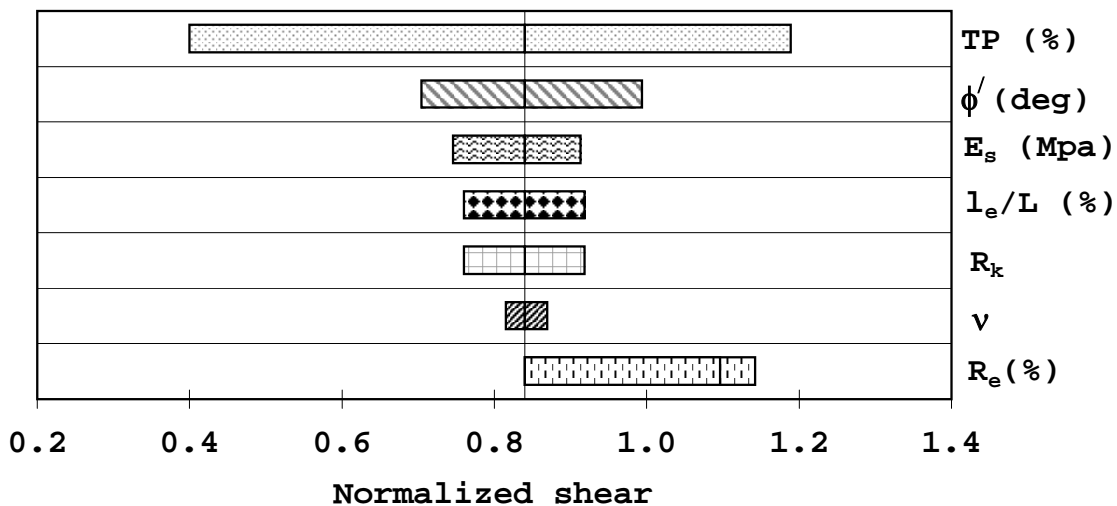


Figure 5.14: Tornado diagram for normalized shear demand

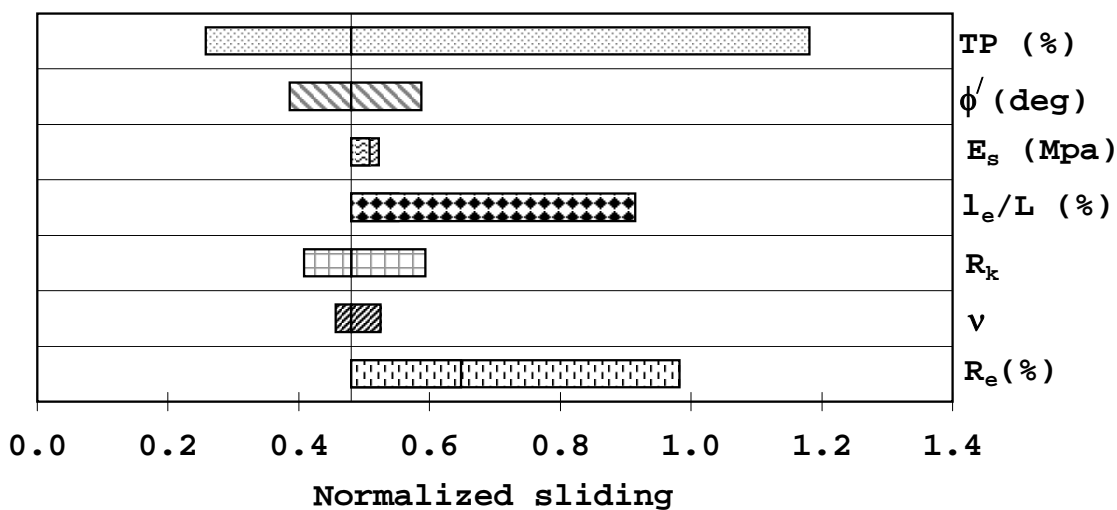


Figure 5.15: Tornado diagram for normalized sliding demand

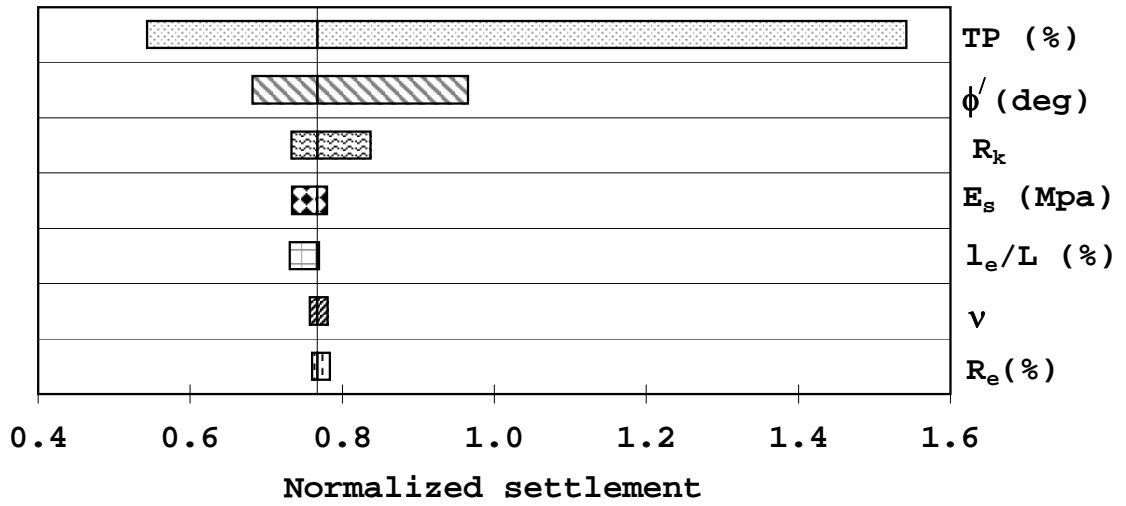


Figure 5.16: Tornado diagram for normalized settlement demand

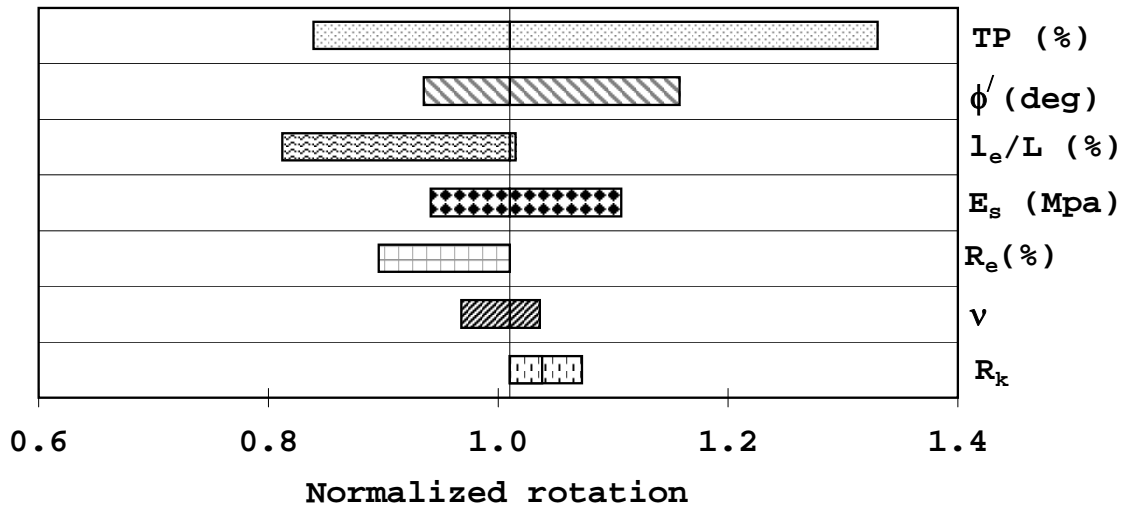


Figure 5.17: Tornado diagram for normalized rotation demand

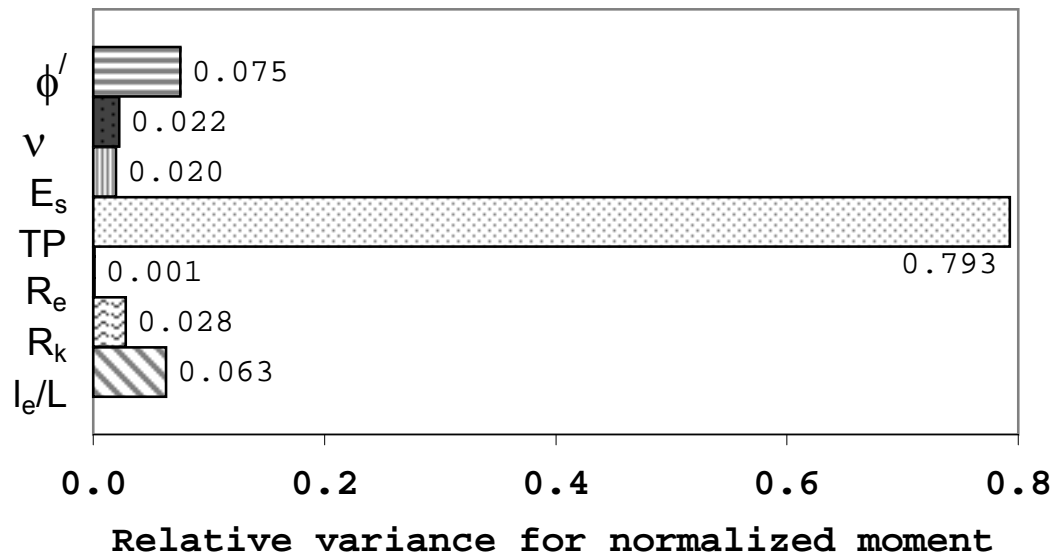


Figure 5.18: Relative variance contribution for normalized moment demand from FOSM analysis

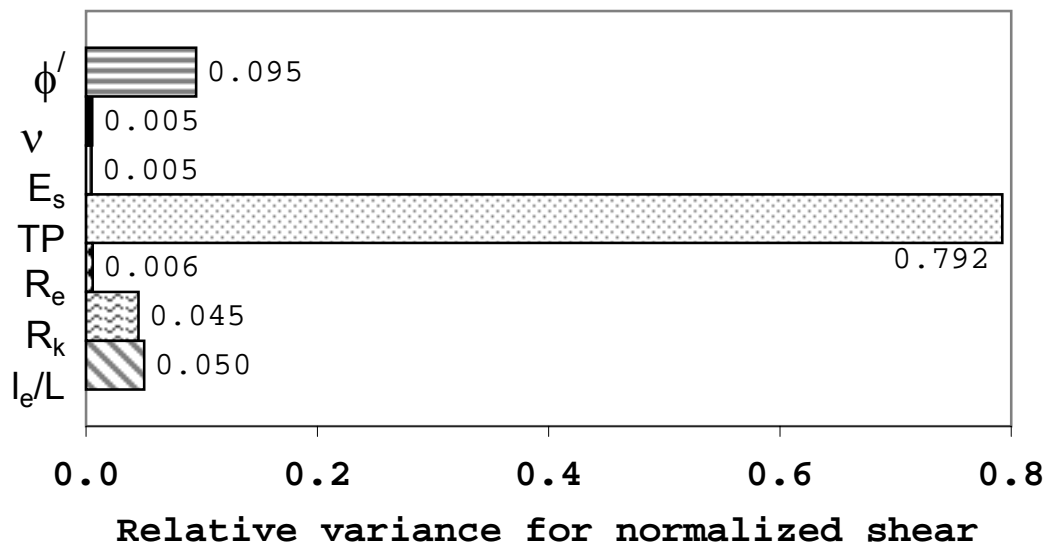


Figure 5.19: Relative variance contribution for normalized shear demand from FOSM analysis

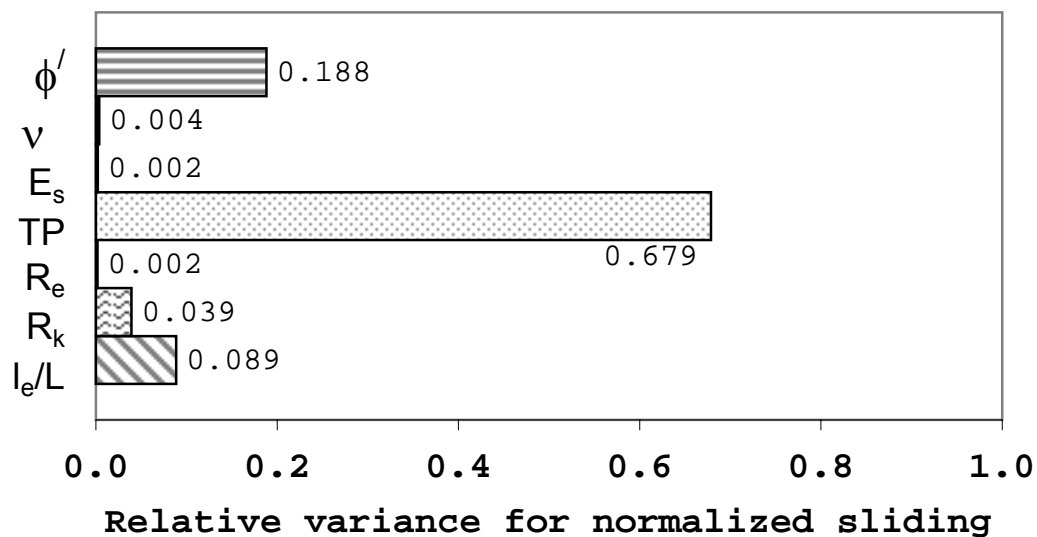


Figure 5.20: Relative variance contribution for normalized sliding demand from FOSM analysis

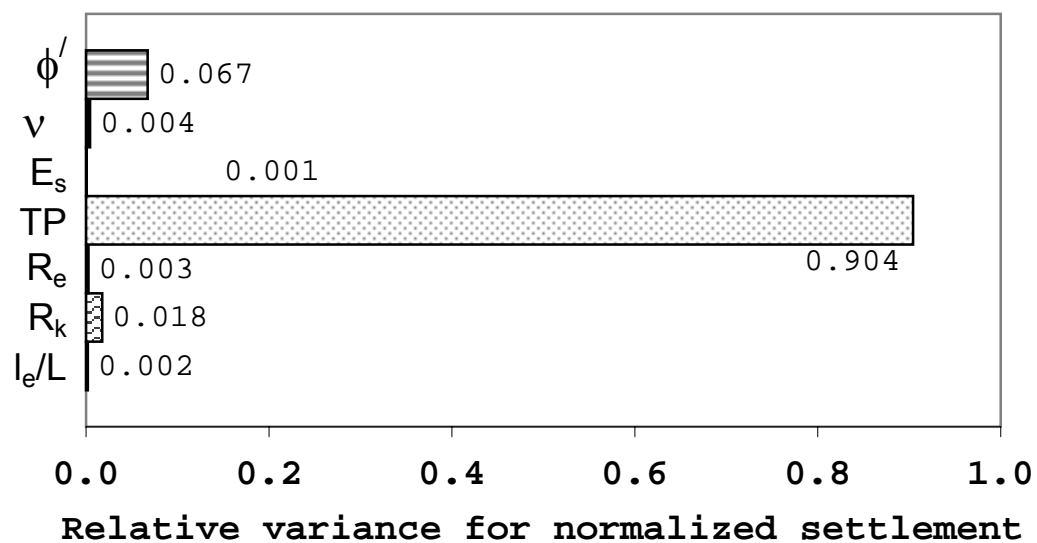


Figure 5.21: Relative variance contribution for normalized settlement demand from FOSM analysis

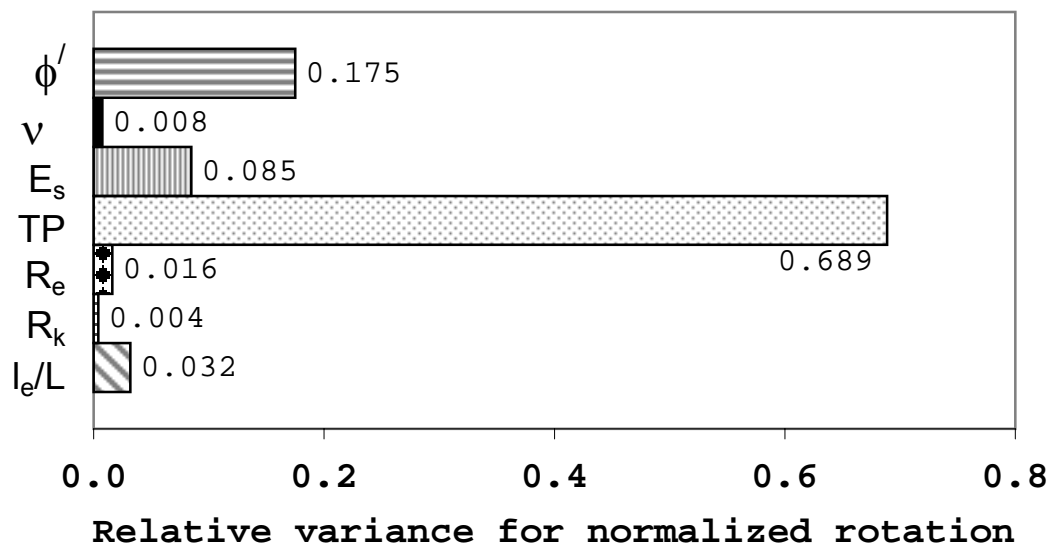


Figure 5.22: Relative variance contribution for normalized rotation demand from FOSM analysis

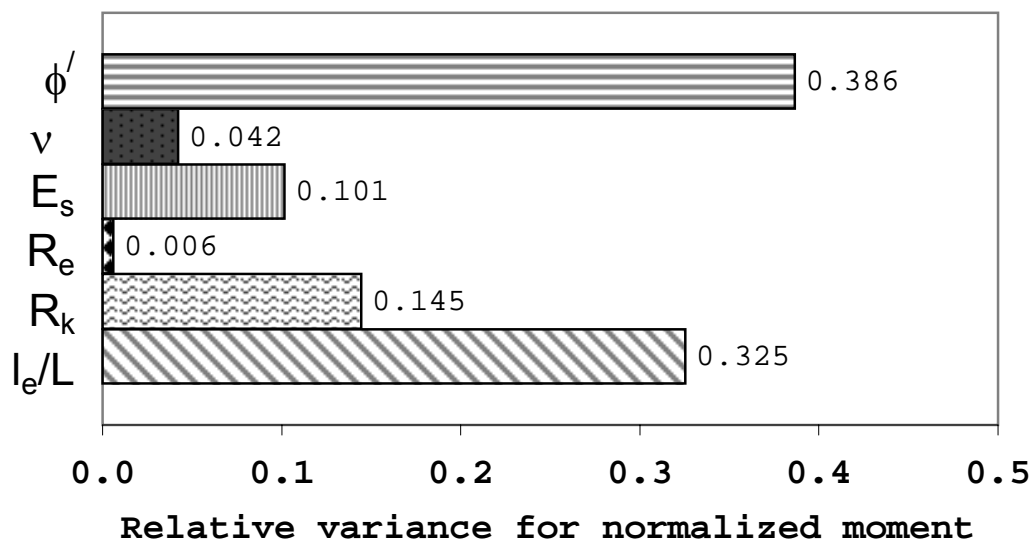


Figure 5.23: Relative variance contribution for normalized moment demand from FOSM analysis (keeping TP constant)

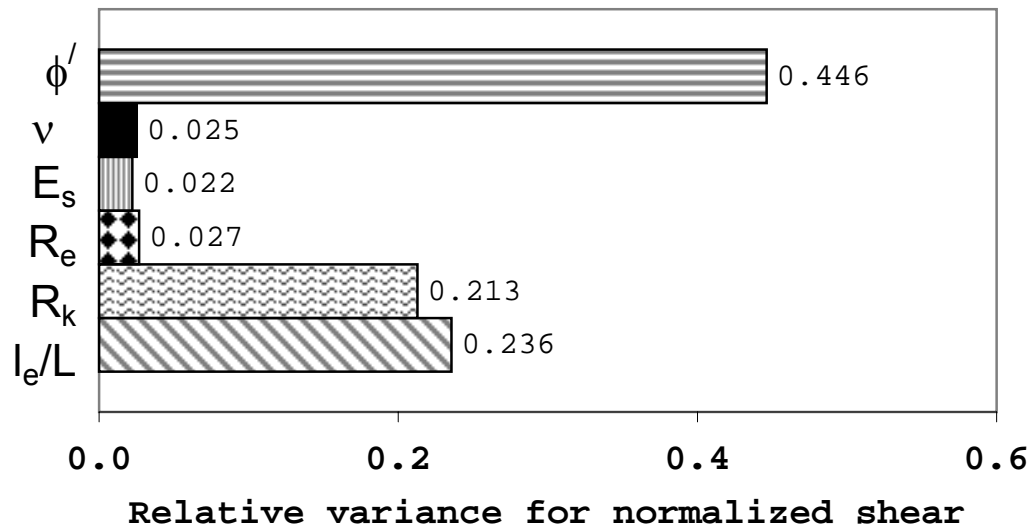


Figure 5.24: Relative variance contribution for normalized shear demand from FOSM analysis (keeping TP constant)

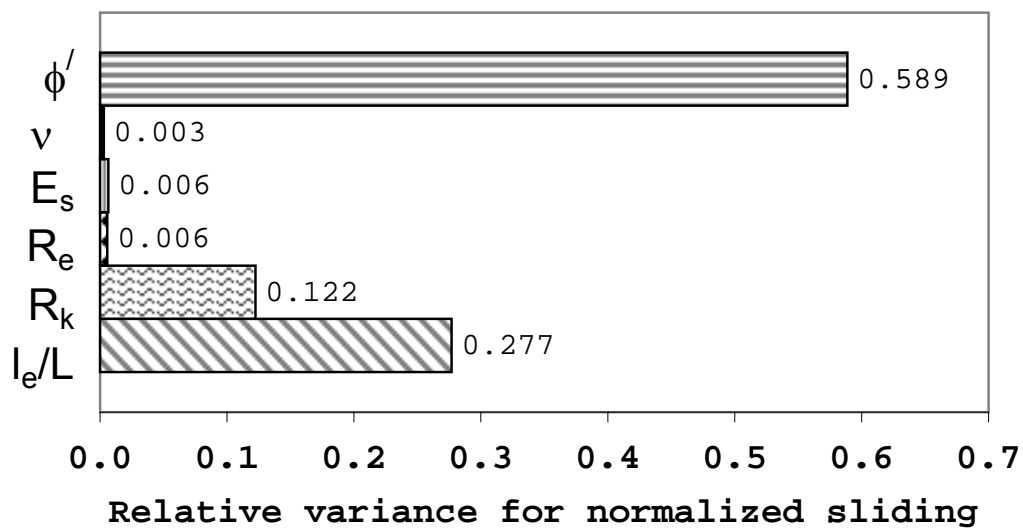


Figure 5.25: Relative variance contribution for normalized sliding demand from FOSM analysis (keeping TP constant)

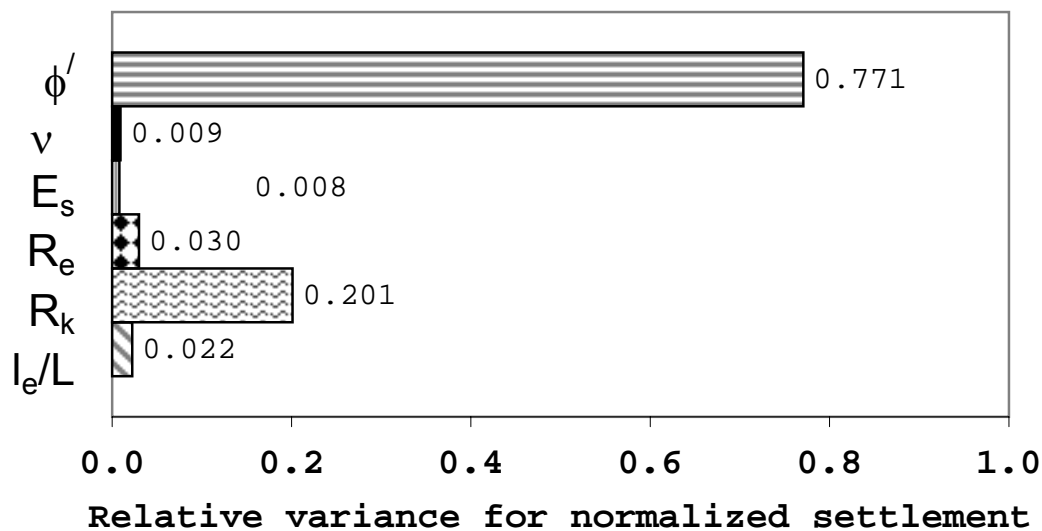


Figure 5.26: Relative variance contribution for normalized settlement demand from FOSM analysis (keeping TP constant)

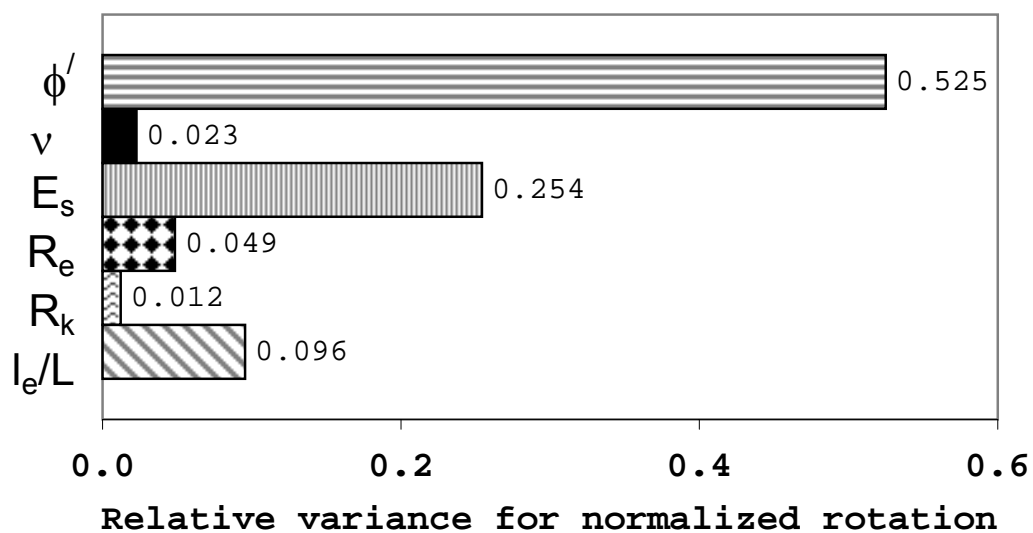


Figure 5.27: Relative variance contribution for normalized rotation demand from FOSM analysis (keeping TP constant)

5.5.2 Sensitivity of Overall Footing Response

The L^1 relative norm error is used to evaluate the error of the simulation compared to the experiments, when all experiments are given equal weight. In this study, L^1 norm relative error is calculated considering all 14 tests, for all parameters and all decision variables. The L^1 relative norm error can be expressed as:

$$e_{L^1} = \frac{1}{N} \sum_{i=1}^N \frac{|u_{(i)}^{sim} - u_{(i)}^{exp}|}{|u_{(i)}^{exp}|} \quad (5.13)$$

where N = number of experiments considered (=14 in this case), $u_{(i)}^{sim}$ = value of decision variable from the simulation (max moment, max shear etc.) for i th experiment, $u_{(i)}^{exp}$ = value of the same decision variable from the same experiment.

In order to express the error associated with all the demand parameters (moment, shear etc.) using a single parameter, the term overall relative norm error is introduced here. In absence of specific relative importance of these five demand variables, the overall relative norm error is calculated as follows:

$$e_{L^1} = \frac{1}{5}(e_{ML^1} + e_{VL^1} + e_{uL^1} + e_{SL^1} + e_{\theta L^1}) \quad (5.14)$$

where $e_{ML^1} = L^1$ norm relative error for the moment demand, $e_{VL^1} = L^1$ norm relative error for the shear demand, $e_{uL^1} = L^1$ norm relative error for the sliding demand, $e_{SL^1} = L^1$ norm relative error for the settlement demand, $e_{\theta L^1} = L^1$ norm relative error for the rotation demand.

Figure 5.28 shows the sensitivity on overall norm relative error. It is observed from Figure 5.28, that the overall norm relative error is within 48% for all the variables, except

for tension capacity, TP , where the error deviates from 40% to 90%. It can also be seen from Figure 5.28 that the overall error is highly dependant on the input parameter values.

Since it can be seen from Figure 5.28, that the overall error parameters vary moderate to highly nonlinearly with the input parameters, the tornado diagram analysis is not done for this case. However, to show the effect of each parameter sensitivity on the overall error in footing response, FOSM analysis is conducted and presented in Figure 5.29. It can be seen that the overall error in predicting footing response is also mostly sensitive to the tension capacity (with a relative variance of 78%). In case, one ignores the tension capacity as an important parameter, friction angle is most important as shown in Figure 5.30.

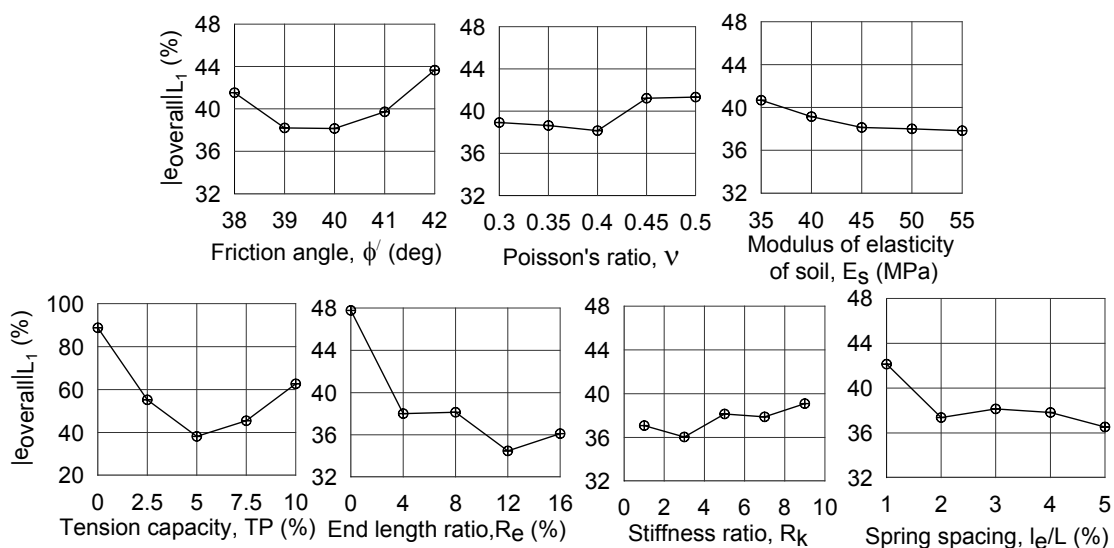


Figure 5.28: Sensitivity of overall norm relative error

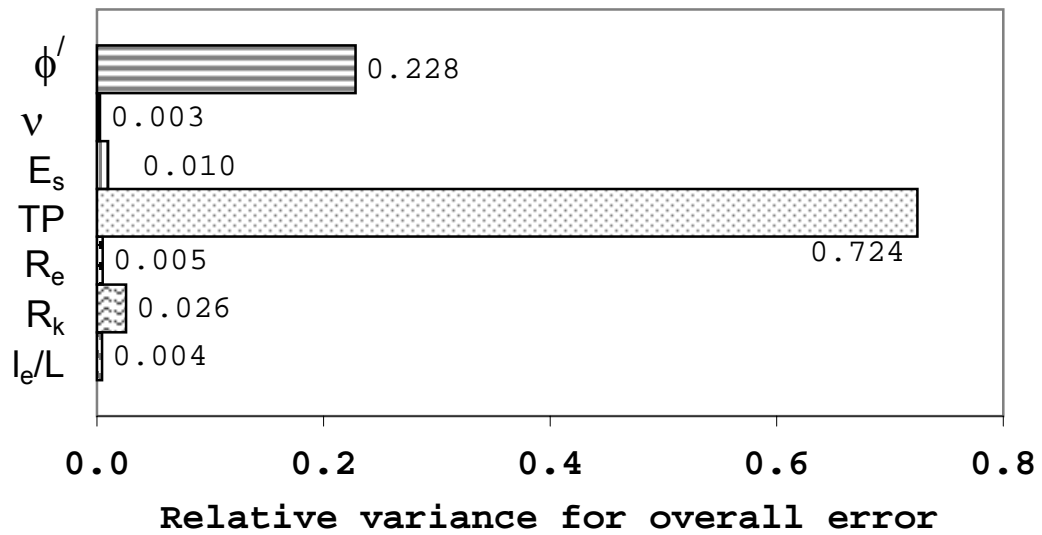


Figure 5.29: Relative variance contribution for overall norm relative error from FOSM analysis

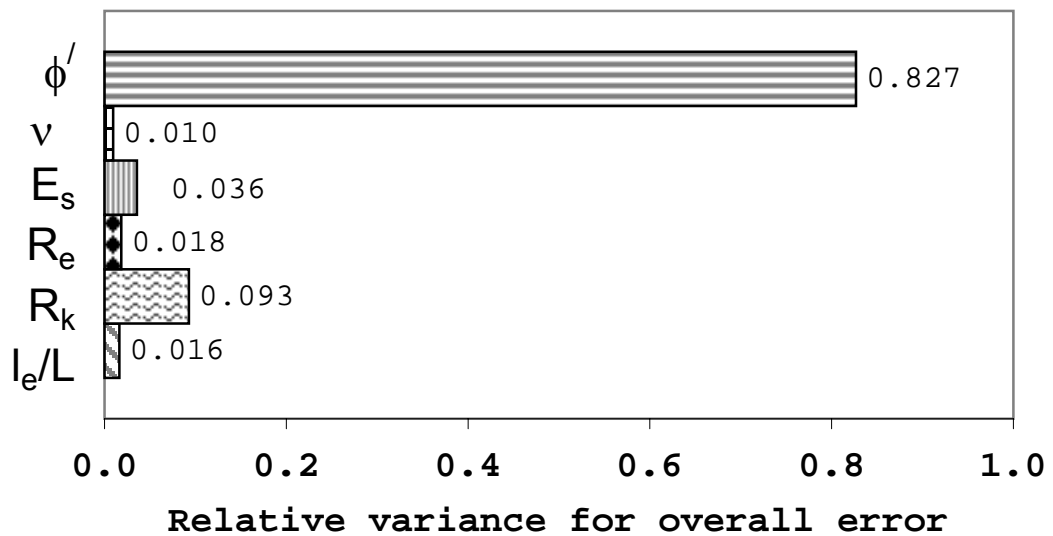


Figure 5.30: Relative variance contribution for overall norm relative error ignoring tension capacity

5.6 Summary Remarks

A sensitivity study has been conducted to better understand the effect of the parameters on the footing responses based on a series of centrifuge test data. Following observations are made:

- It is observed that tension capacity has the most sensitivity on force and displacement demands.
- Other parameters having significant effect on the footing response are: stiffness intensity, end length ratio, friction angle and spring spacing. Poisson's ratio seems to have least effect on the footing response.
- The L^1 relative norm error with respect to the experimental results is calculated and it is found that the error is also most sensitive to the tension capacity.
- If the uncertainty in tension capacity is ignored (for a typical sand case), it is observed that friction angle is the most important parameter to control the force and displacement demands.

Chapter 6

Effect of SFSI on Shearwall Buildings

6.1 Introduction

In this chapter, the effect of soil-foundation-structure-interaction (SFSI) of shearwall buildings resting on a shallow rectangular footing is investigated using the previously described shallow foundation BNWF model. For this purpose, a typical benchmark shearwall building designed by a group within PEER (Pacific Earthquake Engineering Research Center) is used. The footing was designed for a combination of gravity lateral seismic forces as prescribed in the Uniform Building Code (1997). An interior shearwall-footing region of the benchmark building is extracted and studied in detail (as shown in Figures 6.1). Additionally, two more structural configurations are also considered to study the effect of SFSI on shearwall buildings with different attributes (Figures 6.2). The four-story model was developed first. It includes core consisting of four concrete shear walls to carry all lateral loads and vertical loads within the tributary area (Figures 6.1). All three structures considered in this study are different with respect to their story heights, aspect ratios and number of stories. However, all of them are supported by the same spread footing with

the same soil underneath. The details of the structures used, soil and modeling properties, loading protocols, selection of ground motions and effect of SFSI on seismic responses are discussed in the following sections.

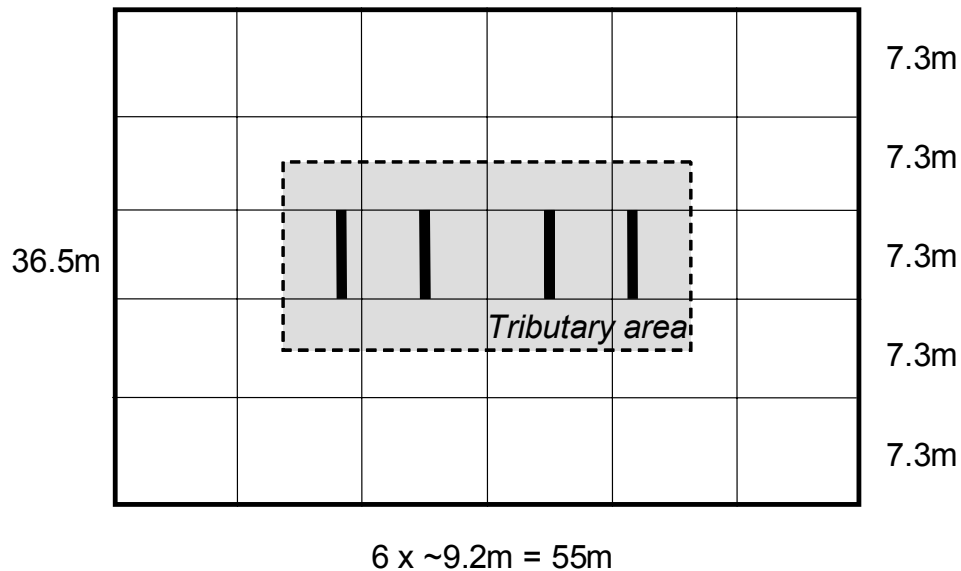


Figure 6.1: Plan view of the benchmark structure with shear walls considered in OpenSees simulations. Tributary area for the vertical loads carried by the wall footings is shown in grey (adapted from Gajan et al. (2008))

6.2 Description of Structures

Figures 6.2(a)–(c) show the elevation and plan of three building models. Each model has a concrete shear wall, the height of which varies to represent different height of buildings. All of the models are supported by rectangular footings of same size and properties. Table 6.1 presents some important properties of the buildings including total weight and seismic mass applied at each floor level. Note that the total weight of each structure is calculated based on the tributary contribution from the whole building.

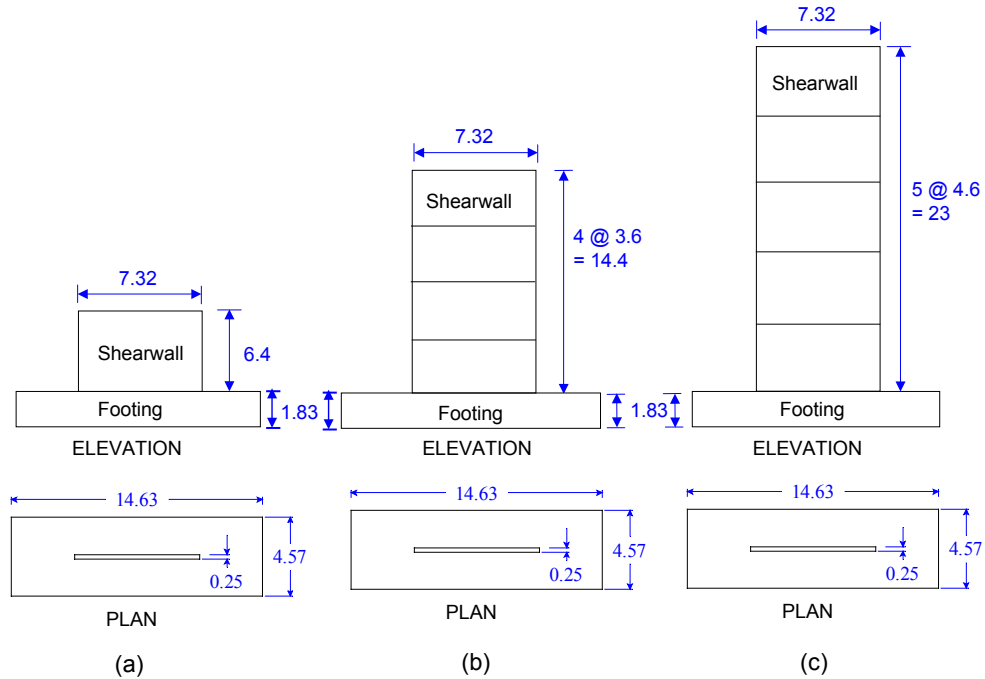


Figure 6.2: Geometry and dimensions of the shearwall-footing models (units in m): (a) 1-story building, (b) 4-story building, (c) 5-story building

Table 6.1: Properties of three models considered in this study

Model	Total height (m)	No of stories	Total weight (MN)	Seismic mass applied at each floor ($\times 10^5$ kg)	Vertical factor of safety, FS_v
1-story	6.4	1	6.34	6.46	4.8
4-story	14.4	4	14.68	3.75	3.2
5-story	23	5	13.35	2.72	2.6

6.3 Footing and Soil Conditions

The same footing is used for all of the structures. The footing is a spread foundation resting on medium clay. The plan dimension of the footing is 14.6m x 4.37m, and the height of the footing is 1.82 m as shown in Figure 6.2. The footing is assumed to be resting on the ground surface, i.e., no embedment is considered. The soil under all of the

structures is undrained clay with an undrained shear strength, $c_u = 52$ kPa, shear modulus, $G = 26$ MPa and a Poisson's ratio, $\nu = 0.5$. Based on the self weight of each model and soil properties, and using conventional bearing capacity equations, the static vertical factors of safety of all of the foundations is calculated as 4.8, 3.1 and 2.6 for 1-story, 4-story, and 5-story building models, respectively. Vertical and sliding stiffness for all of the structures are selected based on recommendations by Gazetas (1991a), while vertical load bearing capacity is calculated after Terzaghi (1943) when using foundation shape and depth factors proposed by Meyerhof (1963). Tension capacity of the soil is considered as 10% of q_{ult} is assumed for soil modeling. Table 6.2 shows the derived capacity and stiffness parameters of the foundations of three models. One can observe from Table 6.2 that the vertical stiffness K_x is slightly higher than the lateral stiffness K_v , while the vertical capacity Q_{ult} is almost five times higher than the lateral capacity T_{ult} . The elastic beam column element of the footing is considered to have an EI value of $2.1e10$ N-m² and $2.45e12$ N-m², respectively.

Table 6.2: Derived capacity and stiffness of the foundation

Vertical capacity, Q_{ult} (MN)	Lateral capacity, T_{ult} (MN)	Vertical stiffness, K_v (MN/m)	Lateral stiffness, K_x (MN/m)
18.11	3.32	814	750

6.4 Numerical Modeling

Numerical models of all three structures shown in Figure 6.2 are developed in OpenSees (OpenSees, 2008). Each OpenSees model consists of an idealized 2-dimensional lumped mass model with nodes at each floor level and elastic beam-column elements joining the nodes. The shallow foundation is modeled using proposed BNWF model. Figure 6.3 shows the numerical representation of the four-story building. A total of 60 elastic beam-column elements and 62 zero length springs (i.e. a total number of 61 zero-length vertical springs at a spacing of 2% of the total length and one lateral spring) are used to model the footing and footing-soil interface, respectively. Since the buildings are surface resting, there is no passive resistance. The middle region stiffness of the vertical springs is 3 times smaller than that of the end region of vertical springs, which extends across a distance of 12% of total length laterally from the edge of the footing (symmetrically) inward. A tension capacity of 10% of ultimate load is provided. Since the energy dissipated through hysteretic behavior is the primary focus of the study, a small value of viscous damping is added to account for the radiation damping.

6.4.1 Types of Input Loads

All of the buildings are subjected to gravity load due to self weight and lateral loads. The following analysis cases are performed:

1. Gravity analysis - Self weight is applied in 10 equal load steps. This is a static analysis. This step is a common first step to all subsequent load applications.
2. Pushover analysis - After applying the self weight, the structures are subjected to horizontal loading to characterize the nonlinear backbone response, particularly the yield

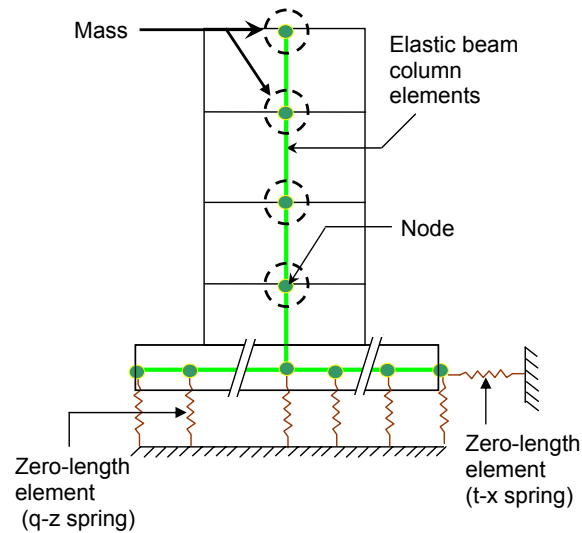


Figure 6.3: Numerical model of 4-story reference structure

and post-yield characteristics of the footing-wall structures. The pushover analysis conducted here is a displacement controlled static lateral push. During this incremental static analysis, the structures are pushed to a maximum of five times the yield displacement of respective structures.

3. Slow cyclic analysis - To conduct the slow cyclic analysis, a ramped sinusoidal horizontal displacement is applied to the top of the structure. This input motion, presented in terms of drift ratio, is shown in Figure 6.4.
4. Ground motion analysis - Nonlinear time history analysis is conducted using the Saratoga W. Valley College motion, recorded a distance of 13 km from the San Andreas fault, during the magnitude 6.9 1989 Loma Prieta Earthquake, is selected. This motion is then amplitude scaled at the first modal period of each model to different hazard levels: 50% in 50 years, 10% in 50 years and 2% in 50 years. Figure 6.5 and 6.6 show the acceleration time history and acceleration response spectra (5% damp-

ing ratio) for these three motions, respectively. The peak ground accelerations of these three motions are 0.22g, 0.44g and 0.66g, respectively. Figure 6.6 also shows the fundamental periods of the building models.

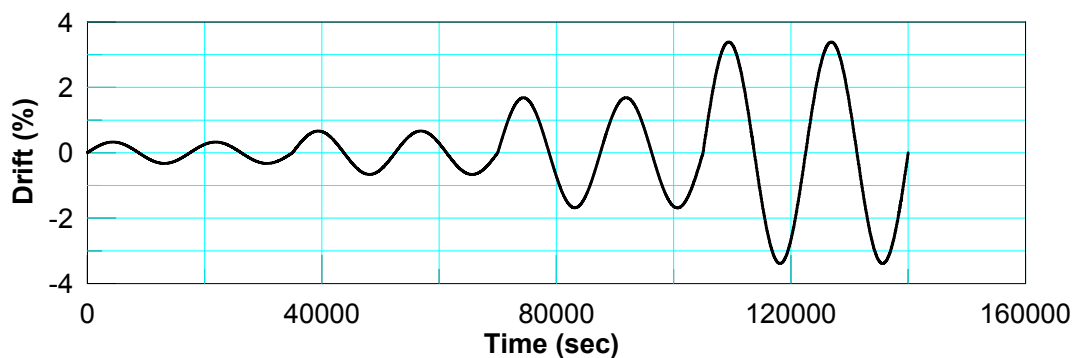


Figure 6.4: Slow cyclic input drift

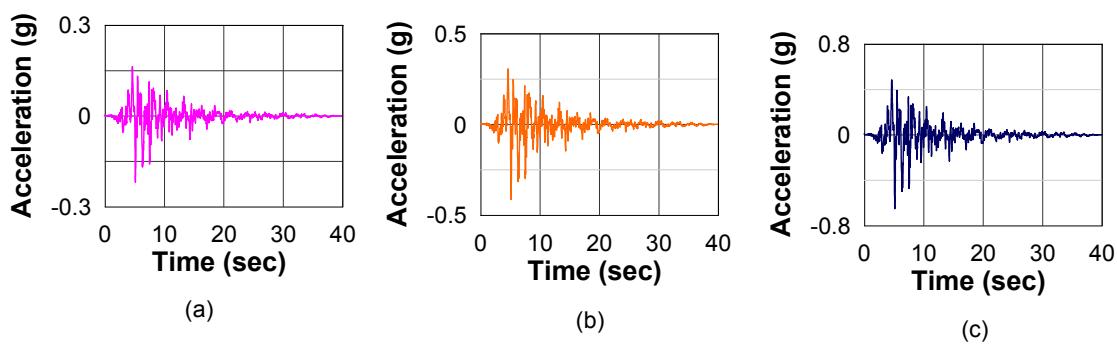


Figure 6.5: Acceleration time history of (a) gm-1 (50% in 50 yrs), (b) gm-2 (10% in 50 yrs), and (c) gm-3 (2% in 50 yrs)

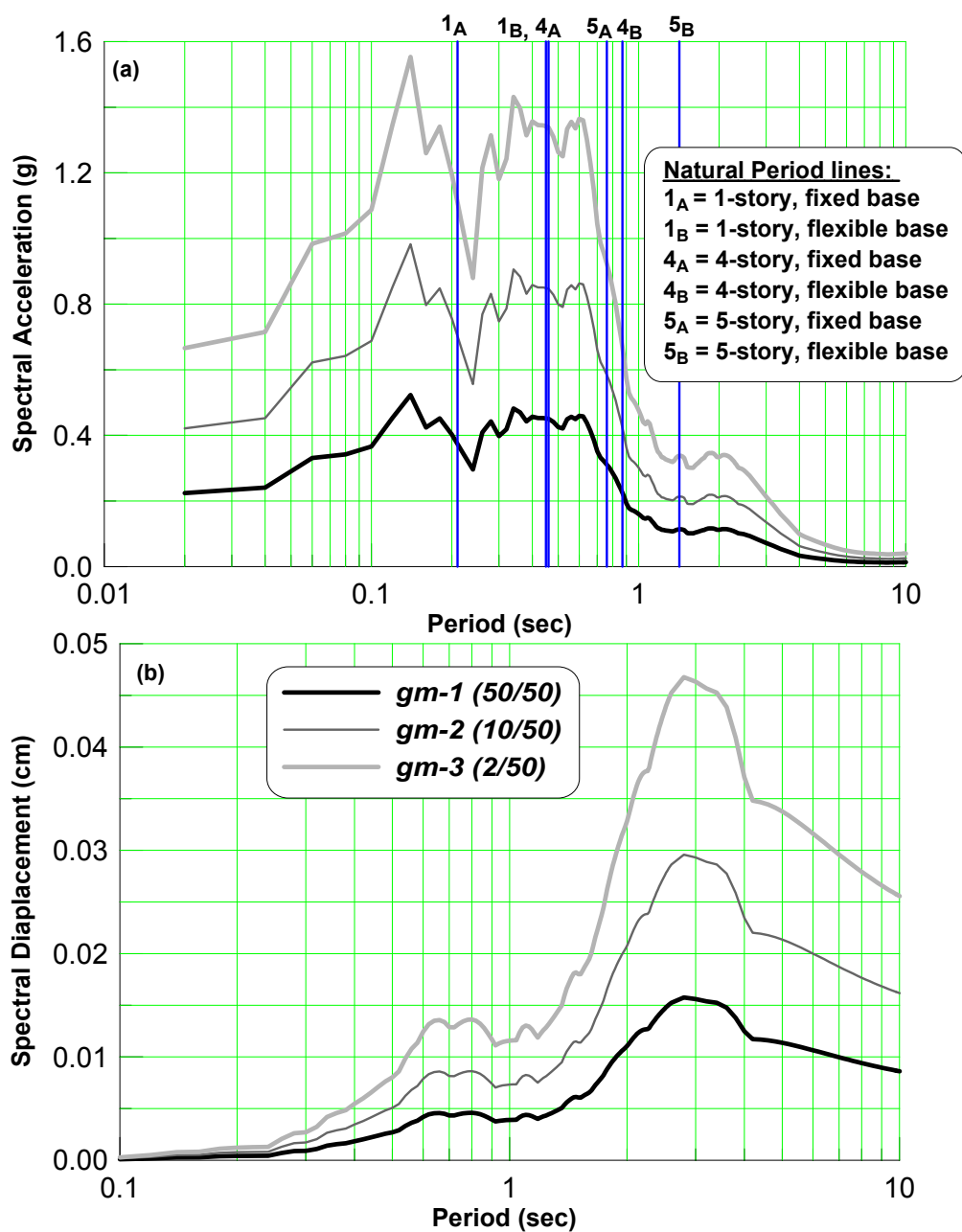


Figure 6.6: Elastic 5% damped (a) acceleration response spectra and (b) displacement response spectra for motions shown in Figure 6.5 with the fundamental periods of three buildings overlaid

6.4.2 Numerical Analysis Parameters

The Newmark beta method has been used for conducting the transient analysis, with a constant time step and solution parameters of 0.25 and 0.5 (linear acceleration method), respectively. Five percent Rayleigh damping has been assumed for the first two modes of the models. The transformation method used in analysis in the framework of OpenSees is constraint. Also, to solve the nonlinear equilibrium equations, the modified Newton-Raphson algorithm is used with a maximum of 40 iterations and a convergence tolerance of 1e-8 (which is found to be suitable for this application).

6.5 Results and Discussion

The following subsections discuss the Eigenvalue, static pushover, slow cyclic and ground motion analyses that have been conducted with the three models considered in this study.

6.5.1 Eigenvalue Analysis

Eigenvalue analysis is performed to determine the fixed and flexible-base periods of the structures. The fixed base period range is approximately 0.2–0.8 seconds, while accounting for flexibility at the base typically doubles the first mode period for each of the different models.

The flexible base period is also calculated using the following expression proposed by Veletsos and Meek (1974):

$$\frac{\tilde{T}}{T} = \sqrt{1 + \frac{k}{k_u} + \frac{kh^2}{k_\theta}} \quad (6.1)$$

where \tilde{T} = Flexible base period of a surface foundation, T = fixed base period, k = stiffness

of the structure, m = mass of the structure, h = distance from the base to the centroid of the inertial force associated with the fundamental mode, k_u and k_θ are horizontal and rotational stiffness of the foundation, respectively, on an elastic half-space.

The Eigenvalue analysis results are also compared with the proposed method after a recent study on effect of SSI on building periods by Khalil et al. (2007). Khalil et al. (2007) conducted an extensive numerical study to show the relation between fundamental period ratio of flexible system to rigid base system with a parameter defined as soil-structure relative rigidity (K_{ss}) derived as:

For single-story buildings:

$$K_{ss} = \frac{\rho v_s^2 H^3}{E_c I_c^{3/4}} \quad (6.2)$$

For multi-story buildings:

$$K_{ss} = \frac{\rho v_s^2 H^3 \sqrt{\frac{A}{A_0}}}{N_s E_c I_c^{3/4}} \quad (6.3)$$

where K_{ss} = soil-structure relative rigidity, ρ = soil density, v_s = shear wave velocity of soil, H = story height, E_c and I_c = Young's modulus and moment of inertia of vertical resisting structural element, respectively; N_s = number of storey (for a multi-storey building), A = Footing area, A_0 = reference area (1 m² in this case).

Table 6.3 summarizes the results from these analyses. It is observed from Table 6.3 that the period ratio (\tilde{T}/T) obtained from Eigenvalue analysis, the method proposed by Veletsos and Meek (1974) and the method following Khalil et al. (2007) give fairly comparable results for all the three models considered here in.

Table 6.3: Eigenvalue analysis results

Model	Fixed base Period, T (sec)	Flexible base Period, \check{T} (sec)	Period ratio, \check{T}/T	Period ratio, \check{T}/T (Veletsos & Meek, 1974)	Period ratio, \check{T}/T (Khalil et al., 2007)
1-story	0.21	0.46	2.19	1.95	1.81
4-story	0.45	0.87	1.93	1.82	2.08
5-story	0.76	1.42	1.86	1.64	1.96

6.5.2 Pushover Analysis

Nonlinear static pushover analysis is conducted to assess the capacity of the footing-structure system (Figure 6.7). Using the BNWF model results, and defining yield as the point at which the first base spring yields (the yield drift ratio is defined at the point at which the first spring reaches 80% of its capacity), the yield drift ratio is determined as: 0.38%, 0.12% and 0.1% for building models with 1-story, 4-stories and 5-stories, respectively. The peak strengths are determined as 0.45, 0.23 and 0.15 times the structure weight, for models with 1-story, 4-stories and 5-stories, respectively. The yield strength and yield drift ratios of the models are summarized in (Figure 6.4).

Table 6.4: Capacity assessment (from pushover analysis)

Model	Flexible base		
	Period (sec)	Yield strength as a fraction of total weight	Yield drift ratio (%)
1-story	0.57	0.45	0.38
4-story	0.98	0.23	0.12
5-story	1.42	0.15	0.1

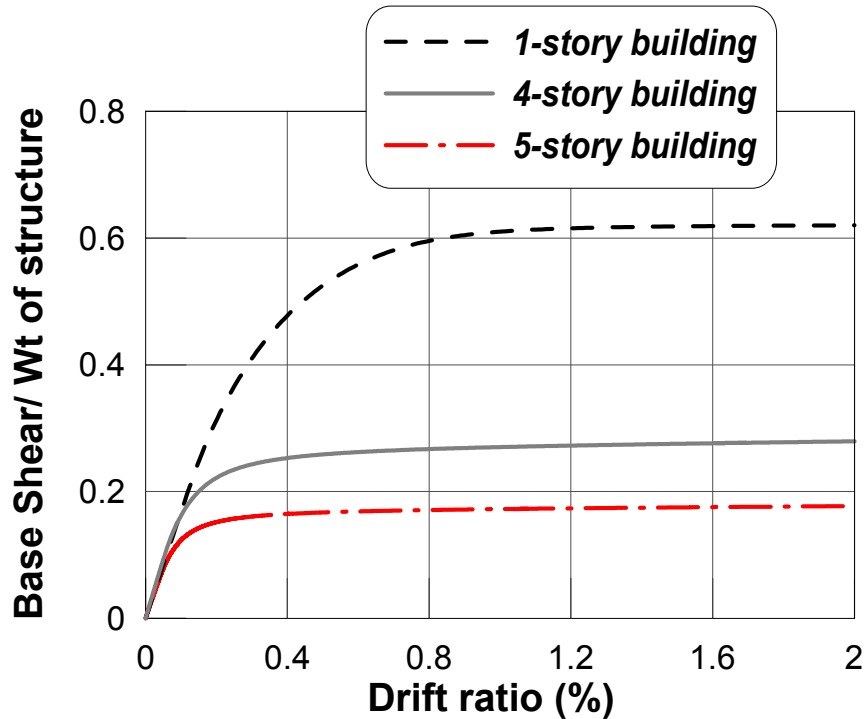


Figure 6.7: Nonlinear pushover analysis

6.5.3 Slow Cyclic Analysis

Results from slow cyclic analysis are presented in this section, in terms of footing moment-rotation, shear-sliding, settlement-rotation, and settlement-sliding. Figure 6.8 through 6.10 present the response of the three models for the cyclic motion. The results indicate that the shortest model shows a significant amount of sliding. The shear demand of this building reaches its capacity in this case, which results in permanent sliding. The settlement is small in this case compared to the other two buildings which is expected from lower amount of rocking in this case. The 4-story model reaches its design moment capacity (≈ 29 MN-m), however, responds linearly in the shear mode (shear capacity = 3.32 MN). Therefore, a fairly significant amount of permanent settlement (≈ 140 mm) is observed, whereas very little sliding displacement (≈ 3 mm) is calculated. A similar trend is observed for the 5-

story building. The settlement observed in this case is about 100 mm. Energy dissipation is observed only in rocking mode. No permanent sliding is observed.

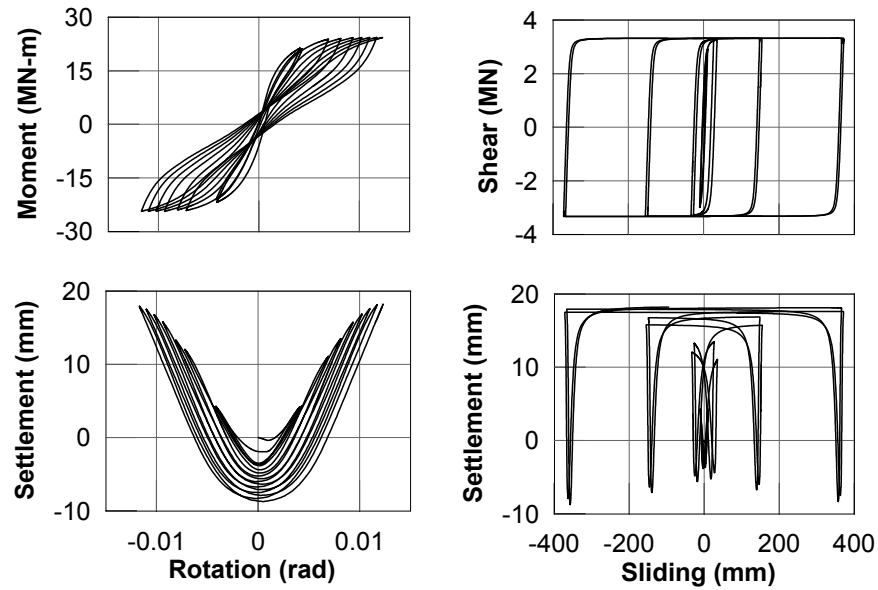


Figure 6.8: Footing response for cyclic loading of 1-story building

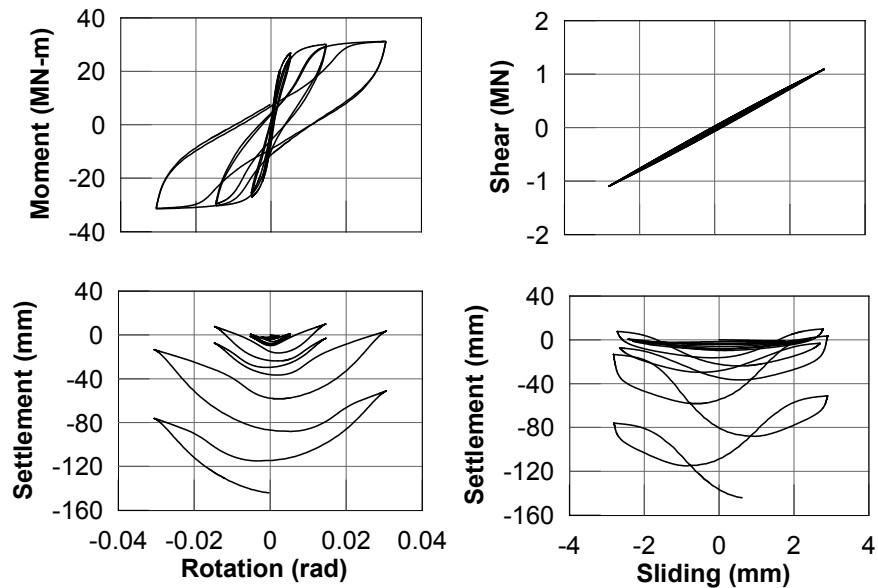


Figure 6.9: Footing response for cyclic loading of 4-story building

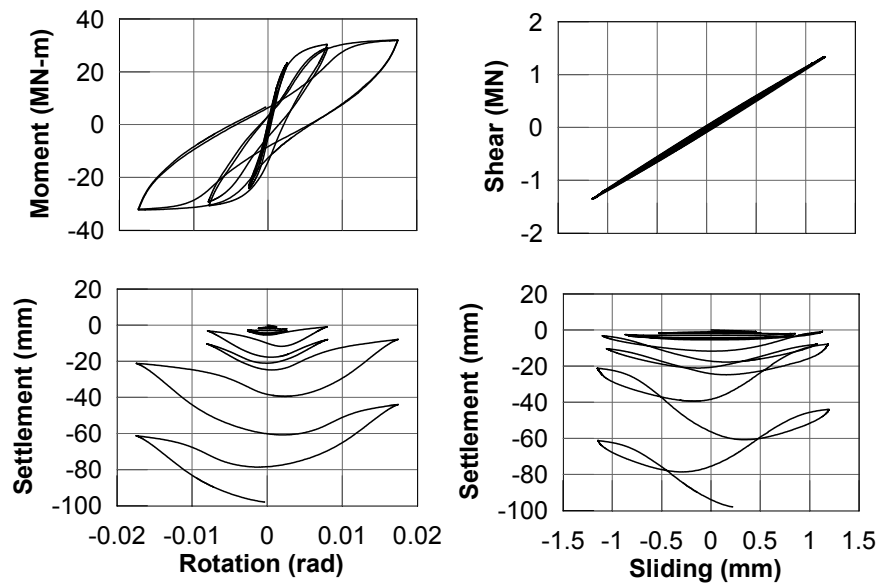


Figure 6.10: Footing response for cyclic loading of 5-story building

6.5.4 Ground Motion Analysis

Nonlinear time history analysis is conducted for all three motions described here using base excitation command in the framework of OpenSees. Figure 6.11– 6.15 summarize the footing response for all wall-footing structures. Figure 6.12– 6.16 summarize the time histories of the structural responses for the same cases. It is observed that for the taller structures the moment-rotation hysteretic results show more energy dissipation and permanent settlement than shear-sliding response, while for the shorter structure (1-story building), a large amount of sliding, but very small permanent settlement and rotation is observed. The lower period benchmark models respond in nearly an elastic uplifting fashion for the lowest level (50% in 50 year) motion, however, capacity is mobilized and a reasonable amount of moment-rotational energy can be observed for the 2% in 50 year motion.

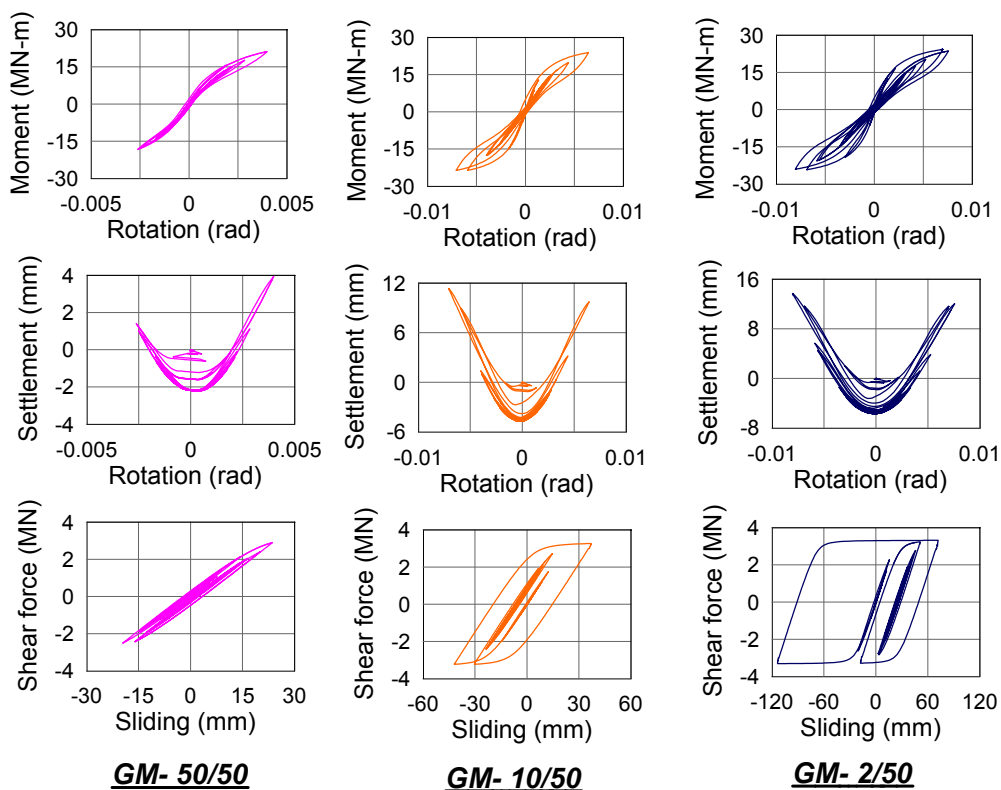


Figure 6.11: Footing response for 1-story building

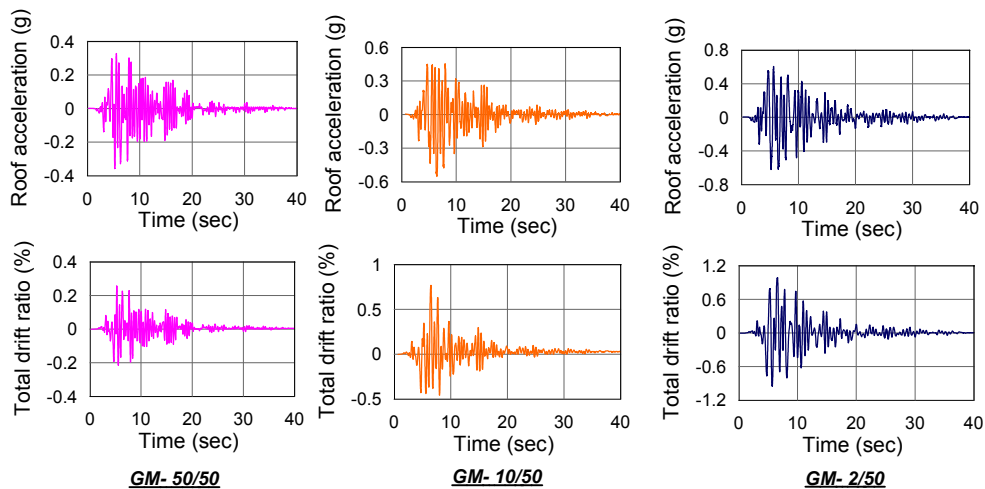


Figure 6.12: Structural response for 1-story building

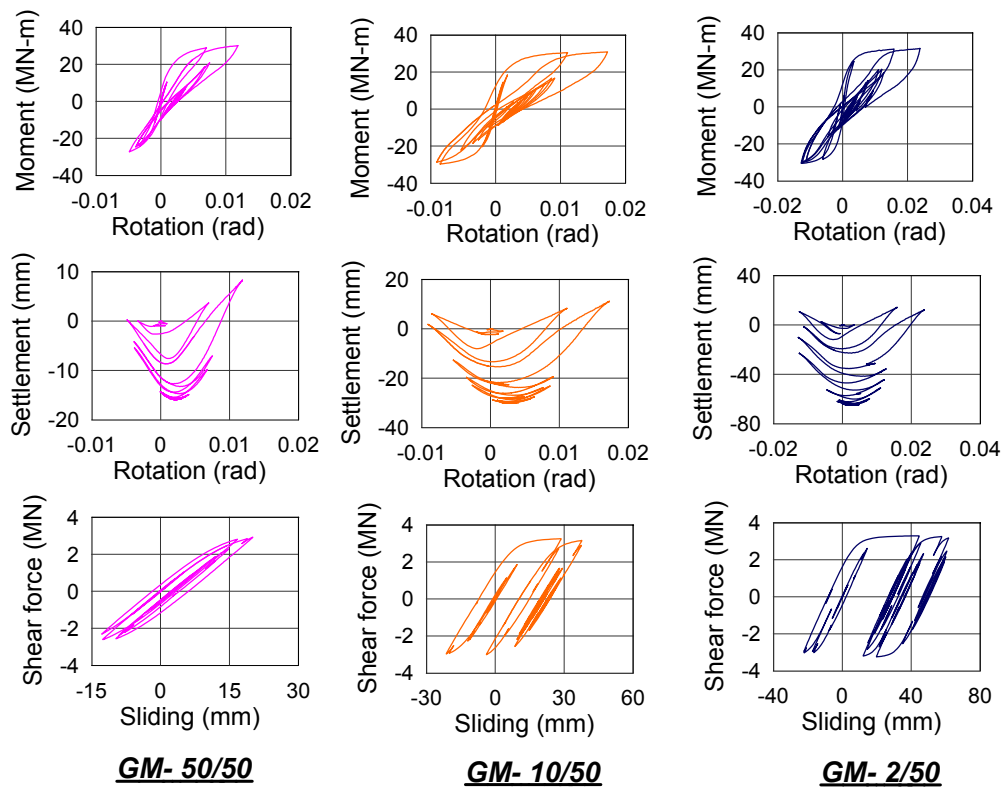


Figure 6.13: Footing response for 4-story building

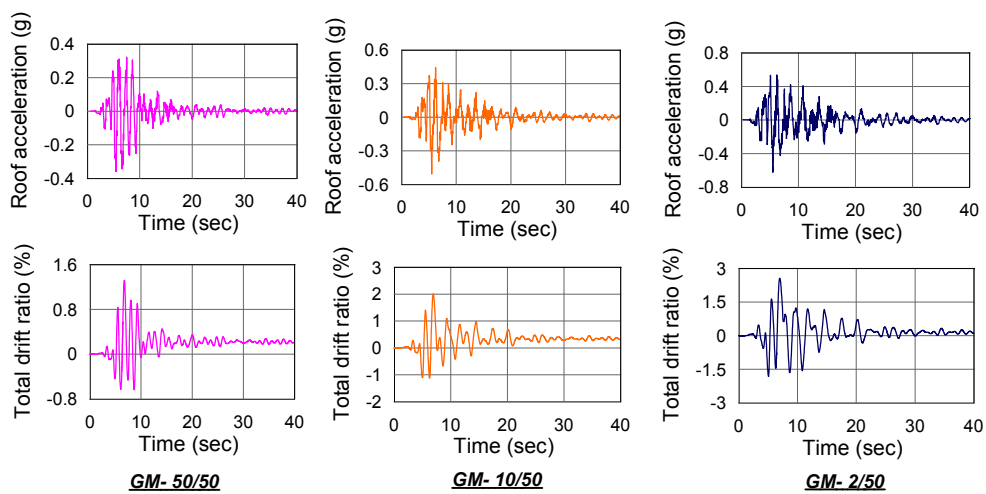


Figure 6.14: Structural response for 4-story building

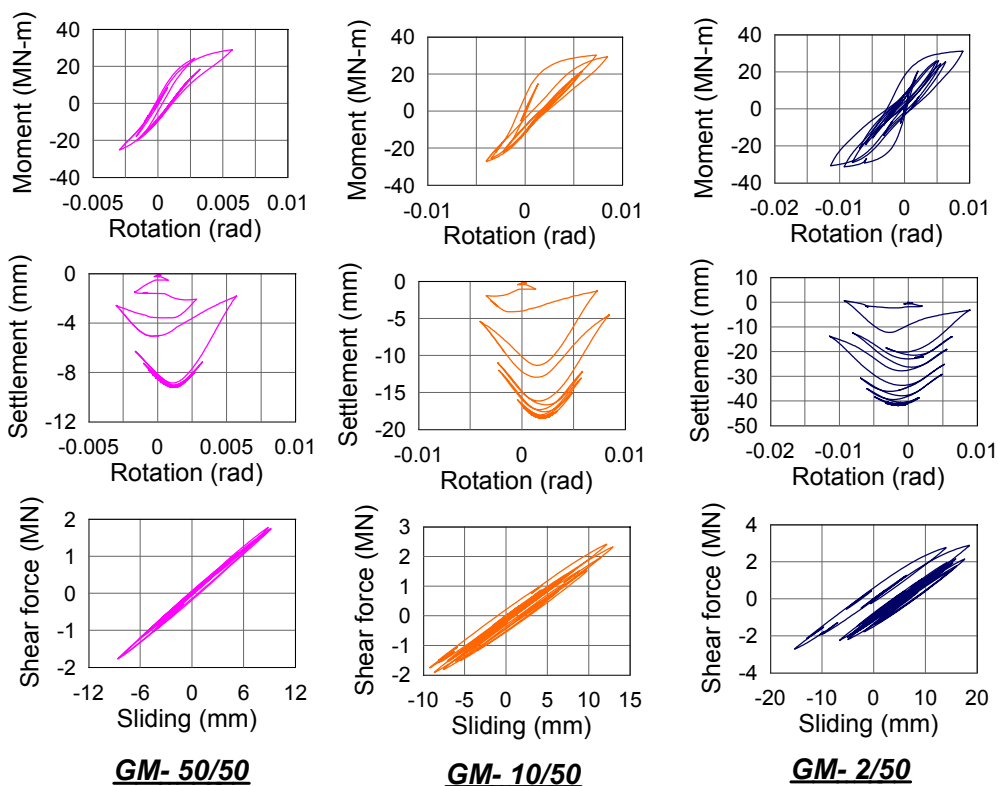


Figure 6.15: Footing response for 5-story building

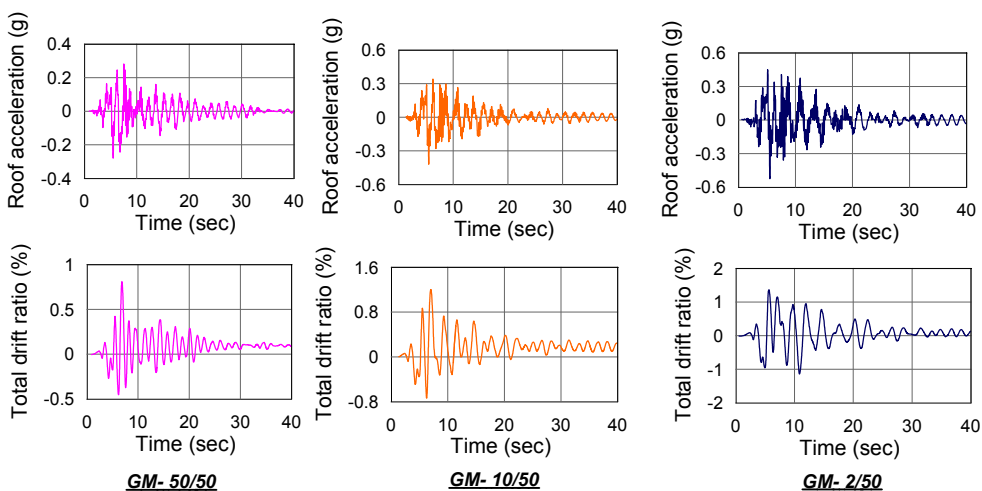


Figure 6.16: Structural response for 5-story building

Table 6.5 summarizes the footing demands for all the buildings corresponding to all the motions. The force demands (max moment and max shear) are also shown as a ratio of the respective capacities, such that one can see whether the footings reached their capacities in those modes or not. It is observed that moment demands reach the capacities (theoretical) for almost all cases in 4-story and 5-story building; whereas the shortest building (1-story) does not reach the moment capacity in any of the motions. Note that since the moment capacity is not a direct input to the springs, the overall moment demand of the footing may exceed the theoretical design moment capacity of the footing depending on the loading intensity and spring property selection. The opposite trend is observed for shear demand. The shortest building reaches the capacity for ground motions with 10% in 50 years and 2% in 50 years hazard levels, while the medium height building (4-story) reaches the shear capacity for only 2% in 50 years motion. The tallest building (5-story) is always well below the capacity in the shear mode. The sliding is also greater for the shorter structure, which is due to yielding in shear-sliding mode. Conversely, settlement is less in the shorter structure, while the taller structure shows less sliding displacement.

Table 6.6 shows the summary of roof acceleration and the drift demands. It is seen that for taller buildings, the displacement ductility is fairly large ranging from 7 to 20. Whereas for the short building, the displacement ductility is within a range of 0.61–2.4 times the yield drift. Table 6.6 also presents the ratio of peak roof acceleration to peak ground acceleration (the input motion), provide a sense of the acceleration amplification of the system. The 4-story ($\tilde{T} = 0.98\text{sec}$) shows most amplification as it can be seen from the acceleration response spectra that the spectral acceleration corresponding to a period of 0.98sec has a greater value than other two building periods (0.57 sec and 1.42 sec,

respectively). Acceleration amplification is moderate for the short building ($\tilde{T} = 0.57$ sec) and lowest for tallest building ($\tilde{T} = 1.42$ sec).

Table 6.5: Summary table of maximum footing demands

Model	GM	Max moment (MNm)	Mmax/Mcap	Max shear (MN)	Vmax/Vcap	Max sliding (mm)	Max settlement (mm)	Max rotation (rad)
1-story	1	21.80	0.75	2.83	0.85	23.15	2.20	0.004
	2	24.20	0.83	3.34	1.00	40.90	5.00	0.007
	3	24.40	0.84	3.32	0.99	109.10	5.75	0.008
4-story	1	29.90	1.03	2.90	0.87	19.40	16.10	0.011
	2	30.50	1.05	3.16	0.95	38.30	30.80	0.016
	3	31.40	1.08	3.23	0.97	62.70	66.04	0.023
5-story	1	28.10	0.97	1.78	0.53	8.90	9.29	0.006
	2	30.40	1.05	2.35	0.70	12.60	18.50	0.008
	3	30.60	1.06	2.80	0.84	18.80	42.40	0.011

Table 6.6: Summary peak drift and roof acceleration demands

Model	GM	Max drift ratio, γ_{\max} (%)	$\mu_D = \gamma_{\max}/\gamma_{\text{yield}}$	Peak roof acceleration, PRA (g)	PRA/PGA
1-story	1	1.28	10.67	0.36	1.64
	2	1.94	16.17	0.50	1.14
	3	2.38	19.83	0.64	0.97
4-story	1	0.23	0.61	0.34	1.55
	2	0.74	1.95	0.50	1.14
	3	0.92	2.42	0.60	0.91
5-story	1	0.74	7.40	0.28	1.27
	2	1.15	11.50	0.40	0.91
	3	1.31	13.10	0.51	0.77

To demonstrate the effect of SFSI on these structure-footing systems, Tables 6.7 summarizes the moment, shear, settlement, rotation and sliding demands of the footing. Table 6.8 shows peak drift ratio and roof acceleration demands of structures. From Table 6.7, one can observe that the settlement, sliding and rotational demands are highly under-predicted if the elastic base is considered instead of nonlinear base conditions for all the models and motions considered here. This under-prediction results in a smaller structural drift (total) prediction for the elastic base condition as shown in Table 6.8.

Table 6.7: Summary footing demands for fixed, elastic and nonlinear base conditions

1-story building															
	GM-1 (50 % in 50 years)					GM-2 (10 % in 50 years)					GM-3 (2 % in 50 years)				
Base condition	$ M _{max}$	$ V _{max}$	$ u _{max}$	$ S _{max}$	$ \theta _{max}$	$ M _{max}$	$ V _{max}$	$ u _{max}$	$ S _{max}$	$ \theta _{max}$	$ M _{max}$	$ V _{max}$	$ u _{max}$	$ S _{max}$	$ \theta _{max}$
	(MNm)	(MN)	(mm)	(mm)	(rad)	(MNm)	(MN)	(mm)	(mm)	(rad)	(MNm)	(MN)	(mm)	(mm)	(rad)
Fixed base	27	2.6	0	0	0	47	4.6	0	0	0	70	6.7	0	0	0
Elastic base	17	1.7	4.9	0.04	0.001	36	2.9	8.4	0.07	0.0023	44	4.3	12.4	0.1	0.0034
Nonlinear base	21.8	2.83	23.15	2.2	0.004	24.2	3.34	40.9	5	0.007	24.4	3.32	109.1	5.75	0.008
4-story building															
	GM-1 (50 % in 50 years)					GM-2 (10 % in 50 years)					GM-3 (2 % in 50 years)				
Base condition	$ M _{max}$	$ V _{max}$	$ u _{max}$	$ S _{max}$	$ \theta _{max}$	$ M _{max}$	$ V _{max}$	$ u _{max}$	$ S _{max}$	$ \theta _{max}$	$ M _{max}$	$ V _{max}$	$ u _{max}$	$ S _{max}$	$ \theta _{max}$
	(MNm)	(MN)	(mm)	(mm)	(rad)	(MNm)	(MN)	(mm)	(mm)	(rad)	(MNm)	(MN)	(mm)	(mm)	(rad)
Fixed base	41	1.8	0	0	0.000	77	3.4	0	0	0	122	5.4	0	0	0
Elastic base	61	3	6	0.06	0.005	113	5.7	11	0.15	0.01	186	8.9	17	0.23	0.016
Nonlinear base	30	2.9	19.4	16.1	0.011	30.5	3.16	38.3	30.8	0.016	31.4	3.23	62.7	66.04	0.023
5-story building															
	GM-1 (50 % in 50 years)					GM-2 (10 % in 50 years)					GM-3 (2 % in 50 years)				
Base condition	$ M _{max}$	$ V _{max}$	$ u _{max}$	$ S _{max}$	$ \theta _{max}$	$ M _{max}$	$ V _{max}$	$ u _{max}$	$ S _{max}$	$ \theta _{max}$	$ M _{max}$	$ V _{max}$	$ u _{max}$	$ S _{max}$	$ \theta _{max}$
	(MNm)	(MN)	(mm)	(mm)	(rad)	(MNm)	(MN)	(mm)	(mm)	(rad)	(MNm)	(MN)	(mm)	(mm)	(rad)
Fixed base	68	2.2	0	0	0	120	3.9	0	0	0	178	5.8	0	0	0
Elastic base	64	2.1	2.7	0.06	0.005	114	3.8	4.8	0.18	0.089	170	5.6	7.1	0.33	0.013
Nonlinear base	28.1	1.78	8.9	9.29	0.006	30.4	2.35	12.6	18.5	0.008	30.6	2.8	18.8	42.4	0.011

Table 6.8: Summary of peak drift ratio and roof acceleration demands for fixed, elastic and nonlinear base conditions

1-story building						
	GM-1		GM-2		GM-3	
Base condition	γ_{max} (%)	PRA (g)	γ_{max} (%)	PRA (g)	γ_{max} (%)	PRA (g)
Fixed base	0.09	0.43	0.16	0.73	0.24	1.08
Elastic base	0.22	0.09	0.39	0.16	0.57	0.23
Nonlinear base	0.23	0.34	0.74	0.5	0.92	0.6
4-story building						
	GM-1		GM-2		GM-3	
Base condition	γ_{max} (%)	PRA (g)	γ_{max} (%)	PRA (g)	γ_{max} (%)	PRA (g)
Fixed base	0.15	0.43	0.3	0.8	0.45	1.3
Elastic base	0.77	0.63	1.5	1.12	2.3	1.8
Nonlinear base	1.28	0.36	1.94	0.5	2.38	0.64
5-story building						
	GM-1		GM-2		GM-3	
Base condition	γ_{max} (%)	PRA (g)	γ_{max} (%)	PRA (g)	γ_{max} (%)	PRA (g)
Fixed base	0.33	0.56	0.59	0.99	0.86	1.5
Elastic base	0.66	0.53	1.18	0.94	1.7	1.4
Nonlinear base	0.74	0.28	1.15	0.4	1.31	0.51

Figure 6.17 shows the footing sliding, settlement and structural drift demands with respect to the peak ground acceleration of the systems. The PGA for each model shows slight different values as the ground motions are amplitude scaled based on the first mode period of each model. It is observed that demands increase with increasing input intensity as expected. The taller buildings show larger drift ratios, which indicates greater rocking and that also results in higher permanent settlement; whereas the shortest model rocks less but slides more than the other models.

Figure 6.18 presents a summarized comparison study for the three base conditions: fixed, elastic and nonlinear. The demand parameters chosen to compare between the base conditions are: peak moment (M_{max}), peak shear (V_{max}), maximum total drift (γ_{max}) and peak roof acceleration (PRA). The above-mentioned response parameters are then normalized with respect to the corresponding response for the fixed base case to show the

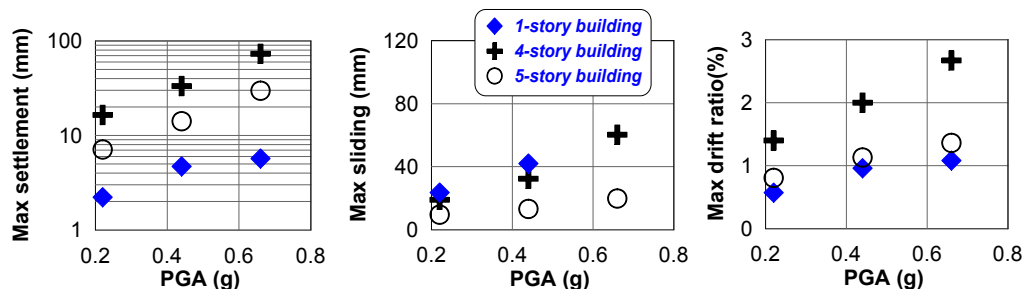


Figure 6.17: Displacement demands of the models

comparison of the fixed and flexible base conditions. One can observe from this figure that the effect of SFSI is different for structures with different height (characterized by the fundamental periods of corresponding flexible base systems).

It is observed from Figures 6.18 (a)–(c) that the moment demand for the elastic base condition is generally higher ($\approx 50\%$) than that of the fixed base condition for the 1-story building. This can be explained by looking at the elastic acceleration spectra in Figure 6.6 (a), where it shows that the spectral acceleration corresponding to the period of 1-story elastic building is higher than that of the 1-story fixed base building. For other two buildings, the moment demand decreases with base flexibility, which can also be explained by using the same logic of response spectrum (Figure 6.6 (a)). However, when the base nonlinearity is introduced, the moment demand is generally lower than that predicted by the elastic base condition, which may be due to energy dissipation at the base resulting in reduced moment demands. The total drift ratio is observed to increase with increasing flexibility of the building, which can also be explained by looking at the displacement response spectra in Figure 6.6 (b). It is also observed from Figures 6.18 (j)–(i) that, in general, the total drift demand increases when nonlinear base condition is considered instead of the elastic base condition. This may be due to the increased deformation at the foundations.

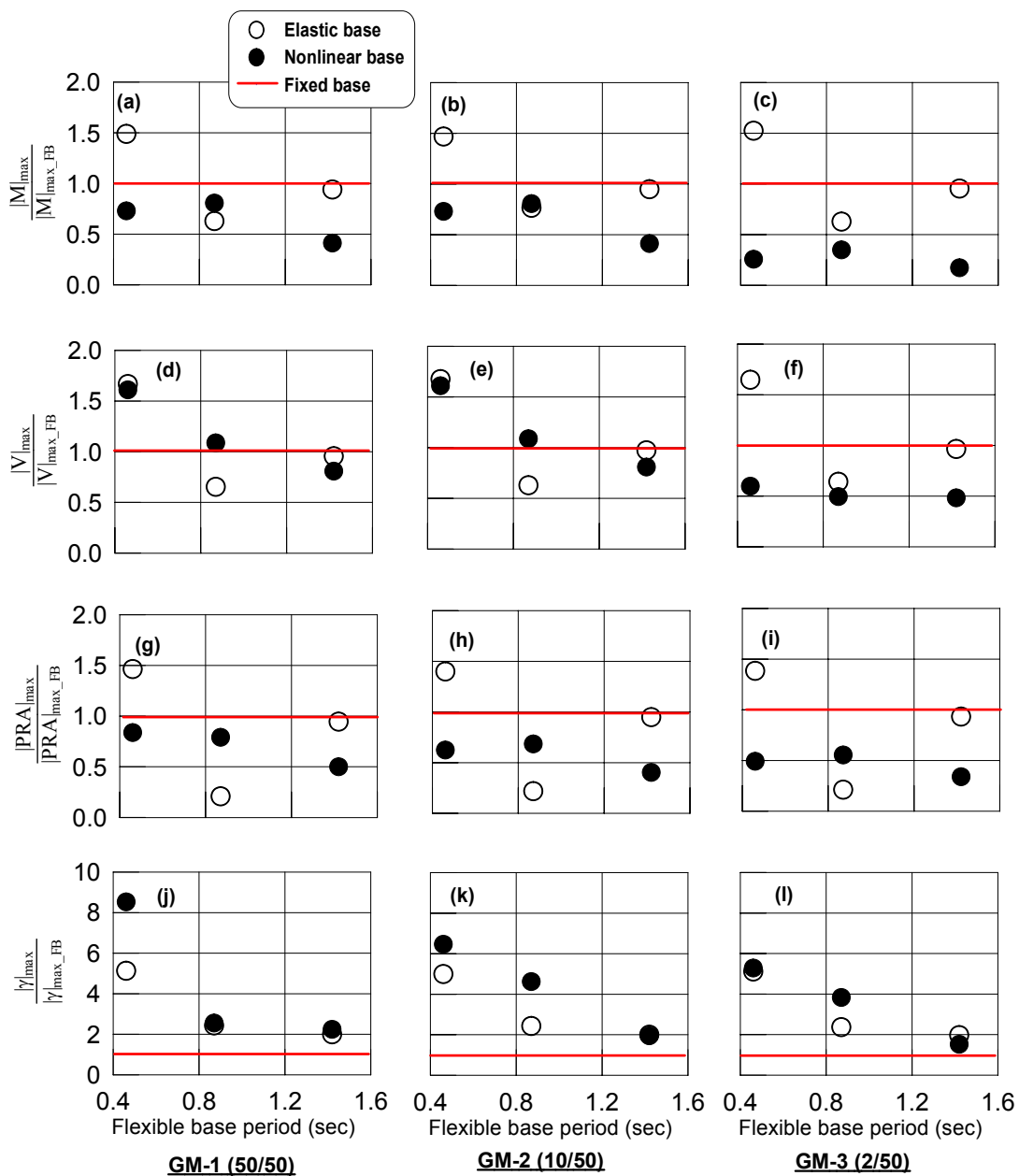


Figure 6.18: Summary of structural and footing demands normalized by fixed base demands: (a)-(c) moment demand, (d)-(f) shear demand, (g)-(i) peak roof acceleration demand, (j)-(l) total drift demand

6.6 Energy Dissipation

Hysteretic moment-rotation and shear-sliding loops shown for both shearwall-footing and bridge-footing test cases show that considerable energy has been dissipated at the base of the footing during the tests. To quantify the amount of energy dissipated, the area under the moment-rotation and shear-sliding loops per cycle are calculated. The energy dissipated in each cycle is then normalized by the linear energy of that cycle and presented in the form of equivalent viscous damping (Chopra, 1995). Equation 6.4 shows the calculation of equivalent viscous damping by equating the energy dissipated in a vibrational cycle of an inelastic system with that of the equivalent linear system (as shown in Figure 6.19).

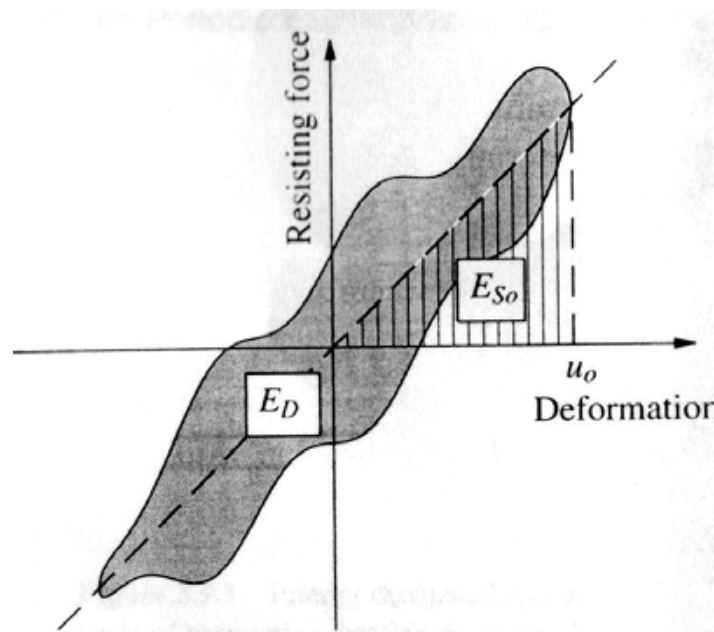


Figure 6.19: Energy dissipation E_D in a cycle of harmonic vibration determined from experiment (Chopra, 1995)

$$\zeta_{eq} = \frac{1}{4\pi} \frac{E_D}{E_S} \quad (6.4)$$

where ζ_{eq} = equivalent viscous damping, E_D = hysteretic energy dissipated by the system during one cycle, E_s = the elastic strain energy associated with that cycle of motion.

For a shallow foundation system having rocking, sliding and axial movements, the total energy dissipated at the base is calculated as:

$$E_D = E_D^\theta + E_D^u + E_D^s \quad (6.5)$$

where E_D^θ = energy dissipated in rocking mode, E_D^u = energy dissipated in sliding mode and E_D^s = energy dissipated in axial mode.

The energy dissipated in these different modes can be calculated as follows:

- Rocking mode

$$E_D^\theta = \int M(t).d\theta(t) \quad (6.6)$$

- Sliding mode

$$E_D^u = \int V(t).du(t) \quad (6.7)$$

- Axial mode

$$E_D^s = \int Q(t).dS(t) \quad (6.8)$$

where M , V and Q are moment, shear and axial load, respectively; and θ , u and S are rotation, sliding and settlement, respectively. Figure 6.20 shows a schematic diagram of shear versus sliding history to demonstrate how the energy dissipation is calculated for a shear-sliding loop. Here, V_{max} and V_{min} are the maximum and minimum shear forces, respectively; and u_{max} and u_{min} are the maximum and minimum sliding displacements, respectively, for the cycle B-C-D-E-B. The dissipated energy E_D^u is calculated by summing

up the area inside the loop (as shown in Equation 6.7) using the trapezoidal rule. The linear energy E_S^u is calculated following Equation 6.9. The equivalent viscous damping for this cycle is then calculated following Equation 6.4. The same procedure is followed for calculated energy in other modes. In this comparison study, only energy dissipated through rocking and sliding modes are considered. Energy dissipation in the axial mode is not considered as the values are negligible.

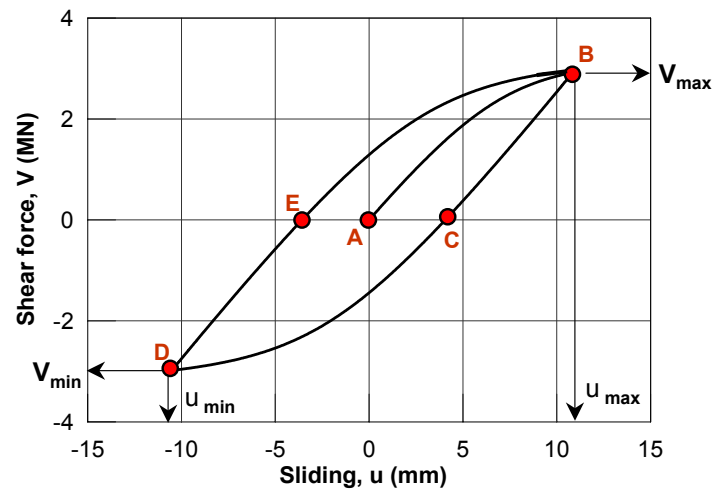


Figure 6.20: Estimation of damping in shear-sliding loop

$$E_S^u = \frac{1}{2} \left[\left(\frac{V_{max} - V_{min}}{2} \right) \left(\frac{u_{max} - u_{min}}{2} \right) \right] \quad (6.9)$$

The energy dissipation via rocking and sliding modes is calculated for all of the shearwall-footing buildings during the aforementioned cyclic and dynamic loading events. The energy dissipation for the cyclic loading cases are shown in Figure 6.21. The equivalent viscous damping in rocking mode is plotted against the rotational amplitude per cycle (Figure 6.21(a)), whereas that in the sliding mode is plotted against the sliding amplitude per

cycle (Figure 6.21(b)). The rotational and sliding amplitudes are defined as follows:

$$\theta_{amp} = \frac{|\theta_{max} - \theta_{min}|}{2} \quad (6.10)$$

$$u_{amp} = \frac{|u_{max} - u_{min}|}{2} \quad (6.11)$$

The results reinforces what we see from the footing responses in Figures 6.8 through 6.10, that more energy is dissipated in the rocking mode for taller buildings, while the short building dissipates more energy in the sliding mode.

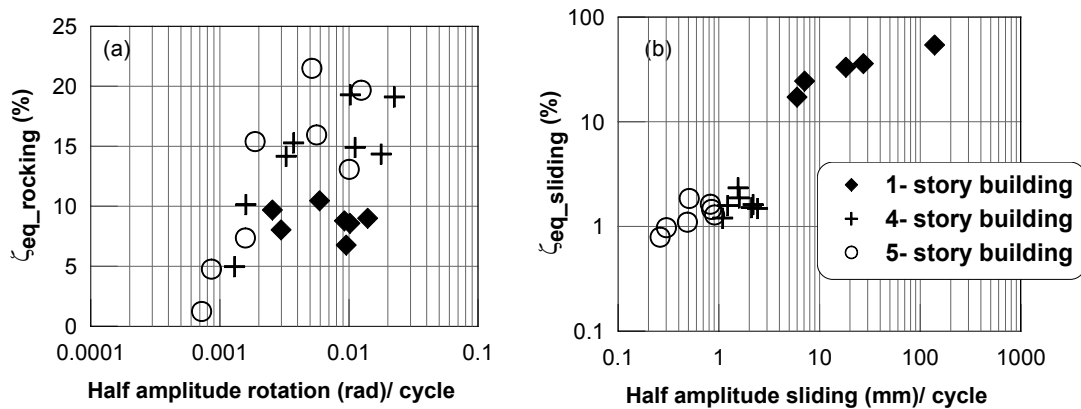


Figure 6.21: Energy dissipation at the base of footings in terms of equivalent viscous damping, ζ_{eq} (%): (a) rocking mode, (b) sliding mode

Figure 6.22 shows the energy dissipation represented as equivalent viscous damping for models in rocking and sliding modes. The viscous damping for all cases is observed to have an increasing trend with increasing demand per loop. It is observed that the 1-story building dissipate more energy in the sliding mode, while the higher period buildings dissipate less energy in the sliding mode and more energy in the rocking mode. This phenomenon is directly shown in Figure 6.23, where the ratio of energy dissipated via $M - \theta$ to the energy dissipated via $V - u$ is plotted versus peak ground acceleration of motions. It is observed

that the energy dissipated by rocking is more than 80% of the total energy for higher period buildings, whereas this ratio is only 10-50% for short period building. The sliding energy dissipated trend is just opposite to what is seen in the rocking energy case.

Figure 6.24 shows the consequence of the energy dissipation. As permanent settlement is one of the consequences of the energy dissipation, it is observed that with increasing energy dissipation, the buildings have more permanent settlement. The maximum energy dissipation is observed for 4-story building subjected to the event 2% in 50 years ground motion. As expected, this event corresponds to the maximum permanent settlement observed ≈ 66 mm (as shown in Figure 6.24), which is 0.45% of the length of the footing.

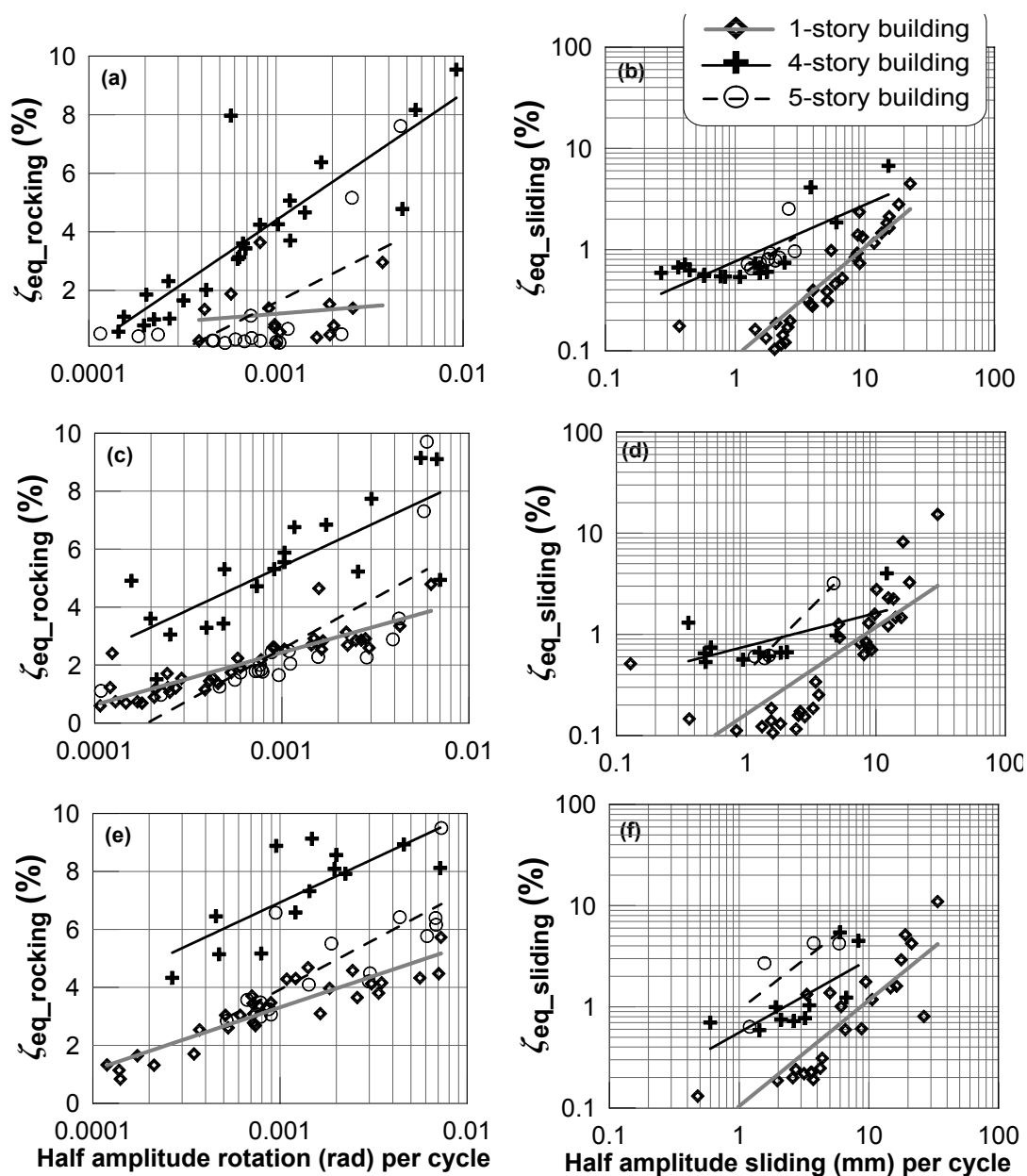


Figure 6.22: Energy dissipation per cycle in (a)rocking mode ($g_m=50/50$), (b)sliding mode ($g_m=50/50$), (c)rocking mode ($g_m=10/50$), (d)sliding mode ($g_m=10/50$), (e)rocking mode ($g_m=2/50$), (f)sliding mode ($g_m=2/50$)

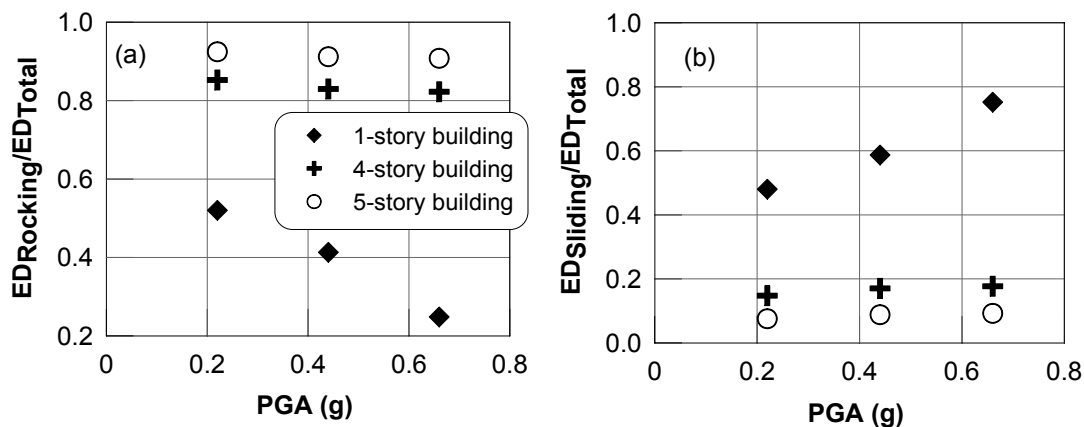


Figure 6.23: Fraction of energy dissipated in (a) rocking mode and (b) sliding mode

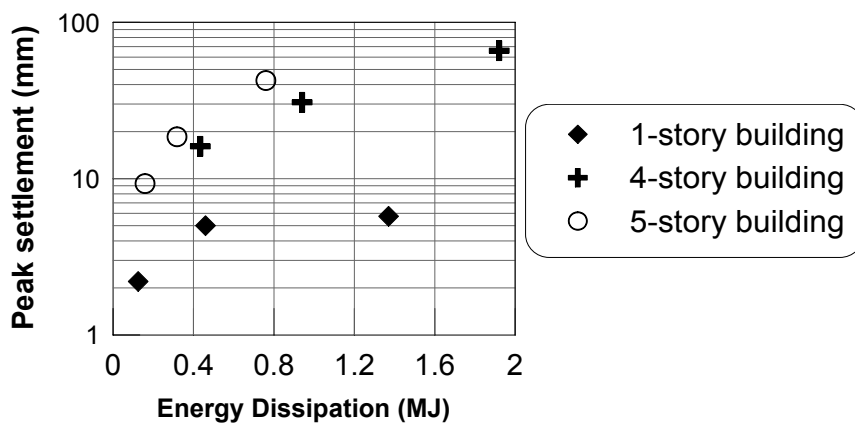


Figure 6.24: Consequence of energy dissipation

6.7 Comparison with Macro Model

The so-called “macro-element” concept for representing a footing’s sliding, settling and rocking response is an interesting concept that has been widely used by researchers. The main advantage of this model is that it significantly reduces the number of elements needed for the overall modeling of the footing. Cremer et al. (2001), for example, presented a

nonlinear macro-element to model the behavior of shallow foundations resting on cohesive soil. The element is based on plasticity theory and accounts for yielding of the soil under the foundation as well as uplift of the foundation. In a recent study, Gajan (2006) developed such an element, which he termed as "contact interface model". The contact interface model provides coupled nonlinear constitutive relations between cyclic loads (axial, shear and moment) and displacements (settlement, sliding, and rotation) of the footing-soil system. The footing and the soil beneath the footing is considered as a macro-element (Figure 6.25). The contact interface model is supposed to predict load capacities, stiffness degradation, permanent and cyclic displacements, and hysteretic energy dissipation.

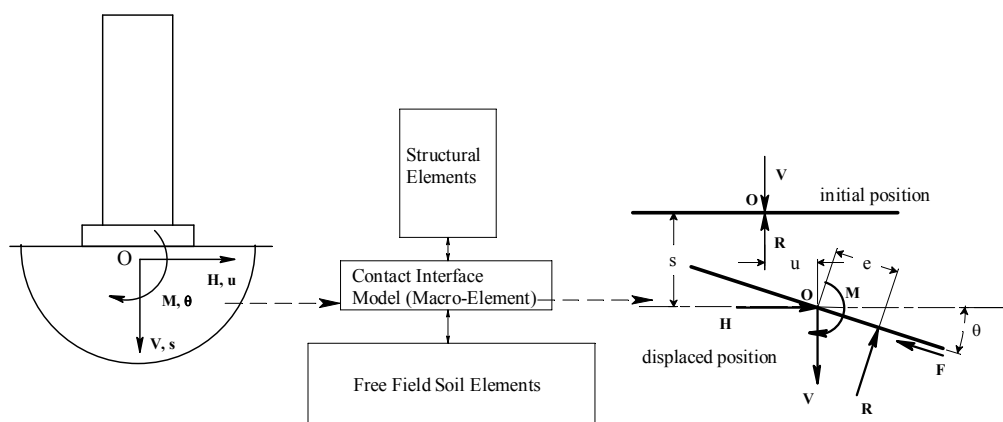


Figure 6.25: Contact Interface Model after Gajan (2006)

In order to compare the response of BNWF model with the contact interface model responses, a study has been conducted considering same structure and soil properties. Figure 6.26 shows comparison of the model responses in terms of moment–rotation and settlement–rotation responses for the 4-story building when subjected to the ground motion of 2% in 50 years hazard level. It is observed from Figure 6.26 that the peak moment, peak rotation and rotational stiffness compare well for two different modeling approaches.

However, the settlement prediction is lower ($\approx 33\%$) for the BNWF model than that predicted by the contact interface model, perhaps due the difference in modeling consideration related to coupling between vertical and lateral mode of movements. Further details of the comparative study and relevant discussions can be found in Gajan et al. (2008).

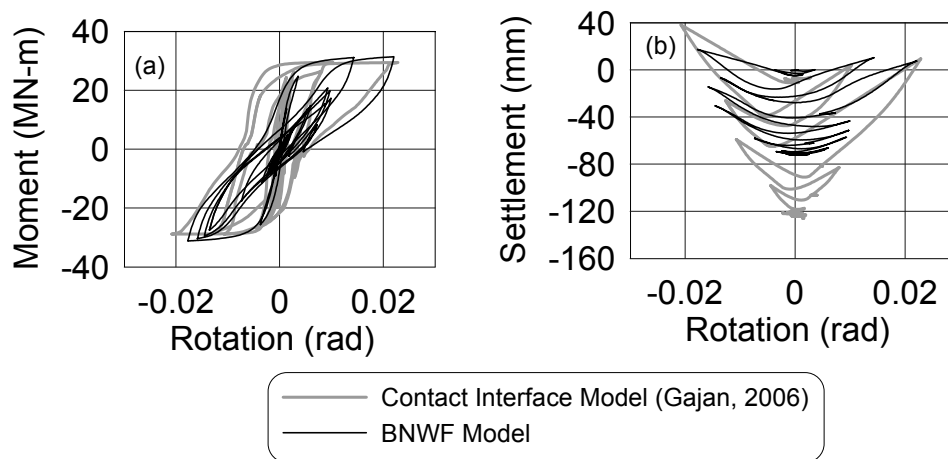


Figure 6.26: Comparison with macro model after Gajan (2006): (a) moment–rotation and (b) settlement–rotation

6.8 Summary Remarks

The effect of soil-foundation-structure-interaction (SFSI) of shearwall buildings resting on a shallow rectangular footing is discussed in this chapter. A numerical study is performed considering three representative buildings, one-, four- and five-story shearwall-footing models. Modeling of the footing, which is assumed to be of the same dimension for all three models, is carried out using the proposed BNWF concept. These models are subjected to gravity load, pushover and slow cyclic lateral displacement controlled demands and few ground motions. The effect of SFSI is evaluated by comparing results against the fixed base cases. Specific findings of the numerical simulations include the following:

- The settlement, sliding and rotational demands of the elastic base models are much lower than that of nonlinear base models.
- Maximum drift demand of the structure is also much lower for the elastic-base condition.
- In this context, moment and shear force demands are much large for the fixed base and elastic base models, than that of the nonlinear base models. Maximum moments may reduce 40-80% that of the fixed base condition. Shear forces may typically be reduced to approximately 50-90% that of the fixed base case. In some instances, shear force demands are increased when considering either an elastic or nonlinear foundation. This is attributed to the spectral characteristics of the input motions.
- The energy dissipation is generally $\approx 10\%$ for the buildings and motions considered.
- For a typical low and medium rise shearwall structures considered, significant energy can be dissipated at the soil-foundation interface through rocking and sliding modes. Short structures dissipate between $\approx 50-80\%$ of total energy through sliding, while medium height structures dissipate only $\approx 10-20\%$ through sliding and the remainder through rocking.

Chapter 7

Frame-Shearwall Dual Structure

7.1 Introduction

Multiple types of lateral load resisting systems are often used in design practice. This may arise due to the practical configuration of the building, e.g., core concrete shearwalls also forming elevator shafts, while other areas of the building require clear space between bays, resulting in the use of moment frames. Often, however, this situation occurs due to the need to retrofit a building. For example, to retrofit an existing moment frame structure that was designed using older seismic design provisions, the option of strengthening the structure by adding shear walls is adopted. Pending suitable soil conditions on site, both the columns and shearwalls may be supported on shallow foundations (isolated footing below the columns and strip footing below shearwall).

Since, shallow foundations add significant base flexibility due to rocking and sliding, accurate evaluation of seismic vulnerability of these structures supported on shallow foundations requires proper modeling of the foundations. Ignoring base flexibility may over or under predict seismic response of these structures. The other practical issue is that in

a multi-type lateral load resisting system, one system may be stiffer than the other, therefore more vulnerable to damage if the foundation is too flexible. This issue is discussed in Chapter 1 and variety of design documents (e.g., ATC-40 (1996)).

The particular focus of this chapter is on the aforementioned situation, namely a shear wall is used in conjunction with a frame to provide lateral resistance. Both structural systems are supported on shallow foundations. A 2D planar model of this dual load resisting system is designed, considering modern seismic design practice for ductile reinforced concrete moment frames. The effects of foundation rocking, sliding, and settling are considered by incorporating flexibility (elastic and inelastic) at the base of the footings. Varying factors of safety at the base of the footings are used in the modeling, to evaluate the effects of the margin of safety of the foundation on the structure-foundation system seismic response. Parameters investigated include the moment and shear demand at the footings, the peak inter-story drift ratio, and the energy dissipated by the ductile moment frame joints.

7.2 Wall-frame-foundation System Description

A prototypical two story, two bay, planar frame connected in series with a rigid, slender shear wall is designed (Figure 7.1) and modeled (Figure 7.2) using OpenSees (2008). The 2D planar system is envisioned to perform as the primary lateral resisting system within a modern low rise building. Loads are estimated by assuming a 3D building, which is supporting surface service loads of 1.3 kPa over tributary bay spans to the nearest lateral and gravity resisting system of 4.6 meters. The wall-frame-foundation system is designed by integrating a moderate ductility reinforced concrete frame with a ‘retrofit’ shear wall. A relatively slender shear wall is selected with an aspect ratio (Height:Width) of 3.75. Frame

bays are designed with an aspect ratio (Span:Floor Height) of 1.60. Service and seismic loads are estimated based on ASCE-7 (2005); FEMA 356 (2000) and applied, while assuring ductile yielding of pre-defined hinges at the ends of typical beam-column joints. Seismic loading is selected using the design spectrum for the Bay Area, California. A target soil-structure fundamental period of $T_n = 0.5$ seconds was chosen when designing the system, to represent the period of typical low-rise systems, where SFSI is incorporated in the design. For comparison, the fixed base period of the prototype structure is calculated as $T_n = 0.2$ seconds. The structure-foundation system is designed considering current geotechnical and structural design practice. The structural design is performed by Chang (2008) and is also reported in Hutchinson et al. (2006). A simplified 2-dimensional finite element (FE) model is constructed of this system, using 1-dimensional beam-column elements and arrays of linear and/or nonlinear spring elements. Figure 7.2 shows the schematic diagram of the FE model.

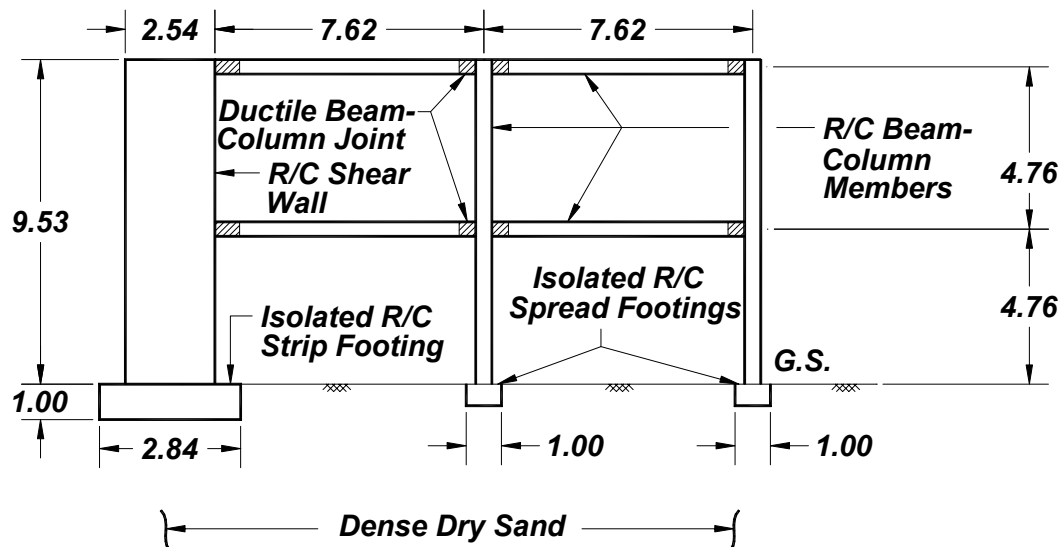


Figure 7.1: Prototype frame-wall-foundation combined system (units in mm)

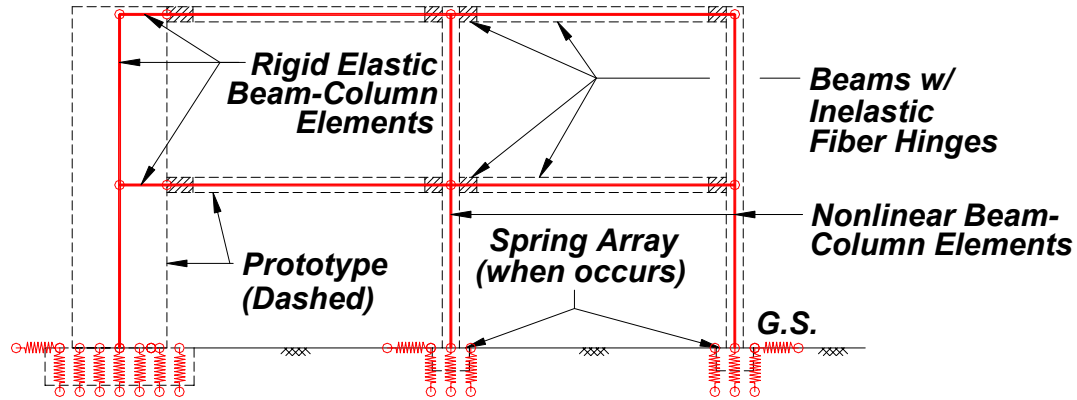


Figure 7.2: Schematic diagram showing frame-wall-foundation OpenSees model

7.3 Structural Modeling

The frame portion of the model is designed based on ACI 318-02 (2002) recommendations for ductile moment resisting frames. Beam cross-section dimensions are 40.6 cm in height and 30.5 cm in width, while square columns of size 50.8 cm are used. Longitudinal reinforcing steel ratios of 1.25% and 1.8% are used for the beams and columns, respectively. Table 7.1 summarizes the structural material properties used and derived for the analyses. Confinement of the concrete in the beams and columns due to transverse hoops is accounted for using the confinement model proposed by Mander and Priestly (1988). Shallow footings for the structure were modeled using unconfined concrete and assumed to remain elastic during the analyses. The OpenSees material model of the structural elements used the uniaxial material *Concrete01* for both the unconfined and the confined concrete and *Steel01* for the steel. *Concrete01* has a backbone curve following Kent-Scott-Park model with stiffness degradation and ignores the tension resistance of concrete.

To model the beams *beamwithHinges* element is used. This element places an elastic portion at the middle of the element and plastic portions at the ends of the element. The

plastic hinge length was approximated to be ten percent of the total span of the beam. Columns were modeled with the fiber section and the *nonlinearBeamColumn* element. The *nonlinearBeamColumn* element models plasticity of the element over the entire length of the element. Using stress and strain output at local fibers within each section, moment-curvature response is generated. The structural shearwall was assumed to remain elastic with Young's modulus equal to that of the concrete (Table 7.1).

Table 7.1: Structural members material properties

Reinforcing Steel					
Material	Young's Modulus (Pa)		Yield strength (Pa)		
<i>Steel 01</i>	1.99×10^{11}		4.14×10^8		
Concrete					
Material	Young's Modulus (Pa)	Peak strength (Pa)	Strain at peak strength	Ultimate strength (Pa)	Ultimate strain
Unconfined concrete	2.16×10^{10}	2.76×10^7	0.003	5.52×10^6	0.006
Confined concrete (beams)	2.16×10^{10}	3.64×10^7	0.005	2.84×10^7	0.02
Confined concrete (columns)	2.16×10^{10}	4.14×10^7	0.007	3.42×10^7	0.026

7.4 SFSI Modeling

In this work, the foundation is modeled using the previously described BNWF modeling approach. In order to show a comparison of results when considering different foundation modeling assumptions, additional two modeling cases are considered. They are: (i) fixed

base (sliding, settling, and rotation at the base restricted), (ii) elastic base. For each base condition, the vertical factor of safety FS_v of the strip footing (below the shear wall) is varied to encompass a typical range in design practice ($FS_v = 3, 5, 7, \text{ and } 10$).

The foundation subgrade is assumed to be dense, dry sand with an 80% relative density. The basic parameters used for the soil subgrade and the resulting capacity and stiffness values obtained for the strip and square footings are listed in Table 7.2 and Table 7.3, respectively. The capacities and stiffnesses are derived as per the equations and citations given in Section 2.5 of Chapter 2. Note that the capacity and stiffnesses of the strip footing are higher than that of the square footings.

Table 7.2: Basic properties for soil subgrade

Cohesion, c (kPa)	Angle of internal friction, ϕ (deg)	Unit weight of soil, γ (kN/m ³)	Relative density, D_r (%)	Poisson's ratio, ν	Modulus of Elasticity, E_s (MPa)
0	40	16.2	80	0.3	45

Table 7.3: Derived properties of the strip and square footings

Footings	Footing size (m)	Ultimate load capacity, Q_{ult} (MN)	Vertical stiffness, K_v (MN/m)	Horizontal stiffness, K_h (MN/m)
Strip Footing	2.84 x 0.69 x 0.64	2.3	88	79
Square Footings	1.0 x 1.0 x 0.64	1.9	56	46

7.5 Selection of Ground Motions

Ten recorded earthquake motions are selected for use as input into the numerical models. All are recorded motions selected from the Imperial Valley (1979), Landers (1992), Northridge (1994), Kobe (1995), Chi-Chi (1999), San Fernando (1971), North Palm Springs (1986), Whittier Narrows (1987), Loma Prieta (1989), and Duzce (1999) earthquakes. The later five of these motions may be characterized as near-fault, due to the close proximity of the recording to the fault rupture (less than 10 km). Five percent damped elastic response spectra normalized by PGA of corresponding motions are provided in Figure 7.3, where part (a) presents those motions characterized as near-field, and part (b) presents those motions characterized as ordinary motions.

To illustrate the sensitivity at typically envisioned structural performance levels, each ground motion is amplitude scaled such that the displacement ductility (= maximum displacement/yield displacement) is between 2-3, for the fixed base condition. Resulting scaling factors ranged from 0.2-1.6. Peak ground accelerations for the scaled motions ranged from $PGA = 0.12 - 0.94g$. Table 7.4 gives the details of the selected ground motions and PGA of the scaled motions that are used for the analysis.

7.6 Solution Technique Adopted

The Newmark method has been used for conducting the transient analysis, with a constant time step and solution parameters of 0.25 and 0.5, respectively. Five percent Rayleigh damping has been assumed for the structure. The transformation method is used in the analysis as a constraint. This method transforms the stiffness matrix by condensing out the constrained degree of freedoms, while also reducing the size of the system for multi-point

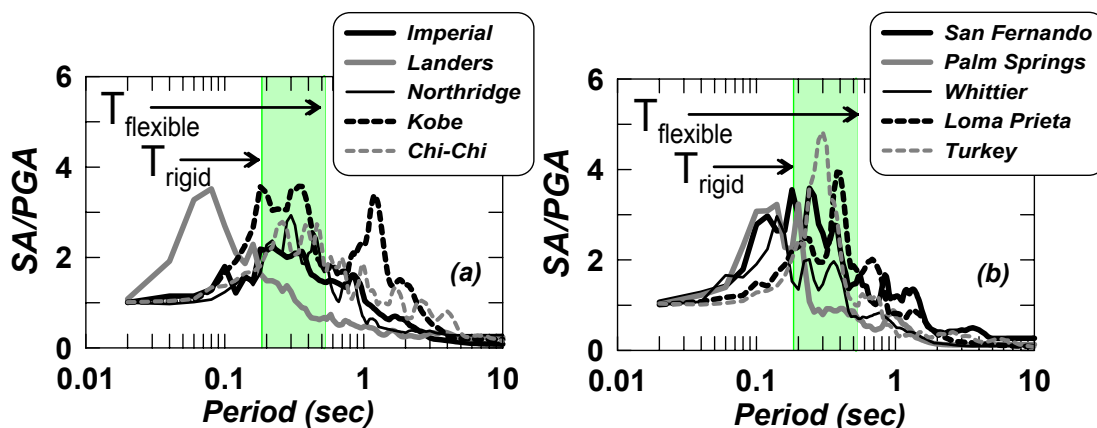


Figure 7.3: Five percent damped acceleration response spectra for: (a) near fault motions and (b) ordinary (other) motions used in this study

Table 7.4: Details of the selected ground motions

Earthquake name and Location of recording	Year	M_w^1	Channel	$D1^2$ (km)	$D2^3$ (km)	PGA (g)	PGV (cm/s)	PGD (cm)	PGV/PGA (s)	Scaled PGA in analyses (g)
(a) Near-fault Motions										
Imperial Valley, Station: 955 El Centro Array # 4	1979	6.5	H-E04140	4.2	6.8	0.485	37.39	20.09	0.08	0.44
Landers, Station: 24 Lucerne	1992	7.3	LCN000	1.1	--	0.785	31.89	16.42	0.04	0.42
Northridge, Station: 0637 Sepulveda VA	1994	6.7	SPV360	8.9	0.4	0.939	75.91	15.03	0.08	0.24
Kobe, Station: 0 Takatori	1995	6.9	TAK090	0.3	--	0.616	120.73	32.74	0.20	0.2
Chi-Chi, Taiwan, Station: CHY024	1999	7.6	CHY024-W	9.06	9.06	0.278	52.94	43.64	0.19	0.6
(b) Ordinary Motions										
San Fernando, Station: 135 LA - Hollywood Storage Lot	1971	6.6	PEL090	21.2	24.6	0.210	18.87	12.43	0.09	0.65
N. Palm Springs, Station: 12331 Hemet Fire Station	1986	6.0	H05270	43.3	--	0.144	4.88	0.73	0.03	1.18
Whittier Narrows, Station: 24461 Alhambra, Fremont Sch	1987	6.0	A-ALH270	13.2	--	0.414	16.30	2.32	0.04	0.86
Loma Prieta, Station: 47380 Gilroy Array # 2	1989	6.9	G02000	12.7	12.1	0.367	32.91	7.15	0.09	0.58
Duzce, Turkey, Station: Mudurnu	1999	7.4	MDR000	33.6	33.6	0.120	9.28	7.64	0.08	1.6

¹As reported by PEER Strong Motion Database (<http://peer.berkeley.edu/smcat/>)

² $D1$ = Closest distance to the rupture surface.

³ $D2$ = Closest to surface projection of rupture

-- = Information not Available

constraints. The Reverse Cuthill-McKee algorithm is used to optimize node numbering and reduce the bandwidth of the system matrices. An un-symmetric banded system of equations object is constructed, which is solved during the analysis using the Lapack band

general solver. To solve the nonlinear equations, the Newton-Raphson algorithm is used, with a maximum of 40 iterations to a convergence tolerance of $1e-12$.

7.7 Results and Discussion

7.7.1 Eigenvalue Analysis

Eigenvalue analysis of the wall-frame-foundation models with different foundation modeling assumptions indicates that the fundamental period is 0.19 and 0.54 seconds for the fixed base and flexible base condition, respectively for the $FS_v = 10$ case. Lower FS_v are created by increasing the mass of the models, which would increase the period, as shown in Table 7.5. Figure 7.4 also shows the first three periods of the system for different base conditions and different factors of safety.

Table 7.5: First three periods of the structures with different base conditions and factors of safety

FS_v	Base Conditions	Period (Mode 1) (sec)	Period (Mode 2) (sec)	Period (Mode 3) (sec)
3	fixed base	0.253	0.058	0.035
3	flexible base	0.746	0.096	0.037
5	fixed base	0.222	0.053	0.032
5	flexible base	0.649	0.084	0.035
7	fixed base	0.203	0.050	0.029
7	flexible base	0.587	0.076	0.033
10	fixed base	0.187	0.048	0.026
10	flexible base	0.535	0.070	0.029

7.7.2 Nonlinear Pushover Analysis

Nonlinear pushover analysis is conducted by pushing on the model through displacement control, from the top node at the frame beam-column corner. Figure 7.5 shows the

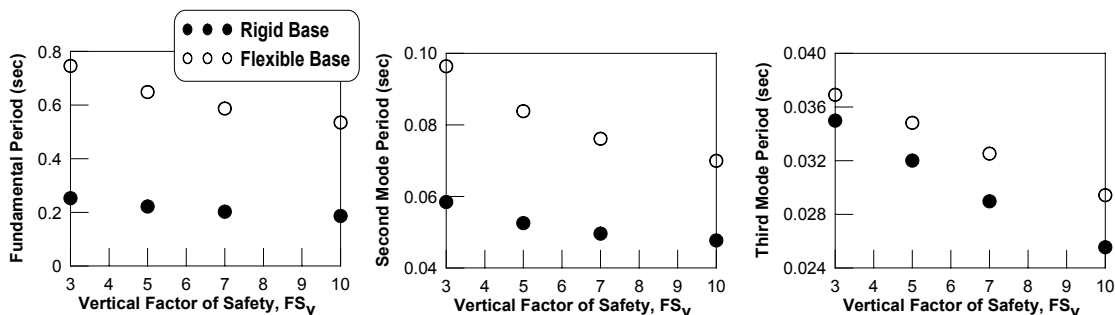


Figure 7.4: First three periods of the structures with different base conditions and factors of safety

nonlinear pushover response of the fixed base, elastic base and nonlinear base wall-frame models. The circles in Figure 7.5 denote the estimated first yield points of the various models. This is determined by tracking the reinforcing steel strains and footing spring force-displacement behavior, and identifying the global shear force and total drift at which the first yielding occur. In all of the cases, it is observed that the beam-column joints are reaching their yield curvatures prior to the foundation springs or columns. Note that nearly simultaneous yielding of all beam-column joints is occurring for the fixed base model, at approximately 0.13-0.15% total drift ratio, whereas subsequent yielding of elements are delayed for both the elastic and nonlinear base models as the load is redistributed to the foundation. For the elastic and nonlinear base systems, the first yielding occurs at a 0.33% drift ratio.

For comparison, Figure 7.6 shows the nonlinear pushover response of the frame only portion of the model (1 bay, 2 story) with the same foundation conditions. The more significant effect of the foundation on the nonlinear response of the wall-frame system is apparent, when compared with the frame only model. Moreover, the effect of the nonlinear base models are apparent. Note that the fundamental period of the frame only model is calculated as 0.41 sec and 0.71 sec for the $FS_v = 10$ case for the fixed and flexible base

conditions, respectively.

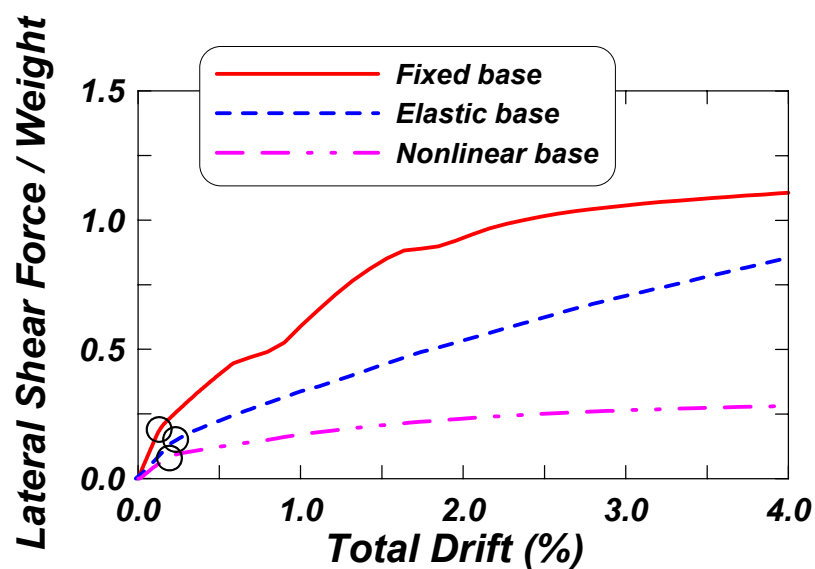


Figure 7.5: Nonlinear pushover response for the shearwall-frame-foundation system

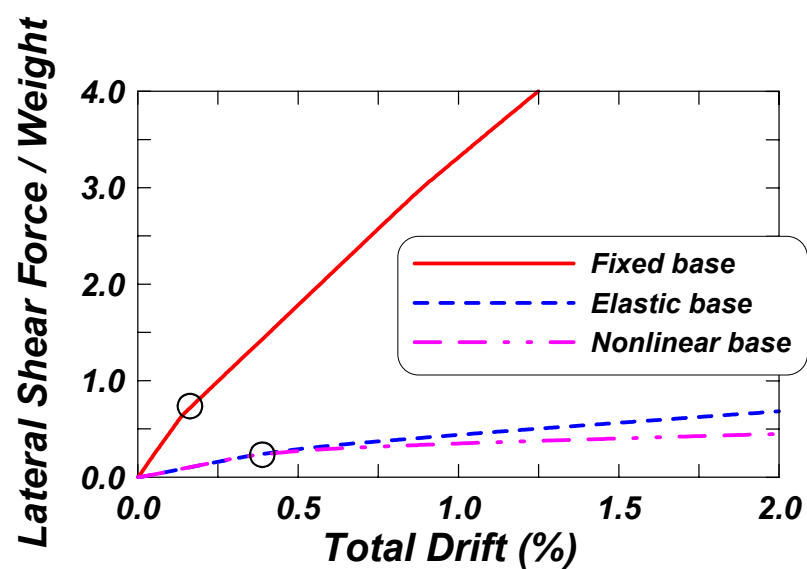


Figure 7.6: Nonlinear pushover response for the 'frame only' system

7.7.3 Time History Response

The dynamic analysis is carried out on the models using the ground motions described in Figure 7.4. The effect of base nonlinearity and factor of safety on the footing and structural response is evaluated by looking at the force and displacement time histories, peak demands and energy dissipation at the beam-column joints as well as at the soil-foundation interfaces.

Sample global force-displacement response for the Whittier and Landers motions are shown in Figure 7.7. These results are shown for the nonlinear foundation for $FS_v = 10$ and 3 cases. These time histories show that although the range of global lateral force absorbed by the system is fairly similar for the different FS_v cases, for each motion, the lower $FS_v = 3$ case results in much larger total drift demands (approximately twice that of the $FS_v = 10$ case).

For the same two motions, the time history responses of the footing forces and displacements are shown in Figures 7.8 and 7.9. Pairs of each figure, parts (a)-(b), parts (c)-(d) and parts (e)-(f) show responses for each of the strip footing, interior square footing, and exterior square footing, respectively. Note that in the case presented in Figures 7.9, instability of the structure is observed following the footing exceeding its theoretical moment capacity. These results also further illustrate the amplified response for the softer ($FS_v = 3.0$) footing systems, which is apparent for each of the strip, exterior square, and interior square footings. Note that the moment capacities for the strip footing are 444 kN and 144 kN for $FS_v = 10$ and $FS_v = 3$ cases, respectively. For the interior square footing, these capacities are 44 kN and 38 kN, respectively, whereas for the interior footing, the moment capacities are 22 kN and 25 kN, respectively. So, it is evident that the strip footing for

$FS_v = 3$ case reaches its design capacity and behaving as nonlinear when subjected to the Whittier motion.

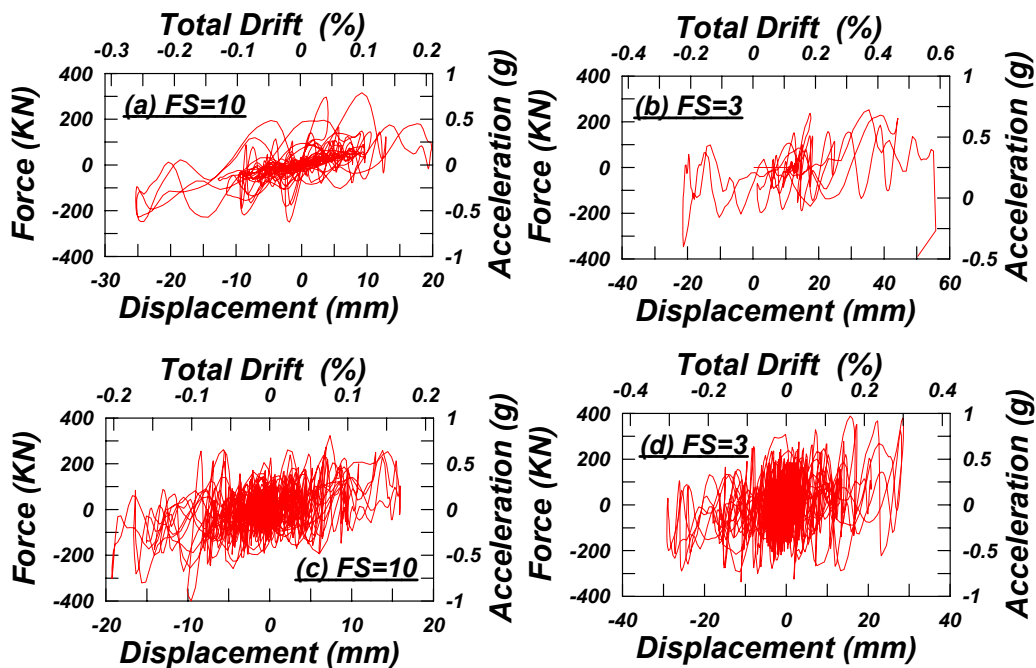


Figure 7.7: Global lateral force-displacement response of the wall-frame structure: Whittier motion (a) $FS_v = 10$ and (b) $FS_v = 3$ and Landers motion (a) $FS_v = 10$ and (b) $FS_v = 3$

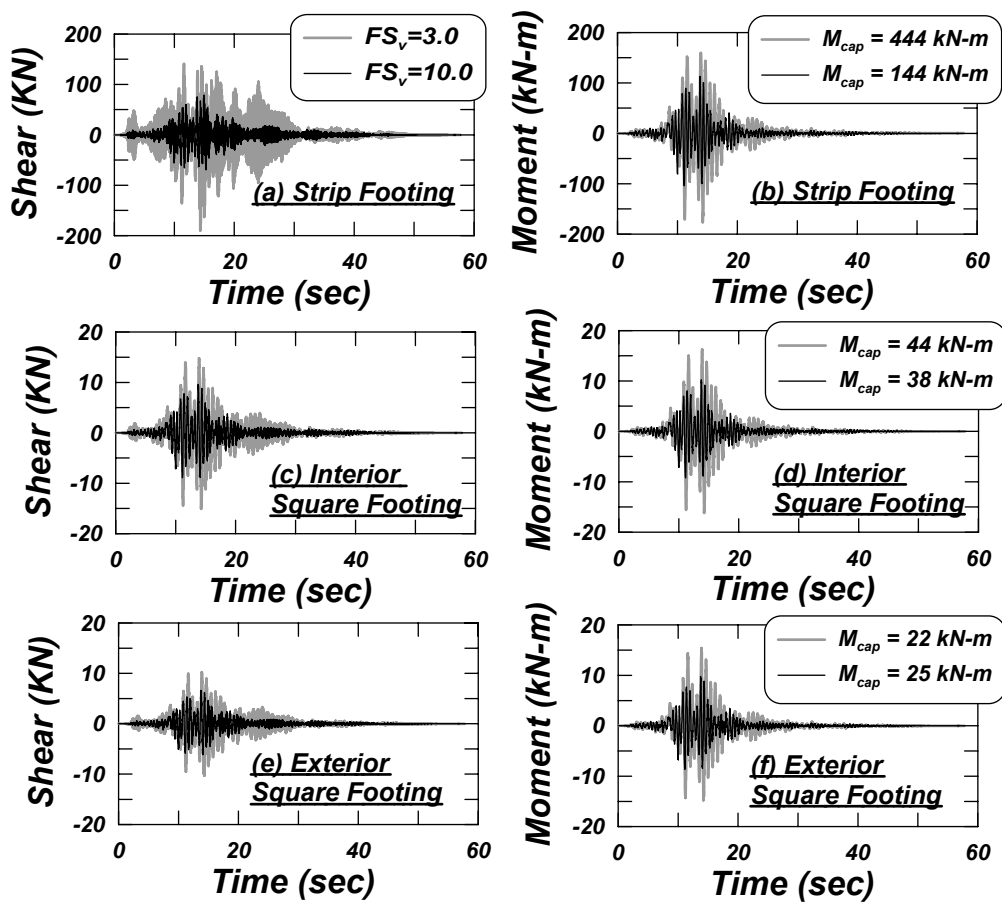


Figure 7.8: Shear and moment response of foundations - Landers Motion

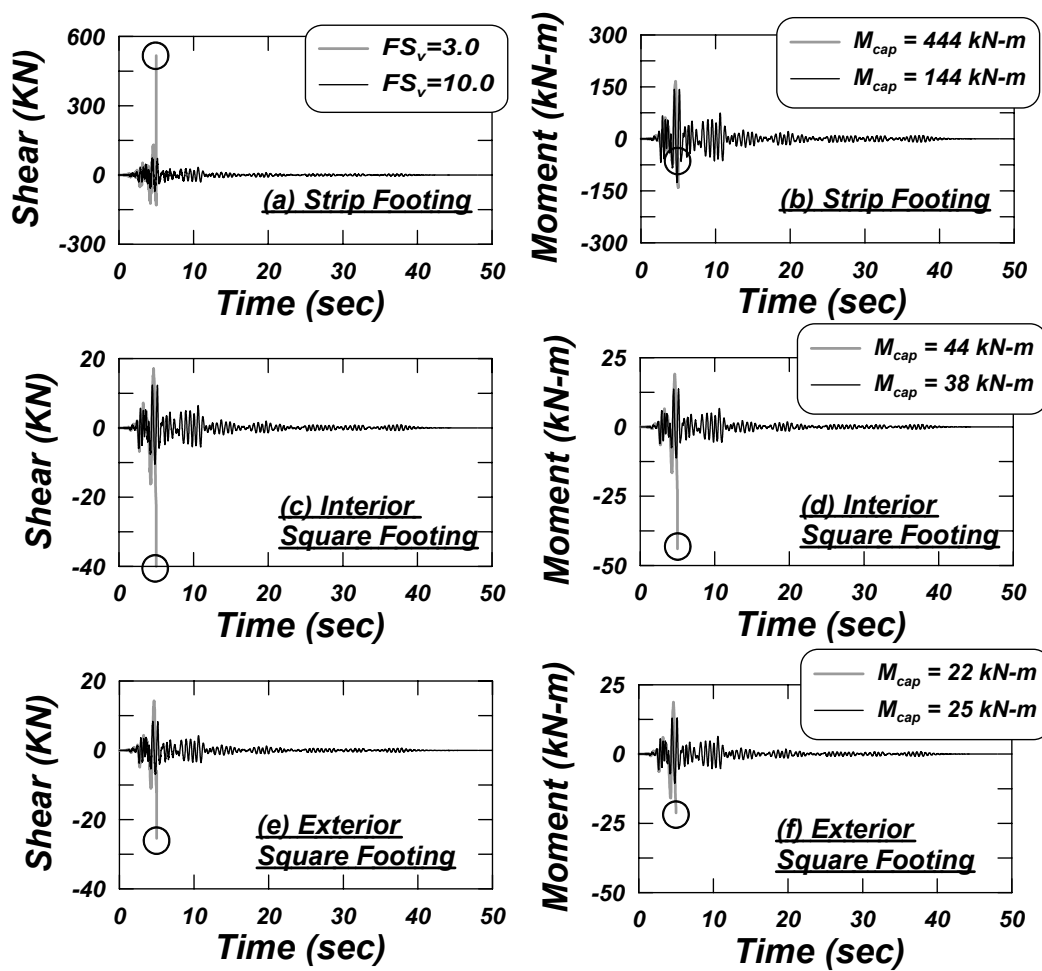


Figure 7.9: Shear and moment response of foundations - Whittier Motion

7.7.4 Response Parameters

Of interest in the design of building systems are response parameters such as the maximum inter-story drift ratio, maximum drift at the roof and foundation base shear and moments, to name a few. Figure 7.10 shows the variation in these four parameters, as a function of the varying foundation conditions for $FS_v = 10$ condition considering all ground motions. Figure 7.10 illustrates that in all cases, considering the foundation flexibility significantly reduces base shear, base moment, and inter-story drift due to the reduction in seismic force. However, the total drift increases if foundation flexibility is introduced either using elastic or nonlinear base conditions. This is due to the fact that the base flexibility gives rise to rocking and sliding of foundations resulting in increased total drift. However, it is observed that the nonlinear base case gives similar result to that considering the elastic base, because the foundation is not yielding for the given set of motions. Whereas for the heavier building ($FS_v = 3$ case), the nonlinear base case generally shows lower force demands and higher total drift demand than the elastic base case for most of the ground motion analyses (Figure 7.11). This makes sense, as the energy dissipated at the nonlinear base decreases the force demands and increases the displacement demands. Since in practice, FS_v is generally considered as $\approx 2-4$, it is presumptive that the footing will reduce force demands and increase displacement demands for these set of ground motions.

Although the force demand to the structure is reducing with nonlinear base, there are few potential consequences that need to be taken care of. In addition to the increase in total drift demand in the structure, the displacement demands in the foundation level may cause concern. Especially the differential settlement between two points can be detrimental for a building. In this building case for the considered ground motions, the maximum settle-

ment observed under the strip, interior and exterior square footings are 350mm, 254mm and 190mm, respectively. The distortion ratio ($= \Delta S_{max}/L$, where, ΔS_{max} is maximum differential settlement between two points, and L is the distance between those two points) between the strip footing and the interior square footing is calculated as 1/80. The distortion ratio for two column is observed as 1/120, whereas this ratio is 1/95 when considered between the shearwall and the exterior column. Note that the allowable limit of distortion ratio for most of the buildings is 1/150 (recommended by Bjerrum, 1977). The above mentioned observations are for the lowest factor of safety case; the higher factor of safety cases show lower absolute and differential settlements.

7.8 Summary Remarks

To study the effect of SFSI on a system level, a model retrofit shear wall is combined with a frame system, and the response of this structure is investigated using nonlinear dynamic time history analyses in this chapter. The effects of foundation rocking, sliding, and settling are incorporated by using a variety of foundation base conditions. In addition, varying vertical factors of safety at the base of the footings are used in the modeling, to evaluate the effects of the margin of safety in the foundation on the seismic response. Results indicate that if reliably quantified and designed, SFSI has great potential for reducing seismic forces and inter-story drift demands, by providing added energy dissipation to the building-foundation system. Moment demands at the base of the foundations were consistently reduced (by as much as 90 % of the fixed base moment) by incorporating SFSI.

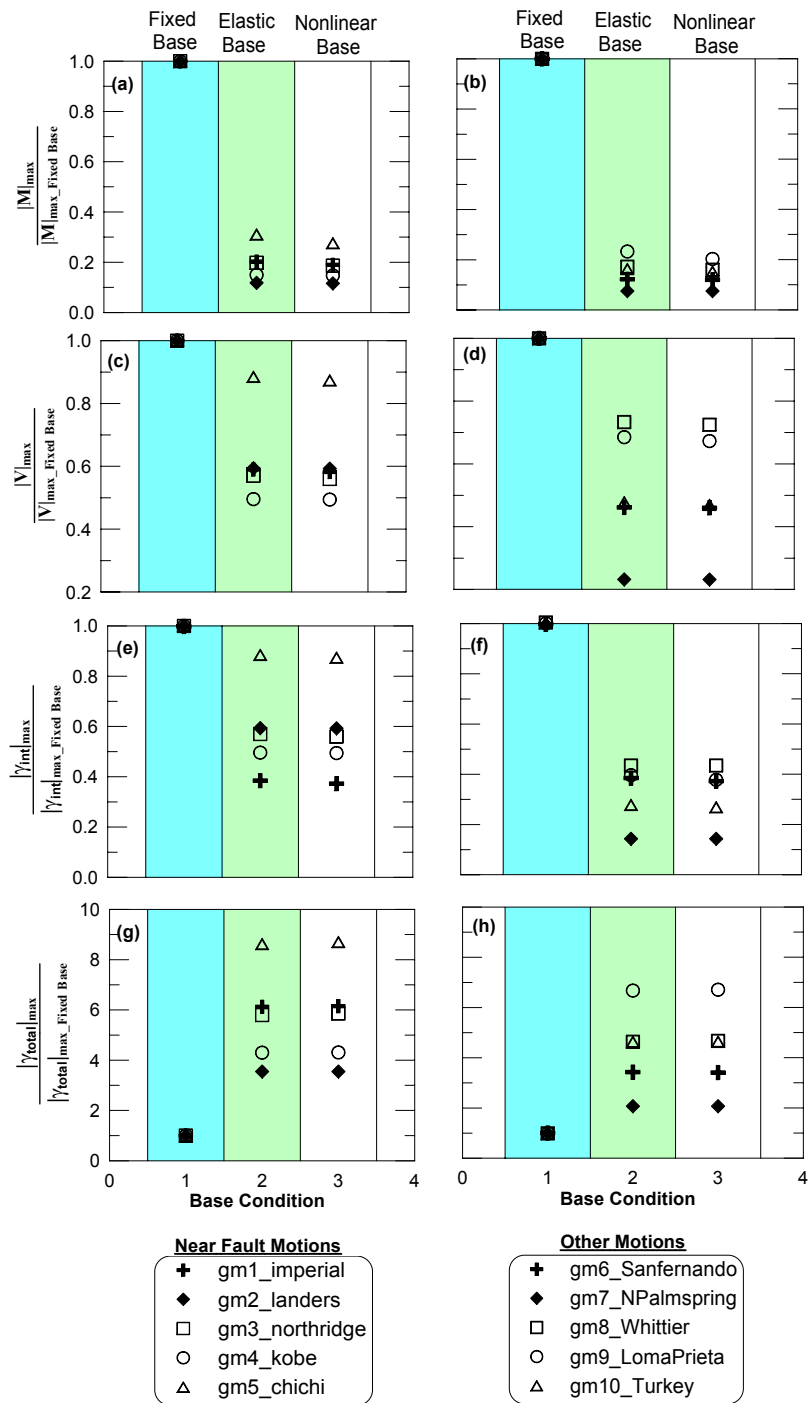


Figure 7.10: Variation of response parameters as a function of foundation condition: (a)–(b) normalized maximum moment, (c)–(d) normalized maximum shear force, (e)–(f) normalized maximum inter-story drift ratio and (g)–(h) normalized maximum total drift ratio for the building with $FS_v = 10$

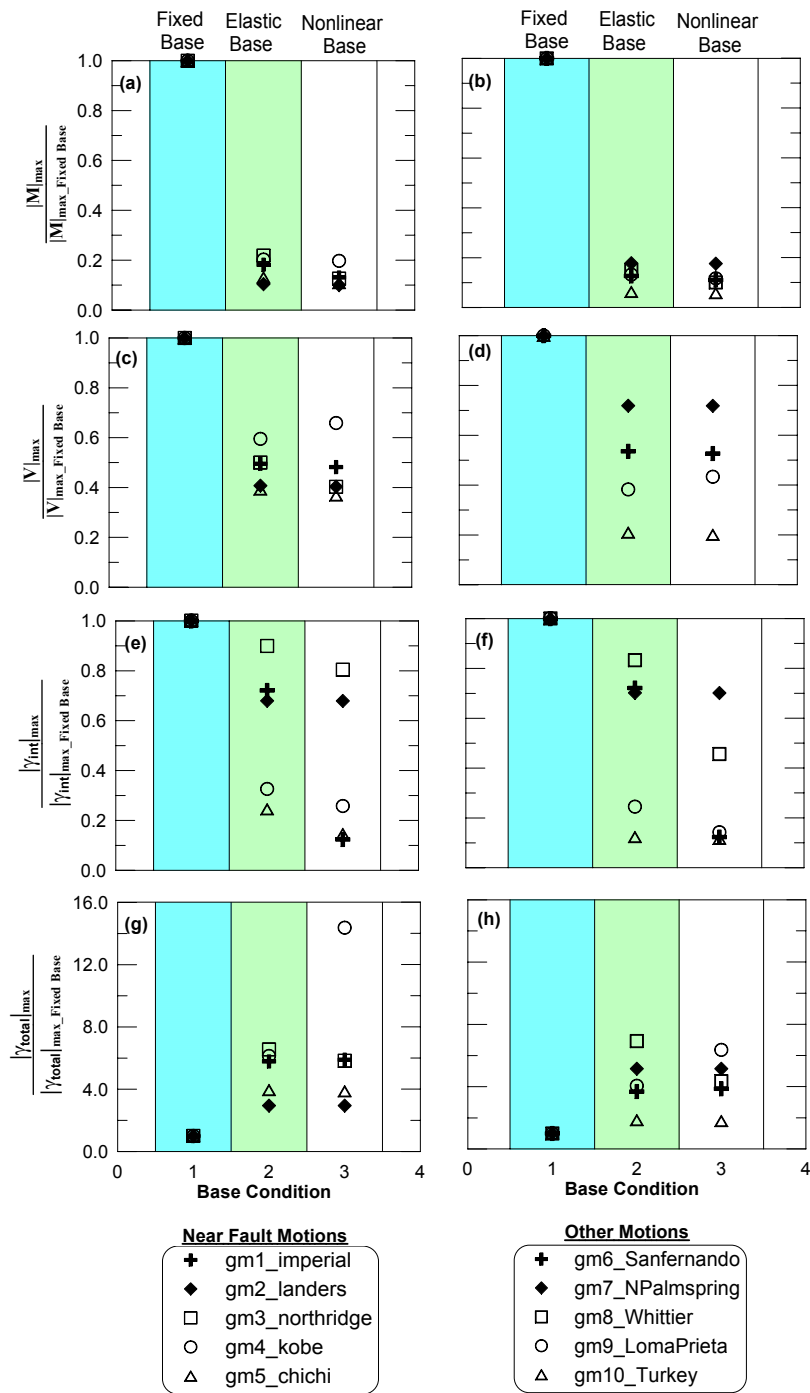


Figure 7.11: Variation of response parameters as a function of foundation condition: (a)–(b) normalized maximum moment, (c)–(d) normalized maximum shear force, (e)–(f) normalized maximum inter-story drift ratio and (g)–(h) normalized maximum total drift ratio for the building with $FS_v = 3$

Chapter 8

OpenSees Implementation

8.1 Introduction

OpenSees is an open source freeware platform developed in the collaborative environment of the Pacific Earthquake Engineering Research Center (PEER). OpenSees is selected due to the following reasons: (i) in its present form, it has a wide range of elements, material constitutive models, and analysis algorithms and (ii) more importantly, its open source nature gives the user the opportunity to add or modify its code easily to incorporate the latest state-of-the-art models. This chapter describes the implementation of the BNWF model in the OpenSees platform. To facilitate the model, a new command, *ShallowFoundationGen*, has been implemented.

In OpenSees, modeling of a shallow foundation using Beams on Nonlinear Winkler Foundation (BNWF) as shown in Figure 2.2 (Chapter 2) is a complicated and cumbersome task. This is because the modeling requires defining (i) the node numbers and corresponding coordinates for foundation elements and zero length elements (p-x, t-x and q-z), (ii) material type and properties of each created elements and (iii) nodal fixity. Currently, this

is achieved by writing many lines of Tcl scripts. For systems with multiple shallow foundations, the procedure becomes even more cumbersome and confusing as one has to keep track of node and element number manually or needs to employ a systematic numbering scheme. The *ShallowFoundationGen* command, which has been implemented in to the OpenSees program, overcomes the above-mentioned difficulties in a very simple and elegant way, while adding some extra modeling options. These options allow a user some flexibility without altering the input file to choose different types of foundation behavior, which are generally required while investigating the effect of SSI in the response of a structure. In addition, the command returns some of the important variables, such as the element numbers required to determine the general response of the foundation.

A brief discussion of the hierarchy of the implementation in OpenSees, using existing elements and materials in OpenSees is presented. Subsequently, the command sequence is discussed and the use of *ShallowFoundationGen* to model soil-foundation systems is demonstrated by two example problems. The first example deals with a shearwall supported on a strip footing system (single foundation) and the second example demonstrates the use of multiple foundations. Input files, master tcl scripts and the OpenSees generated output files for these two examples are presented in the Appendix D.

8.2 OpenSees

The OpenSees software is developed in C++ and wrapped in as scripting language Tcl/Tk Tcl/Tk (2008). One important feature of this software is that it is an object-oriented framework and the components of this frameworks are easily interchangeable. It has three major types of objects: Model Building objects, Recorder objects and Analysis objects

(Figure 8.1). The Model Builder object builds the mesh and defines the nodes, elements, materials, constraints, load patterns etc. The analysis object performs the analysis using the specified solution algorithm, integrator, constraint handler, and solver. The Recorder object records the analysis results in output files as specified by the user. Figure 8.1 hierarchically presents the elements of OpenSees, as they are structured in their class framework, with the *ShallowFoundationGen* command integrated.

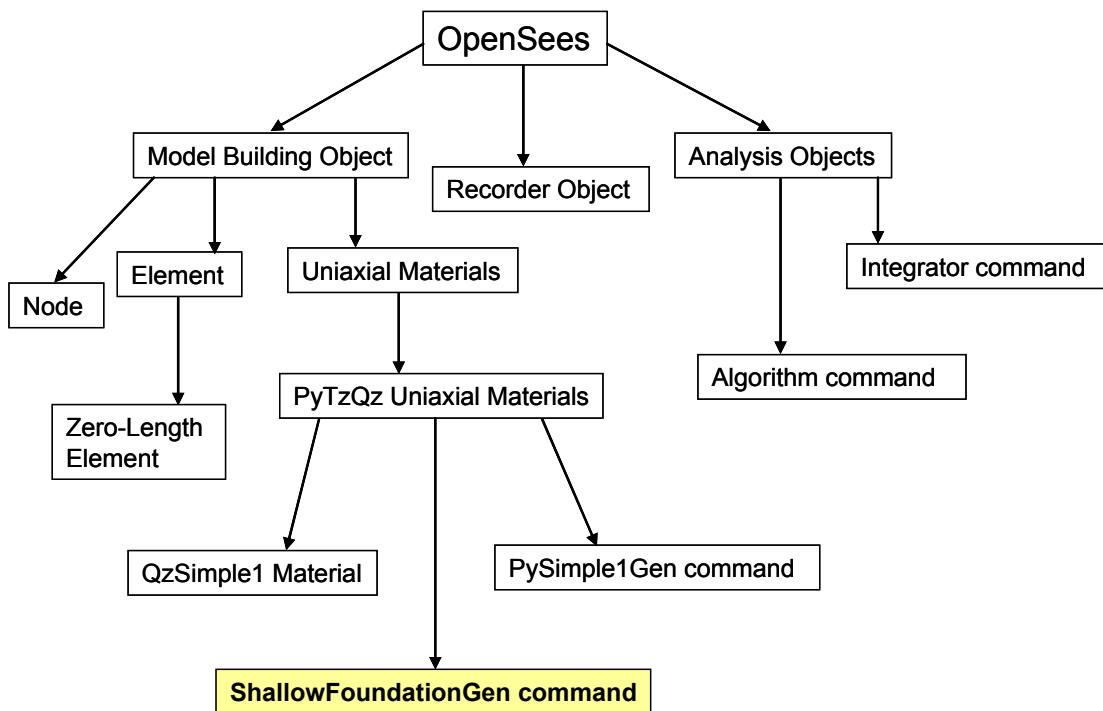


Figure 8.1: Part of the OpenSees class hierarchy

8.3 *ShallowFoundationGen* Command

The *ShallowFoundationGen* command, which requires four arguments, is invoked as follows:

***ShallowFoundationGen* \$FoundationTag \$ConnectNode \$InputFile \$FootingCondition**

The first argument is a tag associated with the foundation under consideration. The second argument is the node tag of the structural node that is to be connected with the middle node of the foundation. The third argument is the name of the input file, which contains soil and foundation properties that are required to define the springs of the Winkler mesh. The fourth argument, which provides some extra modeling options, is the foundation condition tag. The foundation condition tag specifies whether the foundation is modeled as fixed base, elastic or nonlinear. The command *ShallowFoundationGen* creates a Tcl output file with all information needed to describe the foundation, including the nodes, footing elements, spring zerolength elements and necessary materials to define those elements. This is then sourced in the next line of the master Tcl source file. Sample scripts demonstrating the use of *ShallowFoundationGen* are provided in Appendix D.

8.3.1 Argument 1: \$FoundationTag

The foundation tag is an integer number denoting the foundation number. The output file generated by the *ShallowFoundationGen* command will be named as per the foundation tag specified. For example, if a structure has three shallow foundations, and the foundations are numbered as 1, 2 and 3, then the foundation tags for those three foundations would be 1, 2 and 3, respectively, and the OpenSees generated output files will automatically be named as “*Foundation_1.tcl*”, “*Foundation_2.tcl*” and “*Foundation_3.tcl*”, respectively.

8.3.2 Argument 2: \$ConnectNode

The analyst has to specify the node of the structure that is to be connected with the middle node of the foundation. Note that the code assumes that the structure is supported at the center of a symmetric footing. For example, if the user specifies the *ConnectNode* to

be 1, node 1 will be connected to the mid node of the shallow foundation, and the degrees of freedom of these two nodes will be the same (i.e. same generalized displacements for these two nodes).

8.3.3 Argument 3: \$InputFile

The analyst must provide an input file containing the soil and footing properties required to calculate the strength and stiffness parameters for the BNWF springs. The name of the file can be arbitrary. The first uncommented line (lines that do not begin with #) of this file should contain parameters describing the soil in the following sequence:

SoilProp \$SoilType \$c \$φ \$γ \$G \$ν \$c_{rad} \$TP

where Soil type = type of soil, i.e., sand or clay should be denoted by number 1 or 2, where Soil type = 1 represents clay and Soil type = 2 represents sand; c = cohesion, φ = friction angle (in degrees), γ = soil unit weight, G = shear modulus, ν = Poisson's ratio, c_{rad} = viscous damping term to represent radiation damping effect, TP = tension capacity (in fraction).

Tension capacity for the axial springs (QzSimple1 material) is calculated as the user input fraction multiplied by the total bearing capacity. A maximum of 10% tension capacity can be provided. If the user provides a tension capacity greater than 10%, then the OpenSees will automatically consider it as 10% of total bearing (axial) capacity. Note also, unloading stiffness is not provided as input as it is assumed to be equal to the loading stiffness of a vertical or lateral spring.

Using the aforementioned parameters, capacity and stiffness of the foundation are calculated. For vertical QzSimple2 springs, the ultimate bearing capacity is calculated based

on the general bearing capacity equation (Equation 2.5). For the PxSimple1 material, the ultimate lateral load capacity is determined as the total passive resisting force acting on the front side of the embedded footing (Equation 2.19). For the TxSimple1 material, the lateral capacity is the total sliding resistance (Equation 2.20). The vertical and lateral stiffness are calculated using expressions given by Gazetas (1991c)

Alternatively, the command *CapSoil* can be invoked, signifying that the user can input strength and stiffness directly. The command requires the following input in the given sequence:

CapSoil Q_{ult} P_{ult} T_{ult} K_v K_h

where Q_{ult} = vertical load bearing capacity, P_{ult} = passive load resistance capacity, T_{ult} = sliding load resistance capacity, K_v = vertical stiffness of footing and K_h = lateral stiffness of footing. The units load and stiffness parameters must be consistent.

The next line of the input file contains essential footing dimensions and properties given in the following sequence:

FootProp L_f B_f H_f D_f E_f W_g β

where L_f = length of footing, B_f = width of footing, H_f = height of footing, D_f = depth of embedment, E_f = Young's modulus for footing material, β = inclination of the load on the foundation with respect to vertical, (in degree).

The final line of the input file requires important parameters regarding the mesh generation that are to be specified by the user in the following sequence:

MeshProp R_k R_e l_e/L_f

where R_k = stiffness intensity ratio (k_{end}/k_{mid}), R_e = end length ratio (L_{end}/L_f) and l_e/L_f = vertical spring spacing as a fraction of total footing length. In the implementation, the recommendation of Harden et al. (2005) is used when providing R_e and R_k . The length of each element is also a user-defined parameter. The user has to specify the fraction of the element length with respect to the total footing length.

8.3.4 Argument 4: \$FootingCondition

The user has the option of defining a variety of foundation conditions by providing an integer value from 1 to 5 (Figure 8.2), where:

- \$FootingCondition = 1: fixed in x, z and θ degrees of freedom
- \$FootingCondition = 2: linear elastic in z and θ , fixed in x degrees of freedom
- \$FootingCondition = 3: linear elastic in x, z and θ degrees of freedom
- \$FootingCondition = 4: nonlinear, inelastic in z and θ degree of freedom, fixed in x degrees of freedom
- \$FootingCondition = 5: nonlinear, inelastic in x, z and θ degrees of freedom

Condition 1 means the foundation will be rigid, and therefore no displacement will be allowed. Condition 2 will generate a mesh of vertical linear, elastic springs interconnected with linear elastic beam-column elements to represent the footing. However, the footing will be restrained from lateral movement. Condition 3 is similar to condition 2, with the addition of linear elastic response in the lateral direction. Condition 4 will use a modified version of the nonlinear springs (QzSimple2 material) introduced by Boulanger et al.

(1999) and with modifications by Raychowdhury and Hutchinson (2008) in the vertical direction to account for inelastic axial and rocking movement of the footing. The footing will be restrained against sliding in this case. The fifth condition (Condition 5) will be similar to the fourth, with the addition of two inelastic springs (PxSimple1 and TxSimple1) to model lateral movement Figure 2.2.

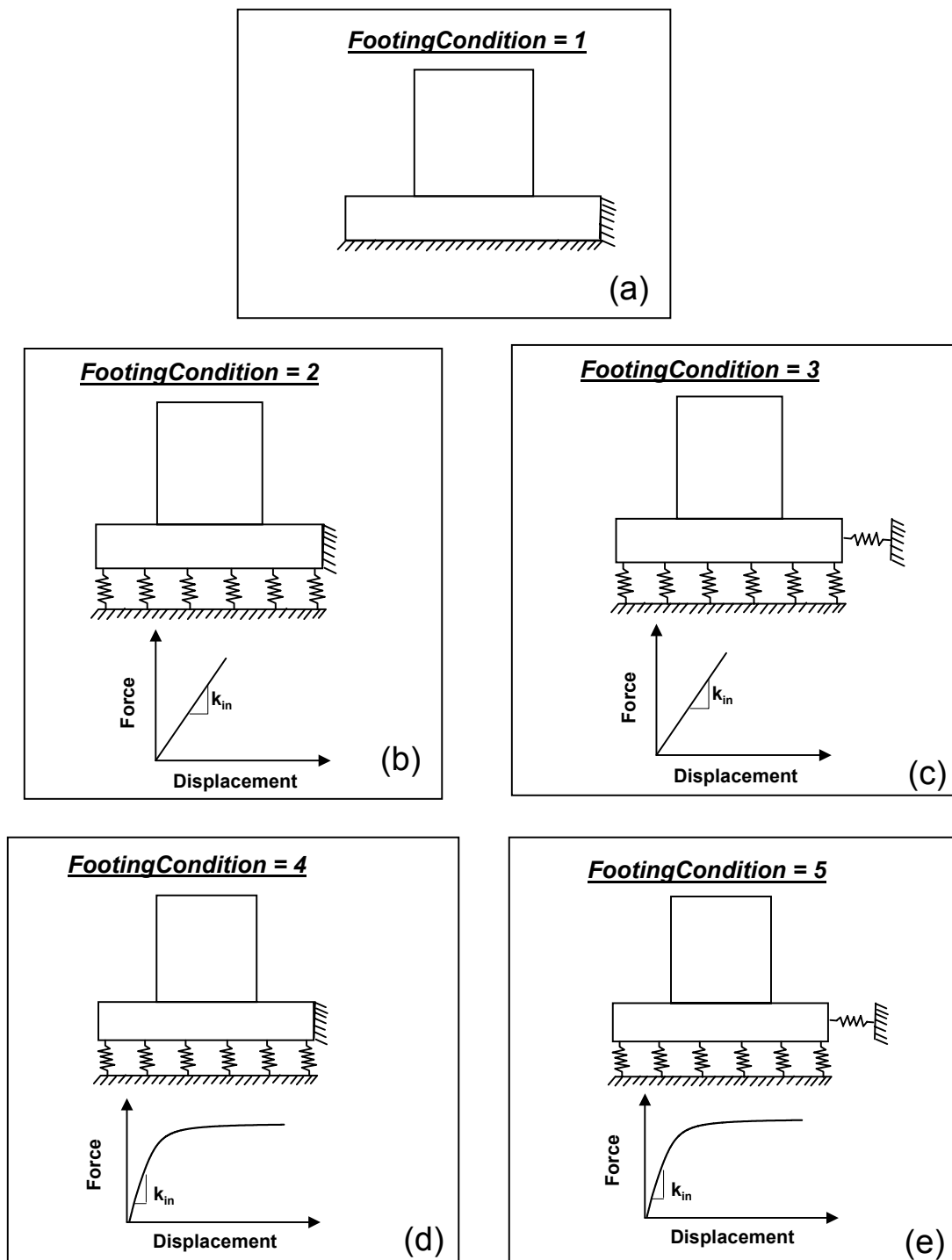


Figure 8.2: Different footing conditions: (a) Fixed base, (b) Elastic base sliding restricted, (c) Elastic base with sliding allowed, (d) Nonlinear base sliding restricted and (e) Nonlinear base with nonlinear sliding allowed

8.4 Important Implementation Details

To balance simplicity and numbering needed, a systematic node, element and material type numbering scheme is used in the *ShallowFoundationGen* command. The details of the numbering scheme are as follows:

8.4.1 Node Numbering

If the foundation tag is 1, then the footing node numbers will start from 1001 and the connecting spring node numbers will start from 100001. Similarly, for the second foundation (foundation tag 2), the footing node numbers will start from 2001 and connecting spring node numbers will start from 200001. Note that by following this numbering scheme, it has been assumed that the last node tag used in the structure is less than 1001 and the maximum number of nodes in a single foundation should not exceed 99000.

8.4.2 Material Numbering

The material tags in *ShallowFoundationGen* start from 101, which implies that the material tags used in the structure must be less than (or equal to) 100 to avoid confusion with the material tags used for the foundation springs. If there is more than one foundation to be analyzed, then for the foundation with tag 1, the material tags will start from 101, while for the second foundation (foundation tag 2), the material tag will automatically start from 201. The material tags for different footing conditions are specified in the following fashion. For the fixed base case ($\text{FootingCondition} = 1$), no additional elements will be created, and the foundation will be fixed against vertical, horizontal and rotational movements. For $\text{FootingCondition} = 2$, three types of foundation materials will be created, namely mater-

ial tags for the two extreme end springs, other end zone springs and the mid zone springs defined as 101, 102 and 103, respectively (Figure 8.3). Creating the three types of vertical springs allows the generator to account for variation in spring spacing (a corresponding tributary area variation within the different regions). In addition, the extreme end springs will have one-half of the tributary area of the other end springs and thus half the stiffness and capacity.

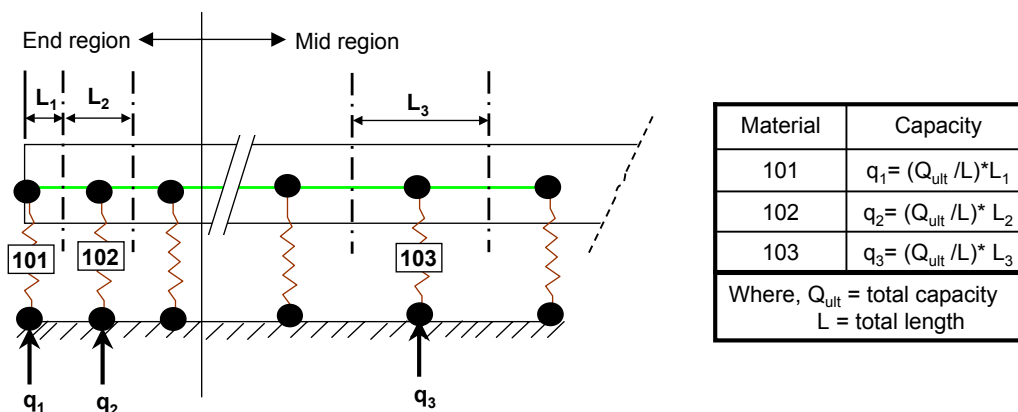


Figure 8.3: Tributary area capacity calculation

For the FootingCondition = 3, in addition to the vertical elastic springs, one horizontal elastic spring is introduced (with material tag =104). The material tag assignment for the FootingCondition = 4 case is similar to FootingCondition = 2 case, except the springs assigned in this case are nonlinear QzSimple2 springs. FootingCondition = 5 is similar to FootingCondition = 4, with the addition of two nonlinear horizontal springs provided at the ends of the footing: one is a TxSimple1 spring to account for sliding behavior and the another a PxSimple1 spring to account for passive pressure for embedded footings (Figure 2.2). The material tag for PxSimple1 is assigned as 105 and that for TxSimple1 is assigned as 106. Table 8.4.2 summarizes the material tag assignments for the various footing conditions.

Table 8.1: Material Tag assignment for the various footing conditions

Material Tag	Spring Description	\$FootCondition applicable
101	Vertical springs (Elastic/ QzSimple2) at two extreme ends	2, 3, 4, 5
102	Vertical springs (Elastic/ QzSimple2) at end region	2, 3, 4, 5
103	Vertical springs (Elastic/ QzSimple2) at mid region	2, 3, 4, 5
104	Lateral spring (Elastic)	3
105	Lateral spring (PySimple2)	5
106	Lateral spring (TzSimple2)	5

8.4.3 Element Numbering

The elements are numbered following a method similar to the node numbering scheme (Figure 8.4). The footing elements (elastic beam-column elements) are numbered starting with 1001 for a foundation with FoundationTag = 1. The numbering is assigned from left to right. The zerolength springs are numbered starting from 100001 from left to right for a foundation with FoundationTag = 1.

8.4.4 Geometric Transfer Tag

To avoid confusion between the transfer tags provided in the structure with those provided in the foundation, the geometric transfer tags in the foundation begins with 10, assuming that the maximum number of transfer tags given in the structure will not exceed 9. The geometric transfer tag of a foundation with FoundationTag = 1 will be assigned a geometric transfer tag = 10 automatically. Similarly foundations with FoundationTag = 2 and 3 will be assigned the geometric transfer tag = 20 and 30, respectively. Herein, the

geometric transfer tag is assumed to be a linear transfer tag.

8.4.5 Some Useful Variables

The command generates some useful variables that are usually required for evaluating foundation response. These are as follows:

1. `endFootNodeL_$FoundationTag`: extreme left end node for the foundation associated with any `FoundationTag`
2. `endFootNodeR_$FoundationTag`: extreme right end node for the foundation associated with any `FoundationTag`
3. `endSprEleL_$FoundationTag`: extreme left end vertical spring element for the foundation associated with any `FoundationTag`
4. `endSprEleR_$FoundationTag`: extreme right end vertical spring element for the foundation associated with any `FoundationTag`
5. `midSprEle_$FoundationTag`: middle vertical spring element for the foundation associated with any `FoundationTag`

8.4.6 Example Problems

Two example problems are described to illustrate the use of the `ShallowFoundationGen` command. One is a shearwall building supported by a single strip footing. The second example is of a single-story single-bay frame, the columns of which are supported by two square footings. The following subsections discuss the example problems along with the

node and element generation schemes. The input files, master tcl files and OpenSees generated output files are presented in Appendix D.

8.4.6.1 Example 1: Shearwall Supported by a Strip Footing

Figure 8.4 schematically shows an example single shearwall resting on a strip footing. The footing condition = 5 case is used in this example. Element numbers are shown in circles, while node numbers are not. The foundation tag given here is 1, so the foundation node numbers start from 1001 automatically. The footing element numbers will also be designated from 1001, while the spring end nodes and spring elements will be numbered from 100001. The footing input parameters are shown in File-1. The master tcl file to describe the structure and call the ShallowFoundationGen command is shown in File-2. File-3 shows the tcl file that is generated by the ShallowFoundationGen command. The shearwall-footing system is subjected to and analyzed for a simple monotonic lateral push and the results obtained are shown in Figure 8.5.

8.4.6.2 Example 2: Frame Supported by Two Square Footings

In this example, a multi-foundation system is analyzed. The system consists a single-story single-bay frame. The two columns of the frame are supported by two isolated footings of different sizes. The foundation tags for the two foundations are 1 and 2 (Figure 8.6 and Figure 8.7). Here, the ShallowFoundationGen command is used twice within the main code to create two different output files “*Foundation_1.tcl*” and “*Foundation_2.tcl*” for the two shallow foundations, respectively. In this example, two different footing conditions are used for two footings to demonstrate the different spring responses. Footing-1 is assigned $\$FootingCondition = 5$, while Footing-2 is assigned with $\$FootingCondition = 4$,

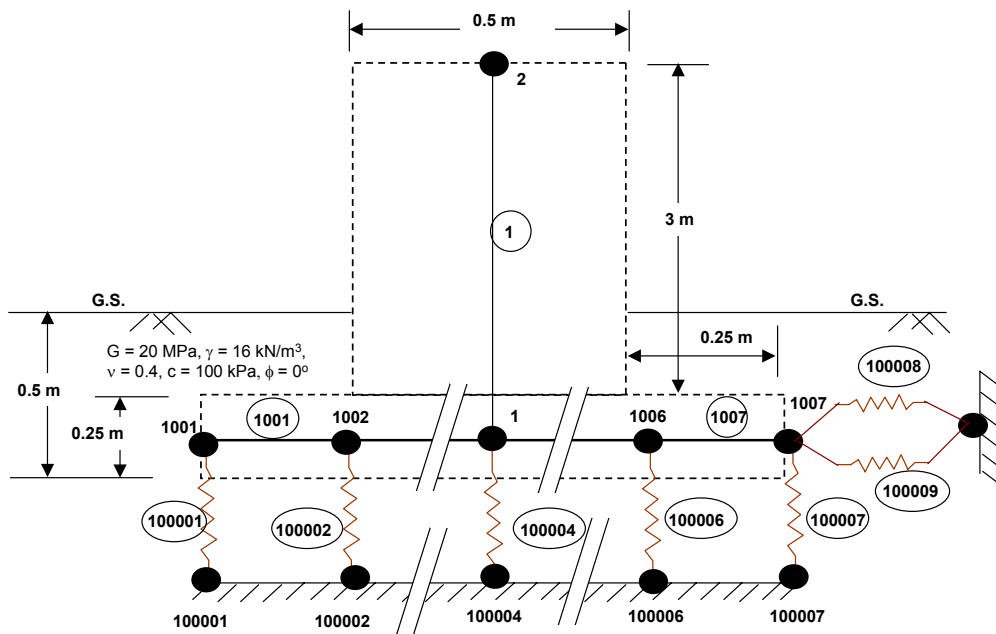


Figure 8.4: Example 1: Shearwall resting on a strip footing

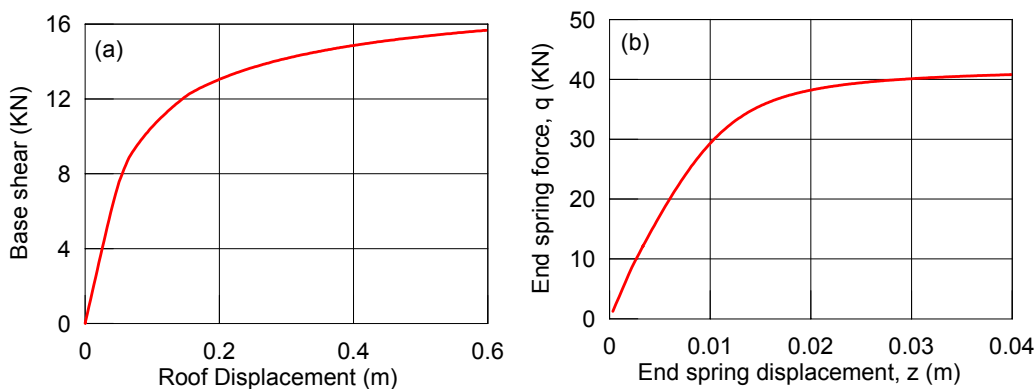


Figure 8.5: Results for (a) Wall force-displacement response (b) Extreme end vertical spring response (Example 1)

i.e. that sliding restrained case assuming that this foundation is attached to a larger foundation system. Figure 8.8 shows the results of half cycle of push-pull applied to the frame structure.

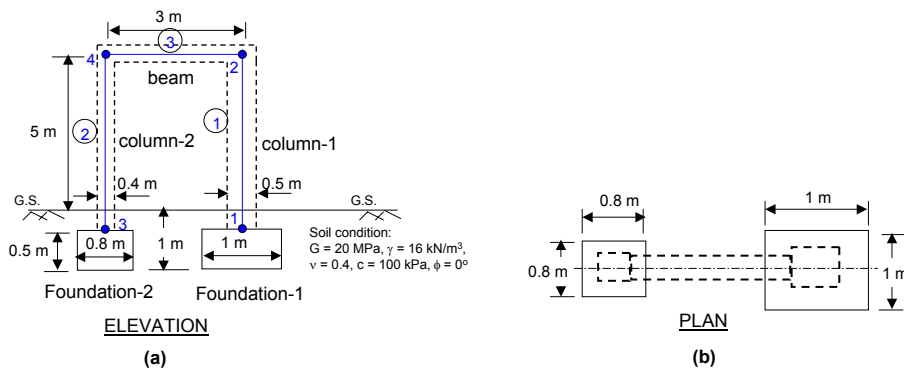


Figure 8.6: Example 2:(a) Elevation and (b) Plan of the single-bay frame

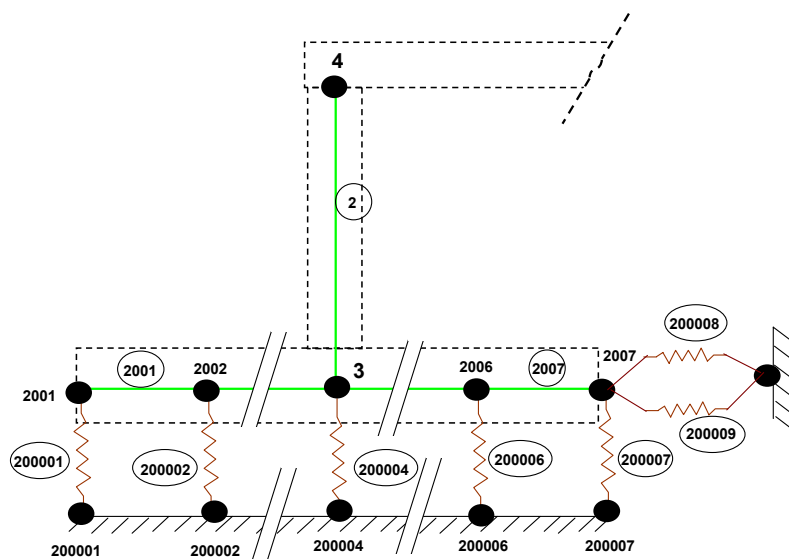


Figure 8.7: Example 2: Node and element configuration for foundation-2 and column-2

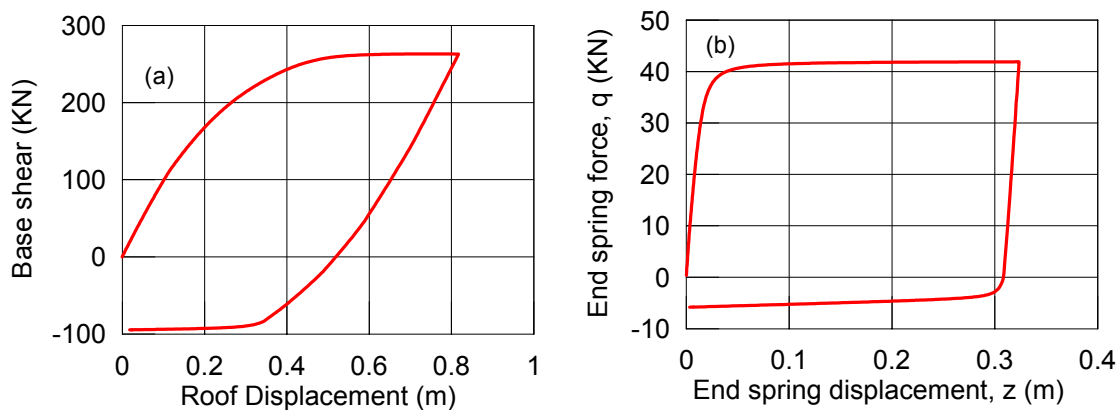


Figure 8.8: Example 2: (a)Force-displacement response (b) Extreme end vertical spring response

Chapter 9

Summary and Conclusions

9.1 Summary

A structure resting on a shallow foundation system has the potential to dissipate energy through various footing displacement modes such as sliding, settlement and rocking, when subjected to earthquake ground motions. This energy dissipation can be beneficial in terms of reducing the force demand to the superstructure if the adverse consequences on the foundation (e.g. excessive permanent or transient settlement, sliding, rocking or bearing failure), as well as on the structure (e.g. excessive displacement demands at the beam-column joints of a framed structure) can be properly considered in the design. For proper consideration in design, a suitable modeling tool is needed.

In this work, the soil-foundation-interface is modeled using an assembly of discrete, nonlinear Winkler elements composed of springs, dashpots and gap elements. The numerical model, known as a Beam-on-Nonlinear-Winkler-Foundation (BNWF) is intended to capture the moment–rotation, shear–sliding and axial force–settlement behavior of shallow foundations realistically. Backbone curves typically used for modeling soil–pile response

are used as a baseline and then further modified for their usefulness in shallow footing modeling, by calibrating against a variety of shallow foundation tests. The model is validated against a set of centrifuge test data on shallow footings involving square and strip footings, bridge and building models, static and dynamic loading, sand and clay tests, a range of vertical factors of safety and aspect ratios. The important parameters involved in the BNWF modeling are identified and a sensitivity study has been carried out using tornado diagram analysis and the First-Order-Second-Moment (FOSM) method to determine the effect of these parameters on the overall foundation response. The effect of soil-foundation-structure-interaction (SFSI) on shearwall-footing system and shearwall-frame-footing systems is then evaluated by exercising the model. Finally, the model developed in this work has been implemented within the framework of OpenSees (an open source software developed by Pacific Earthquake Engineering Research center (PEER) for earthquake engineering simulations) for use by the engineering community and researchers.

9.2 Major Conclusions

Based on this work, the following specific conclusions are drawn:

- The BNWF model response compares reasonably with the experiments in terms of capturing moment, shear, settlement and rotational demands, and shape of moment-rotation, settlement-rotation and shear-sliding curves. However, the primary inadequacy observed is in predicting sliding demand. It is generally observed that the BNWF model under estimates the sliding demand when compared with that obtained from experiments. This may be due to the lack of coupling between the vertical and lateral modes of response. Moment demand is also slightly under-predicted using

the proposed model in some cases. This may be due to the inability of the model to capture the increase of soil capacity from previous loading cycles and ignoring the side friction at the front of the footing.

- Among the parameters related to BNWF model input, the tension capacity has the most significant effect on the force and displacement demands of the footing. Other parameters having considerable effect on the footing response are the friction angle, stiffness intensity, and spring spacing. The footing response is least sensitive to Poisson's ratio. For soils with little to no tension capacity, response of the footing is mostly controlled by the friction angle.
- It is observed from the shearwall-foundation analyses that SFSI is able to significantly reduce the force demand to the structure. The energy dissipated in the sliding mode is dominant for stiffer (and shorter) shearwall structures, while energy dissipated in the rocking mode has a larger relative contribution for taller and higher period structures. Short structures dissipate $\approx 50\text{-}80\%$ of total energy through sliding, while taller structures dissipate $\approx 10\text{-}20\%$ through sliding and the remainder through rocking. It is also observed that the maximum transient settlement and sliding demands for an elastic base foundation are much lower than that of a nonlinear base.
- The shearwall-frame-foundation structure also indicates the reduction in force demand to the structure, when the effect of SFSI is considered. Moment demands at the base of the foundations are consistently reduced (by as much as 90 % of the fixed base moment) by incorporating SFSI.

9.3 Scope of Future Work

The following issues should be considered in the future:

- The backbones for the material models are currently defined for pure sand or pure clay. The backbone curves for $c - \phi$ soils may be developed by calibrating against tests on soils having both cohesion and friction (such as silt, sandy clay or clayey sand).
- It has been observed in the study that the proposed BNWF model under predicts the sliding response. The model needs to be improved by introducing a form of coupling between different modes of response.
- For the sensitivity analysis, simple methods like the tornado diagram analysis and the FOSM analysis methods are used, which have some limitations such as the assumption of a linear relation between the response and input random variables. However, in this study, some of the input variables showed moderately nonlinear variation with different response parameters. Detailed and more accurate methods such as Monte-carlo simulations can be used to verify the variability of footing response due to uncertainty in the model parameters.
- For this study, only competent soils, such as medium to dense dry sand and medium clay are considered. Exercising this model to evaluate the behavior of shallow foundations in incompetent soil such as liquefiable, unstable or reduced-strength soils may be a further scope of investigation.
- The current model is two-dimensional. It could be extended to represent the three-dimensional behavior of a typical soil-foundation interface system.

Appendix A

Normalized Footing Demands

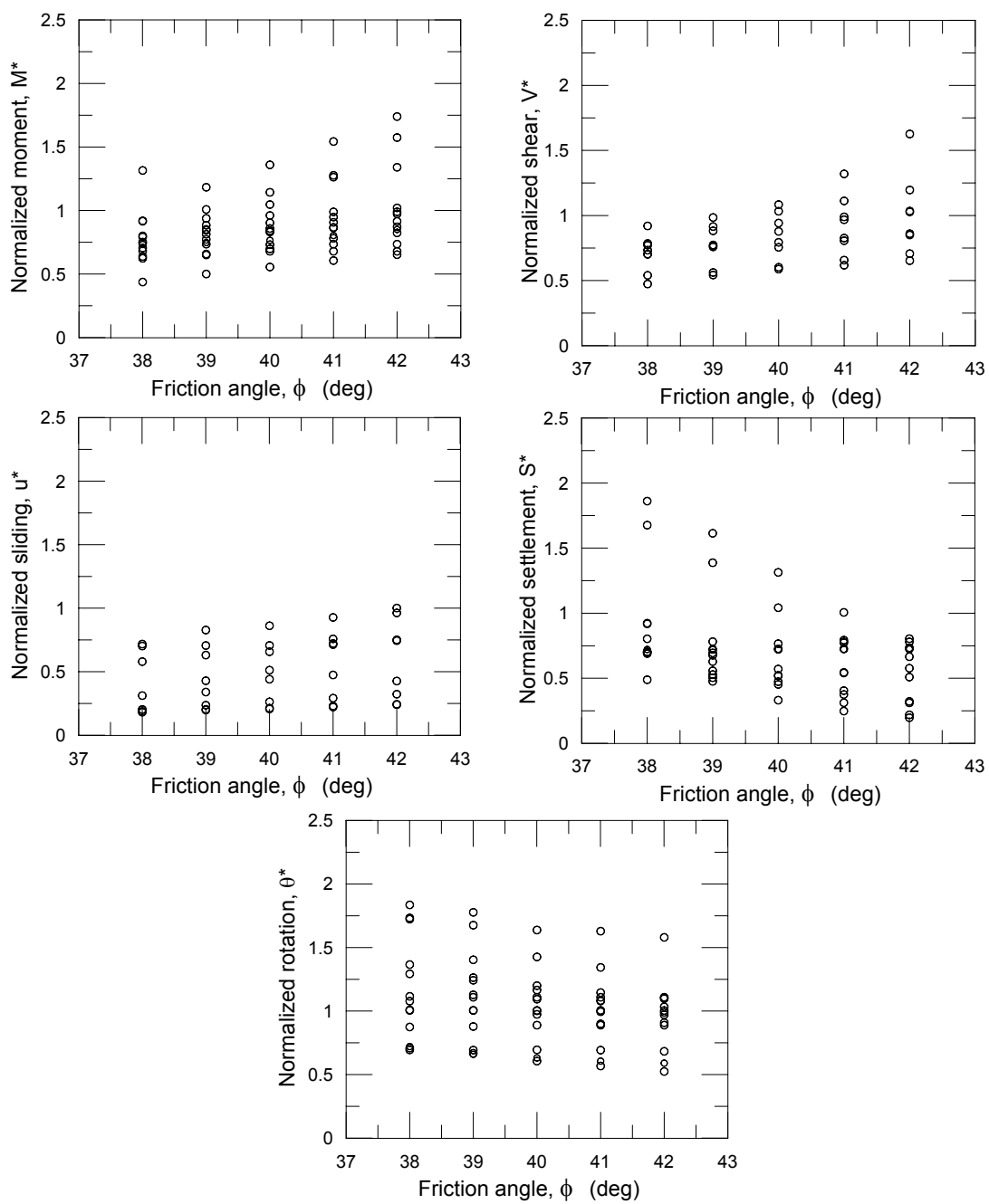


Figure A.1: Normalized demands for all tests (with varying ϕ)

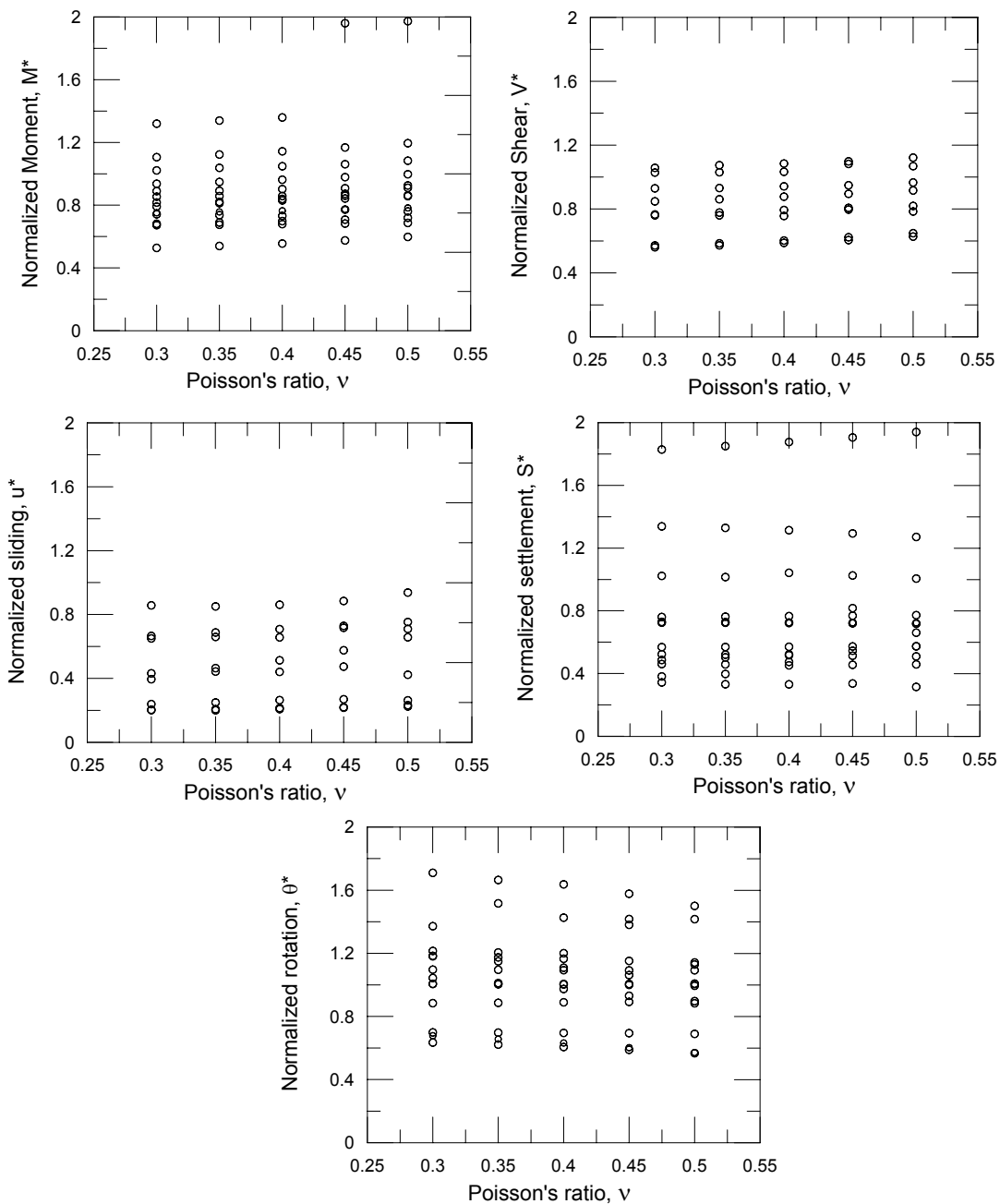


Figure A.2: Normalized demands for all tests (with varying ν)

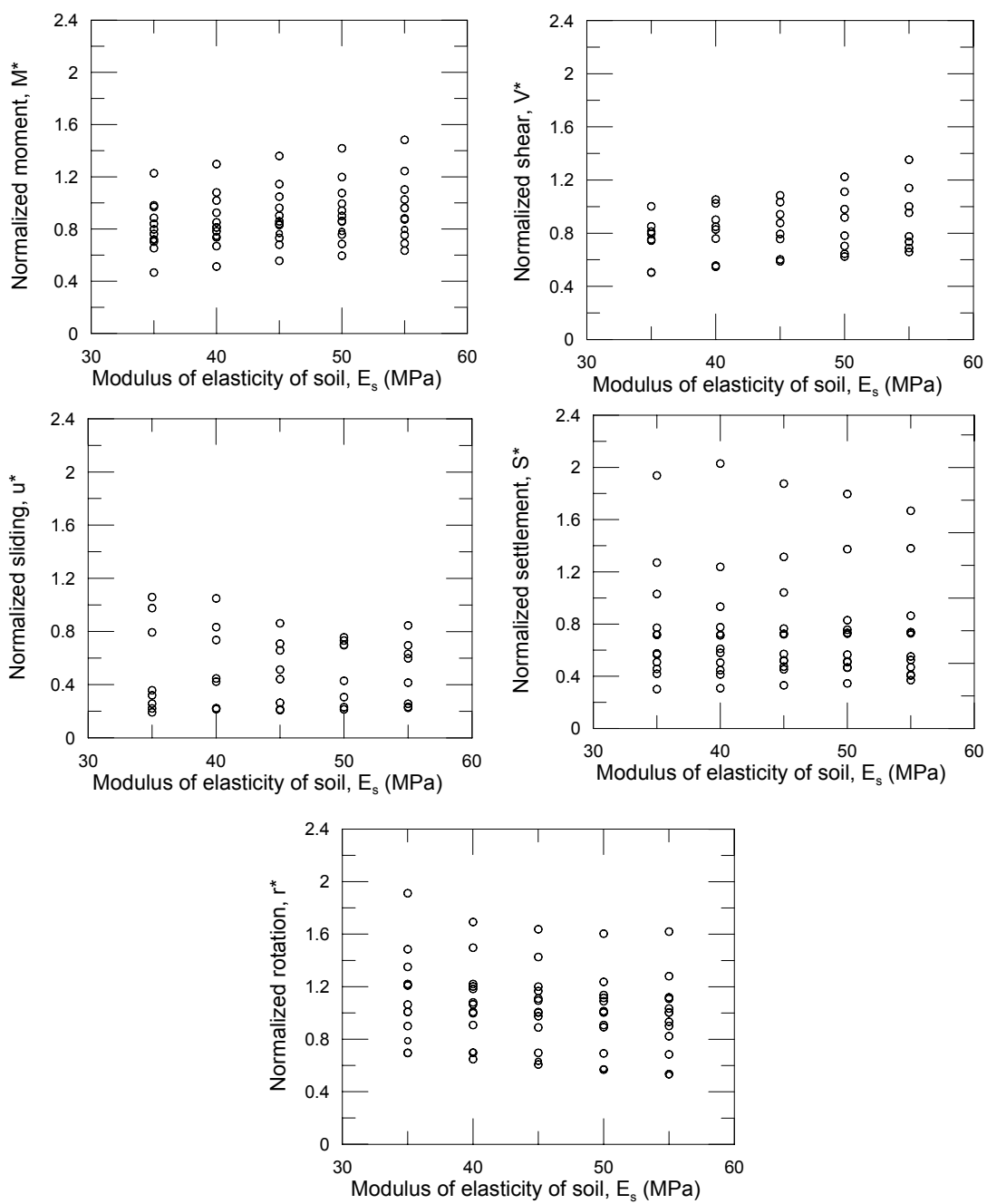


Figure A.3: Normalized demands for all tests (with varying E_s)

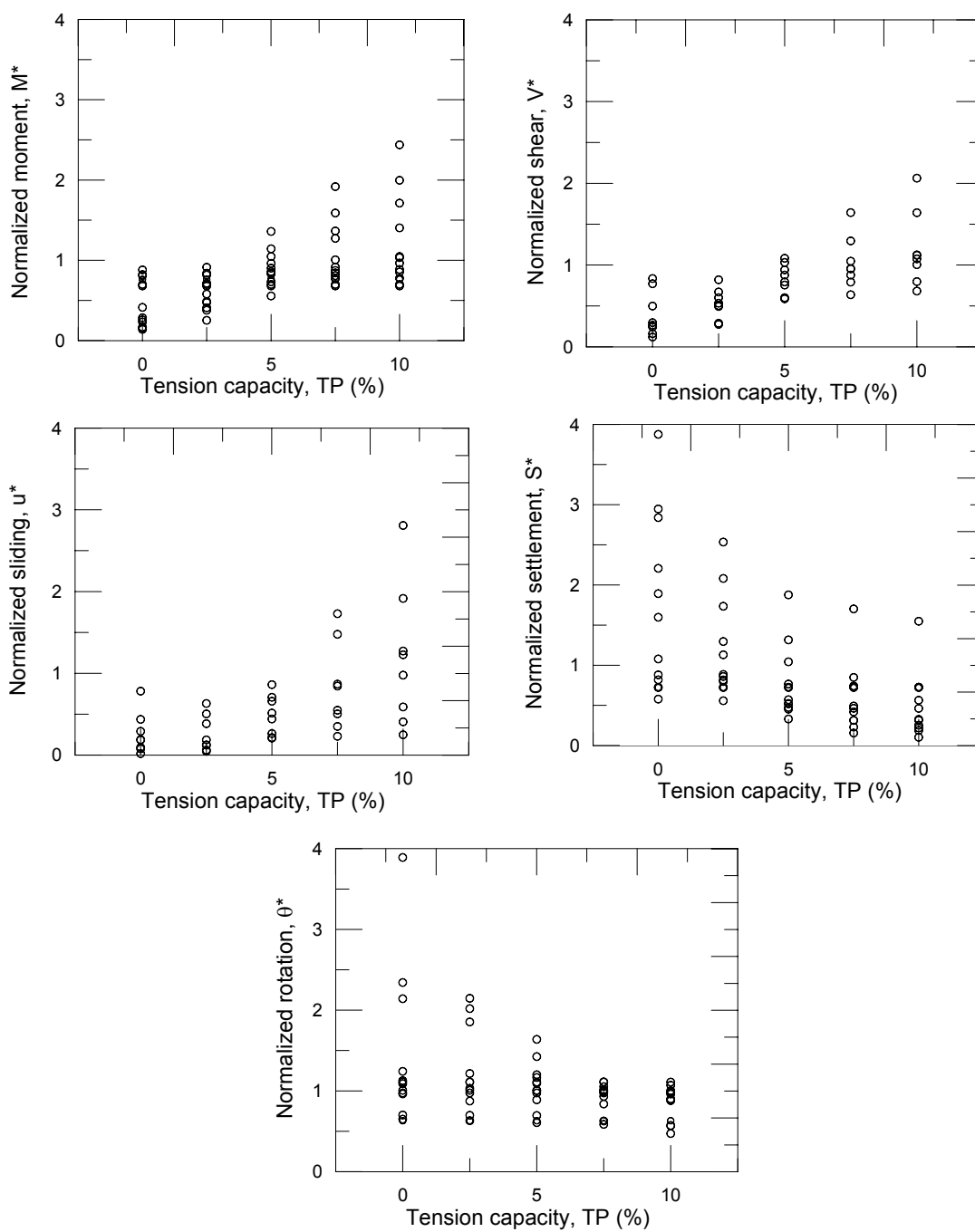
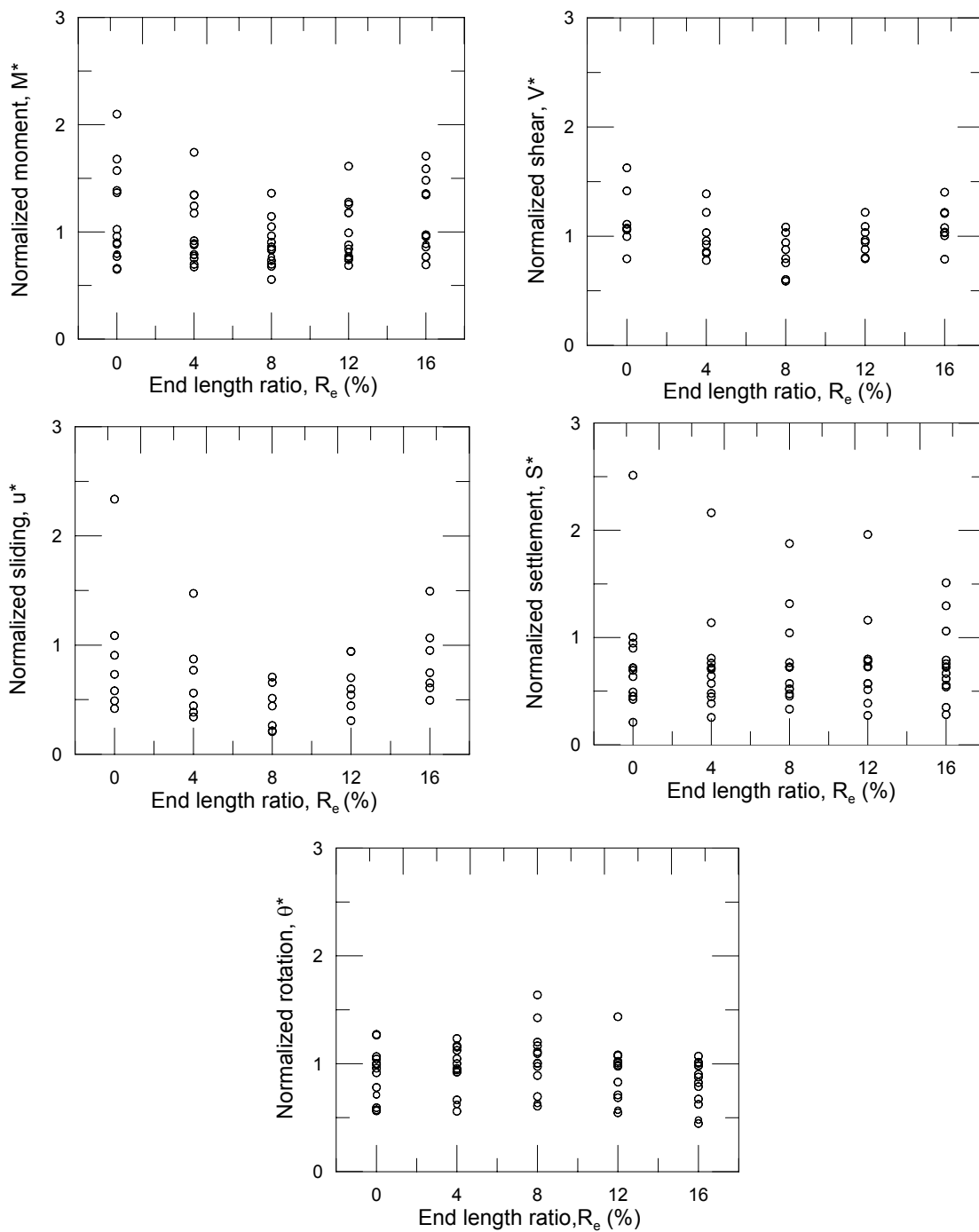


Figure A.4: Normalized demands for all tests (with varying TP)

Figure A.5: Normalized demands for all tests (with varying R_e)

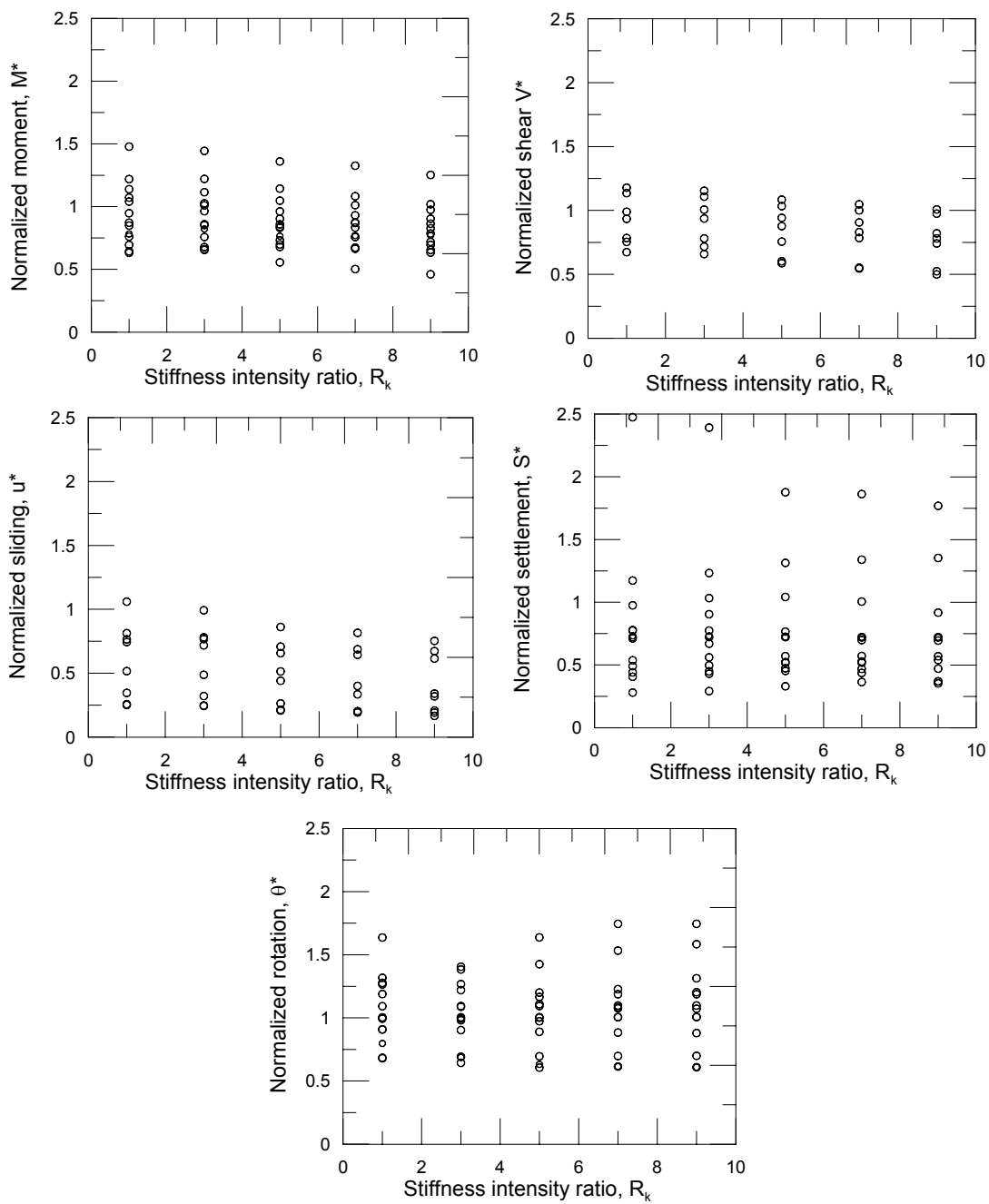


Figure A.6: Normalized demands for all tests (with varying R_k)

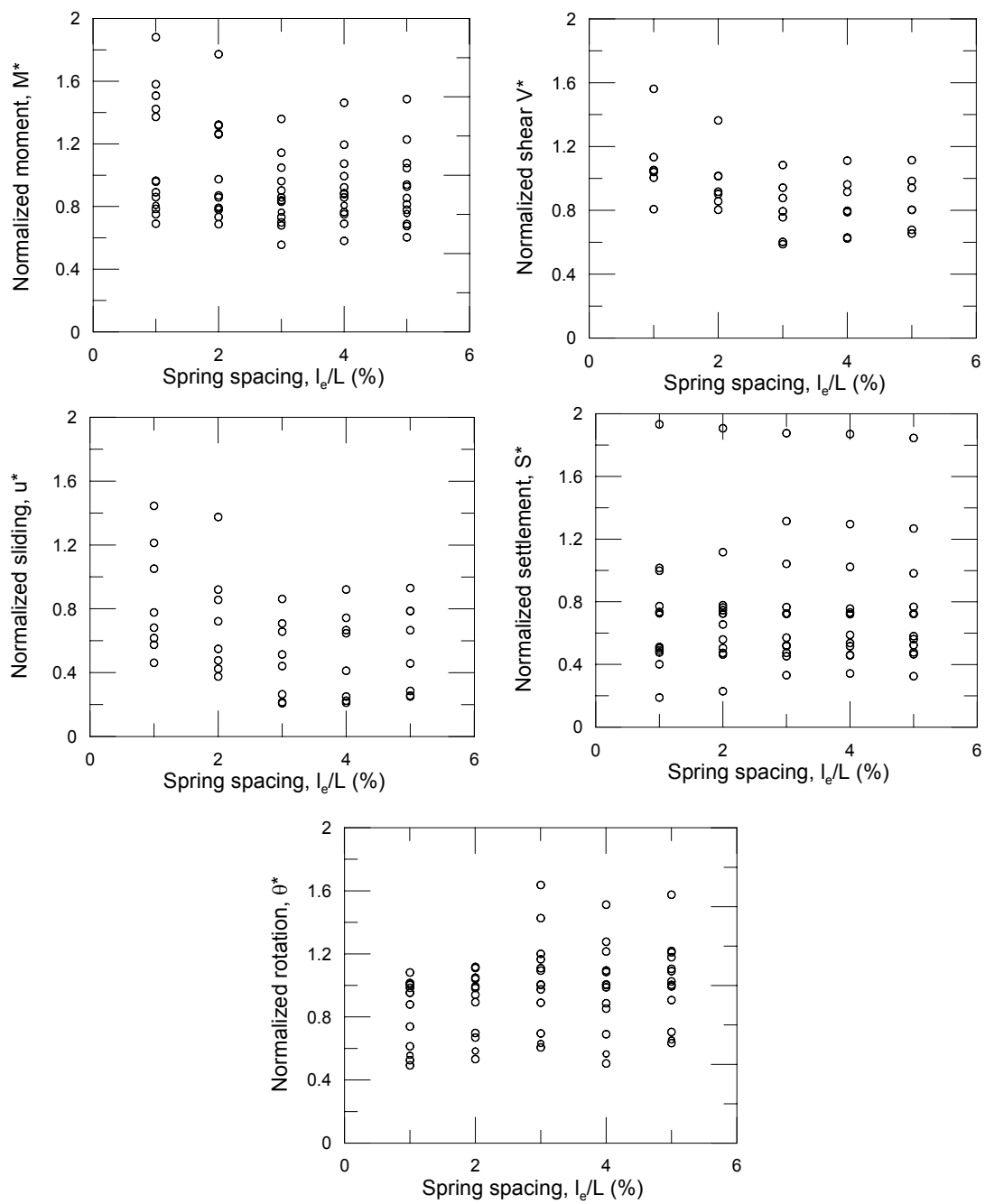


Figure A.7: Normalized demands for all tests (with varying l_e/L)

Table A.1: Normalized force and displacement demands (with varying ϕ)

Parameter =Friction angle, phi (deg)															
Norm Moment															
Values	Test-1	Test-2	Test-3	Test-4	Test-5	Test-6	Test-7	Test-8	Test-9	Test-10	Test-11	Test-12	Test-13	Test-14	MEAN
38	0.75	0.92	0.75	0.68	0.92	0.44	1.32	0.70	0.73	0.80	0.79	0.62	0.64	0.80	0.78
39	0.84	1.01	0.88	0.73	0.94	0.50	1.18	0.77	0.75	0.81	0.85	0.65	0.66	0.81	0.81
40	0.90	1.14	1.05	0.73	0.96	0.56	1.36	0.84	0.76	0.83	0.86	0.68	0.70	0.81	0.87
41	0.95	1.26	1.28	0.78	0.99	0.61	1.54	0.91	0.80	0.87	0.86	0.68	0.74	0.82	0.93
42	0.99	1.34	1.57	0.82	1.02	0.65	1.74	0.97	0.85	0.91	0.87	0.68	0.74	0.83	1.00
Norm Shear															
Values	Test-1	Test-2	Test-3	Test-4	Test-5	Test-6	Test-7	Test-8	Test-9*	Test-10	Test-11	Test-12	Test-13	Test-14	MEAN
38	0.79	0.70	0.77	0.70	0.54	0.47	0.92	0.73	0.70
39	0.88	0.77	0.91	0.76	0.56	0.54	0.99	0.76	0.77
40	0.94	0.88	1.08	0.76	0.59	0.60	1.03	0.79	0.83
41	0.99	0.97	1.32	0.81	0.62	0.66	1.11	0.83	0.91
42	1.03	1.03	1.63	0.85	0.65	0.71	1.20	0.86	0.99
Norm Sliding															
Values	Test-1	Test-2	Test-3	Test-4	Test-5	Test-6	Test-7	Test-8	Test-9*	Test-10	Test-11	Test-12	Test-13	Test-14	MEAN
38	0.18	0.20	0.72	0.31	0.20	0.19	0.58	0.70	0.39
39	0.24	0.34	0.83	0.43	0.20	0.20	0.63	0.71	0.45
40	0.26	0.51	0.86	0.44	0.21	0.21	0.66	0.71	0.48
41	0.29	0.76	0.93	0.47	0.22	0.23	0.71	0.72	0.54
42	0.32	1.00	0.96	0.43	0.24	0.24	0.75	0.75	0.59
Norm settlement															
Values	Test-1	Test-2	Test-3	Test-4	Test-5	Test-6	Test-7	Test-8	Test-9	Test-10	Test-11	Test-12	Test-13	Test-14	MEAN
38	1.68	0.70	1.86	0.70	0.49	0.92	0.92	0.70	0.72	0.80	1.93	0.69	0.70	0.70	0.97
39	1.39	0.63	1.61	0.48	0.50	0.68	0.53	0.56	0.72	0.78	1.97	0.70	0.72	0.70	0.85
40	1.04	0.57	1.31	0.33	0.52	0.52	0.47	0.45	0.72	0.77	1.88	0.72	0.72	0.70	0.77
41	0.79	0.54	1.01	0.25	0.55	0.40	0.31	0.37	0.72	0.77	1.95	0.72	0.78	0.88	0.72
42	0.67	0.51	0.73	0.20	0.58	0.32	0.22	0.31	0.73	0.80	2.09	0.72	0.78	0.90	0.68
Norm rotation															
Values	Test-1	Test-2	Test-3	Test-4	Test-5	Test-6	Test-7	Test-8	Test-9	Test-10	Test-11	Test-12	Test-13	Test-14	MEAN
38	1.84	0.69	1.12	1.72	1.01	1.01	1.73	0.88	0.72	0.71	1.29	1.37	1.08	1.05	1.16
39	1.78	0.69	1.11	1.68	1.01	1.00	1.40	0.88	0.66	0.67	1.26	1.24	1.13	0.91	1.10
40	1.64	0.70	1.09	1.43	1.01	1.00	1.20	0.89	0.63	0.61	1.17	1.11	0.97	0.74	1.01
41	1.63	0.69	1.08	1.34	1.01	1.00	1.08	0.90	0.61	0.57	1.15	1.11	0.89	0.62	0.98
42	1.58	0.68	1.03	1.11	1.00	0.99	0.97	0.91	0.59	0.52	1.10	1.11	0.89	0.61	0.94

* No lateral test data available for Test 9-14

Table A.2: Normalized force and displacement demands (with varying ν)

Parameter = neu (Poisson's ratio)

Norm Moment															
Values	Test-1	Test-2	Test-3	Test-4	Test-5	Test-6	Test-7	Test-8	Test-9	Test-10	Test-11	Test-12	Test-13	Test-14	MEAN
0.3	0.89	1.11	1.02	0.74	0.94	0.53	1.32	0.79	0.75	0.82	0.85	0.67	0.68	0.80	0.851
0.35	0.89	1.12	1.04	0.74	0.95	0.54	1.34	0.81	0.76	0.82	0.86	0.68	0.69	0.80	0.860
0.4	0.90	1.14	1.05	0.73	0.96	0.56	1.36	0.84	0.76	0.83	0.86	0.68	0.70	0.81	0.870
0.45	0.91	1.17	1.06	0.77	0.98	0.57	1.96	0.87	0.77	0.84	0.86	0.68	0.71	0.81	0.926
0.5	0.93	1.19	1.08	0.76	1.00	0.60	1.97	0.91	0.78	0.86	0.86	0.69	0.72	0.81	0.940
Norm Shear															
Values	Test-1	Test-2	Test-3	Test-4	Test-5	Test-6	Test-7	Test-8	Test-9*	Test-10	Test-11	Test-12	Test-13	Test-14	MEAN
0.3	0.93	0.85	1.06	0.77	0.56	0.57	1.03	0.76	0.815
0.35	0.93	0.86	1.07	0.76	0.57	0.59	1.03	0.78	0.824
0.4	0.94	0.88	1.08	0.76	0.59	0.60	1.03	0.79	0.835
0.45	0.95	0.90	1.10	0.80	0.61	0.62	1.08	0.81	0.857
0.5	0.97	0.92	1.12	0.78	0.63	0.65	1.07	0.82	0.869
Norm Sliding															
Values	Test-1	Test-2	Test-3	Test-4	Test-5	Test-6	Test-7	Test-8	Test-9*	Test-10	Test-11	Test-12	Test-13	Test-14	MEAN
0.3	0.24	0.43	0.86	0.39	0.20	0.20	0.65	0.67	0.456
0.35	0.25	0.46	0.85	0.44	0.20	0.21	0.66	0.69	0.470
0.4	0.26	0.51	0.86	0.44	0.21	0.21	0.66	0.71	0.483
0.45	0.27	0.58	0.88	0.47	0.22	0.22	0.72	0.73	0.511
0.5	0.26	0.66	0.94	0.42	0.22	0.23	0.71	0.75	0.525
Norm settlement															
Values	Test-1	Test-2	Test-3	Test-4	Test-5	Test-6	Test-7	Test-8	Test-9	Test-10	Test-11	Test-12	Test-13	Test-14	MEAN
0.3	1.02	0.57	1.34	0.34	0.49	0.52	0.38	0.46	0.72	0.76	1.83	0.73	0.72	0.70	0.757
0.35	1.02	0.57	1.33	0.33	0.50	0.52	0.40	0.46	0.72	0.76	1.85	0.73	0.72	0.70	0.758
0.4	1.04	0.57	1.31	0.33	0.52	0.52	0.47	0.45	0.72	0.77	1.88	0.72	0.72	0.70	0.767
0.45	1.02	0.57	1.29	0.34	0.55	0.51	0.82	0.46	0.72	0.77	1.91	0.72	0.72	0.70	0.793
0.5	1.01	0.57	1.27	0.31	0.57	0.51	0.66	0.46	0.72	0.77	1.94	0.72	0.72	0.70	0.781
Norm rotation															
Values	Test-1	Test-2	Test-3	Test-4	Test-5	Test-6	Test-7	Test-8	Test-9	Test-10	Test-11	Test-12	Test-13	Test-14	MEAN
0.3	1.71	0.70	1.10	1.37	1.01	1.01	1.21	0.88	0.68	0.63	1.18	1.18	1.04	0.79	1.04
0.35	1.66	0.70	1.10	1.52	1.01	1.00	1.21	0.89	0.66	0.62	1.17	1.15	1.01	0.77	1.03
0.4	1.64	0.70	1.09	1.43	1.01	1.00	1.20	0.89	0.63	0.61	1.17	1.11	0.97	0.74	1.01
0.45	1.58	0.69	1.09	1.42	1.01	1.00	1.38	0.89	0.60	0.59	1.15	1.06	0.93	0.70	1.01
0.5	1.50	0.69	1.09	1.14	1.01	0.99	1.42	0.90	0.57	0.57	1.13	1.01	0.88	0.66	0.97

* No lateral test data available for Test 9-14

Table A.3: Normalized force and displacement demands (with varying E_s)

Parameter = Young's modulus of soil, E (MPa)

Norm Moment															
Values	Test-1	Test-2	Test-3	Test-4	Test-5	Test-6	Test-7	Test-8	Test-9	Test-10	Test-11	Test-12	Test-13	Test-14	MEAN
35	0.76	0.98	0.97	0.72	0.88	0.47	1.23	0.70	0.72	0.80	0.84	0.65	0.65	0.81	0.80
40	0.81	1.08	1.02	0.74	0.93	0.51	1.30	0.78	0.74	0.81	0.85	0.67	0.67	0.80	0.84
45	0.90	1.14	1.05	0.73	0.96	0.56	1.36	0.84	0.76	0.83	0.86	0.68	0.70	0.81	0.87
50	0.94	1.20	1.08	0.76	1.00	0.59	1.42	0.90	0.78	0.86	0.86	0.69	0.72	0.80	0.90
55	0.96	1.24	1.10	0.75	1.03	0.63	1.48	0.96	0.80	0.88	0.87	0.69	0.73	0.81	0.92
Norm Shear															
Values	Test-1	Test-2	Test-3	Test-4	Test-5	Test-6	Test-7	Test-8	Test-9*	Test-10	Test-11	Test-12	Test-13	Test-14	MEAN
35	0.80	0.75	1.00	0.74	0.50	0.51	0.85	0.81	0.75
40	0.85	0.83	1.05	0.76	0.55	0.56	1.02	0.90	0.81
45	0.94	0.88	1.08	0.76	0.59	0.60	1.03	0.79	0.83
50	0.98	0.92	1.11	0.78	0.62	0.64	1.22	0.70	0.87
55	1.00	0.95	1.14	0.78	0.66	0.69	1.35	0.74	0.91
Norm Sliding															
Values	Test-1	Test-2	Test-3	Test-4	Test-5	Test-6	Test-7	Test-8	Test-9*	Test-10	Test-11	Test-12	Test-13	Test-14	MEAN
35	0.26	0.36	0.98	0.32	0.22	0.19	0.79	1.06	0.52
40	0.22	0.45	0.83	0.42	0.22	0.22	0.74	1.05	0.52
45	0.26	0.51	0.86	0.44	0.21	0.21	0.66	0.71	0.48
50	0.31	0.70	0.76	0.43	0.23	0.21	0.73	0.70	0.51
55	0.26	0.60	0.85	0.41	0.23	0.23	0.70	0.63	0.49
Norm settlement															
Values	Test-1	Test-2	Test-3	Test-4	Test-5	Test-6	Test-7	Test-8	Test-9	Test-10	Test-11	Test-12	Test-13	Test-14	MEAN
35	1.03	0.58	1.27	0.30	0.57	0.51	0.42	0.46	0.72	0.77	1.94	0.72	0.72	0.70	0.764
40	0.93	0.58	1.24	0.31	0.61	0.51	0.41	0.45	0.72	0.78	2.03	0.71	0.71	0.70	0.763
45	1.04	0.57	1.31	0.33	0.52	0.52	0.47	0.45	0.72	0.77	1.88	0.72	0.72	0.70	0.767
50	0.83	0.57	1.37	0.35	0.47	0.51	0.51	0.46	0.72	0.76	1.80	0.73	0.73	0.70	0.750
55	0.86	0.55	1.38	0.37	0.41	0.52	0.41	0.47	0.72	0.74	1.67	0.73	0.73	0.71	0.734
Norm rotation															
Values	Test-1	Test-2	Test-3	Test-4	Test-5	Test-6	Test-7	Test-8	Test-9	Test-10	Test-11	Test-12	Test-13	Test-14	MEAN
35	1.91	0.69	1.06	1.48	1.01	1.01	1.22	0.90	0.79	0.70	1.21	1.35	1.21	0.95	1.11
40	1.69	0.70	1.07	1.50	1.01	1.00	1.20	0.91	0.70	0.65	1.18	1.22	1.08	0.83	1.05
45	1.64	0.70	1.09	1.43	1.01	1.00	1.20	0.89	0.63	0.61	1.17	1.11	0.97	0.74	1.01
50	1.60	0.69	1.09	1.11	1.00	1.00	1.24	0.91	0.57	0.57	1.14	1.01	0.89	0.67	0.96
55	1.62	0.68	1.11	1.03	1.00	1.00	1.28	0.90	0.53	0.53	1.12	0.93	0.82	0.61	0.94

* No lateral test data available for Test 9-14

Table A.4: Normalized force and displacement demands (with varying TP)

Parameter = Tension capacity, TP (%)

Norm Moment															
Values	Test-1	Test-2	Test-3	Test-4	Test-5	Test-6	Test-7	Test-8	Test-9	Test-10	Test-11	Test-12	Test-13	Test-14	MEAN
0	0.23	0.16	0.28	0.26	0.88	0.14	0.41	0.17	0.76	0.81	0.82	0.68	0.70	0.80	0.507
2.5	0.47	0.38	0.58	0.49	0.91	0.25	0.71	0.41	0.76	0.82	0.84	0.68	0.70	0.80	0.629
5	0.90	1.14	1.05	0.73	0.96	0.56	1.36	0.84	0.76	0.83	0.86	0.68	0.70	0.81	0.870
7.5	0.92	1.37	1.59	0.77	1.01	0.81	1.92	1.27	0.77	0.84	0.87	0.68	0.70	0.81	1.022
10	0.97	1.40	2.00	0.78	1.05	1.03	2.44	1.71	0.77	0.85	0.88	0.68	0.70	0.81	1.148
Norm Shear															
Values	Test-1	Test-2	Test-3	Test-4	Test-5	Test-6	Test-7	Test-8	Test-9*	Test-10	Test-11	Test-12	Test-13	Test-14	MEAN
0	0.24	0.12	0.30	0.26	0.50	0.16	0.77	0.84	0.40
2.5	0.49	0.29	0.60	0.50	0.53	0.27	0.82	0.67	0.52
5	0.94	0.88	1.08	0.76	0.59	0.60	1.03	0.79	0.83
7.5	0.96	1.05	1.64	0.79	0.64	0.88	1.30	0.95	1.03
10	1.01	1.08	2.06	0.80	0.68	1.12	1.64	1.12	1.19
Norm Sliding															
Values	Test-1	Test-2	Test-3	Test-4	Test-5	Test-6	Test-7	Test-8	Test-9*	Test-10	Test-11	Test-12	Test-13	Test-14	MEAN
0	0.08	0.02	0.18	0.09	0.19	0.29	0.44	0.78	0.26
2.5	0.06	0.05	0.38	0.12	0.19	0.12	0.50	0.63	0.26
5	0.26	0.51	0.86	0.44	0.21	0.21	0.66	0.71	0.48
7.5	0.35	1.73	1.48	0.55	0.23	0.50	0.84	0.87	0.82
10	0.41	2.81	1.92	0.59	0.25	0.98	1.23	1.27	1.18
Norm settlement															
Values	Test-1	Test-2	Test-3	Test-4	Test-5	Test-6	Test-7	Test-8	Test-9	Test-10	Test-11	Test-12	Test-13	Test-14	MEAN
0	3.88	1.89	0.88	1.60	0.58	2.84	1.08	2.95	0.72	0.82	2.21	0.72	0.72	0.70	1.542
2.5	2.54	0.82	1.74	1.13	0.56	1.30	0.86	0.89	0.72	0.80	2.08	0.72	0.72	0.70	1.112
5	1.04	0.57	1.31	0.33	0.52	0.52	0.47	0.45	0.72	0.77	1.88	0.72	0.72	0.70	0.767
7.5	0.42	0.46	0.85	0.15	0.49	0.31	0.23	0.31	0.72	0.74	1.70	0.72	0.72	0.70	0.610
10	0.33	0.32	0.56	0.10	0.46	0.22	0.19	0.25	0.72	0.73	1.55	0.72	0.72	0.70	0.541
Norm rotation															
Values	Test-1	Test-2	Test-3	Test-4	Test-5	Test-6	Test-7	Test-8	Test-9	Test-10	Test-11	Test-12	Test-13	Test-14	MEAN
0	2.34	0.70	1.13	2.14	1.01	1.09	3.89	0.96	0.63	0.65	1.24	1.11	0.97	0.76	1.33
2.5	2.15	0.70	1.11	2.02	1.01	1.03	1.85	0.87	0.63	0.63	1.22	1.11	0.97	0.75	1.15
5	1.64	0.70	1.09	1.43	1.01	1.00	1.20	0.89	0.63	0.61	1.17	1.11	0.97	0.74	1.01
7.5	1.01	0.63	1.05	0.84	1.00	0.98	1.00	0.93	0.63	0.59	1.11	1.11	0.97	0.73	0.90
10	0.88	0.47	0.90	0.57	1.00	0.96	0.89	0.99	0.63	0.57	1.07	1.11	0.97	0.72	0.84

* No lateral test data available for Test 9-14

Table A.5: Normalized force and displacement demands (with varying R_e)

Parameter = End length ratio R_e (%)

Norm Moment															
Values	Test-1	Test-2	Test-3	Test-4	Test-5	Test-6	Test-7	Test-8	Test-9	Test-10	Test-11	Test-12	Test-13	Test-14	MEAN
0	0.958	1.386	1.572	0.769	1.364	1.022	2.098	1.678	0.791	0.898	0.884	0.650	0.659	0.832	1.112
4	0.918	1.347	1.342	0.754	1.173	0.789	1.741	1.242	0.779	0.878	0.890	0.673	0.697	0.810	1.002
8	0.902	1.144	1.048	0.731	0.962	0.555	1.359	0.840	0.764	0.830	0.859	0.679	0.698	0.807	0.870
12	0.991	1.257	1.177	0.770	1.278	0.740	1.612	1.177	0.813	0.878	0.840	0.686	0.752	0.843	0.987
16	0.966	1.345	1.357	0.767	1.481	0.956	1.708	1.588	0.884	0.973	0.859	0.692	0.767	0.855	1.086
Norm Shear															
Values	Test-1	Test-2	Test-3	Test-4	Test-5	Test-6	Test-7	Test-8	Test-9*	Test-10	Test-11	Test-12	Test-13	Test-14	MEAN
0	0.997	1.062	1.627	0.793	1.060	1.109	1.415	1.075	1.142
4	0.957	1.032	1.388	0.778	0.843	0.856	1.218	0.924	1.000
8	0.942	0.877	1.084	0.756	0.588	0.602	1.033	0.794	0.835
12	1.033	0.964	1.218	0.793	0.946	0.803	1.089	0.879	0.966
16	1.005	1.031	1.403	0.789	1.207	1.037	1.218	1.077	1.096
Norm Sliding															
Values	Test-1	Test-2	Test-3	Test-4	Test-5	Test-6	Test-7	Test-8	Test-9*	Test-10	Test-11	Test-12	Test-13	Test-14	MEAN
0	0.418	2.336	1.305	0.581	0.490	0.731	0.907	1.086	0.982
4	0.385	1.474	0.856	0.560	0.341	0.444	0.770	0.872	0.713
8	0.264	0.513	0.861	0.441	0.207	0.214	0.657	0.708	0.483
12	0.444	0.941	0.994	0.545	0.599	0.307	0.702	0.943	0.684
16	0.495	1.494	0.983	0.653	0.951	0.609	0.747	1.066	0.875
Norm Settlement															
Values	Test-1	Test-2	Test-3	Test-4	Test-5	Test-6	Test-7	Test-8	Test-9	Test-10	Test-11	Test-12	Test-13	Test-14	MEAN
0	0.634	0.491	1.001	0.210	0.946	0.451	0.423	0.449	0.721	0.900	2.513	0.693	0.717	0.858	0.786
4	0.642	0.571	1.138	0.253	0.760	0.479	0.385	0.445	0.721	0.806	2.164	0.705	0.718	0.704	0.749
8	1.042	0.571	1.314	0.331	0.522	0.517	0.474	0.453	0.723	0.766	1.876	0.725	0.722	0.703	0.767
12	0.799	0.572	1.162	0.273	0.779	0.568	0.386	0.514	0.722	0.727	1.960	0.724	0.782	0.895	0.776
16	0.664	0.538	1.060	0.280	1.296	0.555	0.348	0.615	0.731	0.755	1.511	0.721	0.788	0.894	0.768
Norm Rotation															
Values	Test-1	Test-2	Test-3	Test-4	Test-5	Test-6	Test-7	Test-8	Test-9	Test-10	Test-11	Test-12	Test-13	Test-14	MEAN
0	0.780	0.572	1.002	0.562	0.991	0.916	1.066	0.959	0.710	0.592	1.265	1.271	1.043	0.947	0.905
4	1.233	0.665	1.046	0.923	1.001	0.942	1.124	0.922	0.624	0.559	1.153	1.165	0.955	0.755	0.933
8	1.638	0.695	1.094	1.426	1.006	1.002	1.200	0.890	0.631	0.607	1.166	1.109	0.974	0.740	1.013
12	1.435	0.684	1.075	0.709	0.987	1.005	1.076	0.977	0.568	0.545	1.081	1.021	0.829	0.540	0.895
16	0.876	0.624	1.070	0.673	0.983	0.902	1.004	1.013	0.478	0.445	0.824	0.979	0.788	0.487	0.796

* No lateral test data available for Test 9-14

Table A.6: Normalized force and displacement demands (with varying R_k)

Parameter =Stiffness intensity ratio, R_k

Norm Moment															
Values	Test-1	Test-2	Test-3	Test-4	Test-5	Test-6	Test-7	Test-8	Test-9	Test-10	Test-11	Test-12	Test-13	Test-14	MEAN
1	0.95	1.22	1.14	0.76	1.04	0.69	1.48	1.07	0.78	0.87	0.85	0.63	0.64	0.86	0.928
3	0.96	1.22	1.12	0.76	1.03	0.66	1.44	1.01	0.82	0.85	0.86	0.65	0.68	0.83	0.921
5	0.90	1.14	1.05	0.73	0.96	0.56	1.36	0.84	0.76	0.83	0.86	0.68	0.70	0.81	0.870
7	0.87	1.08	1.01	0.76	0.93	0.50	1.33	0.76	0.77	0.83	0.87	0.66	0.67	0.81	0.847
9	0.79	1.02	0.97	0.72	0.90	0.46	1.25	0.70	0.77	0.83	0.86	0.63	0.65	0.82	0.812
Norm Shear															
Values	Test-1	Test-2	Test-3	Test-4	Test-5	Test-6	Test-7	Test-8	Test-9*	Test-10	Test-11	Test-12	Test-13	Test-14	MEAN
1	0.99	0.93	1.18	0.78	0.67	0.75	1.14	0.90	0.92
3	1.01	0.94	1.15	0.78	0.66	0.72	1.11	0.87	0.90
5	0.94	0.88	1.08	0.76	0.59	0.60	1.03	0.79	0.83
7	0.91	0.83	1.05	0.78	0.55	0.54	1.00	0.76	0.80
9	0.82	0.78	1.01	0.74	0.52	0.50	0.98	0.73	0.76
Norm Sliding															
Values	Test-1	Test-2	Test-3	Test-4	Test-5	Test-6	Test-7	Test-8	Test-9*	Test-10	Test-11	Test-12	Test-13	Test-14	MEAN
1	0.35	0.77	1.06	0.52	0.25	0.26	0.74	0.81	0.59
3	0.32	0.77	0.99	0.49	0.25	0.24	0.72	0.78	0.57
5	0.26	0.51	0.86	0.44	0.21	0.21	0.66	0.71	0.48
7	0.20	0.40	0.82	0.34	0.19	0.20	0.64	0.69	0.43
9	0.16	0.32	0.75	0.34	0.21	0.19	0.61	0.67	0.41
Norm Settlement															
Values	Test-1	Test-2	Test-3	Test-4	Test-5	Test-6	Test-7	Test-8	Test-9	Test-10	Test-11	Test-12	Test-13	Test-14	MEAN
1	0.78	0.54	1.17	0.28	0.71	0.49	0.41	0.44	0.73	0.97	2.47	0.72	0.77	1.23	0.837
3	1.03	0.56	1.23	0.29	0.67	0.50	0.43	0.45	0.73	0.90	2.39	0.72	0.77	0.95	0.831
5	1.04	0.57	1.31	0.33	0.52	0.52	0.47	0.45	0.72	0.77	1.88	0.72	0.72	0.70	0.767
7	1.01	0.57	1.34	0.36	0.44	0.53	0.52	0.47	0.72	0.72	1.86	0.70	0.72	0.70	0.761
9	0.92	0.57	1.35	0.37	0.35	0.54	0.37	0.47	0.72	0.72	1.77	0.69	0.72	0.70	0.733
Norm Rotation															
Values	Test-1	Test-2	Test-3	Test-4	Test-5	Test-6	Test-7	Test-8	Test-9	Test-10	Test-11	Test-12	Test-13	Test-14	MEAN
1	1.28	0.68	1.09	0.91	1.00	0.99	1.19	0.91	0.80	0.68	1.32	1.64	1.27	1.27	1.07
3	1.38	0.69	1.09	0.98	1.00	0.99	1.22	0.90	0.69	0.64	1.27	1.41	1.09	0.91	1.02
5	1.64	0.70	1.09	1.43	1.01	1.00	1.20	0.89	0.63	0.61	1.17	1.11	0.97	0.74	1.01
7	1.75	0.70	1.10	1.53	1.01	1.00	1.19	0.88	0.62	0.61	1.23	1.08	1.07	0.76	1.04
9	1.74	0.70	1.10	1.58	1.01	1.01	1.19	0.88	0.61	0.61	1.20	1.31	1.07	0.77	1.06

* No lateral test data available for Test 9-14

Table A.7: Normalized force and displacement demands (with varying l_e/L)

Parameter =Element length ratio, l_e/L (%)

Norm Moment															
Values	Test-1	Test-2	Test-3	Test-4	Test-5	Test-6	Test-7	Test-8	Test-9	Test-10	Test-11	Test-12	Test-13	Test-14	MEAN
5	0.94	1.23	1.08	0.78	1.04	0.60	1.49	0.93	0.76	0.81	0.85	0.68	0.69	0.80	0.905
4	0.92	1.20	1.07	0.76	0.99	0.58	1.46	0.88	0.81	0.88	0.86	0.69	0.75	0.83	0.907
3	0.90	1.14	1.05	0.73	0.96	0.56	1.36	0.84	0.76	0.83	0.86	0.68	0.70	0.81	0.870
2	0.97	1.32	1.32	0.78	1.26	0.79	1.77	1.27	0.79	0.87	0.86	0.69	0.73	0.82	1.018
1	0.96	1.37	1.51	0.78	1.42	0.96	1.88	1.58	0.81	0.89	0.86	0.69	0.75	0.84	1.093
Norm Shear															
Values	Test-1	Test-2	Test-3	Test-4	Test-5	Test-6	Test-7	Test-8	Test-9*	Test-10	Test-11	Test-12	Test-13	Test-14	MEAN
5	0.98	0.94	1.11	0.80	0.68	0.65	1.04	0.80	0.88
4	0.96	0.92	1.11	0.79	0.62	0.63	1.04	0.80	0.86
3	0.94	0.88	1.08	0.76	0.59	0.60	1.03	0.79	0.83
2	1.02	1.01	1.36	0.80	0.92	0.86	1.17	0.90	1.01
1	1.01	1.05	1.56	0.81	1.13	1.04	1.29	1.05	1.12
Norm Sliding															
Values	Test-1	Test-2	Test-3	Test-4	Test-5	Test-6	Test-7	Test-8	Test-9*	Test-10	Test-11	Test-12	Test-13	Test-14	MEAN
5	0.29	0.79	0.93	0.46	0.26	0.25	0.67	0.79	0.55
4	0.25	0.65	0.92	0.41	0.22	0.21	0.67	0.74	0.51
3	0.26	0.51	0.86	0.44	0.21	0.21	0.66	0.71	0.48
2	0.42	1.38	0.86	0.55	0.48	0.38	0.72	0.92	0.71
1	0.46	1.45	1.21	0.62	0.57	0.68	0.78	1.05	0.78
Norm Settlement															
Values	Test-1	Test-2	Test-3	Test-4	Test-5	Test-6	Test-7	Test-8	Test-9	Test-10	Test-11	Test-12	Test-13	Test-14	MEAN
5	0.98	0.58	1.27	0.32	0.56	0.52	0.48	0.46	0.72	0.77	1.85	0.72	0.72	0.70	0.762
4	1.02	0.59	1.29	0.34	0.54	0.52	0.46	0.46	0.72	0.73	1.87	0.72	0.76	0.75	0.769
3	1.04	0.57	1.31	0.33	0.52	0.52	0.47	0.45	0.72	0.77	1.88	0.72	0.72	0.70	0.767
2	0.66	0.56	1.12	0.23	0.78	0.50	0.46	0.47	0.72	0.75	1.91	0.72	0.76	0.73	0.741
1	0.50	0.51	1.02	0.19	1.00	0.49	0.40	0.48	0.72	0.73	1.93	0.73	0.77	0.76	0.731
Norm Rotation															
Values	Test-1	Test-2	Test-3	Test-4	Test-5	Test-6	Test-7	Test-8	Test-9	Test-10	Test-11	Test-12	Test-13	Test-14	MEAN
5	1.58	0.70	1.09	1.22	1.00	0.99	1.21	0.91	0.65	0.63	1.18	1.11	1.03	0.78	1.01
4	1.51	0.69	1.09	1.28	1.01	1.00	1.22	0.89	0.57	0.50	1.09	0.99	0.85	0.55	0.94
3	1.64	0.70	1.09	1.43	1.01	1.00	1.20	0.89	0.63	0.61	1.17	1.11	0.97	0.74	1.01
2	1.12	0.67	1.05	0.70	0.99	0.98	1.11	0.94	0.58	0.53	1.12	1.04	0.89	0.61	0.88
1	0.74	0.61	1.01	0.52	0.98	0.95	1.00	0.95	0.56	0.49	1.08	1.01	0.88	0.55	0.81

* No lateral test data available for Test 9-14

Appendix B

Comparison of Experiment Versus Simulation Results

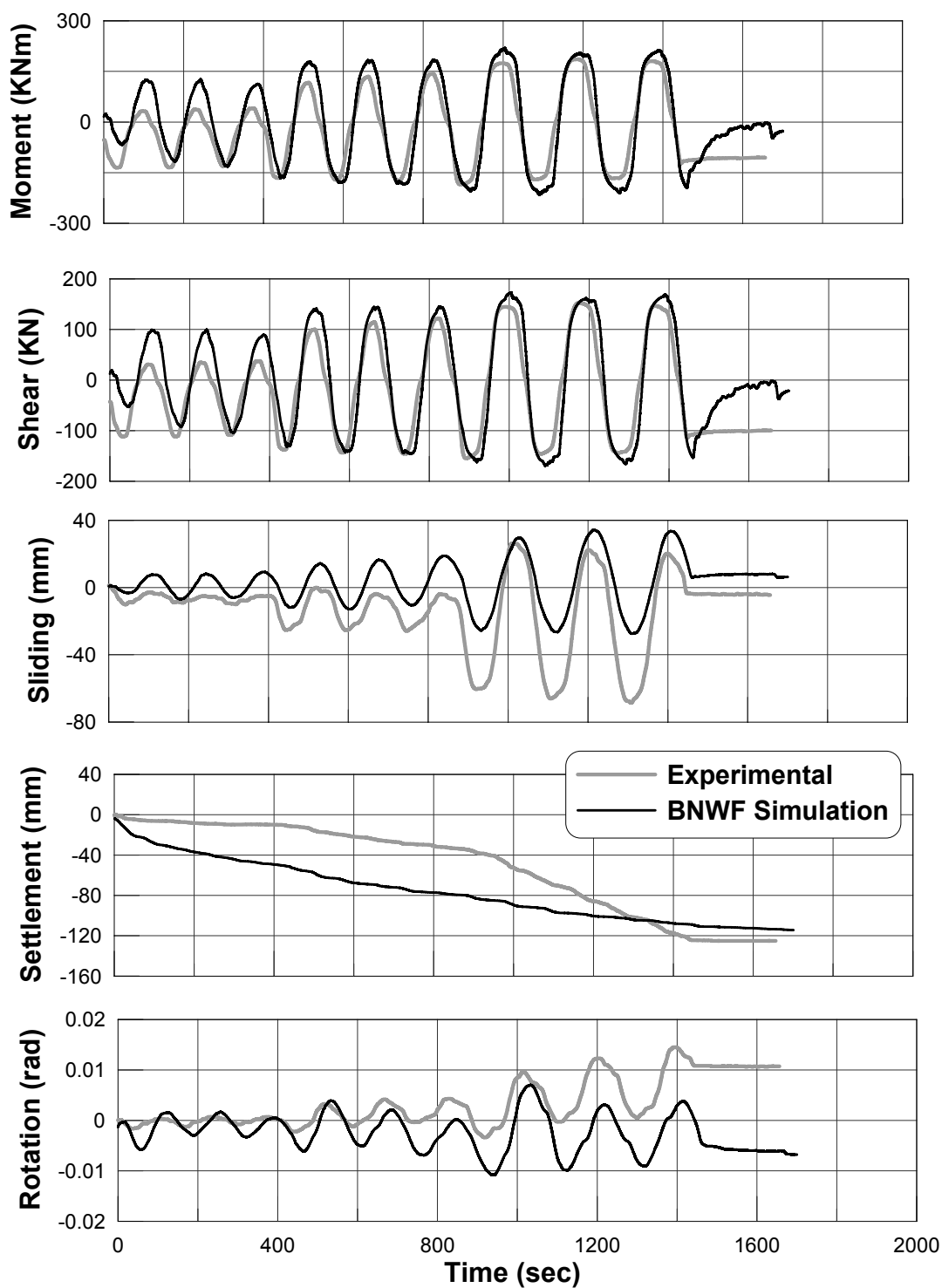


Figure B.1: Footing response comparison for test *SSG02 – 02* (static cyclic test on dense sand ($D_r = 80\%$) with $FS_v = 5.2$ and $M/H/L = 0.41$)

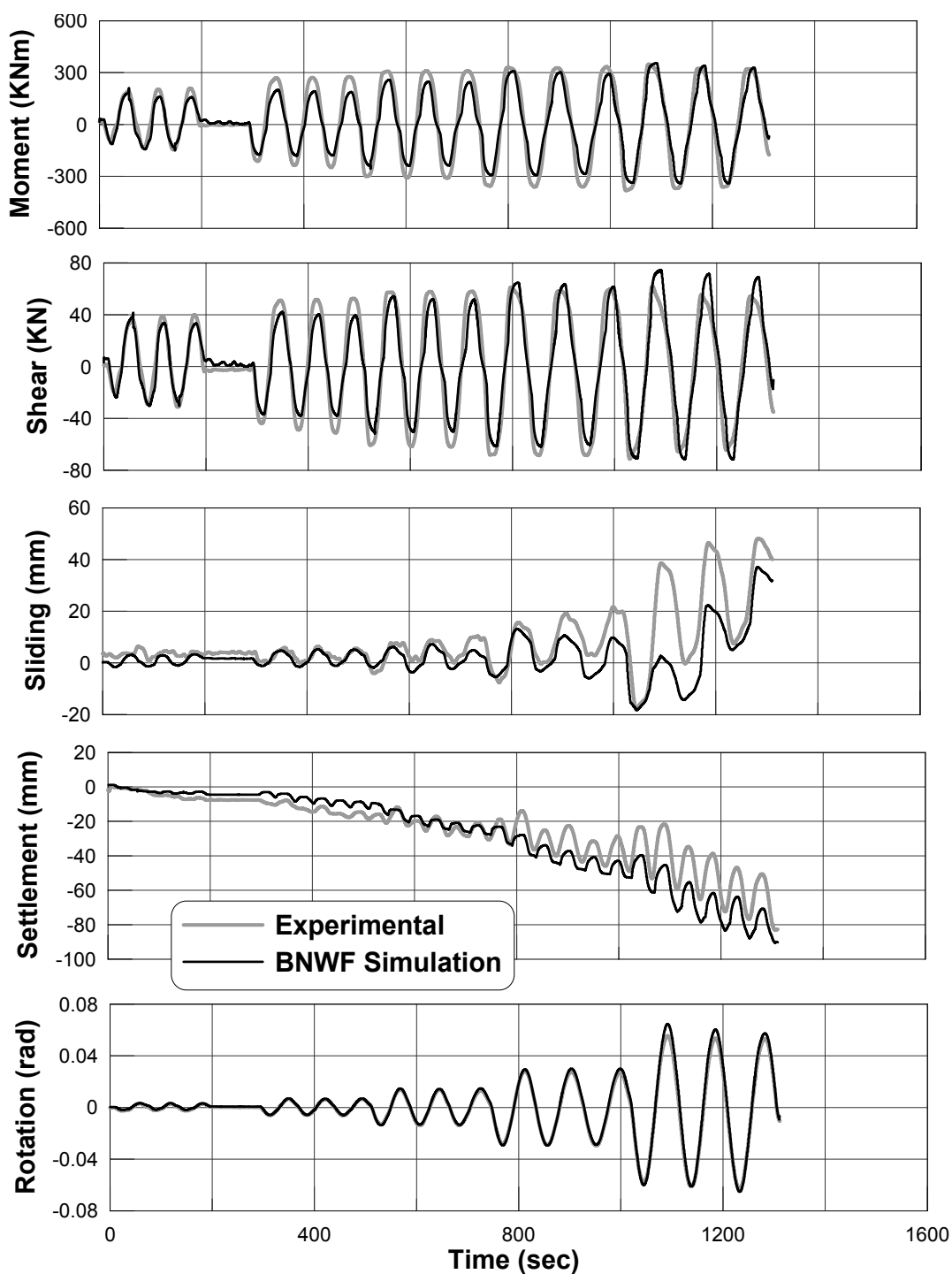


Figure B.2: Footing response comparison for test *SSG02 – 03* (static cyclic test on dense sand ($D_r = 80\%$) with $FS_v = 5.2$ and $M/H/L = 1.75$)

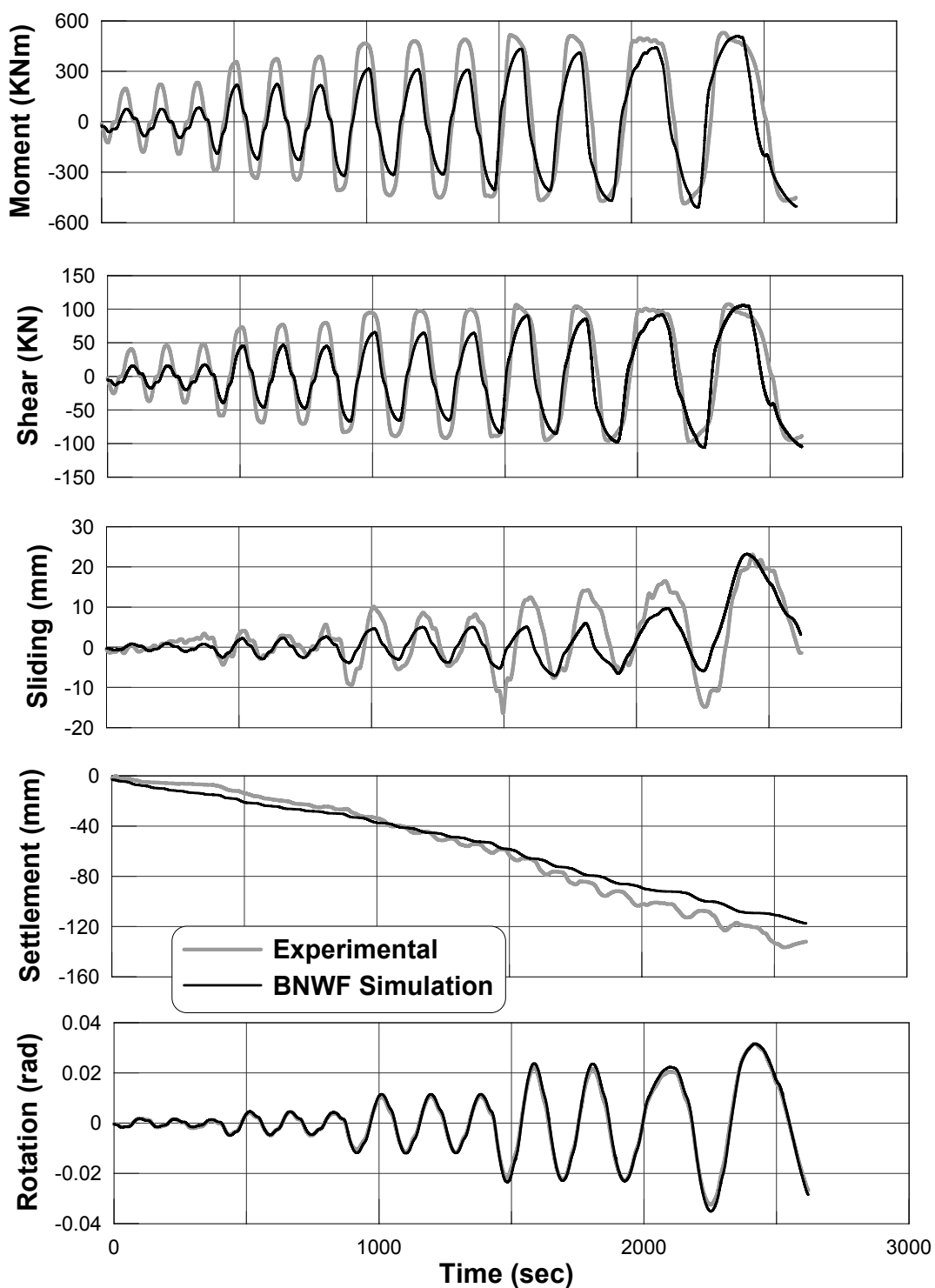


Figure B.3: Footing response comparison for test *SSG02 – 05* (static cyclic test on dense sand ($D_r = 80\%$) with $FS_v = 2.6$ and $M/H/L = 1.72$)

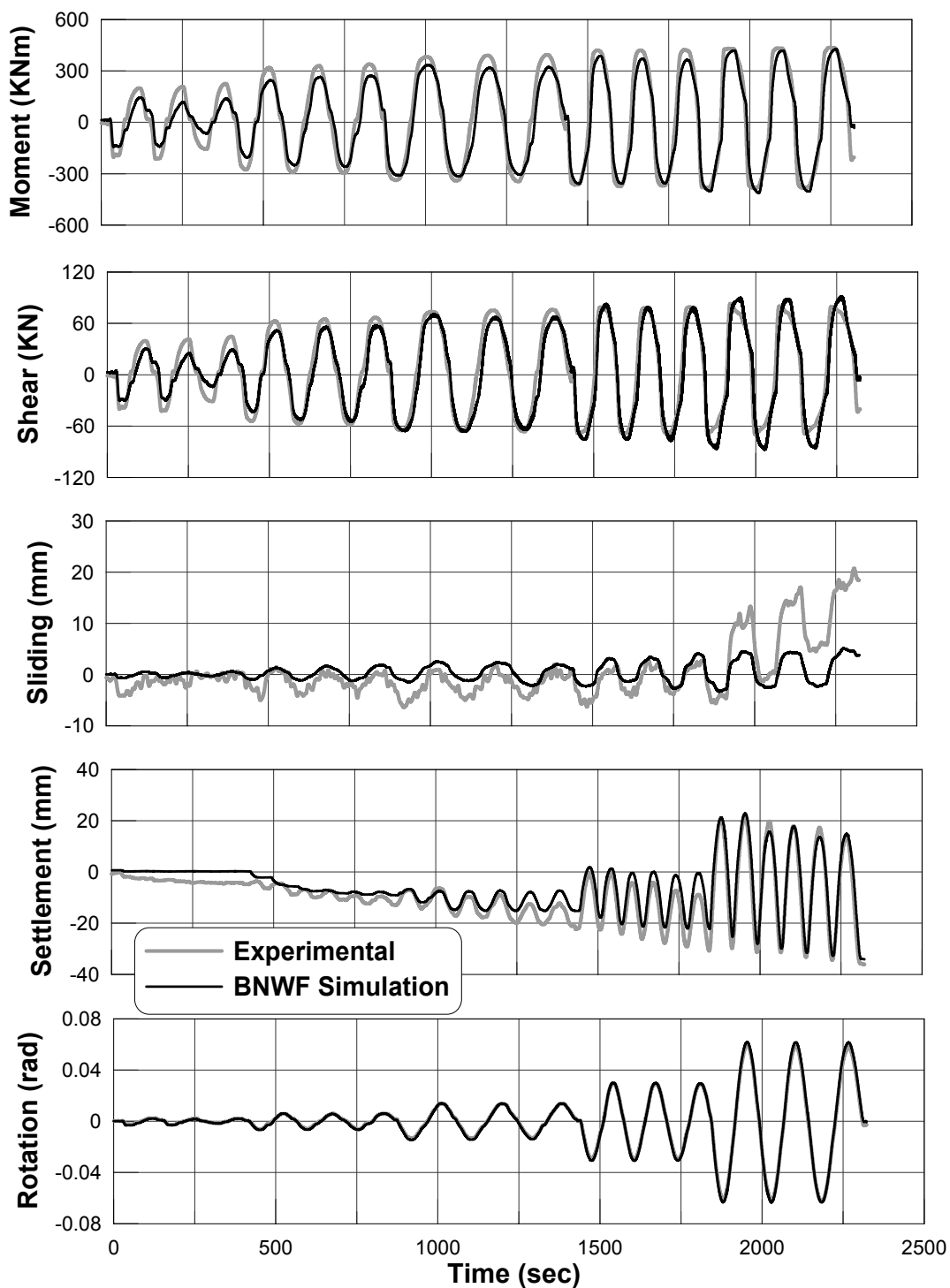


Figure B.4: Footing response comparison for test *SSG03 – 03* (static cyclic test on dense sand ($D_r = 80\%$) with $FS_v = 14.0$ and $M/H/L = 1.77$)

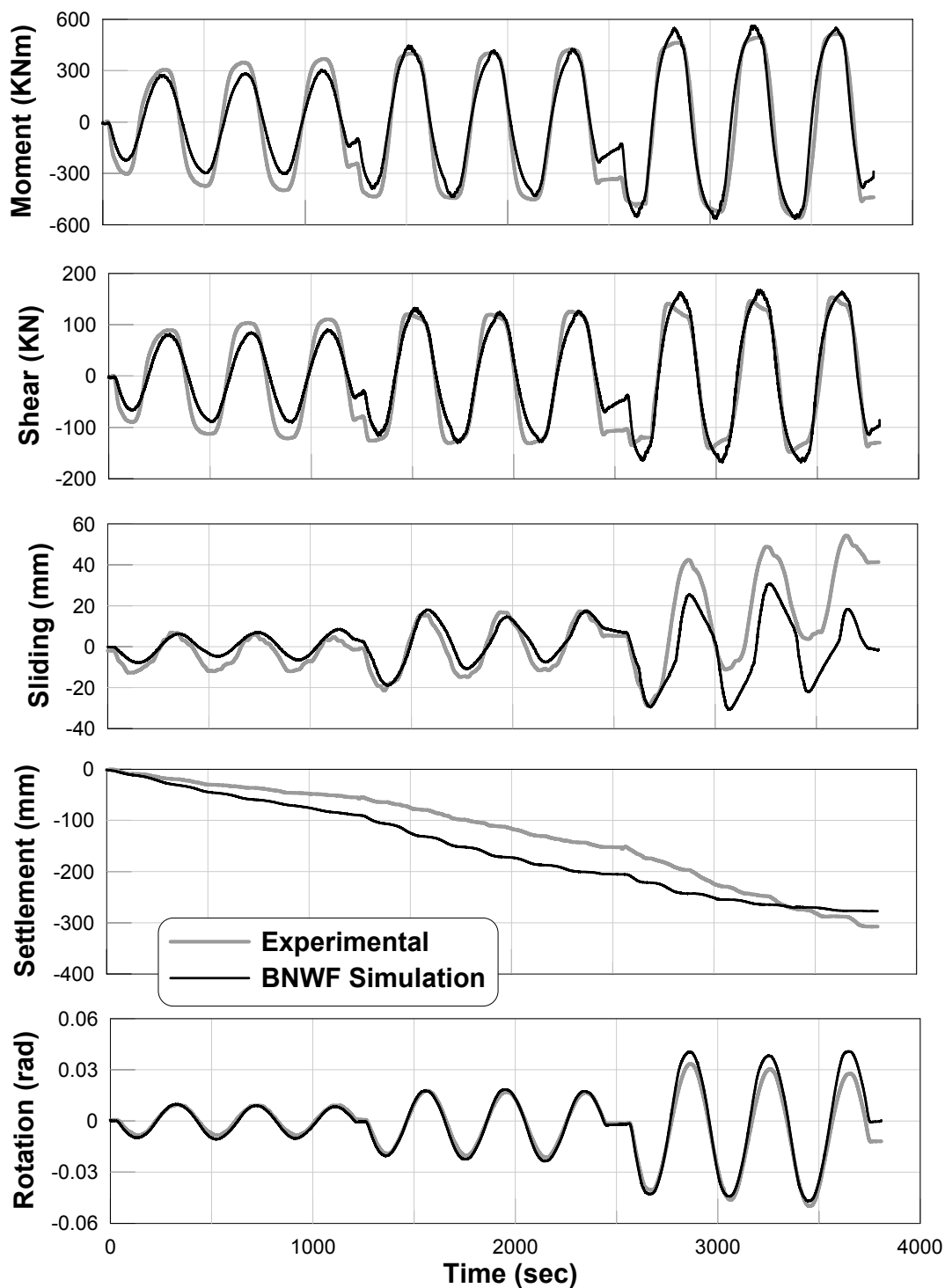


Figure B.5: Footing response comparison for test *SSG04 – 06* (static cyclic test on dense sand ($D_r = 80\%$) with $FS_v = 2.3$ and $M/H/L = 1.20$)

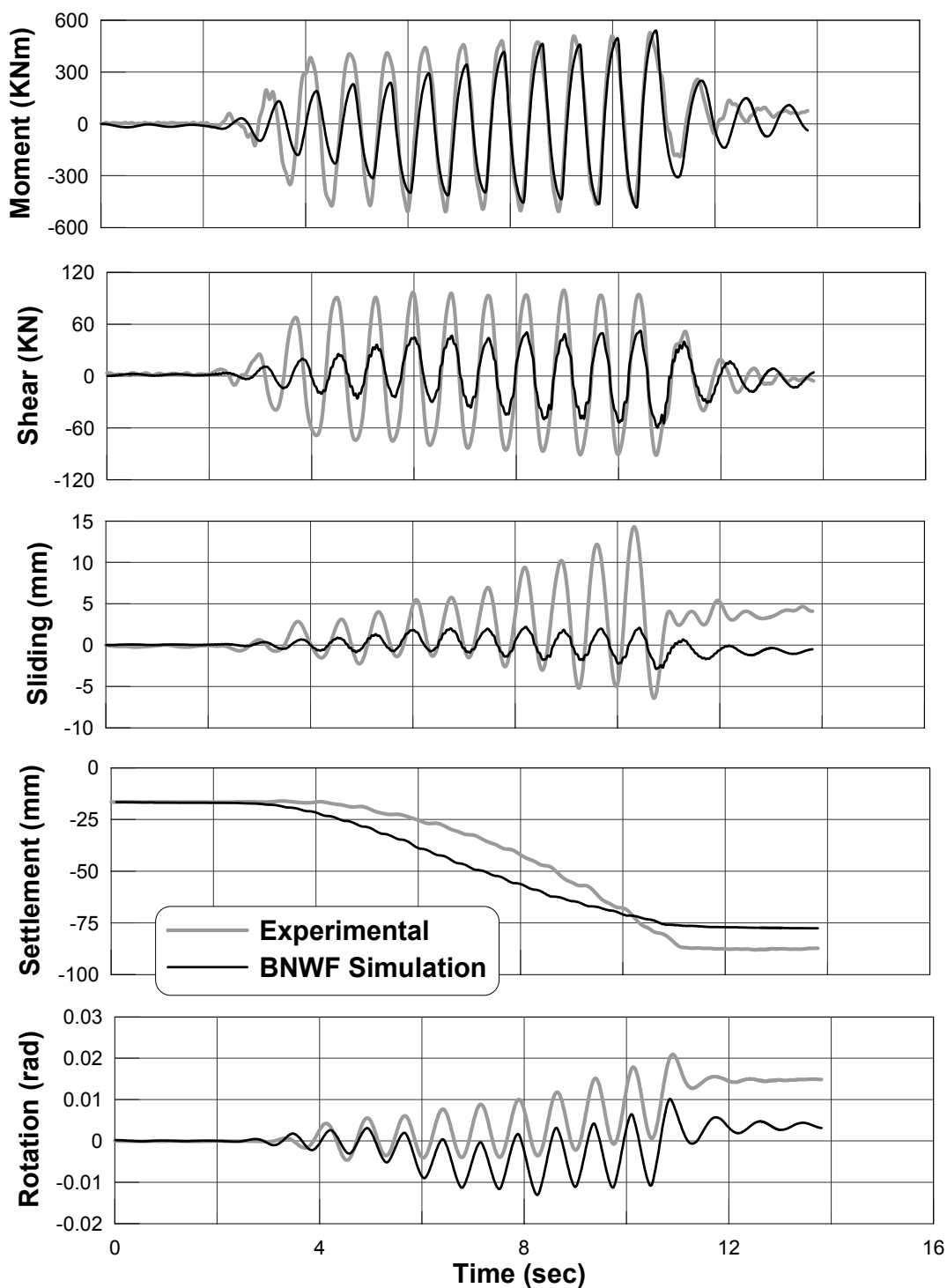


Figure B.6: Footing response comparison for test *SSG03-07* (dynamic test on dense sand ($D_r = 80\%$) with $FS_v = 7.2$ and $M/H/L = 1.80$)

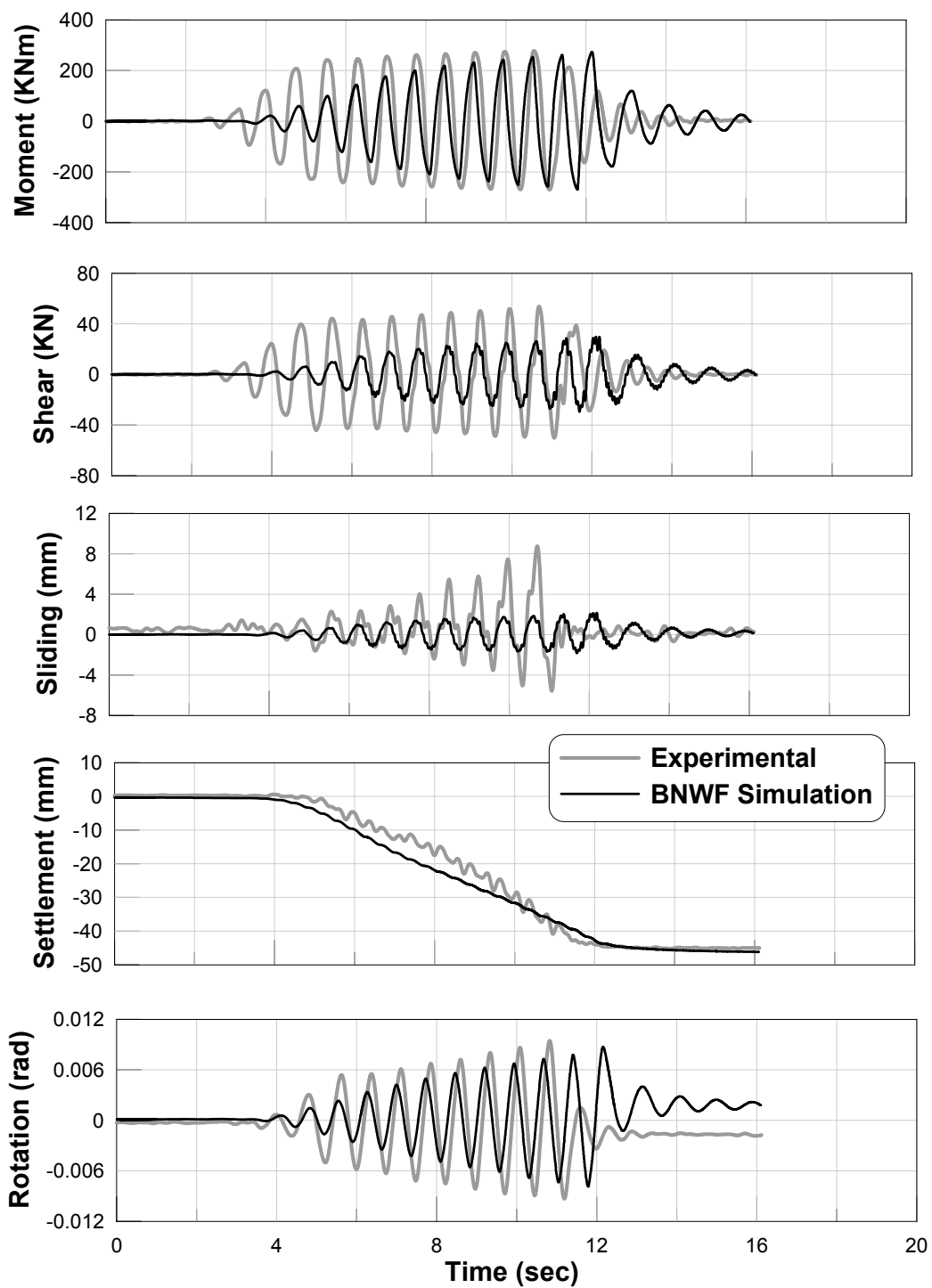


Figure B.7: Footing response comparison for test *SSG04 – 10* (dynamic test on dense sand ($D_r = 80\%$) with $FS_v = 4.0$ and $M/H/L = 1.80$)

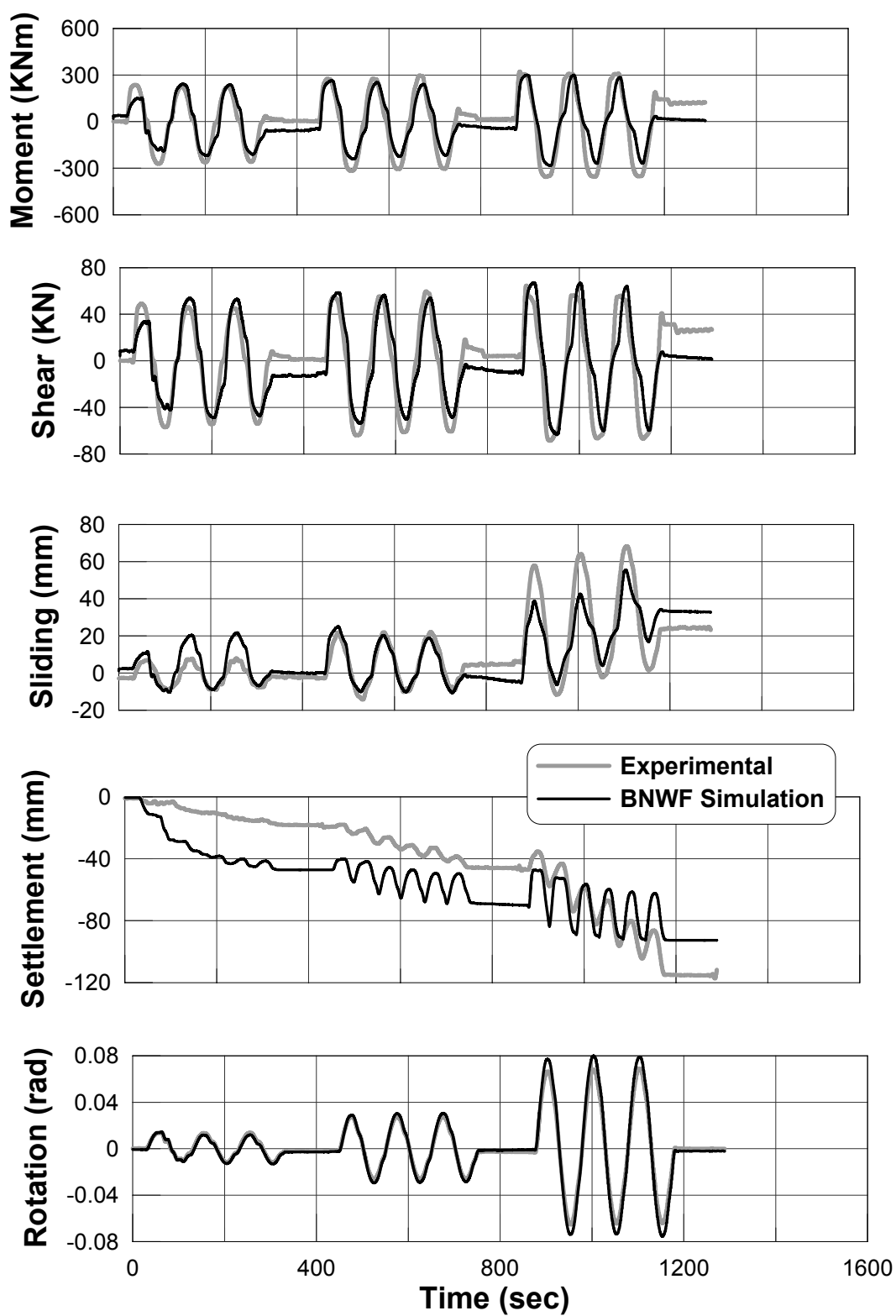


Figure B.8: Footing response comparison for test *KRR03 – 02* (static cyclic test on 100 kPa clay with $FS_v = 2.8$ and $M/H/L = 1.80$)

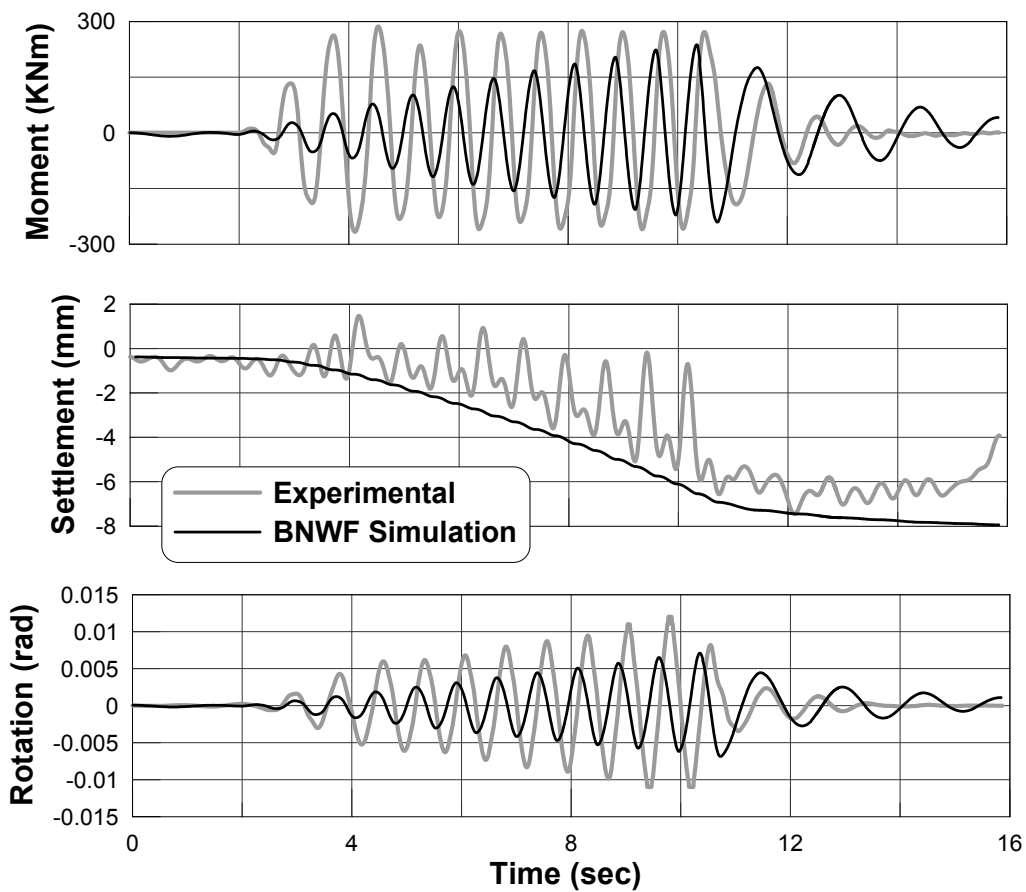


Figure B.9: Footing response comparison for test *KRR03 – 03* (dynamic test on 100 kPa clay with $FS_v = 2.8$ and $M/H/L = 1.70$)

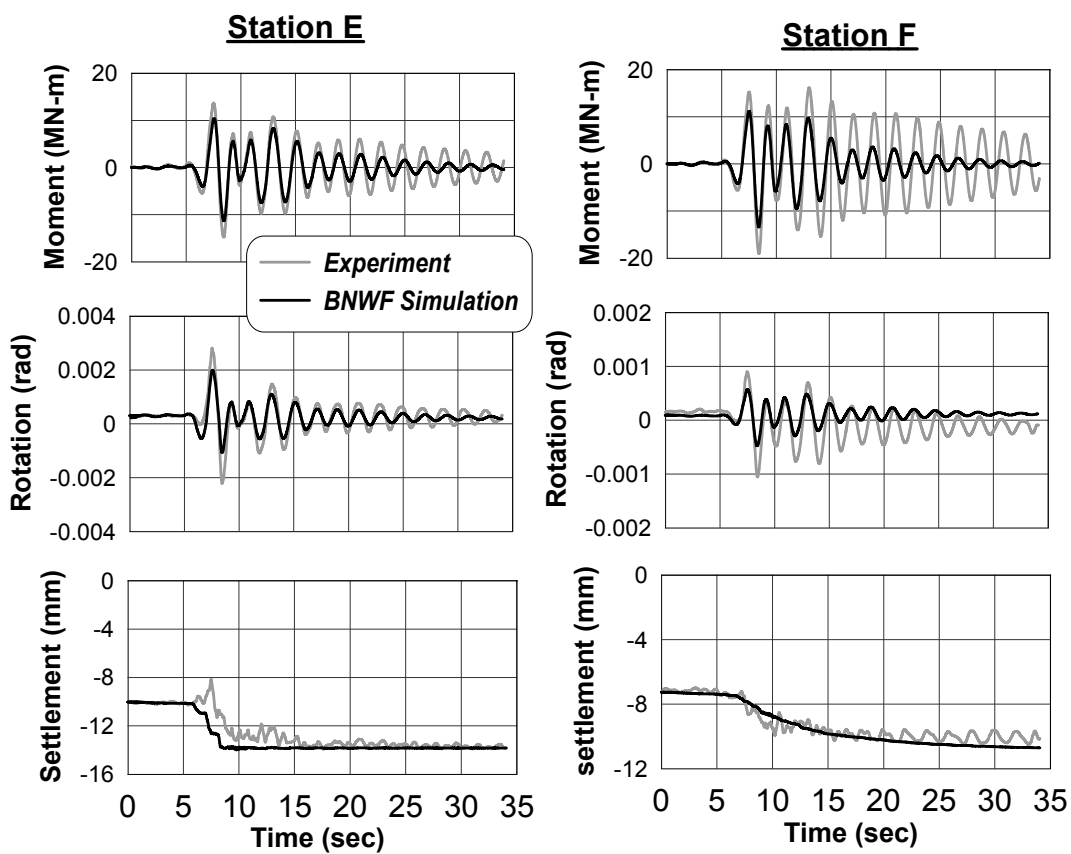


Figure B.10: Footing response comparison for (a) Station E and (b) Station F during shake-5 (dynamic test on dense sand with $D_r = 80\%$)

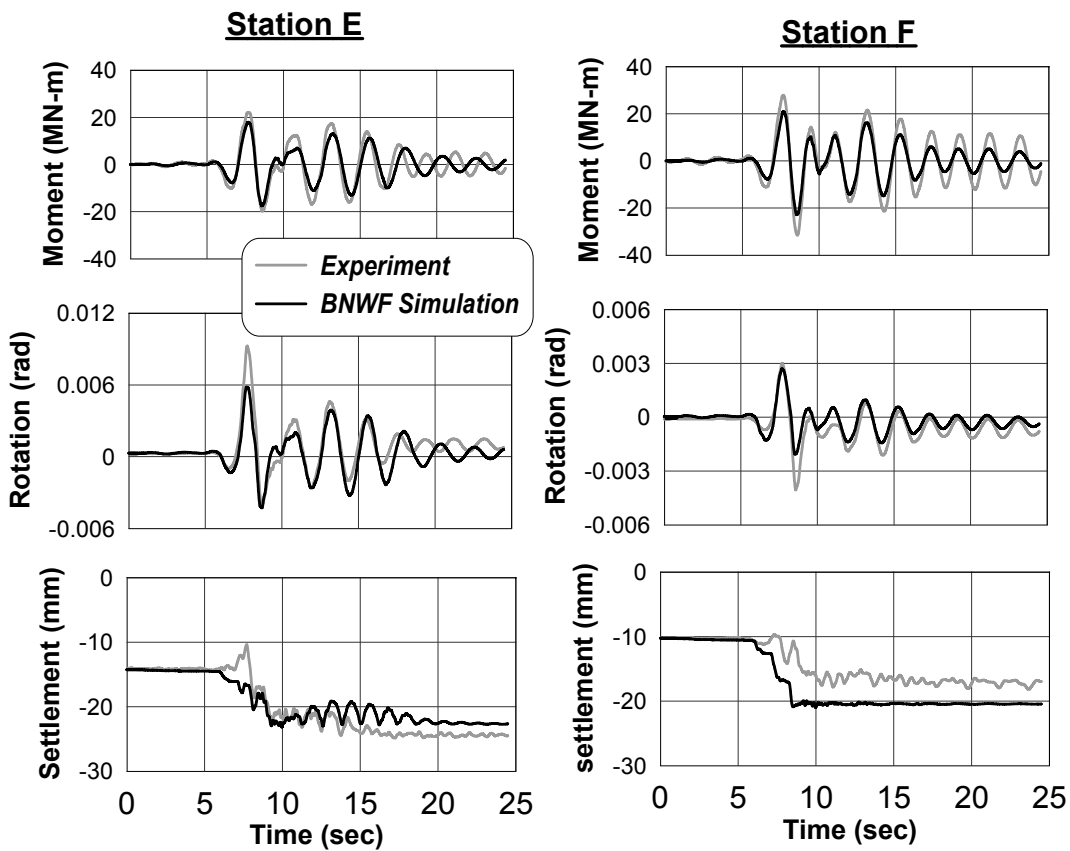


Figure B.11: Footing response comparison for (a) Station E and (b) Station F during event shake-6 (dynamic test on dense sand with $D_r = 80\%$)

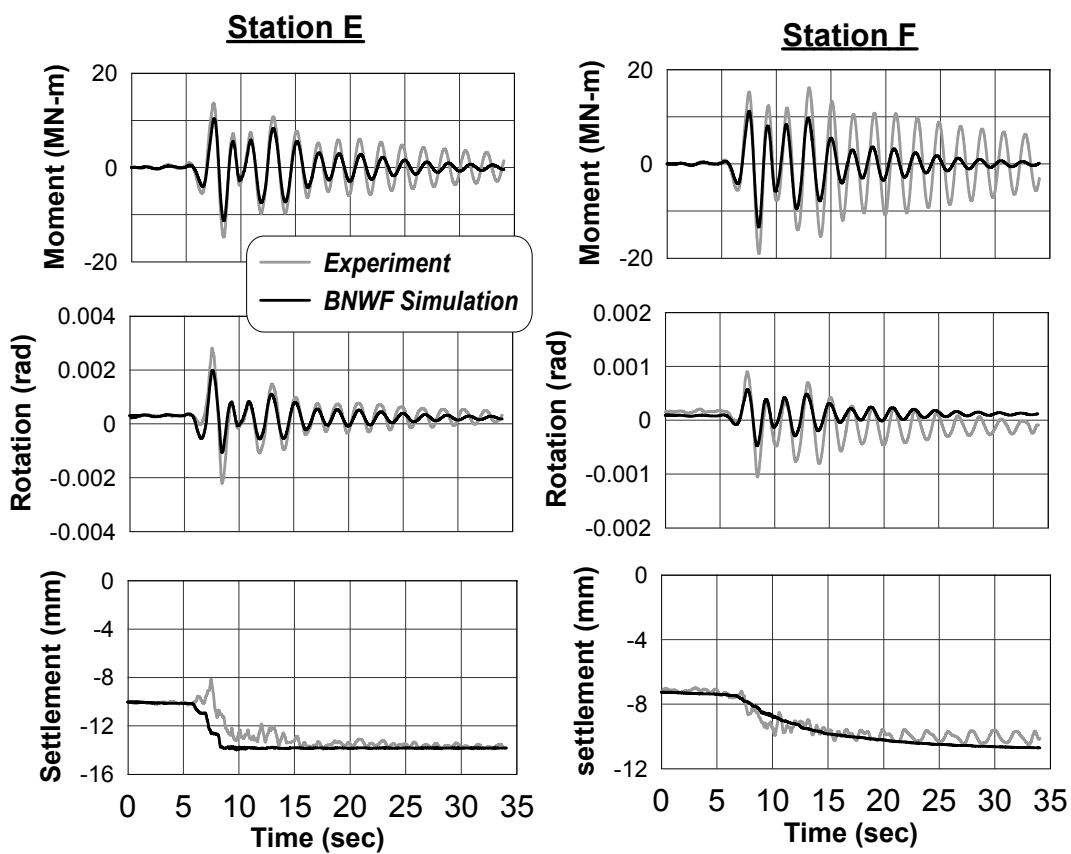


Figure B.12: Footing response comparison for (a) Station E and (b) Station F during event shake-8 (dynamic test on dense sand with $D_r = 80\%$)

Appendix C

Ground Motion Details

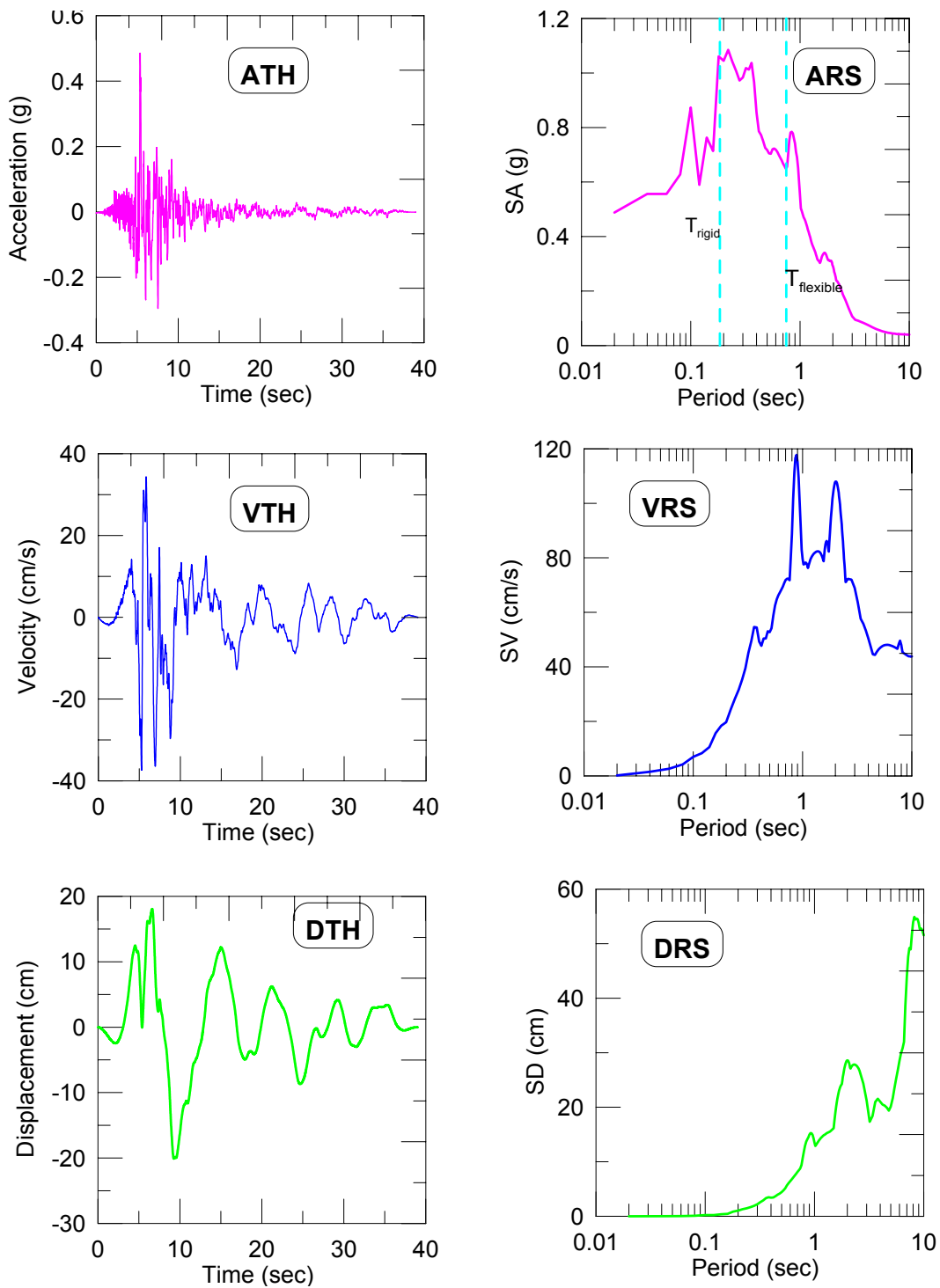


Figure C.1: Acceleration, velocity, displacement time histories and response spectra for GM1: Imperial Motion

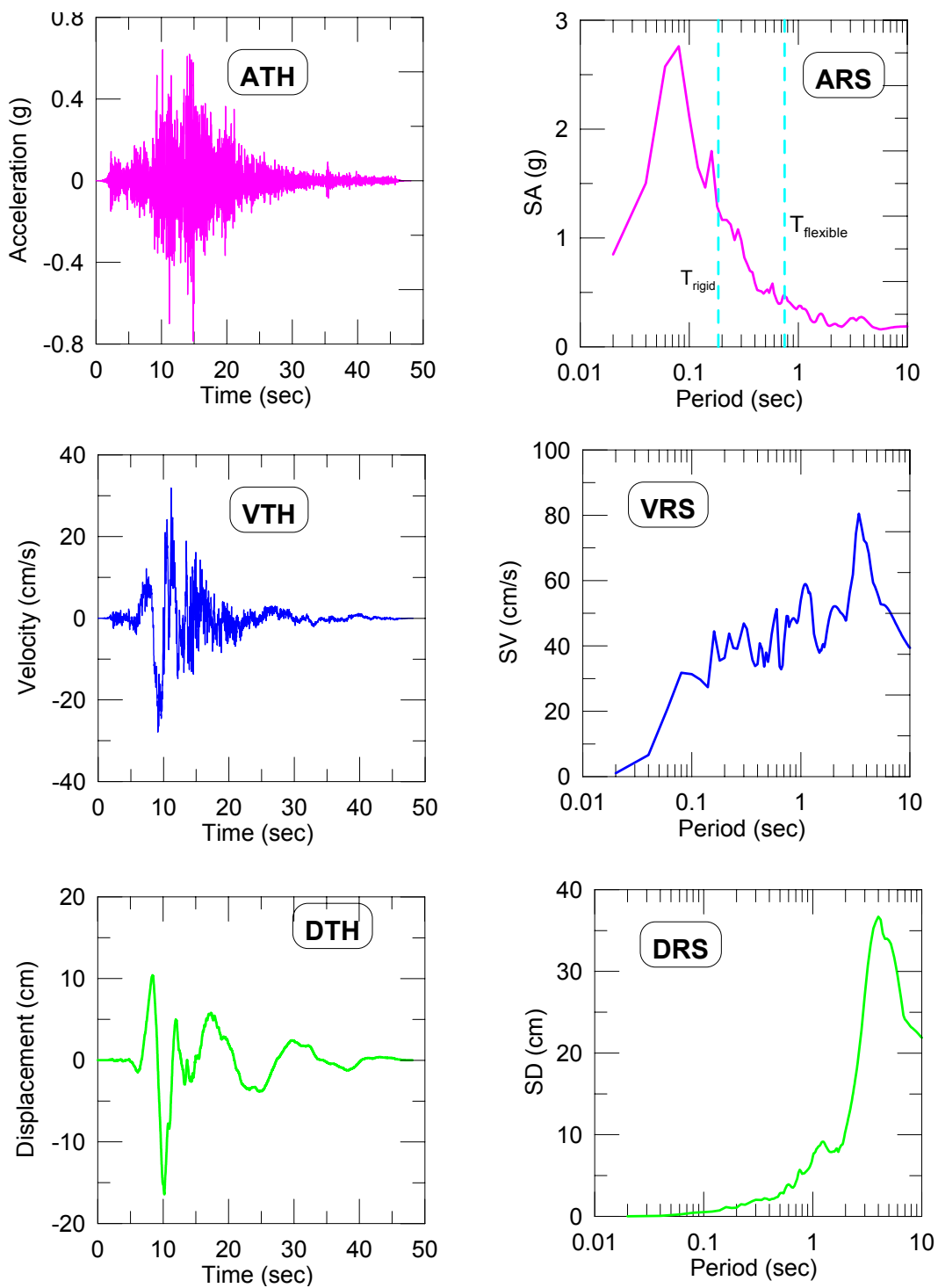


Figure C.2: Acceleration, velocity, displacement time histories and response spectra for GM2: Landers Motion

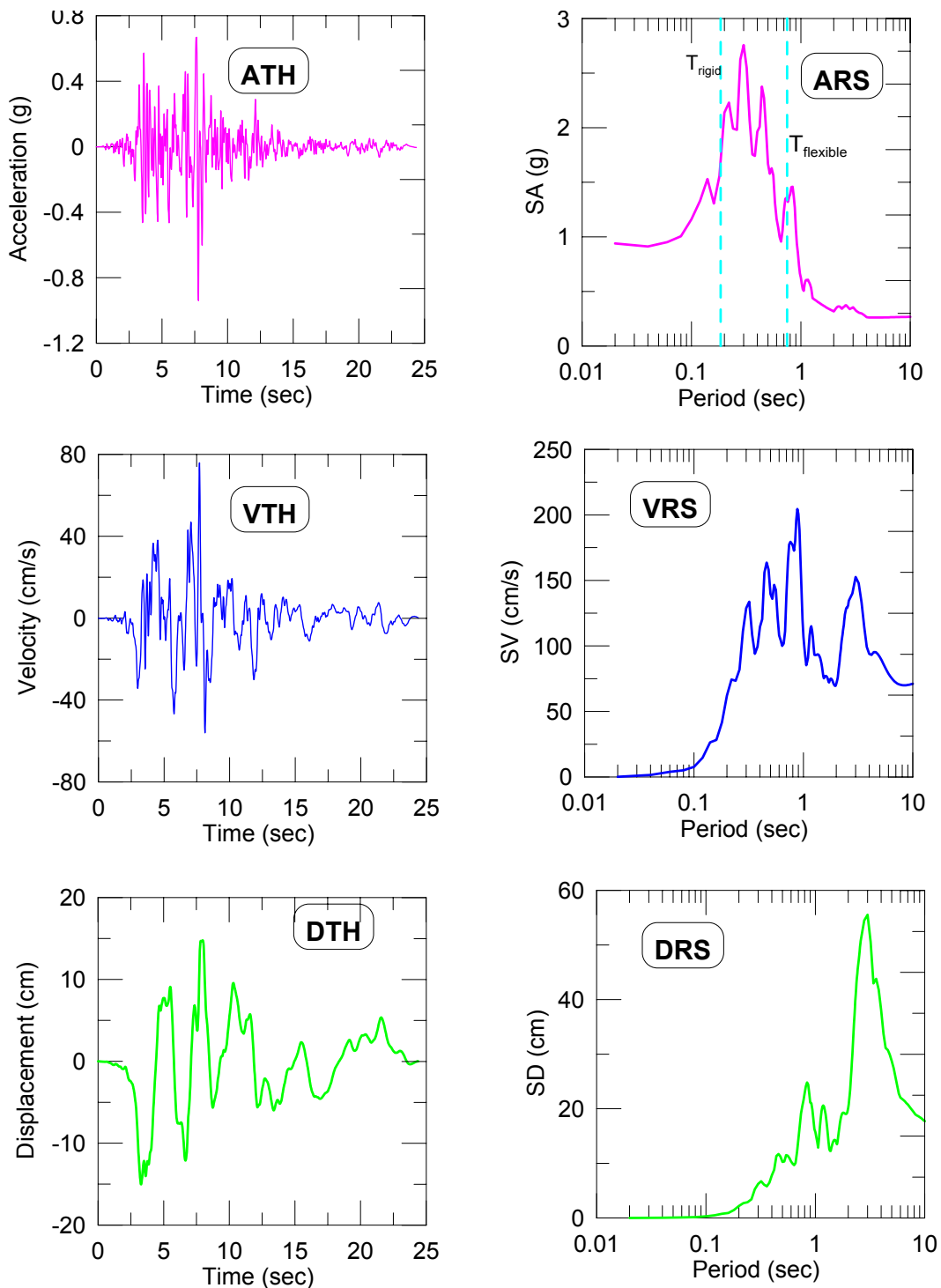


Figure C.3: Acceleration, velocity, displacement time histories and response spectra for GM3: Northridge Motion

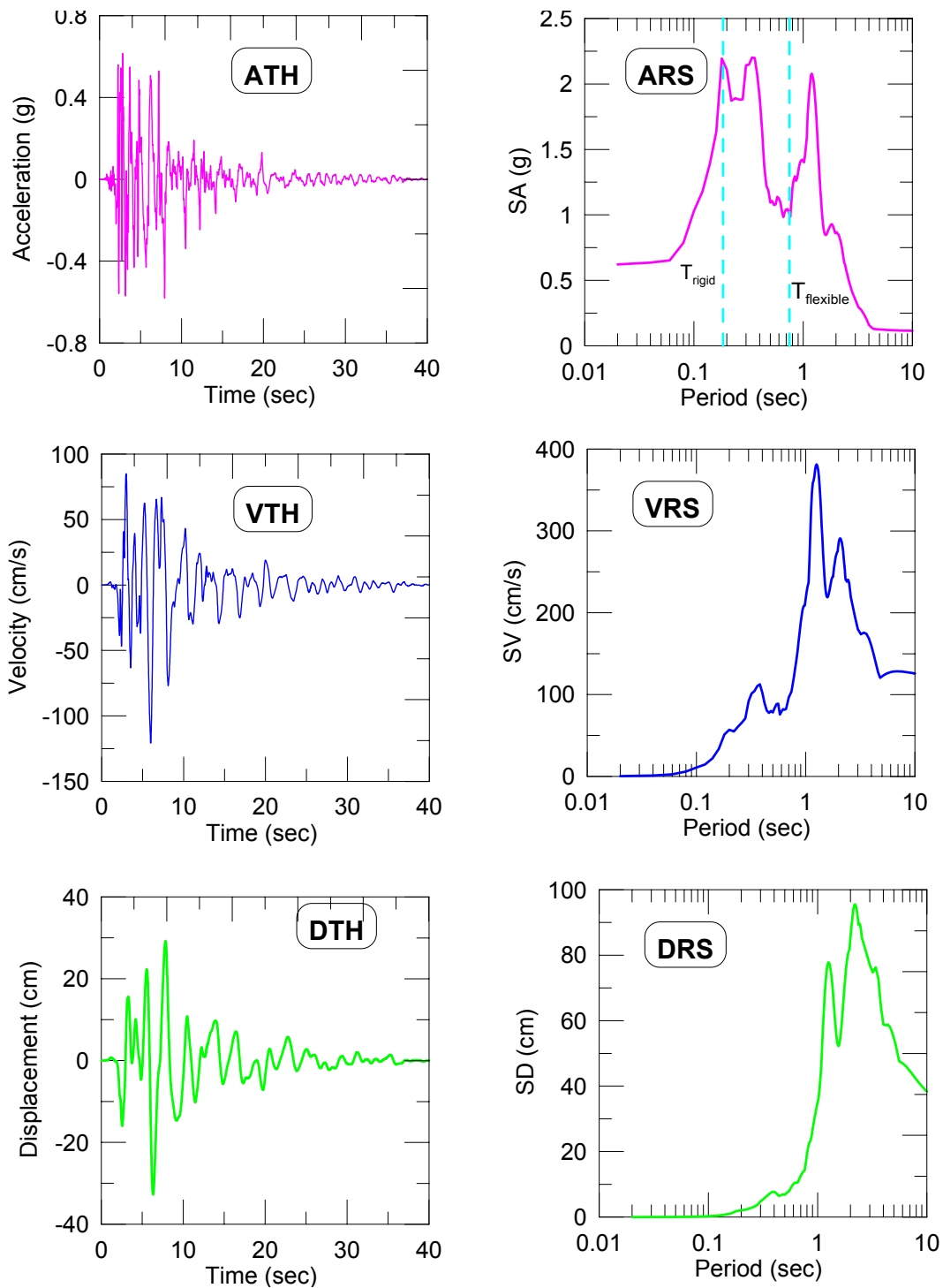


Figure C.4: Acceleration, velocity, displacement time histories and response spectra for GM4: Kobe Motion

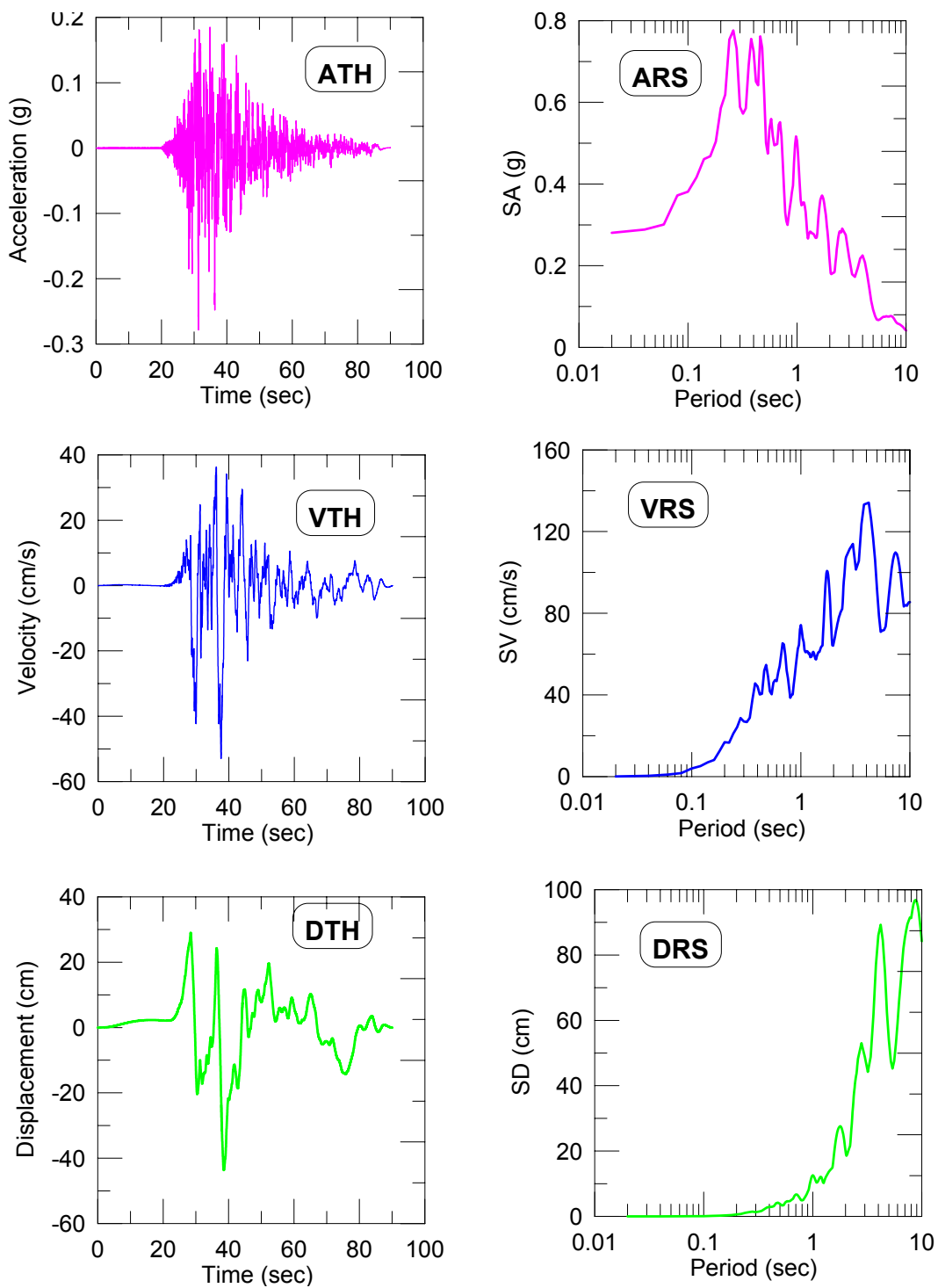


Figure C.5: Acceleration, velocity, displacement time histories and response spectra for GM5: Chi Chi Motion

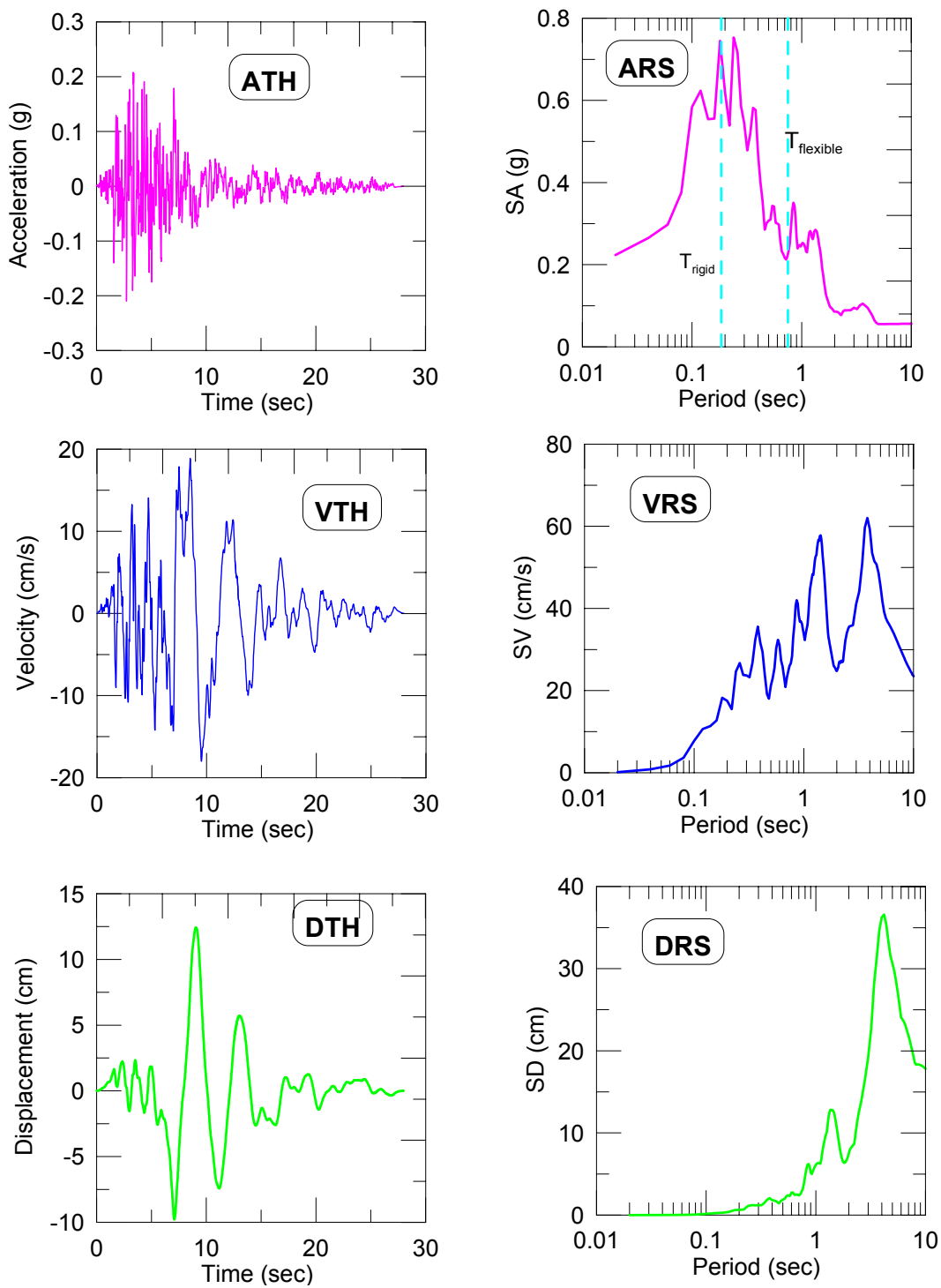


Figure C.6: Acceleration, velocity, displacement time histories and response spectra for GM6: San Fernando Motion

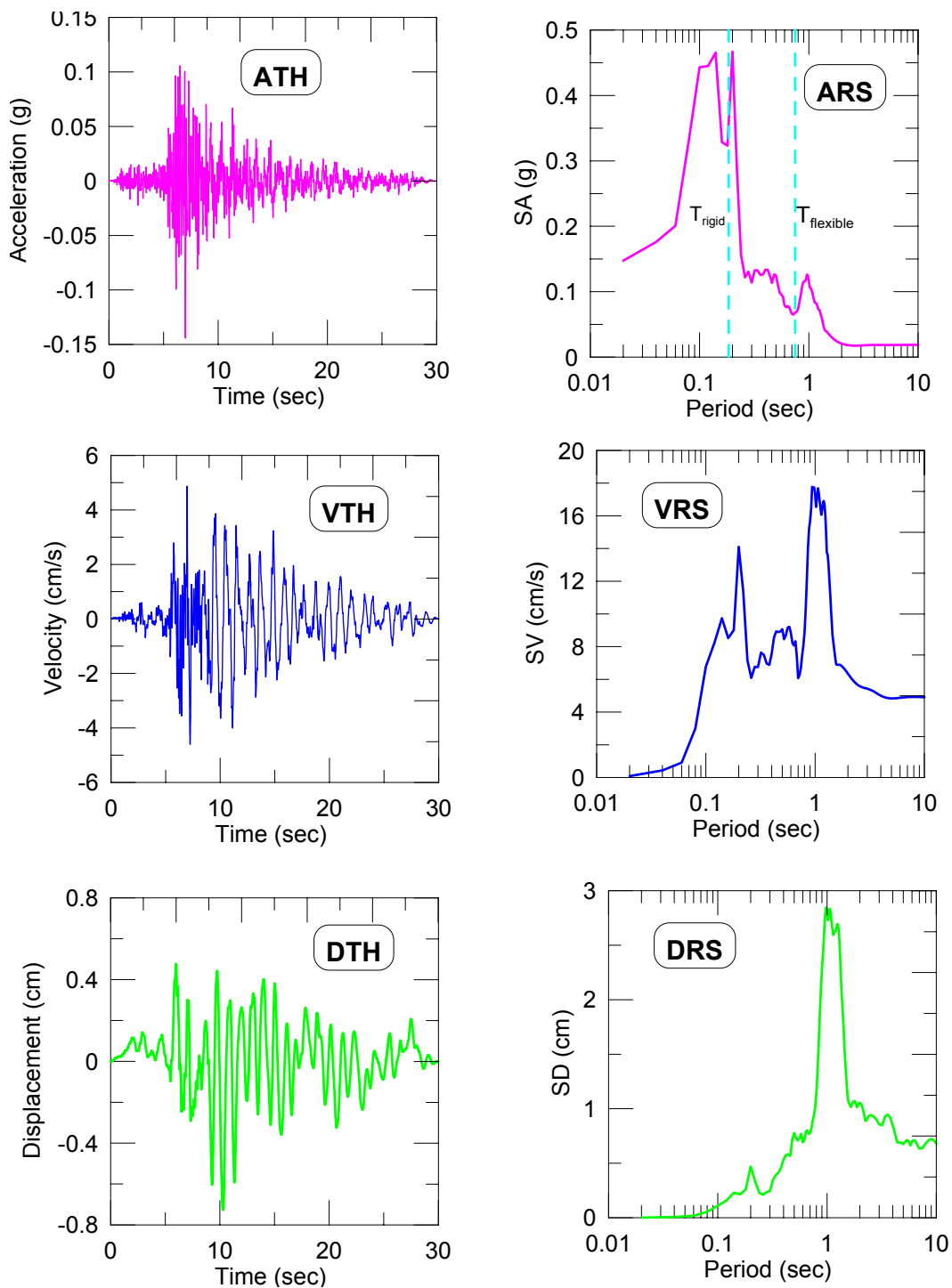


Figure C.7: Acceleration, velocity, displacement time histories and response spectra for GM7: North palmspring Motion

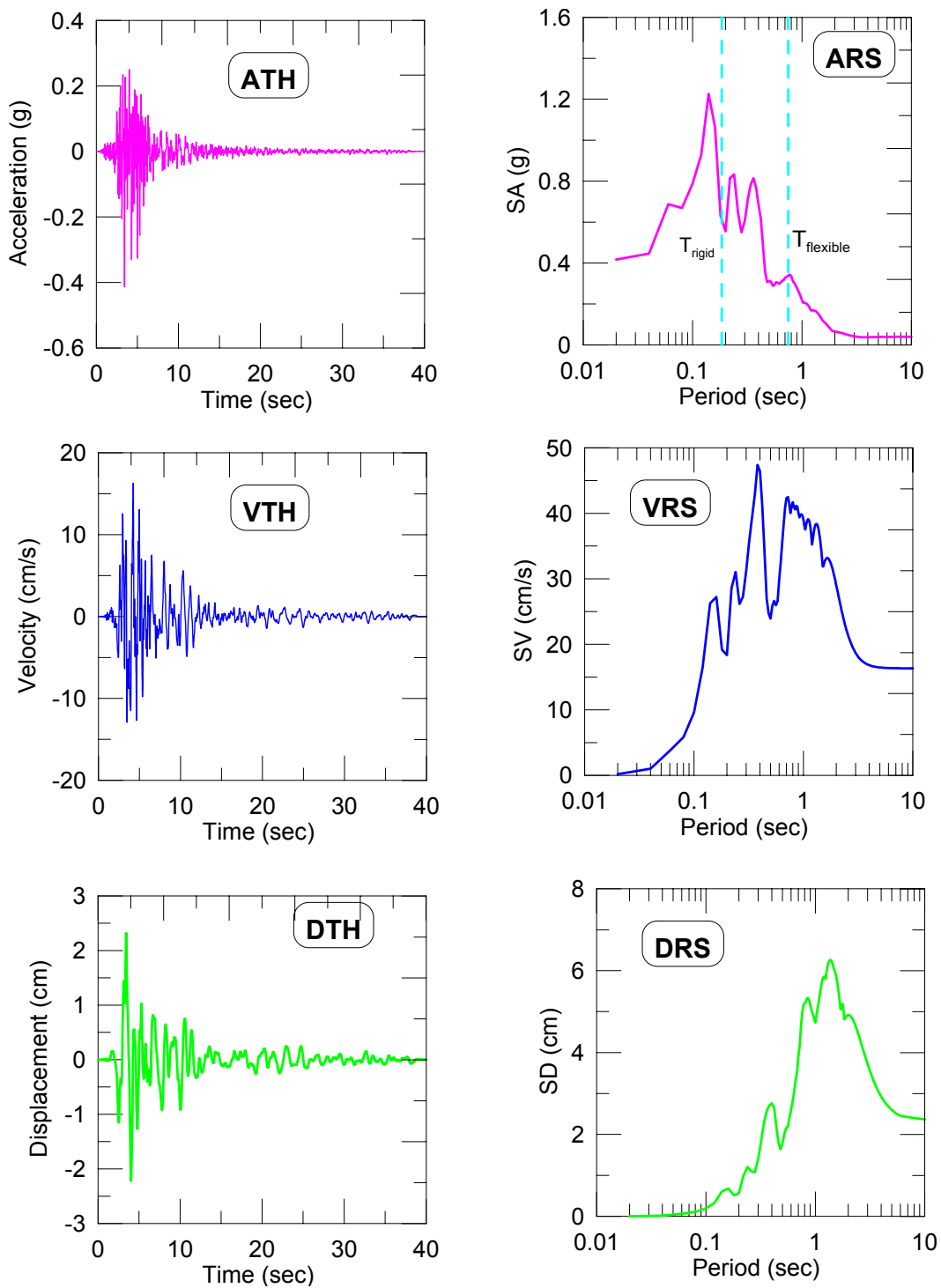


Figure C.8: Acceleration, velocity, displacement time histories and response spectra for GM8: Whittier.pdf

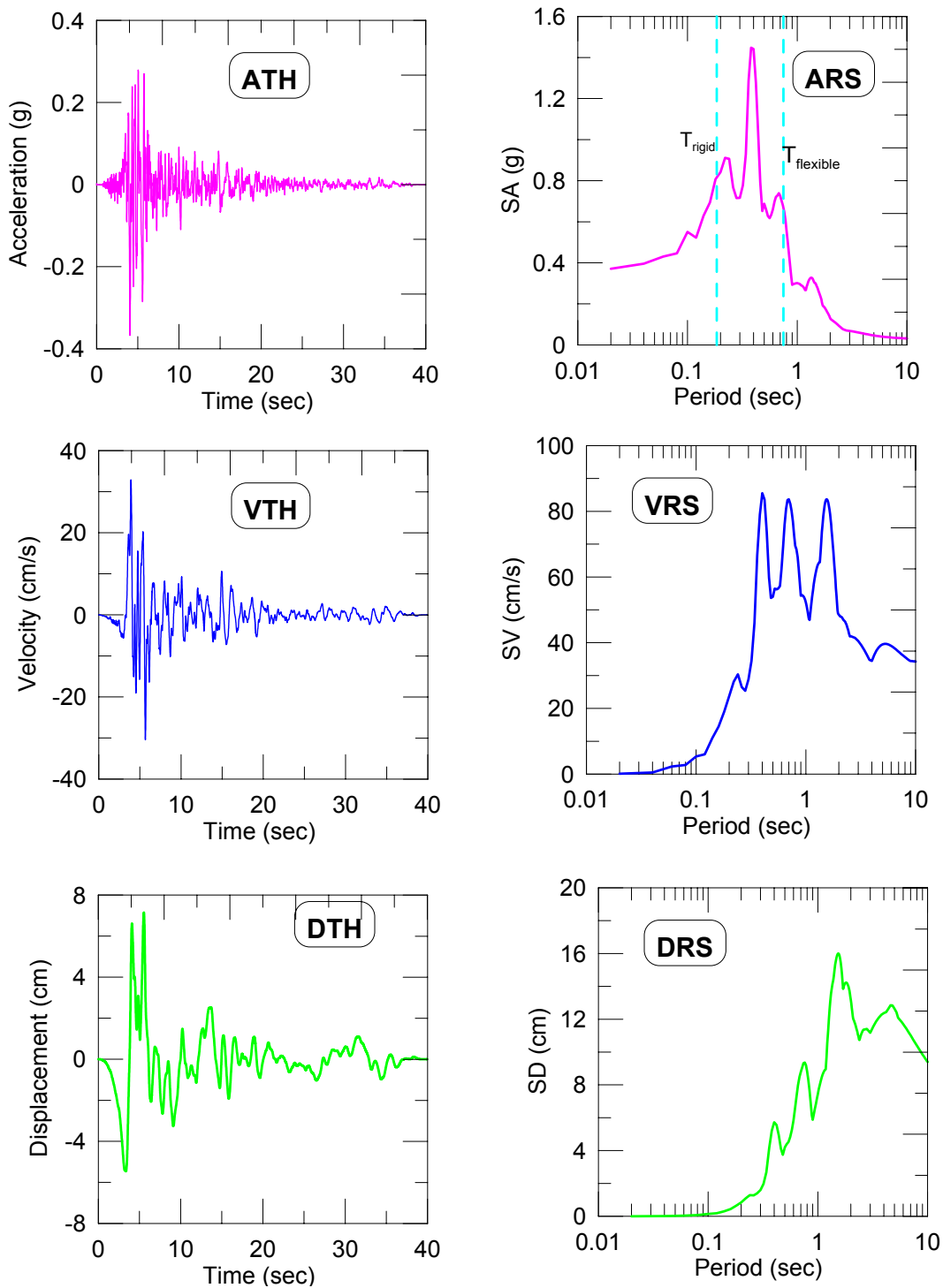


Figure C.9: Acceleration, velocity, displacement time histories and response spectra for GM9: Loma Prieta Motion

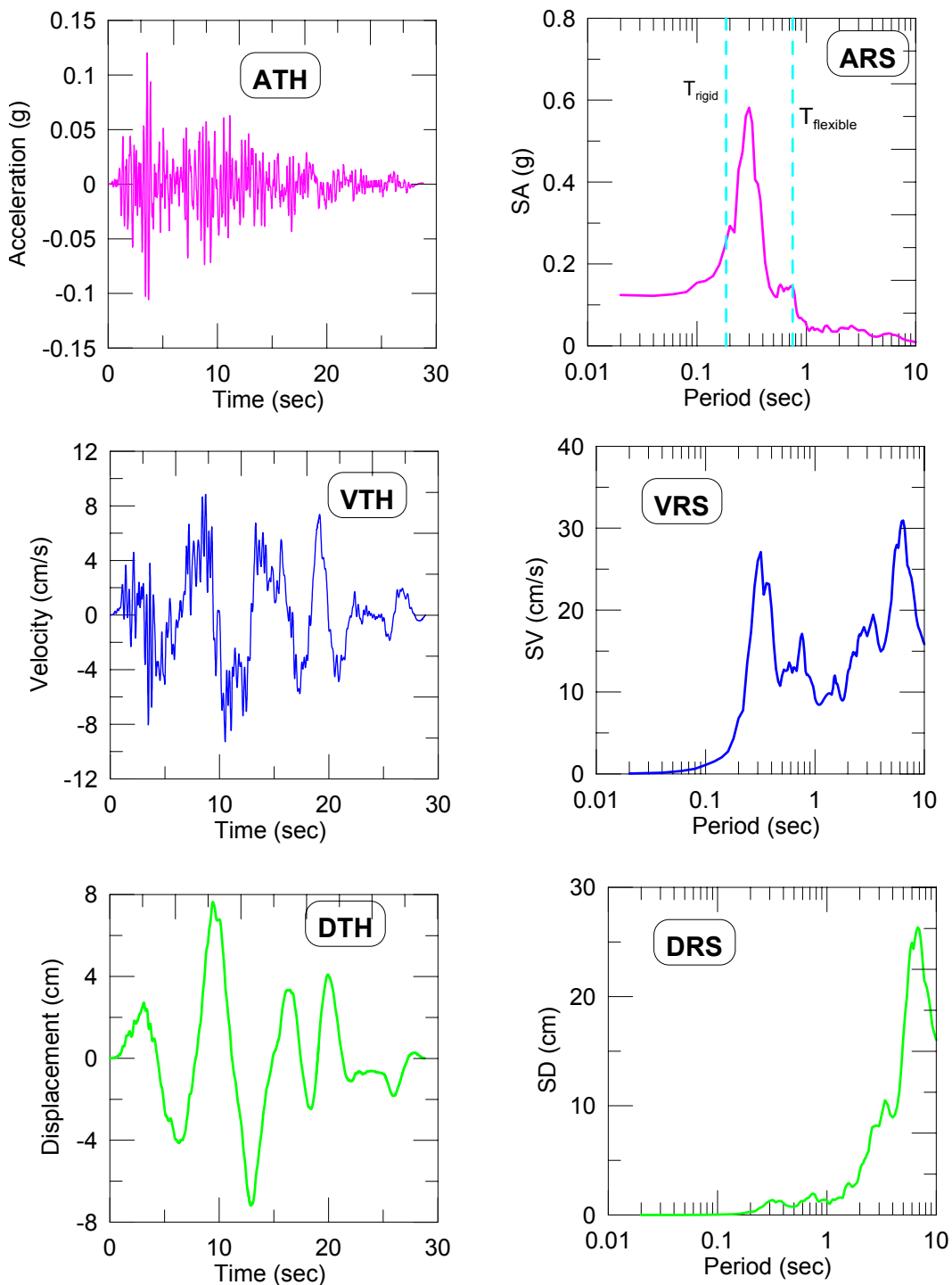


Figure C.10: Acceleration, velocity, displacement time histories and response spectra for GM10: Turkey Motion

Appendix D

Input and Output Files for Example Problems

D.1 Input and Output Files for Example 1

File 1: Input file ("Input1.txt") for soil and footing properties

```
#####
## INPUT FILE FOR SHALLOWFOUNDATIONGEN
#Input data for foundation 1

#SoilProp $SoilType $c $Phi $Gamma $G $Nu $Crad $Tp
SoilProp 1 100000.0 0.0 16000.0 20000000.0 0.4 0.05 0.1

#CapSoil $Qult $Pult $Tult $Kv $Kx
#CapSoil 1800.0 1000.0 1000.0 2000.00 3000.0

#FootProp $Lf $Bf $Hf $Df $Ef $Wg $beta
FootProp 1.0 1.0 0.25 0.5 21500000000.0 120000.0 0.0

#MeshProp $Rk $Re $le/L
MeshProp 5.0 0.2 0.2

#End of input data
#####
```

```
#####
```

File 2: Master Tcl file

```
##--Example # 1 - "A shear wall supported by a strip footing"
##--Written by Prishati Raychowdhury (UCSD)
##--units: N,m
wipe
wipeAnalysis

# Create ModelBuilder
model BasicBuilder -ndm 2 -ndf 3

# Set wall and footing dimensions
set LengthWall 0.5;
set WidthWall 0.2;
set HeightWall 5.0;

# Set structural nodes
node 1 0. 0.
node 2 0. $HeightWall

# set wall properties
set AWall [expr $WidthWall*$LengthWall]
set EWall [expr 2.15*pow(10,10)]; #----[N/m^2] concrete
set IWall [expr $WidthWall*pow($LengthWall,3)/12.]
```



```

# set wall material
uniaxialMaterial Elastic 1 $EWall

# set geometric transformation
geomTransf Linear 1

# set wall element
#element elasticBeamColumn $eleTag $iNode $jNode $A $E $Iz $transfTag
element elasticBeamColumn 1 1 2 $AWall $EWall $IWall 1

# set wall mass
set MWall 1200.0; #---mass of structure (kg)
mass 2 $MWall $MWall 1
#
#
#-----
# Use ShallowFoundationGen command to
# attach shallow foundation with Foundation tag=1
# at node 1
#-----
#
#
set FoundationTag 1
#ShallowFoundationGen $FoundationTag $ConnectNode $InputFileName $FootCondition
ShallowFoundationGen $FoundationTag 1 "Input1.txt" 5
source Foundation $FoundationTag.tcl

set MassFooting 1200.0
mass 1 $MassFooting $MassFooting 1
#-----
# Eigen Value Analysis
#-----
set PI 3.1415926
set lambda [eigen 1]
set lambda [lindex $lambda 0]
set omega [expr pow($lambda,0.5)]
set Tn [expr 2*$PI/$omega]
set fn [expr 1/$Tn]
puts "1st mode, Tn=$Tn sec, fn=$fn Hz"
#-----
# Recorder
#-----
###-wall
recorder Node -time -file WallRoofdisp.dat -node 2 -dof 1 disp
recorder Element -file WallElementforce.dat -time -ele 1 localForce
###-Spring
recorder Node -time -file EndSprLdisp.dat -node $EndFootNodeL_1 -dof 1 2 3 disp
recorder Element -file EndSpringLforce.dat -time -ele $EndSprEleL_1 force
#-----
# Gravity LOAD PATTERNS
#-----
set gacc 9.87
set FSv 5.0
set deadLoad [expr ($MassFooting+$MWall)*$gacc*$FSv]; #---total gravity load on footing (footing+wall)
#puts $deadLoad
pattern Plain 1 "Linear" {

```

```

    load 2 0. [expr -$deadLoad] 0.
}
#-----
# gravity analysis
#-----
system UmfPack
constraints Plain
test NormDisplncr 1.0e-8 40 0
algorithm Newton
numberer RCM
integrator LoadControl 0.1
analysis Static
analyze 10; #use 10 analysis steps
#-----
# Pushover analysis
#-----
#loadConst
loadConst -time 0.0
#-----
# Start of Load Control
#-----
pattern Plain 2 "Linear" {
    load 2 -10.0 0.0 0.
}
analyze 100
##-----
## End of Load Control
##-----

#-----
# Start of Displacement Control
#-----
#Set some parameters
set dU -0.005; # Displacement increment
##integrator DisplacementControl node dof init Jd min max
integrator DisplacementControl 2 1 $dU 3 [expr $dU/2.0] $dU
analyze 300
#-----
# End of Displacement Control
#-----

```

File 3: Output tcl file

```

#####
# This is an intermediate file generated by the command ShallowFoundationGen. #
# Source it after the ShallowFoundationGen command. #
# Use this file to check shallow foundation nodes, elements, fixity details #
# ShallowFoundationGen.cpp is developed by Prishati Raychowdhury (UCSD) #
#####

# Foundation Tag =1
# Foundation Base Condition Tag =5

```

```

#node $NodeTag $Xcoord $Ycoord
node 1001 -0.5 0
node 100001 -0.5 0
node 1002 -0.4 0
node 100002 -0.4 0
node 1003 -0.3 0
node 100003 -0.3 0
node 1004 0 0
node 100004 0 0
node 1005 0.3 0
node 100005 0.3 0
node 1006 0.4 0
node 100006 0.4 0
node 1007 0.5 0
node 100007 0.5 0
node 100008 0.5 0
node 100009 0.5 0

#equalDOF $rNodeTag $cNodeTag $dof1 $dof2 $dof3
equalDOF 1 1004 1 2 3

#Materials for shallow foundation

#uniaxialMaterial QzSimple2 $matTag $SoilType $Qult-end-extreme $z50-end <TpSoil> <CradSoil>
uniaxialMaterial QzSimple2 101 1 38020 0.00274347 0.1 0.05

#uniaxialMaterial QzSimple2 $matTag $SoilType $Qult-end $z50-end <TpSoil> <CradSoil>
uniaxialMaterial QzSimple2 102 1 76040 0.00274347 0.1 0.05

#uniaxialMaterial QzSimple2 $matTag $SoilType $Qult-mid $z50-mid <TpSoil> <CradSoil>
uniaxialMaterial QzSimple2 103 1 228120 0.0137173 0.1 0.05

#uniaxialMaterial PxSimple1 $matTag $SoilType $Pp $xp50 Cd <CradSoil>
uniaxialMaterial PxSimple1 105 1 102000 0.0145067 0.1 0.05

#uniaxialMaterial TxSimple1 $matTag $SoilType $Tult $xt50 <CradSoil>
uniaxialMaterial TxSimple1 106 1 100000 0.0142222 0.1 0.05

#Vertical spring element connectivity
#element zeroLength $eleTag $iNode $jNode -mat$matTag -dir $dir
element zeroLength 100001 100001 1001 -mat 101 -dir 2
element zeroLength 100002 100002 1002 -mat 102 -dir 2
element zeroLength 100003 100003 1003 -mat 103 -dir 2
element zeroLength 100004 100004 1004 -mat 103 -dir 2
element zeroLength 100005 100005 1005 -mat 103 -dir 2
element zeroLength 100006 100006 1006 -mat 102 -dir 2
element zeroLength 100007 100007 1007 -mat 101 -dir 2

#Horizontal spring element connectivity
#element zeroLength $eleTag $iNode $jNode -mat$matTag -dir $dir
element zeroLength 100008 1007 100008 -mat 105 -dir 1
element zeroLength 100009 1007 100009 -mat 106 -dir 1

# geomTransf Linear $stransfTag <-jntOffset $dXi $dYi $dXj $dYj>
geomTransf Linear 10

```

```
#foundation element connectivity
#element elasticBeamColumn $eleTag $iNode $jNode $A $E $Iz $transfTag
element elasticBeamColumn 1001 1001 1002 0.25 2.15e+010 0.00130208 10
element elasticBeamColumn 1002 1002 1003 0.25 2.15e+010 0.00130208 10
element elasticBeamColumn 1003 1003 1004 0.25 2.15e+010 0.00130208 10
element elasticBeamColumn 1004 1004 1005 0.25 2.15e+010 0.00130208 10
element elasticBeamColumn 1005 1005 1006 0.25 2.15e+010 0.00130208 10
element elasticBeamColumn 1006 1006 1007 0.25 2.15e+010 0.00130208 10
```

```
#fixity
fix 100001 1 1 1
fix 100002 1 1 1
fix 100003 1 1 1
fix 100004 1 1 1
fix 100005 1 1 1
fix 100006 1 1 1
fix 100007 1 1 1
fix 100008 1 1 1
fix 100009 1 1 1
```

```
set endFootNodeL_1 1001
set endFootNodeR_1 1007
set endSprEleL_1 100001
set endSprEleR_1 100007
set midSprEle_1 100004
```

```
#####
```

D.2 Input and Output Files for Example 2

File 1: Input file "Input1.txt" for Foundation-1

```
#####
#Input data for foundation 1
#SoilProp $SoilType $c $Phi $Gamma $G $Nu $Crad $Tp
SoilProp 1 100000.0 0.0 16000.0 30000000.0 0.4 0.05 0.1

#CapSoil $Qult $Pult $Tult $Kv $Kx
#CapSoil 1800.0 1000.0 1000.0 2000.00 3000.0

#FootProp $Lf $Bf $Hf $Df $Ef $Wg $beta
FootProp 1.0 1.0 0.5 1.0 21500000000.0 120000.0 0.0

#MeshProp $Rk $Re $le/L
MeshProp 2.0 0.2 0.2

#End of input data
#####
```

File 2: Input file "Input2.txt" for Foundation-2

```
#####
#Input data for foundation 1

#SoilProp $SoilType $c $Phi $Gamma $G $Nu $Crad $Tp
SoilProp 1 100000.0 0.0 16000.0 30000000.0 0.4 0.05 0.1

#CapSoil $Qult $Pult $Tult $Kv $Kx
#CapSoil 1800.0 1000.0 1000.0 2000.00 3000.0

#FootProp $Lf $Bf $Hf $Df $Ef $Wg $beta
FootProp 0.8 0.8 0.4 1.0 21500000000.0 120000.0 0.0

#MeshProp $Rk $Re $le/L
MeshProp 2.0 0.2 0.2

#End of input data
#####
```

File 3: Master Tcl file: MultiFoundation.tcl

```
#####
#--Example # 1 - "A single bay single story Frame supported by two square footings"
#--Written by Prishati Raychowdhury (UCSD)
#--units: N,m
#####
wipe
wipeAnalysis

# Create ModelBuilder
model BasicBuilder -ndm 2 -ndf 3

# Set column dimensions
set LengthCol1 0.5; #Column 1
set WidthCol1 0.5;

set LengthCol2 0.4; #Column 2
set WidthCol2 0.4;

set HeightCol 5.0; #Height of each column
et ColSpacing 3.0; #@c/c column spacing

set HeightBeam 0.4; #Beam
set WidthBeam 0.4;

# Set structural nodes
#node Tag    X        Y
node 1    0.        0.
node 2    0.        $HeightCol
node 3    $ColSpacing    0.
node 4    $ColSpacing    $HeightCol

# set wall properties
set ACol1 [expr $WidthCol1*$LengthCol1]
set ICol1 [expr $WidthCol1*pow($LengthCol1,3)/12.]
set ACol2 [expr $WidthCol2*$LengthCol2]
set ICol2 [expr $WidthCol2*pow($LengthCol2,3)/12.]
set ABeam [expr $WidthBeam*$HeightBeam]
set IBeam [expr $WidthBeam*pow($HeightBeam,3)/12.]
set E [expr 2.15*pow(10,10)]; #----[N/m^2] concrete

# set wall material
uniaxialMaterial Elastic 1    $E

# set geometric transformation
geomTransf Linear 1
```

```

geomTransf Linear 2

# set column and beam elements
#element elasticBeamColumn $eleTag $iNode $jNode $A $E $Iz $tranfTag
element elasticBeamColumn 1 1 2 $ACol1 $E $ICol1 1
element elasticBeamColumn 2 3 4 $ACol2 $E $ICol2 1
element elasticBeamColumn 3 2 4 $ABeam $E $IBeam 2
# set wall mass
set Mass 1200.0; #---nodal mass of structure (kg)
mass 2 $Mass $Mass 1.0
mass 4 $Mass $Mass 1.0
#
#
#-----
# Use ShallowFoundationGen command to
# attach shallow foundation with Foundation tag=1
# connected at node 1
#-----
#
set FoundationTag 1
#ShallowFoundationGen $FoundationTag $ConectNode $inpufile $FootCondition
ShallowFoundationGen $FoundationTag 1 "Input1.txt" 5
source Foundation_.$FoundationTag.tcl
#
#
#-----
# Use ShallowFoundationGen command to
# attach shallow foundation with Foundation tag=2
# connected at node 3
#-----
#
set FoundationTag 2
#ShallowFoundationGen $FoundationTag $ConectNode "Input.dat" $FootCondition
ShallowFoundationGen $FoundationTag 3 "Input2.txt" 4
source Foundation_.$FoundationTag.tcl

#-----
# Eigen Value Analysis
#-----
set PI 3.1415926
set lambdax [eigen 1]
set lambda [lindex $lambdax 0]
set omega [expr pow($lambda,0.5)]
set Tn [expr 2*$PI/$omega]
set fn [expr 1/$Tn]
puts "1st mode, Tn=$Tn sec, fn=$fn Hz"

```

```

#-----
# Recorder
#-----
# Column
recorder Node -time -file Coldisp1.dat -node 2 -dof 1 disp
recorder Element -file Colforce1.dat -time -ele 1 localForce
#Foundation 1: End Spring
recorder Node -time -file EndSprLdisp1.dat -node $endFootNodeL_1 -dof 1 2 3 disp
recorder Element -file EndSpringLforce1.dat -time -ele $endSprEleL_1 force
#Foundation 2: End Spring
recorder Node -time -file EndSprLdisp2.dat -node $endFootNodeL_2 -dof 1 2 3 disp
recorder Element -file EndSpringLforce2.dat -time -ele $endSprEleL_2 force

#-----
# Gravity LOAD PATTERNS
#-----
set gacc 9.87
set FSv 5.0
set deadLoad [expr $Mass*$gacc*$FSv]; #---total gravity load on footing (footing+wall)
#puts $deadLoad
pattern Plain 1 "Linear" {
    load 2 0. [expr -$deadLoad] 0.
    load 4 0. [expr -$deadLoad] 0.
}

#-----
# gravity analysis
#-----
system UmfPack
constraints Plain
test NormDispIncr 1.0e-8 40 0
algorithm Newton
numberer RCM
integrator LoadControl 0.1
analysis Static
analyze 10; #use 10 analysis steps

#-----
# Pushover analysis
#-----
#loadConst
loadConst -time 0.0
#-----
#puts $deadLoad
pattern Plain 2 "Linear" {
    load 2 -10.0 0.0 0.
}
analyze 100

```



```

# -----
# Start of Displacement Control
# -----
#Set some parameters
set dU -0.005;      # Displacement increment
#integrator DisplacementControl node dof init Jd min max
integrator DisplacementControl 2 1 $dU 3 [expr $dU/2.0] $dU
analyze 300

set dU 0.005;      # Displacement increment
##integrator DisplacementControl node dof init Jd min max
integrator DisplacementControl 2 1 $dU 3 [expr $dU/10.0] $dU
#analyze 160
# End of the analysis

```

```
#####
```

File 4: Output Tcl file: "Foundation_1.tcl"

```
#####
#
# This is an intermediate file generated by the command ShallowFoundationGen.
# Source it after the ShallowFoundationGen command.
# Use this file to check shallow foundation nodes, elements, fixity details
# ShallowFoundationGen.cpp is developed by Prishati Raychowdhury (UCSD)
#
#####

```

```

# Foundation Tag =1
# Foundation Base Condition Tag =5

#node $NodeTag $Xcoord $Ycoord
node 1001 -0.5 0
node 100001 -0.5 0
node 1002 -0.4 0
node 100002 -0.4 0
node 1003 -0.3 0
node 100003 -0.3 0
node 1004 0 0
node 100004 0 0
node 1005 0.3 0
node 100005 0.3 0
node 1006 0.4 0
node 100006 0.4 0
node 1007 0.5 0
node 100007 0.5 0
node 100008 0.5 0
node 100009 0.5 0

```

```

#equalDOF $rNodeTag $eNodeTag $dof1 $dof2 $dof3
equalDOF 1 1004 1 2 3

#Materials for shallow foundation

#uniaxialMaterial QzSimple2 $matTag $SoilType $Qult-end-extreme $z50-end <TpSoil> <CradSoil>
uniaxialMaterial QzSimple2 101 1 41840 0.00270946 0.1 0.05

#uniaxialMaterial QzSimple2 $matTag $SoilType $Qult-end $z50-end <TpSoil> <CradSoil>
uniaxialMaterial QzSimple2 102 1 83680 0.00270946 0.1 0.05

#uniaxialMaterial QzSimple2 $matTag $SoilType $Qult-mid $z50-mid <TpSoil> <CradSoil>
uniaxialMaterial QzSimple2 103 1 251040 0.00541893 0.1 0.05

#uniaxialMaterial PxSimple1 $matTag $SoilType $Pp $xp50 Cd <CradSoil>
uniaxialMaterial PxSimple1 105 1 208000 0.0197215 0.1 0.05

#uniaxialMaterial TxSimple1 $matTag $SoilType $Tult $xt50 <CradSoil>
uniaxialMaterial TxSimple1 106 1 100000 0.00948148 0.1 0.05

#Vertical spring element connectivity
#element zeroLength $eleTag $iNode $jNode -mat$matTag -dir $dir
element zeroLength 100001 100001 1001 -mat 101 -dir 2
element zeroLength 100002 100002 1002 -mat 102 -dir 2
element zeroLength 100003 100003 1003 -mat 103 -dir 2
element zeroLength 100004 100004 1004 -mat 103 -dir 2
element zeroLength 100005 100005 1005 -mat 103 -dir 2
element zeroLength 100006 100006 1006 -mat 102 -dir 2
element zeroLength 100007 100007 1007 -mat 101 -dir 2

#Horizontal spring element connectivity
#element zeroLength $eleTag $iNode $jNode -mat$matTag -dir $dir
element zeroLength 100008 1007 100008 -mat 105 -dir 1
element zeroLength 100009 1007 100009 -mat 106 -dir 1

# geomTransf Linear $transfTag <-jntOffset $dXi $dYi $dXj $dYj>
geomTransf Linear 10

#foundation element connectivity
#element elasticBeamColumn $eleTag $iNode $jNode $A $E $Iz $transfTag
element elasticBeamColumn 1001 1001 1002 0.5 2.15e+010 0.0104167 10
element elasticBeamColumn 1002 1002 1003 0.5 2.15e+010 0.0104167 10
element elasticBeamColumn 1003 1003 1004 0.5 2.15e+010 0.0104167 10
element elasticBeamColumn 1004 1004 1005 0.5 2.15e+010 0.0104167 10
element elasticBeamColumn 1005 1005 1006 0.5 2.15e+010 0.0104167 10
element elasticBeamColumn 1006 1006 1007 0.5 2.15e+010 0.0104167 10

#fixity
fix 100001 1 1 1
fix 100002 1 1 1
fix 100003 1 1 1

```

```

fix 100004 1 1 1
fix 100005 1 1 1
fix 100006 1 1 1
fix 100007 1 1 1
fix 100008 1 1 1
fix 100009 1 1 1

```

```

set endFootNodeL_1 1001
set endFootNodeR_1 1007
set endSprEleL_1 100001
set endSprEleR_1 100007
set midSprEle_1 100004

```

```
#####
```

File 5: Output Tcl file: "Foundation_2.tcl"

```
#####
```

```

#
# This is an intermediate file generated by the command ShallowFoundationGen.
# Source it after the ShallowFoundationGen command.
# Use this file to check shallow foundation nodes, elements, fixity details
# ShallowFoundationGen.cpp is developed by Prishati Raychowdhury (UCSD)
#####

```

```

# Foundation Tag =2
# Foundation Base Condition Tag =4

```

```
#node $NodeTag $Xcoord $Ycoord
```

```

node 2001 -0.4 0
node 200001 -0.4 0
node 2002 -0.32 0
node 200002 -0.32 0
node 2003 -0.24 0
node 200003 -0.24 0
node 2004 0 0
node 200004 0 0
node 2005 0.24 0
node 200005 0.24 0
node 2006 0.32 0
node 200006 0.32 0
node 2007 0.4 0
node 200007 0.4 0

```

```

#equalDOF $rNodeTag $cNodeTag $dof1 $dof2 $dof3
equalDOF 3 2004 1 2 3

```

```
#Materials for shallow foundation
```

```

#uniaxialMaterial QzSimple2 $matTag $SoilType $Qult-end-extreme $z50-end <TpSoil> <CradSoil>
uniaxialMaterial QzSimple2 201 1 27872 0.00225616 0.1 0.05

```

```
#uniaxialMaterial QzSimple2 $matTag $SoilType $Qult-end $z50-end <TpSoil> <CradSoil>
uniaxialMaterial QzSimple2 202 1 55744 0.00225616 0.1 0.05
```

```
#uniaxialMaterial QzSimple2 $matTag $SoilType $Qult-mid $z50-mid <TpSoil> <CradSoil>
uniaxialMaterial QzSimple2 203 1 167232 0.00451232 0.1 0.05
```

```
#fix $midNode 1 0 0
```

```
fix 3 1 0 0
```

```
#Vertical spring element connectivity
```

```
#element zeroLength $eleTag $iNode $jNode -mat$matTag -dir $dir
```

```
element zeroLength 200001 200001 2001 -mat 201 -dir 2
```

```
element zeroLength 200002 200002 2002 -mat 202 -dir 2
```

```
element zeroLength 200003 200003 2003 -mat 203 -dir 2
```

```
element zeroLength 200004 200004 2004 -mat 203 -dir 2
```

```
element zeroLength 200005 200005 2005 -mat 203 -dir 2
```

```
element zeroLength 200006 200006 2006 -mat 202 -dir 2
```

```
element zeroLength 200007 200007 2007 -mat 201 -dir 2
```

```
# geomTransf Linear $transfTag <-jntOffset $dXi $dYi $dXj $dYj>
```

```
geomTransf Linear 20
```

```
#foundation element connectivity
```

```
#element elasticBeamColumn $eleTag $iNode $jNode $A $E $Iz $transfTag
```

```
element elasticBeamColumn 2001 2001 2002 0.32 2.15e+010 0.00426667 20
```

```
element elasticBeamColumn 2002 2002 2003 0.32 2.15e+010 0.00426667 20
```

```
element elasticBeamColumn 2003 2003 2004 0.32 2.15e+010 0.00426667 20
```

```
element elasticBeamColumn 2004 2004 2005 0.32 2.15e+010 0.00426667 20
```

```
element elasticBeamColumn 2005 2005 2006 0.32 2.15e+010 0.00426667 20
```

```
element elasticBeamColumn 2006 2006 2007 0.32 2.15e+010 0.00426667 20
```

```
#fixity
```

```
fix 200001 1 1 1
```

```
fix 200002 1 1 1
```

```
fix 200003 1 1 1
```

```
fix 200004 1 1 1
```

```
fix 200005 1 1 1
```

```
fix 200006 1 1 1
```

```
fix 200007 1 1 1
```

```
set endFootNodeL_2 2001
```

```
set endFootNodeR_2 2007
```

```
set endSprEleL_2 200001
```

```
set endSprEleR_2 200007
```

```
set midSprEle_2 200004
```

```
#####
```

References

- Aiban, S. A. and Znidarcic, D. (1995). "Centrifuge modeling of bearing capacity of shallow foundations on sands." *ASCE Journal of Geotechnical Engineering*, 121(10), 704–712.
- Allotey, N. and Naggar, M. H. E. (2003). "Analytical moment-rotation curves for rigid foundations based on a winkler model." *Soil Dynamics and Earthquake Engineering*, 23, 367–381.
- Allotey, N. and Naggar, M. H. E. (2007). "An investigation into the winkler modeling of the cyclic response of rigid footings." *Soil Dynamics and Earthquake Engineering*, 28, 44–57.
- API (1987). *Recommended Practice for Planning, Designing and Constructing Fixed Off-shore Platforms API Recommended Practice 2A (RP2A), Seventeenth Edition, April 1*. American Petroleum Institute.
- Apostolou, M., Thorel, L., Gazetas, G., Garnier, J., and Rault, G. (2007). "Physical and numerical modeling of soil-footing-structure under lateral cyclic loading." *Proceedings, 4th International Conference on Earthquake Geotechnical Engineering*, Thessaloniki, Greece.
- ASCE-7 (2005). *Seismic Evaluation and Retrofit of Concrete Buildings*. Structural Engineering Institute (SEI) and American Society of Civil Engineers (ASCE), Reston, Virginia.
- ATC-40 (1996). *Seismic Evaluation and Retrofit of Concrete Buildings*. Applied Technology Council (ATC), Redwood City, California.

- Barlett, P. E. (1976). "Foundation rocking on a clay soil. Master's thesis, University of Auckland, New Zealand.
- Bjerrum, L. (1977). "Allowable settlement of structures." *Proceedings, European Conference on Soil Mechanics and Foundation Engineering*, Wiesbaden, Germany. Vol III. 135–137.
- Boulanger, R. W. (2000a). "The PySimple1 Material, Document for the OpenSees platform. URL: <http://opensees.berkeley.edu>.
- Boulanger, R. W. (2000b). "The QzSimple1 Material, Document for the OpenSees platform. URL: <http://opensees.berkeley.edu>.
- Boulanger, R. W. (2000c). "The TzSimple1 Material, Document for the OpenSees platform. URL: <http://opensees.berkeley.edu>.
- Boulanger, R. W., Curras, C. J., Kutter, B. L., Wilson, D. W., and Abghari, A. (1999). "Seismic soil-pile-structure interaction experiments and analyses." *Journal of Geotechnical and Geoenvironmental Engineering*, 125(9), 750–759.
- Briaud, J. L. and Gibbens, R. M. (1994). "Predicted and measured behavior of five spread footings on sand." *Geotechnical Special Publication*, 41.
- Caquot, A. and Kerisel, J. (1948). *Tables for Calculation of Passive Pressure, Active Pressure and Bearing Capacity of Foundations*. Gauthier-Villars, Paris, France.
- Chang, B. (2008).," PhD thesis, University of California, San Diego.
- Chang, B., Thomas, J. M., Raychowdhury, P., Gajan, S., L., K. B., and Hutchinson, T. C. (2007). "Soil-foundation-structure interaction: Shallow foundations." Centrifuge Data Report for the JMT02 Test Series: SSRP 07/24, University of California, Davis.

- Chopra, A. (1995). *Dynamics of Structures: Theory and Application to Earthquake Engineering*. Prentice Hall, New Jersey.
- Chopra, A. and Yim, S. C. (1984). "Earthquake response of structures with partial uplift on winkler foundation." *Earthquake Engineering and Structural Dynamics*, 12(4), 263–281.
- Chopra, A. and Yim, S. C. (1985). "Simplified earthquake analysis of structures with foundation uplift." *ASCE Journal of Structural Engineering*, 111(4), 906–930.
- Coulomb, C. A. (1776). "Essai sur une application des rgles des maximis et minimis quelques problmes de statique relatifs l'architectute." *Mm. acad. roy. prs. Divers savants, Paris*, 3, 38.
- Cremer, C., Pecker, A., and Davenne, L. (2001). "Cyclic macro-element for soil-structure interaction: Material and geometrical nonlinearities." *International Journal for Numerical and Analytical methods in Geomechanics*, 25(12), 1257–1284.
- Das, B. M. (2007). *Principles of Foundation Engineering*. Brooks/Cole Publishing Company, California.
- DeBeer, E. E. (1970). "Experimental determination of the shape factors and bearing equation factors of sand." *Geotechnique*, 20(4), 387–411.
- Dobry, R. and Abdoun, T. (2001). "Recent studies on seismic centrifuge modeling of liquefaction and its effect on deep foundation." *Proceedings, 4th International Conference on Recent Advances in Geotechnical Earthquake Engineeirng and Soil Dynamics and Symposium in Honor of Professor W.D. Liam Finn*, San Diego, CA.
- Dormieux, L. and Pecker, A. (1995). "Seismic bearing capacity of foundation on cohesionless soil." *ASCE Journal of Geotechnical Engineering*, 121(3), 300–303.
- Duncan, J. and Mokwa, R. L. (2001). "Passive earth pressures: Theories and tests." *ASCE Journal of Geotechnical and Geoenvironmental Engineering*, 127(3), 248–257.

- Dutta, S. C. and Roy, R. (2002). "A critical review on idealization and modeling for interaction among soil-foundation-structure system." *Computers and Structures*, 80, 1579–1594.
- EPRI (1990). *Manual on Estimating Soil Properties for Foundation Design, Electric Power Research Institute*. Palo Alto, California.
- FEMA 356 (2000). *Prestandard and Commentary for the Seismic Rehabilitation of Buildings*. American Society of Engineers, Virginia.
- Fenves, G. L. (1998). "Effects of footing rotation on earthquake behavior of pile supported bridge piers." Technical Report for Earth Mechanics, Inc.
- Fishman, K. L., Mander, J. B., and Richards, R. (1995). "Laboratory study of seismic free-field response of sand." *Soil Dynamics and Earthquake Engineering*, 14, 33–43.
- Gadre, A. and Dobry, R. (1998). "Lateral cyclic loading centrifuge tests on square embedded footing." *ASCE Journal of Geotechnical and Geoenvironmental Engineering*, 124(11), 1128–1138.
- Gajan, S. (2006). "Physical and numerical modeling of nonlinear cyclic load-deformation behavior of shallow foundations supporting rocking shear walls," PhD thesis, University of California, Davis.
- Gajan, S., Hutchinson, T. C., Kutter, B., Raychowdhury, P., Ugalde, J. A., and Stewart, J. P. (2008). "Numerical models for the analysis and performance-based design of shallow foundations subjected to seismic loading." PEER Data Report, Pacific Earthquake Engineering Research Center.
- Gajan, S., Phalen, J., and Kutter, B. (2003a). "Soil-foundation structure interaction: Shallow foundations: Centrifuge data report for the ssg02 test series." Center for Geotechnical Modeling Data Report UCD/CGMDR-02, University of California, Davis.

- Gajan, S., Phalen, J., and Kutter, B. (2003b). "Soil-foundation structure interaction: Shallow foundations: Centrifuge data report for the ssg03 test series, university of california, davis." Center for Geotechnical Modeling Data Report: UCD/CGMDR-03.
- Gajan, S., Thomas, J. M., and Kutter, B. L. (2006). "Soil-foundation-structure interaction: Shallow foundations." Centrifuge Data Report for test series SSG04. UCD/CGMDR, Center for Geotechnical Modeling, University of California, Davis, California.
- Gazetas, G. (1991a). "Displacement and soil-structure interaction under dynamic and cyclic loading." *Proceedings, Tenth European Conference on Soil Mechanics and Foundation Engineering*, Florence.
- Gazetas, G. (1991b). "Formulas and charts for impedances of surface and embedded foundations." *Journal of Geotechnical Engineering*, 117(9), 1363–1381.
- Gazetas, G. (1991c). *Foundation Engineering Handbook*. Fang, H.Y. (Ed). Van Nostrand Rienhold.
- Gazetas, G. (2006). "Seismic design of foundations and soilstructure interaction." *Proceedings, First European Conference on Earthquake Engineering and Seismology*, Geneva, Switzerland,.
- Gazetas, G. and Tassoulas, J. (1987). "Horizontal stiffness of arbitrary shaped embedded foundations." *ASCE Journal of Geotechnical Engineering*, 113(5), 440–457.
- Goulet, C. A., Haselton, C. B., Mitrani-Reiser, J., Beck, J. L., Deierlein, G. G., Porter, K. K., and Stewart, J. P. (2007). "Evaluation of the seismic performance of a code-conforming reinforced-concrete frame building from seismic hazard to collapse safety and economic losses." *Earthquake Engineering and Structural Dynamics*, 36, 1973–1997.
- Hansen, J. B. (1970). "A revised and extended formula for bearing capacity." *Danish Geotechnical Institute Bulletin, Copenhagen*, 28.

- Harden, C. W. (2003). "Numerical modeling of the nonlinear cyclic response of shallow foundations. Master's thesis, University of California, Irvine.
- Harden, C. W., Hutchinson, T., Martin, G. R., and Kutter, B. L. (2005). "Numerical modeling of the nonlinear cyclic response of shallow foundations." *Report No. 2005/04*, Pacific Earthquake Engineering Research Center, PEER.
- Harden, C. W., Hutchinson, T., and Moore, M. (2006). "Investigation into the effects of foundation uplift on simplified seismic design." *Earthquake Spectra*, 22(3), 663–692.
- Horvath, J. S. (1993). "Beam-column-analogy model for soil-structure interaction analysis." *ASCE Journal of Geotechnical Engineering*, 119(2), 358–364.
- Housner, G. W. (1963). "The behavior of inverted pendulum structures during earthquakes." *Bulletin of the Seismic Society of America*, 53(2), 403–417.
- Hutchinson, T., Raychowdhury, P., and Chang, B. (2006). "Nonlinear structure and foundation response during seismic loading: Dual lateral load resisting systems." *Proceedings, 8th US National Conference in Earthquake Engineering*, San Francisco, CA.
- Iai, S. and Sugano, T. (1999). "Soil-structure interaction studies through shaking table tests." *Proceedings, 2nd International Conference on Earthquake Geotechnical Engineering*, Vol. 3, Lisbon, Portugal. 927–940.
- IBC (2006). *International Building Code*. International Code Council, Delmar Publishers.
- Jeremic, B. and Zhaohui, Y. (2002). "Elastic-plastic computations in geomechanics." *International Journal for Numerical and Analytical methods in Geomechanics*, 26(14), 1407–1427.
- Khalil, L., Sadek, M., and Shahrour, I. (2007). "Influence of the soil-structure interaction on the fundamental period of buildings." *Earthquake Engineering and Structural Dynamics*, 36, 2445–2453.

- Knappett, J. A., Haigh, S. K., and Madabhushi, S. P. G. (2004). "Mechanisms of failure for shallow foundations under earthquake loading." *Proceedings, 11th International Conference on Soil Dynamics and Earthquake Engineering*, Vol. 2, University of California, Berkeley. 713–725.
- Konagai, K., Yin, Y., and Murono, Y. (2003). "Single-beam analogy for describing soil-pile group interaction." *Soil Dynamics and Earthquake Engineering*, 23, 213–221.
- Kutter, B. (1997). "Dynamic centrifuge modeling of geotechnical structures." Transportation Research Record 1336, University of California, Davis.
- Kutter, B., Martin, G., Hutchinson, T., Harden, C., Gajan, S., and Phalen, J. (2003). "Status report on study of modeling of nonlinear cyclic load-deformation behavior of shallow foundations." PEER Workshop March 5, 2003 Documentation, Pacific Earthquake Engineering Research Center.
- Lambe, W. T. and Whitman, R. V. (1969). *Soil Mechanics*. John Wiley and Sons, Inc. New York.
- Mander, J. B. and Priestly, M. (1988). "Theoretical stress-strain model for confined concrete." *ASCE Journal of Structural Engineering*, 114(8), 1804–1826.
- Martin, G. and Yan, L. (1997). "Development and implementation of improved seismic design and retrofit procedures for bridge abutments." University of Southern California.
- Martin, G. and Yan, L. (1999). *Simulation of Moment Rotation Behavior of a Model Footing*. FLAC and Numerical Modeling in Geomechanics, Detournay and Hart (Eds), Balkema, Rotterdam.
- Matlock, H. (1970). "Correlations for design of laterally loaded piles in soft clay." *Proceedings, 2nd Annual Offshore Technological Conference*, Vol. 1. Paper number 1204, Houston, Texas. 577–594.

- Maugeri, M., Musumeci, G., Novita, D., and Taylor, C. A. (2000). "Shaking table test of failure of a shallow foundation subjected to an eccentric load." *Soil Dynamics and Earthquake Engineering*, 20, 435–444.
- Mazzoni, S., McKenna, F., Scott, M. H., Fenves, G. L., and Jeremic, B. (2003). "OpenSees Users Manual, version 2.0. URL: <http://peer.berkeley.edu/~silvia/OpenSees/manual/html>.
- McKenzie, N. P. and Pender, M. J. (1996). "Representative shear modulus for shallow foundation seismic soil-structure interaction." *Proceedings, 11th World Conference on Earthquake Engineering*, Acapulco, Mexico. Paper no. 931.
- Meek, J. W. (1975). "Effects of foundation tipping on dynamic response." *Journal of the Structural Division*, 101(ST7), 1297–1311.
- Meek, R. A. (1967). "Building-foundation interaction effects." *Journal of the Engineering Mechanics Division*, 93(EM2), 131–152.
- Meyerhof, G. G. (1963). "Some recent research on the bearing capacity of foundations." *Canadian Geotechnical Journal*, 1(1), 16–26.
- Miranda, E. and Bertero, V. (1994). "Evaluation of strength reduction factors for earthquake-resistant design." *Earthquake Spectra*, 10(2).
- Mosher, R. (1984). "Load transfer criteria for numerical analysis of axially loaded piles in sand." *Report No. K-84 (1)*, US Army Engineers Waterways Experiments Station, Vicksburg, MS.
- Nakaki, D. K. and Hart, G. C. (1987). "Uplifting response of structures subjected to earthquake motions." U.S.-Japan Coordinated Program for Masonry Building Research. Report No. 2.1-3. Ewing, Kariotis, Englekirk and Hart.
- Negro, P., Verzeletti, G., Molina, J., Pedretti, S., Lo Presti, D., and Pedroni, S. (1998).

- “Large-scale geotechnical experiments on soil-foundation interaction: (trisee task 3).” *European Commission, Joint Research Center, Special Publication*, (1).
- NEHRP (2000). *Recommended Provisions for Seismic Regulations for New Buildings*. Building Seismic Safety Council, Washington, D.C.
- OpenSees (2008). “Open System for Earthquake Engineering Simulation:OpenSees.” Pacific Earthquake Engineering Research Center (PEER), University of California, Berkeley. URL: <http://opensees.berkeley.edu>.
- Paolucci, R. (1997). “Simplified evaluation of earthquake-induced permanent displacements of shallow foundations.” *Journal of Earthquake Engineering*, 1(3), 563–579.
- Paolucci, R. and Faccioli (1996). “Seismic behavior shallow foundations by simple elastoplastic models.” *Proceedings, 11th World Conference on Earthquake Engineering*, Acapulco, Mexico. Paper no. 2077.
- Paolucci, R. and Pecker, A. (1997). “Seismic bearing capacity of shallow strip foundations on dry soils.” *Soils and Foundations, Japanese Geotechnical Society*, 37(3), 95–105.
- Paolucci, R., Shirato, M., and Yilmaz, M. T. (2007). “Seismic behavior of shallow foundations: Shaking table experiments vs numerical modeling.” *Earthquake Engineering and Structural Dynamics*.
- Phalen, J. (2003). “Physical modeling of the soil-foundation interaction of spread footings subjected to lateral cyclic loading. Master’s thesis, University of California, Davis.
- Prandtl, L. (1921). “Über die eindringungsfestigkeit harte plastischer baustoffe and die festigkeit von schneiden.” *Zeitschrift für angewandte Mathematik und Mechanik*, 1(1), 15–20.
- Psycharis, I. (1983). “Dynamics of flexible systems with partial lift-off.” *Earthquake Engineering and Structural Dynamics*, 2, 501–521.

- Psycharis, I. N. (1981). "Dynamic behavior of rocking structures allowed to uplift," PhD thesis, California Institute of Technology.
- Rankine, W. J. M. (1847). "On the stability of loose earth." *Philosophical transactions of the Royal Society of London*.
- Raychowdhury, P. and Hutchinson, T. (2008). "Nonlinear material models for winkler-based shallow foundation response evaluation." *GeoCongress 2008*, Sacramento, CA.
- Reese, L. C. and ÓNeill, M. *Field Load Tests of Drilled Shafts*. Deep Foundations on Board and Auger Piles, Van IMpe (Ed), Balkema, Rotterdam.
- Reissner, H. (1924). "Zum erddruckproblem." *Proceedings, First International Congress of Applied Mechanics*, Delft. 295–311.
- Rollins, K. and Cole, R. (2006). "Cyclic lateral load behavior of a pile cap and backfill." *ASCE Journal of Geotechnical and Geoenvironmental Engineering*, 132(9), 1143–1153.
- Rosebrook, K. R. (2001). "Moment loading on shallow foundations: Centrifuge test data archives. Master's thesis, University of California Davis.
- Rosebrook, K. R. and Kutter, B. L. (2001a). "Soil-foundation structure interaction: Shallow foundations." Centrifuge Data Report for the KRR01 Test Series: Center for Geotechnical Modeling Data Report UCD/CGMDR-01, University of California, Davis.
- Rosebrook, K. R. and Kutter, B. L. (2001b). "Soil-foundation structure interaction: Shallow foundations." Centrifuge Data Report for the KRR01 Test Series: Center for Geotechnical Modeling Data Report UCD/CGMDR-02, University of California, Davis.
- Rosebrook, K. R. and Kutter, B. L. (2001c). "Soil-foundation structure interaction: Shallow foundations." Centrifuge Data Report for the KRR01 Test Series: Center for Geotechnical Modeling Data Report UCD/CGMDR-03, University of California, Davis.

- Salgado, R. (2006). *The Engineering of Foundations*. McGraw-Hill Science Engineering.
- Sato, A. A. and Mohajeri, M. (2004). "Ultra large laminar box design and sample preparation plan for tests on the largest shake table in the world." *Proceedings, 11th International Conference on Soil Dynamics and Earthquake Engineering*, University of California, Berkeley.
- Soubra, A. (1999). "Upper-bound solutions for bearing capacity of foundations." *ASCE Journal of Geotechnical and Geoenvironmental Engineering*, 125(1), 59–68.
- Spyrakos, C. C. and Xu, C. (2003). "Seismic soil-structure interaction of massive flexible strip-foundations embedded in layered soils by hybrid bem-fem." *Soil Dynamics and Earthquake Engineering*, 23, 383–389.
- Stewart, J. P., Fenves, G. L., and Seed, R. B. (1999). "Seismic soil-structure in buildings. i: Analytical methods." *ASCE Journal of Geotechnical and Geoenvironmental Engineering*, 125(1), 26–37.
- Stewart, J. P., Kim, S., Bielak, J., Dobry, R., and Power, M. S. (2003). "Revisions to soil-structure interaction procedures in NEHRP design provisions." *Earthquake Spectra*, 19(3), 677–696.
- Taylor, P. W., Bartlett, P. E., and Weissing, P. R. (1981). "Foundation rocking under earthquake loading." *Proceedings, 10th International Conference on Soil Mechanics and Foundation Engineering*, Vol. 3. 313–322.
- Taylor, P. W. and Williams, R. L. (1979). "Foundations for capacity designed structures.
- Tcl/Tk (2008). "Tcl Developer Xchange. URL: <http://www.tcl.tk/>.
- Terzaghi, K. (1943). *Theoretical Soil Mechanics*. J. Wiley, New York.

- Thomas, J., Gajan, S., and Kutter, B. (2004). "Centrifuge tests on square footings at University of California, Davis. Master's thesis, University of California Davis.
- Ugalde, J. (2007). "Centrifuge tests on bridge columns on shallow square footings. Master's thesis, University of California, Davis.
- Uniform Building Code (1997). *Structural Engineering Design Provisions, Volume 2, August*. International Conference of Building Officials, Whittier, California.
- Veletsos, A. and Meek, J. W. (1974). "Dynamic behavior of a building-foundation system." *Journal of Earthquake Engineering and Structural Dynamics*, 3(2), 121–138.
- Vijayvergiya, V. (1977). "Load-movement characteristics of piles." *Proceeding, Ports 77 Conference, American Society of Civil Engineers*, Long Beach, California, March.
- Weissmann, G. F. (1972). "Tilting foundation." *Journal of the Soil Mechanics and Foundation Division*, 98(SM1), 59–78.
- Wiessing, P. R. (1979). "Foundation rocking on sand." School of Engineering Report No. 203, University of Auckland, New Zealand.
- Winkler, E. (1867). "Die lehre von der elasticitaet und festigkeit. prag, dominicus.
- Yao, S., Kobayashi, K., Yoshida, N., and Matsuo, H. (2004). "Interactive behavior of soil-pile-superstructure system in transient state to liquefaction by means of large shake table tests." *Soil Dynamics and Earthquake Engineering*, 24, 397–409.
- Yim, S. C. and Chopra, A. (1985). "Simplified earthquake analysis of multistory structures with foundation uplift." *ASCE Journal of Structural Engineering*, 111(12), 2708–2731.
- Zhang, J. and Tang, Y. (2007). "Radiation damping of shallow foundations on nonlinear soil medium." *Proceedings, 4th International Conference on Earthquake Geotechnical*

Engineering, Thessaloniki, Greece.